2021

Toward Non-invasive in vivo Dosimetry of Proton Therapeutic Beam Using Prompt Gamma

Melek Zarifi
University of Wollongong

UNIVERSITY
OF WOLLONGONG
AUSTRALIA

Toward Non-invasive *in vivo* Dosimetry of Proton Therapeutic Beam Using Prompt Gamma

Melek Zarifi

This thesis is presented as required for the conferral of the degree:

Doctor of Philosophy

Supervisor: Dist. Prof. A. B. Rosenfeld
Co-Supervisors: Dr. D. Prokopovich, Assoc. Prof. S. Guatelli, Dr. Y. Qi

University of Wollongong
School of Physics, Faculty of Engineering and Information Sciences

30 March 2021

Declaration

I, Melek Zarifi, declare that this thesis, submitted in fulfilment of the requirements for the conferral of the degree Doctor of Philosophy, Faculty of Engineering and Information Sciences, School of Physics, University of Wollongong, is wholly my own work unless otherwise referenced or acknowledged. The document has not been submitted for qualifications at any other academic institution.

30 March 2021

Contents

DECLARATION **II**
LIST OF TABLES **V**
LIST OF FIGURES **VII**
LIST OF ACRONYMS **XII**
LIST OF PUBLICATIONS **XIV**
ABSTRACT **XVI**
ACKNOWLEDGMENTS **XVIII**
1 INTRODUCTION **19**
1.1 General Aspects of Particle Therapy 19
1.2 Requirements and Challenges of *in vivo* Range Verification and Dosimetry in Particle Therapy 20
1.3 Overview of *in vivo* Range Verification and Dosimetry Methods 21
1.4 Challenges of *in vivo* Range Verification and Dosimetry Using Prompt Gamma 27
1.5 Research Scope and Motivation of this Thesis 29
2 LITERATURE REVIEW **31**
2.1 The Physics of Particle Therapy 31
2.1.1 Electromagnetic Interactions 32
2.1.1.1 Energy Loss 32
2.1.1.2 Lateral Beam Spread 35
2.1.2 Nuclear Interactions 36
2.1.3 Comparison of Different Ion Species 39
2.2 Gamma Ray Detection and Measurement 41
2.2.1 General Properties of Radiation Detectors 41
2.2.1.1 Energy Resolution and Detection Efficiency 41
2.2.1.2 Dead Time 42
2.2.2 Conventional Gamma Detector Technology 42
2.2.2.1 Scintillation Detectors 42
2.2.2.2 Photo-detectors for Scintillation Light Readout 44
2.2.2.3 Pulse Processing, Shaping and Timing 46
2.2.3 Challenges of Detector Technology for Prompt Gamma Measurement 48
2.2.4 Overview of Advanced Detectors for Prompt Gamma Detection 49
2.3 Current Research Status of Prompt Gamma for *in vivo* Beam Range Verification and Dosimetry 52
2.3.1 Prompt Gamma Imaging (PGI) 55
2.3.1.1 Passive Collimation Imaging System 55
2.3.1.2 Active Collimation Imaging System 57
2.3.2 Prompt Gamma Spectroscopy (PGS) 60
2.3.3 Prompt Gamma Timing (PGT) 60
2.3.4 Prompt Gamma Peak Integration (PGPI) 62
2.4 The Role of Monte Carlo Simulations in *in vivo* Dosimetry Using Prompt Gamma 63
2.5 Further Research Required in the Prompt Gamma Method 65

3 CHARACTERISATION OF PROMPT GAMMA RAYS FOR BEAM RANGE VERIFICATION 67
3.1 Monte Carlo Geant4 Simulation Set-up 68
3.1.1 Homogeneous Spherical and Cylindrical Phantoms 68
3.1.2 Realistic DICOM-formulated Head Phantom 71
3.2 Energy Spectra of Prompt Gamma Emission 72
3.2.1 Homogeneous Phantoms 72
3.2.2 Realistic Head Phantom 76
3.3 Spatial Correlation between Prompt Gamma Emission and Particle Beam Range 77
3.3.1 Homogeneous Phantoms 77
3.3.2 Realistic Head Phantom 80
3.4 Prompt Gamma Emission and Detectable Yield 82
3.4.1 Homogeneous Phantoms 83
3.4.2 Realistic Head Phantom 86
3.5 Angular Distribution for Detectable Prompt Gamma Rays 87
3.5.1 Homogeneous Phantoms 88
3.6 Temporal Properties of Prompt Gamma Emission and Detection: Relationship with Particle Beam Range 90
3.6.1 Homogeneous Phantoms 90
3.6.2 Realistic Head Phantom 101
3.7 Discussion 103
4 SCINTILLATION DETECTOR CHARACTERISATION FOR PROMPT GAMMA MEASUREMENT 105
4.1 Experimental Set-up of Scintillation Detector Characterisation 105
4.2 Response Time of the Scintillation Detectors 108
4.3 Spectroscopy: Energy Resolution and Detection Efficiency 111
4.4 Discussion 114
5 SIMULATING PROMPT GAMMA RAYS FOR CLINICAL RANGE VERIFICATION 116
5.1 Experimental Set-up of the Prompt Gamma Detection System 116
5.2 Data Acquisition and Processing 118
5.3 Modelling of the Prompt Gamma Detection System 119
5.4 Comparison Study of Simulation and Experimental Results 122
5.4.1 Evaluating Geant4 Physics Lists: *QGSP_BIC_HP* and *QGSP_BIC_AllHP* 123
5.4.2 Evaluating the Reproducibility of Oxygen and Carbon: Water and HDPE 127
5.4.3 Comparison of Geant4 Versions: 10.05.p01 and 10.06.p01 130
5.5 Discussion 132
CONCLUSION 135
APPENDIX 1 – PREVIOUS PUBLICATION 140
REFERENCES 150

List of Tables

Table 1: Summary of energy resolutions and timing properties of several scintillators published in the literature, with reference given. 51
Table 2: Particle beam range and corresponding PG range for the applied energy threshold and window studied, for each particle beam type and energy. The Δ*fall-off* and Δ*FWHM*, defined in Section 3.1.1, are reported for quantitative evaluation. 79
Table 3: Particle beam range and corresponding PG range in water, PMMA and adipose tissue for the applied energy threshold and window studied, for each particle beam type with ~16 cm range. The Δ*fall-off*, defined in Section 3.1.1, is reported for quantitative evaluation. 80
Table 4: Particle beam range and corresponding PG range in the water-based and realistic head phantom for the applied energy threshold and window studied, for a proton beam of 100 MeV. The Δ*fall-off*, defined in Section 3.1.1, is reported for quantitative evaluation. 82
Table 5: Yield of gamma photons originating within the spherical water phantom and those reaching the detection sphere once emitted from the phantom. The simulation statistical uncertainty is within 5%. 84
Table 6: Yield values of gamma photons originating within the cylindrical water, PMMA and adipose tissue phantoms for the beam energy corresponding to a range of ~16 cm, and the gamma yield reaching the detection sphere once emitted from the phantom. The simulation statistical uncertainty is within 1%. 85
Table 7: Yield values of PG rays within 3.0-7.0 MeV emitted per MeV deposited at the BP maximum within the cylindrical water, PMMA and adipose tissue phantoms for the beam energy corresponding to a range of ~16 cm. The simulation statistical uncertainty is within 1%. 86
Table 8: Yield values of gamma photons originating within the water-based and realistic head phantoms for 100 MeV proton beams, as well as the gamma yield reaching the detection sphere once emitted from the phantom. The simulation statistical uncertainty is within 3%. 87
Table 9: Radiation sources used for detector characterisation measurements. The emission energies and intensity of emission were taken from Ref. [235]. 106
Table 10: Instruments used for detector characterisation measurements. The amplifier and power supply were mounted on a Nuclear Instrument Module (NIM). 106
Table 11: Scintillation detectors characterised in terms of timing and spectroscopy. * indicates the detectors connected to a PMT and ** indicates the detectors connected to a SiPM. $LaBr_3$(Ce) and $LaCl_3$(Ce) were studied with and without a built-in preamplifier. 108
Table 12: Timing properties of each scintillation detector, measured at 10-90% (rise time) and 90-10% (decay time) the signal amplitude. The uncertainty is given by the standard deviation of three repeated measurements. 110

Table 13: Energy resolution and detection efficiency at 662 keV, for each scintillator studied. Uncertainties were calculated with reference to error propagation (see for example, Knoll (2000) [66]). 113
Table 14: Total gamma, proton- and neutron-induced gamma counts in the energy range of 1.40-7.19 MeV per giga-proton (GP) in the detector rows, obtained with Geant4 (10.06.p01) *QGSP_BIC_HP* and *QGSP_BIC_AllHP* physics lists, from proton beam irradiation of the water phantom. The total neutron-induced count was taken as the background (it does not include prompt counts with discrete energy lines). Rounding of the counts was done only taking into account statistical errors..... 126
Table 15: Absolute counts per giga-proton (GP) for the proton-induced 4.44 and 6.13 MeV PG peaks, and the neutron-induced 2.22 MeV peak, obtained with Geant4 (10.06.p01) *QGSP_BIC_HP* and *QGSP_BIC_AllHP* physics lists, from proton beam irradiation of the water phantom. The proton-induced counts from *QGSP_BIC_AllHP* are omitted since this physics list does not contain the relevant proton data. Rounding of the counts was done only taking into account statistical errors..... 127
Table 16: Total gamma, proton- and neutron-induced gamma counts in the energy range of 1.40-7.19 MeV per giga-proton (GP) in the detector rows, obtained with Geant4 (10.06.p01) *QGSP_BIC_HP* and *QGSP_BIC_AllHP* physics lists, from proton beam irradiation of the HDPE phantom. The total neutron-induced count was taken as the background (it does not include prompt counts with discrete energy lines). Rounding of the counts was done only taking into account statistical errors. 129
Table 17: Absolute counts per giga-proton (GP) for the proton-induced 4.44 and 6.13 MeV PG peaks, and the neutron-induced 2.22 MeV peak, obtained with Geant4 (10.06.p01) *QGSP_BIC_HP* and *QGSP_BIC_AllHP* physics lists, from proton beam irradiation of the HDPE phantom. The proton-induced counts from *QGSP_BIC_AllHP* are omitted since this physics list does not contain the relevant proton data. Rounding of the counts was done only taking into account statistical errors..... 130
Table 18: Total gamma, proton- and neutron-induced gamma counts in the energy range of 1.40-7.19 MeV per giga-proton (GP) in the detector rows, obtained with Geant4 (10.05.p01) *QGSP_BIC_HP* physics list, from proton beam irradiation of the water phantom. The total neutron-induced count was taken as the background (it does not include prompt counts with discrete energy lines). Rounding of the counts was done only taking into account statistical errors. Data from version 10.06.p01 (Table 14) are also added for comparison. 131
Table 19: Absolute counts per giga-proton (GP) for the proton-induced 4.44 and 6.13 MeV PG peaks, and the neutron-induced 2.22 MeV peak, obtained with Geant4 (10.05.p01) *QGSP_BIC_HP* physics list, from proton beam irradiation of the water phantom. Rounding of the counts was done only taking into account statistical errors. Data from version 10.06.p01 (Table 15) are also added for comparison..... 132

List of Figures

Figure 1: Depth dose curves for photon and proton (pristine BP and SOBP) beams. From Ref. [10]..... 20
Figure 2: Schematic showing the time scale in emission of a PG ray and PET gamma rays. 23
Figure 3: Illustration of particle interaction mechanisms: electromagnetic interactions (a) inelastic Coulomb interaction of the particle with atomic electrons (energy loss) and (b) elastic Coulomb scattering of the particle with atomic nucleus (lateral scattering/beam spread), and nuclear interactions (c) non-elastic interaction of the particle with the atomic nucleus (loss of beam fluence and fragmentation). (p: proton, e: electron, n: neutron, γ: gamma ray). From Ref. [22]..... 31
Figure 4: Plots showing the mass stopping power S as a function of proton energy E in liquid water, and the corresponding range R calculated using the S values with the CSDA. From Ref. [22]..... 33
Figure 5: Left: Shape of a mono-energetic pristine BP (absorbed dose D vs depth z) for an initial 154 MeV broad proton beam. The protonic buildup region (buildup of secondary protons) is mainly attributed to proton-induced non-elastic nuclear interactions. The sub-peak region is where the stopping power's dependence on the inverse-square of the proton velocity is most significant, nuclear reactions cause removal of protons and liberation of secondary particles, and accumulation of lateral deflections (very small fields) from MCS. (z_{BP}, z_{d80}, z_{d20}: depth of maximum dose at the BP, distal-80% and distal-20% depths, respectively. $l_{\mathrm{80\text{-}80}}$, $l_{\mathrm{d80\text{-}20}}$: 80%-to-80% pristine peak width, distance between distal-80% and distal-20% depths, respectively). From Ref. [22]. Right: Energy E distributions of an initially mono-energetic beam of charged particles along penetration depth X. From Ref. [66]..... 35
Figure 6: Left: Depth dose profiles of primary 330 MeV/u ^{12}C ions and the associated secondary/tertiary fragments in water. Right: Build-up curves of secondary fragments produced by 400 MeV/u ^{12}C ions in water. From Ref. [87]. 38
Figure 7: Top: Illustration showing a nucleon-nucleus reaction for protons, whereby a neutron is created and a gamma emitted from the residual target nucleus. Bottom: Illustration showing a nucleus-nucleus reaction for heavy ions, whereby light fragments are created and gamma rays can be emitted from both residual projectile and target nuclei. From Ref. [65]. 39
Figure 8: The components and basic principles of a PMT. From Ref. [30]..... 44
Figure 9: Top: Time jitter in leading edge triggering resulting from random noise. Signal pulses with the same amplitude and shape, but with random noise, are enclosed in an envelope. Bottom: Amplitude walk in leading edge triggering. Two pulses that have the same time of occurrence and shape, but different amplitude, cross the trigger level at different times. From Ref. [66]. .. 48
Figure 10: Yield of PG rays (blue and red) and neutrons (black) registered in the detector, and depth dose profile for a mono-energetic 100 MeV proton pencil beam, as a function of the longitudinal distance z in a PMMA phantom (purple), without (left) and with (right) a 1 ns

shifting TOF acceptance window. PG profiles are shown for a narrow angular collimation window $\Delta\theta_2$ (red) and a wide window $\Delta\theta_1$ (blue). Simulated data with Geant4 is presented as (1) and MCNPX as (2). Bin width along z is 1 mm. Depth dose was calculated with Geant4 and is given in arbitrary units (a.u.). From Ref. [145]..... 54
Figure 11: Left: Concept of the PGI method with a slit camera, whereby the slit collimation gives a 1D projection of PG emissions along the beam path on a scintillation detector. From Ref. [158]. Right: Simulated incident 160 MeV protons (blue) and secondary photons (green) which are emitted and reach the detector after passing through the collimator. From Ref. [150]..... 56
Figure 12: Concept of a three-stage Compton camera (two scatter detectors and one absorber detector). The gamma rays with energies (E_0, E_1, E_2) scatter in the detectors (D1, D2, D3) with Compton scatter angles (θ_1, θ_2). The projected cone (into the target/patient) is used to reconstruct the images. The interaction position and energy deposition in each detector is shown. From Ref. [155]. 58
Figure 13: Range-dependent mean μ_γ (left) and standard deviation σ_γ (right) values of modelled PGT spectra. Proton energies are in the range of 50 to 230 MeV, corresponding to proton ranges of 2 to 27 cm in a PMMA target. The assumed system time resolution is 450 ps. From Ref. [171]..... 62
Figure 14: Left: Geometrical simulation set-up of the spherical water phantom in an air-filled detection sphere. Right: The angle θ is formed from the longitudinal beam direction (z-axis) with the line connecting the centre of the coordinate system and the point P. P is the PG detection position on the detection sphere traversed by the photons, and φ is the azimuthal angle. For the case of the cylindrical phantom, it replaces the spherical phantom in the simulation set-up, with the main axis along the direction of the incident beam..... 70
Figure 15: Geant4 visualisation of a slice of the realistic head phantom, as implemented in the Geant4 extended example DICOM [216]. The proton beam is not to scale. 72
Figure 16: Energy spectra of photons generated in the homogeneous spherical water phantom deriving from pencil beams of protons, ^{4}He and ^{12}C ions. The emission lines are characteristic to the major constituent elements of the phantom material. The distinctive PG emission lines of energy 4.44, 5.21 and 6.13 MeV result from ^{12}C, ^{15}O and ^{16}O nuclear de-excitations, respectively. 74
Figure 17: Energy spectra of photons generated in the homogeneous cylindrical water, PMMA and adipose tissue phantoms deriving from pencil beams of protons, ^{4}He and ^{12}C ions with a range of ~16 cm in the materials. The emission lines are characteristic to the major constituent elements of the phantom material. The distinctive PG emission lines of energy 4.44, 5.21 and 6.13 MeV result from ^{12}C, ^{15}O and ^{16}O nuclear de-excitations, respectively..... 75
Figure 18: Energy spectra of photons generated in the water-based and realistic head phantoms irradiated with a 100 MeV proton beam. The emission lines are characteristic to the major constituent elements of the phantom material. The distinctive PG emission lines of energy 4.44, 5.21 and 6.13 MeV result from ^{12}C, ^{15}O and ^{16}O nuclear de-excitations, respectively..... 76
Figure 19: Left: Longitudinal yield distribution of total, primary and secondary gamma rays ≥1 MeV originating in the water phantom for protons (150 MeV), ^{4}He (150 MeV/u) and ^{12}C (285

MeV/u) ions. The percent depth dose is normalised to the dose maximum at the Bragg peak. Right: Lateral yield distribution of total gamma rays ≥1 MeV for a longitudinal width of 10 mm at the BP positions for each of the beam energies. 78
Figure 20: Longitudinal yield distribution of total, primary and secondary gamma rays ≥1 MeV originating in the water-based and realistic head phantom for 100 MeV protons. The percent depth dose is normalised to the dose maximum at the Bragg peak. A (3.6 ± 0.7) mm shift in the proton beam range is seen between the two phantoms, and the PG emission closely correlates (~2 mm) to this shift..... 81
Figure 21: Angular distribution of total gamma rays reaching the idealised detecting sphere once emitted from the spherical water phantom normalised per incident ion per steradian for the lower two beam energies (left) and the higher two beam energies (right) for protons, ^{4}He and ^{12}C ions..... 88
Figure 22: Angular distribution of total gamma rays reaching the idealised detecting sphere once emitted from the cylindrical water, PMMA and adipose tissue phantoms normalised per incident ion per steradian for the lowest beam energy (beam range of ~3 cm) (left) and the highest beam energies (beam range of ~38 cm) (right) for protons, ^{4}He and ^{12}C ions. 89
Figure 23: Emission time distribution of total gamma rays (left) and gamma rays ≥1 MeV (right) originating in the spherical water phantom for protons, ^{4}He and ^{12}C ions. The bin width is 0.01 ns. 91
Figure 24: Emission time distribution of total gamma rays (left) and gamma rays ≥1 MeV (right) originating in the cylindrical PMMA phantom for protons, ^{4}He and ^{12}C ions. The bin width is 0.01 ns. 92
Figure 25: Emission time distribution of total gamma rays (left) and gamma rays ≥1 MeV (right) originating in the cylindrical adipose tissue phantom for protons, ^{4}He and ^{12}C ions. The bin width is 0.01 ns. 93
Figure 26: TOF spectra of total gamma and neutrons (left) and gamma rays ≥1 MeV (right) reaching the detection sphere once emitted from the spherical water phantom for protons, ^{4}He and ^{12}C ions. The bin width is 0.1 ns. 94
Figure 27: TOF spectra of total gamma and neutrons (left) and gamma rays ≥1 MeV (right) reaching the detection sphere once emitted from the cylindrical PMMA phantom for protons, ^{4}He and ^{12}C ions. The bin width is 0.1 ns. 95
Figure 28: TOF spectra of total gamma and neutrons (left) and gamma rays ≥1 MeV (right) reaching the detection sphere once emitted from the cylindrical adipose tissue phantom for protons, ^{4}He and ^{12}C ions. The bin width is 0.1 ns. 96
Figure 29: TOF spectra along the polar angle θ of primary gamma rays reaching the detection sphere once emitted from the phantom for protons, ^{4}He and ^{12}C ions. 97
Figure 30: TOF spectra along the polar angle θ of primary gamma rays ≥1 MeV reaching the detection sphere once emitted from the phantom for protons, ^{4}He and ^{12}C ions. 98
Figure 31: Quantitative comparison of the particle beam range with PG emission and detection data in the spherical water phantom for protons, ^{4}He and ^{12}C ions. Left: Particle beam range and corresponding PG range, with PG emission time. The dotted line joining the particle range

values serves to guide the eye. Right: PG TOF peak mean, width and integral. All PG data are for gamma rays ≥1 MeV. The uncertainty in the beam range is 0.5 mm, PG range is 0.1 mm, emission time/TOF mean is 0.1 ns, and TOF width is 0.2 ns. 99
Figure 32: Quantitative comparison of the particle beam range with PG emission and detection data in the cylindrical PMMA phantom for protons, ^{4}He and ^{12}C ions. Left: Particle beam range and corresponding PG range, with PG emission time. The dotted line joining the particle range values serves to guide the eye. Right: PG TOF peak mean, width and integral. All PG data are for gamma rays ≥1 MeV. The uncertainty in the beam range is 0.5 mm, PG range is 0.1 mm, emission time/TOF mean is 0.1 ns, and TOF width is 0.2 ns. 100
Figure 33: Quantitative comparison of the particle beam range with PG emission and detection data in the cylindrical adipose tissue phantom for protons, ^{4}He and ^{12}C ions. Left: Particle beam range and corresponding PG range, with PG emission time. The dotted line joining the particle range values serves to guide the eye. Right: PG TOF peak mean, width and integral. All PG data are for gamma rays ≥1 MeV. The uncertainty in the beam range is 0.5 mm, PG range is 0.1 mm, emission time/TOF mean is 0.1 ns, and TOF width is 0.2 ns. 101
Figure 34: Top: Emission time distribution of total gamma rays and gamma rays ≥1 MeV originating in the water-based and realistic head phantoms. The bin width is 0.01 ns. Bottom: TOF spectra of total gamma, gamma rays ≥1 MeV and neutrons reaching the detection sphere once emitted from the head phantoms. The bin width is 0.1 ns. The proton beams irradiating the phantoms are of 100 MeV..... 102
Figure 35: Top: Circuit diagram of experimental set-up for timing measurements, showing a capacitor coupling from the detector and a charge sensitive preamplifier. Bottom: Circuit diagram of set-up for spectroscopy, showing a preamplifier, shaping amplifier, MCA and PC. The oscilloscope is connected for display and analysis of signal pulses. The PMT or SiPM (not explicitly shown) is coupled to the detector..... 107
Figure 36: Signal waveforms for each scintillation detector studied. The waveforms in the bottom row figures are normalised in the time axis to the 20 mV signal amplitude for better visual comparison. The CLLBC376 and CLLBC398 waveforms were averaged across four and five signal pulses, respectively, to remove pickup noise. The bin size along the time axis in all figures is 0.4 ns. 110
Figure 37: Intrinsic peak detection efficiency curves for each scintillator studied..... 113
Figure 38: Schematic diagrams showing the experimental set-up configuration for the water phantom (left) and HDPE phantom (right). All units are in mm. The eight (two rows of four detectors) $LaBr_3(Ce)$ detectors are 50.8 mm in diameter and 76.2 mm in length. The collimator consists of five tungsten slabs (each $25.4 \times 203.2 \times 127.0$ mm^3 $\pm$ 0.5 mm) with a (12.7 ± 0.2) mm slit opening after the first and fourth slab (along the beam direction), and (6.4 ± 0.2) mm slit opening after the second slab. For simplicity and clarity, the front plate and aluminium aperture (between collimator and phantom) are omitted. The red line indicates the proton pencil beam incidence on the phantom, and the centre of the target volume (red dotted-square) represents the position of isocentre in the treatment room. The distance from isocentre to the front face of the phantom was (124.0 ± 0.5) mm. The distance between isocentre and the

collimator front plane was (150.0 ± 0.5) mm, with an air gap of (100.0 ± 0.5) mm. Figures adapted from Ref. [59] with permission. 118
Figure 39: TOPAS model of the MGH PGS detection system with the water phantom, based on the experimental set-up. The proton beam is not to scale. 120
Figure 40: Simulated energy spectra of total gamma, proton- and neutron-induced gamma rays in detector row 1 from the water phantom using Geant4 10.06.p01 and the *QGSP_BIC_HP* physics list. 123
Figure 41: Energy spectra of proton-induced gamma rays in detector row 1 from the water phantom. The measured spectrum is shown with the simulated spectra using Geant4 (10.06.p01) physics lists *QGSP_BIC_HP* and *QGSP_BIC_AllHP*. 124
Figure 42: Measured and simulated neutron-induced gamma ray background curves for detector row 1 from the water phantom. The simulated plots were obtained using Geant4 (10.06.p01) physics lists *QGSP_BIC_HP* and *QGSP_BIC_AllHP*. The insert shows the measured plot at 20%, to identify a possible correlation in the trend with the simulated plots. 125
Figure 43: Energy spectra of proton-induced gamma rays in detector row 1 from the HDPE phantom. The measured spectrum is shown with the simulated spectra using Geant4 (10.06.p01) physics lists *QGSP_BIC_HP* and *QGSP_BIC_AllHP*. 128
Figure 44: Measured and simulated neutron-induced gamma ray background curves for detector row 1 from the HDPE phantom. The simulated plots were obtained using Geant4 (10.06.p01) physics lists *QGSP_BIC_HP* and *QGSP_BIC_AllHP*. The insert shows the measured plot at 20%, to identify a possible correlation in the trend with the simulated plots. 129
Figure 45: Energy spectra of proton-induced gamma rays in detector row 1 from the water phantom, using Geant4 versions 10.06.p01 and 10.05.p01 with the *QGSP_BIC_HP* physics list. The measured spectrum is also included for comparison. 131

List of Acronyms

1D one-dimensional

2D two-dimensional

3D three-dimensional

4D four-dimensional

BIC Binary cascade / Binary Light Ion Cascade

BP Bragg peak

CLLB $Cs_2LiLaBr_6(Ce)$

CLLBC $Cs_2LiLaBr_{6-x}Cl_x(Ce)$

CLLC $Cs_2LiLaCl_6(Ce)$

CLYB $Cs_2LiYBr_6(Ce)$

CLYC $Cs_2LiYCl_6(Ce)$

CRT coincidence resolving time

CSDA continuous-slowing-down-approximation

CT computed tomography

DAQ data acquisition

DICOM Digital Imaging and Communication in Medicine

FOV field-of-view

FPGA field-programmable gate array

FWHM full-width-at-half-maximum

HDPE high-density polyethylene

HU Hounsfield unit

HV high voltage

IBA Ion Beam Applications

ICRP International Commission on Radiological Protection

ICRU International Commission on Radiation Units and Measurements

INC intra-nuclear cascade

MCA multichannel analyser

MCS multiple Coulomb scattering

NIST National Institute of Standards and Technology

OAR organs-at-risk

OER oxygen enhancement ratio

PBS pencil beam scanning

pCT proton computed tomography

PET positron emission tomography

PG prompt gamma

PGI prompt gamma imaging

PGPI prompt gamma peak integration

PGS prompt gamma spectroscopy

PGT prompt gamma timing

PMMA polymethyl methacrylate

PMT photomultiplier tube

PSPT passive scattered proton therapy

QA quality assurance

QGS Quark-Gluon String

QMD quantum molecular dynamics

RBE relative biological effectiveness

RF radiofrequency

ROI region of interest

RSP relative stopping power

SiPM silicon photomultiplier

SOBP spread-out-Bragg-peak

SOE stochastic origin ensemble

SRIM Stopping and Range of Ions in Matter

TENDL TALYS-based Evaluated Nuclear Data Library

TOF time-of-flight

TPS treatment planning system

List of Publications

First author peer-reviewed publications:

M Zarifi, S Guatelli, D Bolst, B Hutton, A Rosenfeld, Y Qi, *Characterization of prompt gamma-ray emission with respect to the Bragg peak for proton beam range verification: A Monte Carlo study*, Physica Medica 2017, 33: p. 197-206.

M Zarifi, S Guatelli, Y Qi, D Bolst, D Prokopovich, A Rosenfeld, *Characterization of prompt gamma ray emission for in vivo range verification in particle therapy: A simulation study*, Physica Medica 2019, 62: p. 20-32.

Conference proceedings:

M Zarifi, Y Qi, S Guatelli, B Hutton, A Rosenfeld, *Investigation of optimized prompt gamma detection strategy for real-time Bragg Peak tracking in proton radiation therapy*, IEEE NSS/MIC 2015, p. 1-5.

M Zarifi, S Guatelli, D Bolst, B Hutton, A Rosenfeld, Y Qi, *Characterization of angular detection dependence of prompt gamma-rays with respect to the Bragg peak in a water phantom using proton beam irradiations*, IEEE NSS/MIC/RTSD 2016, p. 1-5.

M Zarifi, S Guatelli, Y Qi, D Bolst, D Prokopovich, A Rosenfeld, *Characterization of prompt gamma rays for in-vivo range verification in hadron therapy: A Geant4 simulation study*, MMND 2018, p. 1-4.

Conference oral presentations:

Characterisation of prompt gamma rays for proton beam range verification: A Monte Carlo study, 3rd Monte Carlo Workshop for Radiotherapy, Imaging and Radiation Protection, University of Wollongong, Wollongong, NSW Australia, 29/04/2016.

A Geant4 simulation study for in-vivo range verification in proton therapy, Geant4 Users Workshop, Sage Hotel, Wollongong, NSW Australia, 20/09/2017.

In-vivo beam range verification in hadrontherapy using prompt gamma rays: A Geant4 simulation study, ANSTO User Meeting, National Centre for Synchrotron Science, Clayton, VIC Australia, 22/11/2017.

In-vivo range verification in particle therapy using prompt gamma: A Geant4 simulation study, MedPhys Student Research Symposium, NSW/ACT Branch, ACPSEM, University of Sydney, Sydney, NSW Australia, 07/12/2017.

In-vivo range verification in hadron therapy using prompt gamma rays: A Geant4 simulation study, MMND ITRO, Mantra Mooloolaba Beach, Mooloolaba, QLD Australia, 08/02/2018.

Characterisation of prompt gamma ray emission and detectability for in vivo dosimetry in particle therapy: A simulation study, National Particle Therapy Symposium, Westmead Institute of Medical Research, Westmead, NSW Australia, 03/07/2018.

Conference poster presentation:

Characterization of prompt gamma ray detectability for real-time beam range verification in particle therapy, IEEE NSS/MIC, International Convention Centre Sydney, Sydney, NSW Australia, 15/11/2018.

Abstract

Technological advancements of particle therapy for high-precision cancer treatment require *in situ* and *in vivo* beam range and dose verifications to ensure safe and accurate targeted dose delivery while sparing healthy tissue and critical organs-at-risk. The use of prompt gamma (PG) rays, which are emitted as secondary by-products during beam irradiation, have been proposed as a promising means for *in vivo* Bragg peak (BP) tracking. Although significant research efforts have been made worldwide in the past two decades, the technological challenges for clinically applicable PG detection device development and associated system integration with the particle therapy treatment still remain to be tackled.

The research effort of this thesis was targeted at those challenges in PG detection methodology and technology. This work thus spans three major aspects: (i) Systematic Geant4 simulation studies of PG emission and detection characteristics from multi-dimensions of energy, space and time. This study aimed to determine optimal PG detection methodologies and technologies. (ii) Characterisation of commercially available advanced scintillation crystals to explore suitable high-performance detectors for energy- and time-resolved PG measurements toward a potential hybrid PG detection system. The measurements were performed at the Australian Nuclear Science and Technology Organisation (ANSTO). (iii) Performance evaluation of Monte Carlo simulation predictions of PG rays with a dedicated PG spectroscopy (PGS) prototype system at the Massachusetts General Hospital (MGH) (Boston, USA).

The PG emission characteristics were investigated for the most commonly used particle therapy ions of proton, ^{12}C and ^{4}He ion beam irradiations of both homogeneous (water, PMMA, adipose tissue) and heterogeneous (DICOM-formulated head phantom) targets, while the detectable PG characteristics were investigated by virtue of an air-filled idealised detecting sphere encompassing the phantoms. Several important results were obtained: the PG signal is a reliable means for *in vivo* BP tracking in particle therapy, particularly the primary PG rays; quantitative data showed that the PG-BP correlation holds for heterogeneous targets as well as homogeneous ones; a movable detector coordinated with respect to the beam range could optimise the PG detection efficiency; and the time-of-flight (TOF) information was seen to correlate with the particle beam range, and so can be utilised not only for interference background rejection but also for beam range extraction. Hence, a hybrid PG detection system that utilises the energy, spatial as well as TOF information could offer superior *in vivo* range and dose monitoring.

The energy- and time-resolved spectroscopy capabilities of several scintillation detectors were characterised, and showed that $LaBr_3$(Ce) offered superior time (34 ns rise time, 790 ns decay time) and energy resolution (3.5% at 662 keV). Elpasolite crystals, such as CLYC and CLLBC, have not yet been studied for the purpose of particle range monitoring using PG rays, but have the added ability of gamma-neutron discrimination, and thus have the potential for hybrid PG systems. In this work, CLYC was seen to offer a good energy resolution of 3.4% at 662 keV.

The performance comparison between Monte Carlo simuations and experimental data from the MGH PGS system was the first comprehensive evaluation study of both PG signal intensity and the interference background in a realistic clinical condition. Several important results were obtained: the Geant4 *QGSP_BIC_HP* physics list showed a suitable prediction of the overall proton-induced PG emission lines, yet it slightly overestimated the PG lines in the lower energy region (1-3.5 MeV) and underestimated the PG lines in the higher energy region (5-7 MeV), whereas *QGSP_BIC_AllHP* provides a better overall spectrum base shape, compared with the measured gamma spectrum; future PG simulations may benefit from taking into account potential neutron sources in close proximity to the measuring device, to more accurately predict the PG signal; and simulation results can greatly depend on the Geant4 version utilised, so it is recommended to perform regression testing on some physical observables among different versions of Geant4, including the latest one.

In conclusion, hybrid PG detection that utilises multi-features of PG rays in energy, space and time dimensions is highly recommended. High-throughput and highly efficient detector systems are needed for simultaneous energy- and time-resolved PG measurements. The current physics lists in the Geant4 simulation package need further improvement for its prediction accuracy of PG emissions and interference backgrounds. The studies in this thesis pave an effective pathway in the development of clinically applicable and reliable PG procedures and detectors, which can further improve cancer treatment precision and release the full clinical efficacy of particle therapy.

Acknowledgments

I would like to express my gratitude to a number of people, many of whom are members of the University of Wollongong (UOW) Centre for Medical Radiation Physics (CMRP), and the Australian Nuclear Science and Technology Organisation (ANSTO) in Australia, as well as Massachusetts General Hospital (MGH) in Boston USA.

I thank my supervisor Dist. Prof. Anatoly Rosenfeld (CMRP) for his constant support, contribution and dedication to the completion of this project.

I thank my supervisor Dr. Dale Prokopovich (ANSTO, MedAustron since July 2020) for his assistance and contribution to this project.

I thank Assoc. Prof. Susanna Guatelli (CMRP) for her support and contribution to this project.

I thank Dr. Yujin Qi (CMRP) for his constant support, guidance and contribution to this project.

I thank Dr. David Bolst (CMRP) for his constant help with Geant4 throughout this project. His assistance is much appreciated. I also thank Dr. Valentina Giacometti for her help with the Geant4 DICOM Head Phantom.

I thank Dr. Thomas Bortfeld (MGH) and Dr. Joost Verburg (MGH) for accepting me to join the Prompt Gamma team at MGH and their contribution to this project. My sincere gratitude goes to Dr. Fernando Hueso-González for his constant support during my time at MGH and for his contribution to this project.

This research has been conducted with the support of the Australian Government Research Training Program Scholarship.

We would like to thank the University of Wollongong Information Management & Technology Services (IMTS) for computing time on the UOW High Performance Computing Cluster.

We would like to thank Australia's National Computing Infrastructure (NCI) for computing time on the Raijin and Gadi cluster. We would like to thank the National Computational Merit Allocation Scheme (NCMAS) 2020 grant scheme which provided computing resources used in the thesis project.

My warmest gratitude and many thanks go to the people who have stood by my side through this time of hard work and dedication, my good friends and my loving family, without whom I would not have had the strength to carry on each day. Thank you.

1 Introduction

1.1 General Aspects of Particle Therapy

Particle therapy uses beams of charged particles, such as protons or the heavier helium and carbon ions, to deliver radiation dose to patients for the treatment of cancers. Robert R. Wilson first proposed the use of protons as a method of radiation therapy in 1946 [1]. The first patient treatment was performed in 1954 at Lawrence Berkeley Laboratory (LBL), Berkeley USA [2], and then heavier ions followed at the Bevalac facility at LBL in1975 [3]. Then in 1990, the first hospital-based proton therapy facility opened at the Loma Linda University Medical Center (LLUMC) in California [4]. Since then, research and developments have paved the way for improvements in radiation therapy dose delivery accuracy and techniques. Currently, there are 98 proton therapy facilities and 12 carbon ion facilities in clinical operation worldwide [5].

The goal of radiation therapy is to deliver a highly localised and uniform dose to the target volume to kill cancer cells while sparing normal healthy tissue. Unlike conventional photon beams which have a high entrance dose as well as exit dose, beams of charged particles deposit most of the energy at the end-of-range with little entrance dose and lateral scattering, where the particles stop inside the patient at the distal edge of the target volume. The maximum energy deposition at the particle beam end-of-range is called the Bragg peak (BP), where a mono-energetic particle beam produces a Bragg curve with a single pristine BP. By summing several pristine BPs of varied energies, a so-called spread-out-Bragg-peak (SOBP) can be achieved, where the dose is uniform and maximum across the entire target volume. Hence, dose can be conformed closely to the target volume. Figure 1 shows the depth dose comparison of photon and proton (pristine BP and SOBP) beams. Particle therapy therefore has the potential for higher probability of local control and disease-free survival, and lower probability of normal tissue damage [6], reducing the risk of side effects and further complications. Additionally, the enhanced relative biological effectiveness (RBE) of heavy ions is beneficial for the treatment of radio-resistant or paediatric tumours [7]. However, the ability to fully exploit the advantages of particle therapy and to release its full clinical efficacy is still limited by various uncertainties in predicting and determining the beam range within the patient [8]. These uncertainties, which are discussed in the next section, affect the achievable treatment precision and lead to the employment of clinical safety margins [9]. Therefore, *in vivo* range verification and dose monitoring in real-time are desired so to ensure high quality particle therapy treatment, eventually limiting collateral effects to organs-at-risk (OAR) close to the treatment target.

Although much progress has been made, these methods are still unavailable in clinical routine and this project contributes to fill the knowledge gap, towards a clinical implementation of PG detection for particle therapy Quality Assurance (QA).

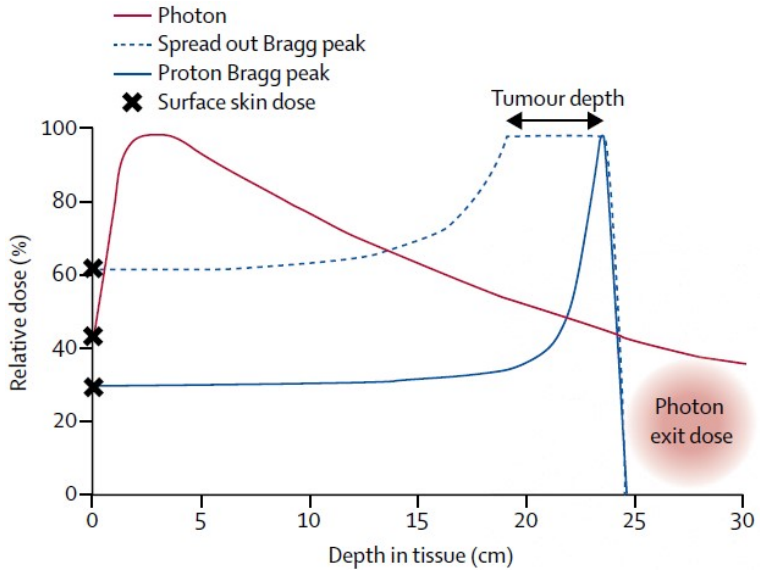

Figure 1: Depth dose curves for photon and proton (pristine BP and SOBP) beams. From Ref. [10].

1.2 Requirements and Challenges of *in vivo* Range Verification and Dosimetry in Particle Therapy

In charged particle therapy, there exists an unavoidable technical issue, referred to as beam range uncertainty [8,9]. Due to the electromagnetic interaction characteristics between charged particles and human tissues, the beam range is very sensitive to the tissue composition and density, and further complicated by multiple Coulomb scattering (MCS) and nuclear reactions. The ion beam BP position and beam range can therefore be difficult to estimate and determine.

The main causes of beam range uncertainty arise from both treatment planning and treatment delivery [11]. There exists some degree of errors in converting Hounsfield units (HUs) of CT images into particle stopping power maps, which can result in an uncertainty in predicting the beam range in tissues during the treatment planning [9]. To address this problem, proton CT (pCT) is a technique under development that directly measures relative proton stopping power with respect to water; uncertainties in proton therapy can be reduced, such that the uncertainty in converting x-ray CT HU to relative stopping power (RSP) and x-ray CT artifacts can be eliminated [12-15]. Additional uncertainties arise from patient position set-up

errors, intra-fractional organ motion and anatomical changes during the course of the treatment delivery.

These uncertainties can largely affect the treatment accuracy and precision of charged particle therapy, and the delivered dose may be different to the prescribed dose distribution, which can result in under-dosing the targeted tumour volume or over-dosing the adjacent critical structures and healthy tissues. Therefore, conservative safety margins have been generally adopted in current clinical practices. For example, MGH employs a proton beam range margin of 3.5% plus an additional 1 mm, which result in about 8 mm of tissue added to the treated target volume [9]. Yet, with range verification techniques, the margins could be reduced. Worldwide research efforts have been made to develop clinically applicable detector systems and procedures for reducing range uncertainties and the safety margins over the past two decades.

As the technology advances to intensity modulated pencil beam scanning (PBS) with sharpening beam spots to give the precision of a scalpel [16], the influence of these uncertainties become more significant, which deeply affect the accuracy of the delivered dose to the tumour target and limit the advantage of the PBS conformity. Significant challenges of clinical dosimetry for PBS charged particle therapy have been comprehensively discussed in a recent review paper, Giordanengo et al. (2017) [17]. In this context, the method of safety margin would inevitably lose its effectiveness. Spot-by-spot based beam range verification *in situ* and *in vivo* dosimetry for 3D treatment verification is required. The combination of prompt gamma (PG) ray measurements with 4D CT and motion monitoring has been proposed to control the range and dose distribution [18].

Moreover, other factors to consider in the clinical implementation of an *in vivo* dosimetry system include: the system itself should not physically interfere with the delivery of treatment; the monitoring process should not lengthen the time in which the patient is in the treatment room, considering the high throughput of patient treatments and operational costs; and the system should be able to handle the delivery characteristics of short irradiation times and high treatment beam intensities [19].

1.3 Overview of *in vivo* Range Verification and Dosimetry Methods

Several approaches for *in vivo* range verification and dosimetry have been and are currently being developed for particle therapy QA. The method can be classified as *direct*, such that the beam range is obtained directly from dose or fluence measurements, or *indirect*, such that the beam range is determined from other signals. *In vivo* range verification methods, both

direct and indirect, have been reviewed in Knopf and Lomax (2013) [20]. Here, indirect methods will mainly be discussed as they are more relevant to this thesis.

Indirect range verification methods use the by-products of secondary radiations that occur during irradiation and escape the patient, since the primary beam stops within the patient. Secondary radiation may include gamma rays, such as PG rays used in the PG imaging (PGI) method, or photons coming from positron-electron annihilation which are used in the positron emission tomography (PET) imaging method. Neutrons, along with photons, can also be used to identify a correlation between secondary radiation and dosimetric parameters [21], but the associated detection challenges are greater than those of photons. Other methods include magnetic resonance imaging (MRI), interaction vertex imaging (IVI), secondary electron bremsstrahlung (SEB), and ionoacoustic tomography.

Prompt gamma for beam range verification in particle therapy is becoming increasingly popular. While traversing tissue, the incident ions undergo nuclear reactions whereby the nucleus is excited to a higher energy state, and decays by emitting gamma rays. If the gamma ray is emitted promptly, i.e. within a few nanoseconds, it is referred to as a prompt gamma (PG). As the energy of the incident ion decreases in the medium, the total non-elastic nuclear interaction cross section increases up to a few millimetres before the BP. Then, the inelastic reaction cross section begins to drop, such that the incident kinetic energy falls below the Coulomb barrier threshold [22]. Hence, the position of production of PG rays is well-correlated with the beam range, but it is not exact, as the PG emission and dose deposition result from different physical processes. Thus, a consistent PG-dose distal fall-off difference is required for beam range verification [23]. Further details on the physics of PG emission via nuclear interactions are given in Section 2.1. Since PG rays are emitted within a few nanoseconds following the nuclear interaction generating an excited nucleus in the medium, they offer the ability to perform real-time monitoring of the dose delivery. This is a major advantage compared to PET, for example, which gives a delayed signal and also suffers biological washout effects. Figure 2 shows a time scale of PG emission compared to PET gamma emission. Furthermore, PG rays have a wide energy spectrum, up to around 15 MeV [24], which are unique and characteristic to the element since the excited nuclear states are quantised. The discrete spectral lines therefore contain valuable information of tissue composition and elemental concentration for spectral analysis [25]. Other advantages of utilising PG rays are the absence of washout effects, on-line treatment monitoring without additional dose, and high count rates [20,23,26-28]. However, the use of PG rays for beam range verification is still unavailable in clinical routine as challenges remain in detection methodology and technology (further discussed in the next section), yet significant efforts continue to be pursued and are discussed in the next chapter of this thesis.

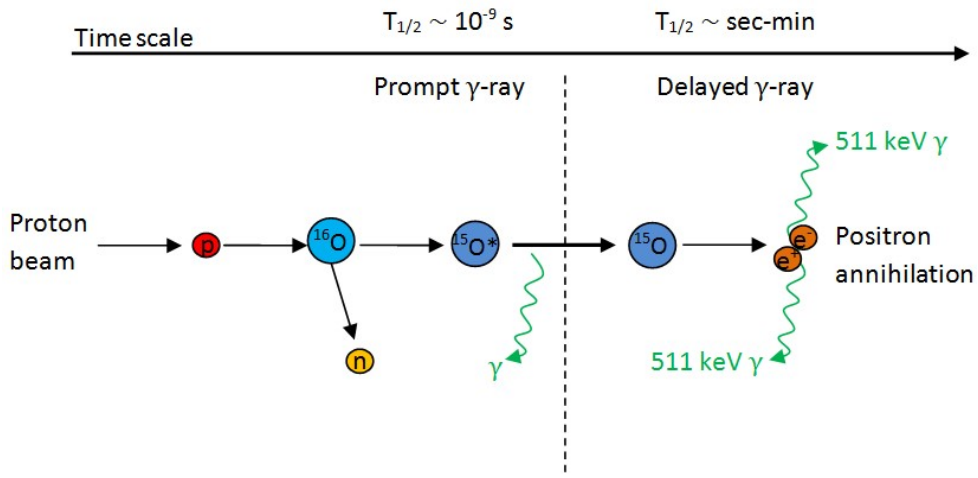

Figure 2: Schematic showing the time scale in emission of a PG ray and PET gamma rays.

Positron emission tomography (PET) uses coincident 511 keV gamma rays resulting from electron-positron annihilation. Inelastic interactions of protons with atomic nuclei can create positron-emitting isotopes (e.g. ^{11}C, ^{13}N and ^{15}O [29]) via β^+-decay. Positrons then annihilate with electrons of the target, resulting in the emission of two coincident annihilation photons of 511 keV, emitted in opposite directions [30]. For proton beams, β^+-activation only results from induced target fragmentation, whereas for heavier ions the activation may arise from projectile as well as target fragmentation [31]. Hence the activation is dependent on the tissue composition, making the relationship between induced activity and dose distributions complicated, such that the same dose distribution delivered to different geometries/tissue composition results in different activity distributions [20,32]. Also, the PET signal is generated from various radionuclides of different half-lives, which translates to a change of the activity distribution with time, so PET imaging for range verification is sensitive to the time of data acquisition [31]. Similarly to PG emission, the threshold energies for β^+ radioisotope production causes the activity distribution to fall before the incident particle dose distribution fall-off [29]. Hence, PET measurements must be compared with predicted activity distributions [31], such as from Monte Carlo calculations or a convolution of the dose distribution with a filter function [20,33]. PET imaging can be performed on-line (during irradiation) or off-line (a certain time after the treatment is completed) [29]. On-line allows shorter imaging times (however gaining sufficient statistics is important) and it minimises the effect of biological washout, patient repositioning errors and anatomical morphological changes since PET data are acquired with the patient at the treatment position, whereas off-line does not require capital investment for the installation of a scanner in the treatment room and has no impact on the patient treatment throughput [20,29,31].

Magnetic resonance imaging (MRI) reveals changes in the formation of human tissue caused by radiation. It involves imaging the nucleus of the hydrogen atom (i.e. the proton) which is abundant in the human body. The angular momentum of a positively charged proton produces a nuclear magnetic moment. In the absence of an external magnetic field, a collection of these moments (or spins) will have random orientations which results in zero net magnetisation, while in an external magnetic field each spin will align either parallel or anti-parallel to the direction of the applied field. A radiofrequency (RF) coil is used for signal reception, to detect the rotating magnetisation, such that the changing magnetic flux through the coil induces voltage changes that are subsequently detected by a receiver [34]. For beam range verification, visual inspection of MRI images alone is not sufficient since the location of greatest signal intensity (SI) gradient does not exactly correspond to the greatest dose gradient, instead a relationship between dose and SI must be established. A dose-SI curve for fatty marrow conversion has been established for a data set of 10 spine patients, and used to estimate range errors in the lumbar spine distal dose fall-off region [35]. Similarly, a conversion has been established with a data set of 5 liver patients [36]. MRI scanners are widely available, the imaging offers superior soft tissue contrast and high spatial resolution, with no additional ionising radiation exposure. However, temporal evolution i.e. side-effects of irradiation (hours to days later) such as cellular depletion, haemorrhage etc, may interfere with the MRI signal as a result of fatty replacement. As well, a ground truth dose-SI relationship is essential. In summary, despite the advantages of MRI, the availability of such scanners, and previous studies showing promising outcomes, further work is necessary for the use of MRI for *in vivo* range verification [20].

Interaction vertex imaging (IVI) is based on the detection of secondary particles (such as protons that escape the patient) to reconstruct nuclear emission vertices. First proposed by Amaldi et al. (2010) [37], the technique has been studied in simulations [38-40] and experiments [39,41,42]. Popular for carbon ion therapy, IVI offers the ability for real-time monitoring since the secondary particles are emitted and detected promptly during irradiation. Yet, since the energy of incident carbon ions decreases significantly at the end-of-range, the corresponding secondary particles produced in this region will also be of low energy and so may not escape the patient for detection. Hence, IVI may not offer a method to directly measure the BP position, but using information from the distribution of reaction sites superficial to the BP can allow indirect localisation [40]. Two methods of IVI for real-time BP localisation have been described in an early study [38]: single-proton IVI (SP-IVI) where the vertex is reconstructed using the incident carbon ion trajectory that is determined by a beam hodoscope; and double-proton IVI (DP-IVI) which detects coincidence between two protons emitted from the same vertex. This study found SP-IVI to be the more promising technique, with target thickness and

ion energy having a major influence on reconstructed vertex profiles. In a recent study [40], the group combined SP-IVI and DP-IVI, using a novel Triangulation IVI technique for reliable sub-millimetre BP localisation, and developed a software filter used to classify secondary particles as appropriate candidates for reconstruction. The study also identified the relationship between the distal edge of the filtered vertex distribution and the BP position using a sigmoid fit of the entire distal edge, rather than using an inflection point as in previous studies [38,39,41]. With improved detector technologies, such as a larger area for reasonable statistics to produce useful images and accurate reference distributions for verification, IVI has the potential to be clinically implemented for carbon ion therapy range monitoring [40].

Secondary electron bremsstrahlung (SEB) involves the detection of bremsstrahlung along the beam path to monitor proton [43,44] and carbon ion [45,46] therapeutic beams. Bremsstrahlung radiation is produced through the acceleration or deceleration of a charged particle (such as the electron) passing through the electric field of a nucleus. An early experiment showed that the SEB process provides the dominant bremsstrahlung contribution [45], and in agreement with simulation results for the characteristic shape of the bremsstrahlung spectrum, the group demonstrated the feasibility of the method to estimate the ion beam range. Similar to PGI, a gamma camera is placed perpendicular to the ion path to acquire a distribution of the SEB production positions along the beam axis, with pinhole cameras [43,44,46] and slit collimators [43] being used in studies. Since SEB is emitted promptly, the method does not suffer from washout effects. As well, the sensitivity can be improved since the emission intensity is relatively large (compared to PG and PET gamma rays) and high-sensitivity imaging devices (collimators and detectors) can be easily fabricated for low-energy photons such as SEB [46]. Yet, the SEB method is limited by the background of PG rays, annihilation photons, scattered beam particles and secondary particles produced by the beam. The distribution of SEB from carbon beams extends beyond the BP position due to fragment components that penetrate beyond the BP and generate SEB, whereas this affect is not an issue for proton beams. Further work is being conducted for SEB therapeutic beam range estimation, where reducing the interference background and improving detection efficiency and sensitivity are required for clinical applicability [44,46].

Ionoacoustic tomography employs the thermoacoustic waves generated by the ions as they traverse tissue, whereby localised heating of the medium and a corresponding pressure pulse result from the ions' energy deposition [47]. The ultrasonic pressure waves are detected by an ultrasound transducer, where the arrival time of the detected pulses relative to the beam pulse time is directly proportional to the distance from the BP to the detector. This provides the basis of the BP localisation within the patient [48]. The ionoacoustic signal depends on parameters such as the beam pulse width, energy, spot size, transducer position and sensitivity,

and measurement noise, where the signal amplitude corresponds to the dose deposition [47-49]. Multiple transducer detectors may be used to reconstruct a tomographic image of the dose distribution [49]. Ionoacoustic range monitoring has the potential to be simpler and more accurate for BP localisation than nuclear-based techniques [47] such as PG, PET and SEB. Studies indicate the possibility of BP localisation with about 1 mm accuracy [49] and the potential for sub-millimetre precision with new or next generation ion accelerators [47]. This method has the advantage of real-time feedback, the spatial resolution is relatively better and ultrasonic instrumentation is generally less expensive than nuclear-based methods [48]. However, in clinical conditions where the ion energies are high, challenges include an increased noise, lower signal amplitude (due to the greater spread in dose deposition), density differences in heterogeneous tissue, and generally higher signal attenuation [47,49]. Since this method relies on beam pulses, localising the SOBP can also be achieved by monitoring all pulses that make up the SOBP. Improved resolution, reduced noise and increasing the sensitivity of detection are necessary for the clinical application of ionoacoustic tomography for *in vivo* dosimetry in particle therapy [48,49].

On the other hand, direct methods of *in vivo* dosimetry utilise detectors positioned on or in the patient for dose or fluence measurements. Such detectors include diodes [50], metal oxide semiconductor field effect transistor (MOSFET) detectors [51,52], plastic scintillation detectors (PSDs) [53,54], thermo-luminescence dosimeters (TLDs) [55], among others. However, direct methods are invasive, such that detectors may need to be positioned on the patient skin surface or within body cavities. As well, dosimeters require calibration to obtain dose, they may suffer from an energy, angular, temperature or LET dependence, sensitivity changes with accumulated dose, and corrections [56]. These direct dose measurements are generally limited to specific locations and provide limited information of point doses only. Challenges are not only on the dosimetry itself, but also on the placement at suitable locations to extract meaningful information. Hence, indirect methods such as the PG method may be more favourable in specific cases, particularly because they eliminate the need for invasive procedures.

The PG signal not only offers information on the BP position and range but also provides tissue composition and density information, which could offer a desirable means for *in vivo* dosimetry in particle therapy. That is, range verification is the determination of the BP position whereas dosimetry requires accurate tissue composition and density information to convert CT numbers into RSP. The PG signal can provide both information and thus lead to *in vivo* dosimetry.

1.4 Challenges of *in vivo* Range Verification and Dosimetry Using Prompt Gamma

This project was aimed at the characterisation and development of PG techniques for *in vivo* beam range verification during charged particle therapy treatment and further advancing toward *in vivo* delivered dose verification. The PG-based method has been considered as the most promising since it can provide *in vivo*, *in situ* and real-time range assessment during treatment delivery [57]. Using the PG method, information of range shifts or deviations of the range from the prescribed treatment plan can be obtained, and the delivered dose distribution in the patient could be reconstructed with Monte Carlo simulation calculations. Thus, the delivered dose distribution could be verified *in vivo* as well.

Several major challenges are currently present in the development of clinically applicable and reliable devices and procedures regarding the PG method [19,57]. These include:

(i) PG detection challenges: PG rays are generated from different nuclear reactions and have a broad and relatively high-energy range (between 2 and 15 MeV) [24], compared to PET, with strong interference background from neutrons and other stray radiations. PG detection systems must face a complex compromise or trade-off between the PG signal and the background. Innovative detection methods, by utilising either or complementary features of PG ray characteristics in spatial, energy and timing dimensions, are pursued to extract the PG signal from the background. Several types of detection methods and techniques, utilising either imaging or non-imaging capabilities, have been proposed and extensively explored worldwide over the past decade. Such detection methods and techniques are further discussed in the next chapter of this thesis.

(ii) PG-based indirect *in vivo* dosimetry challenges: The correlation between PG emission and dose is complicated since the two result from different physical processes. Factors include the knowledge of tissue composition, attenuation of gamma rays within the target, the yield of PG rays emitted from various tissues and the intensity of the characteristic emission lines [58]. For accurate dose calculation, not only does the CT number to RSP conversion need to be accurate, but the detector energy resolution must also be superior to produce sufficient PG emission spectra. Studies on the correlation between PG measurements and relevant dosimetric parameters are still mostly lacking.

(iii) Clinical environment and workflow constraints: These include the limitation of acceptable device size and weight incorporation into the treatment gantry. A compact and light weight PG system with low footprint set-up would be more favourable in clinical practice.

(iv) Beam delivery time structure and intensity constraints: In a PBS treatment, spatially-resolved range verification requires spot-by-spot assessment. The macro time structure of the treatment beam imposes extreme load tolerance, electronic throughput capability and stability of the PG detection system against load leaps. The millisecond-level measurement time for individual beam spots may have statistical issues for both mechanical and electronic collimation based PGI systems to obtain adequate statistics for *in vivo* range verification.

To overcome these challenges, the PG detectors play a crucial role. Hybrid PG detection methods with energy- and time-resolved detectors may be necessary to overcome the challenges of a broad- and high-energy PG distribution with dominating background interferences. High-resolution and high-performance novel detector systems with fast electronics for high-throughput processing are required. As reviewed in Pausch et al. (2020) [19], the key detector parameters required for a hybrid PG system have already been achieved [59-64], such as an energy resolution of 1.2-1.3% at 6.1 MeV, a time resolution (CRT) of 250 ps at 4.5 MeV, 1 Mcps tolerable detector load, 500 kcps electronic throughput at tolerable detector load, 0.1% gain stability, and for detector/array sizes of 1 cm^2 with 3-5 cm thickness for sufficient gamma ray absorption. However, achieving these requirements simultaneously for hybrid PG systems is the challenge.

Furthermore, *in vivo* range verification and dose monitoring based on a PG method (developed methods and those under development are described in Chapter 2) would, in general, rely on comparing the reconstructed PG signal or dose in the patient with expected outcomes from theoretical calculations, to determine deviations from the prescribed treatment plan. Monte Carlo simulations, modelling particle transport and interactions in a medium, play a crucial role in obtaining such expected outcomes, calculating important physical quantities such as spatial distribution (1D, 2D, 3D), energy spectra or timing profiles [65]. Monte Carlo simulations are also important in PG system design and feasibility studies, supporting the development of a detector system for PG range monitoring in particle therapy. Yet, there are challenges with the Monte Carlo modelling that should be improved to advance the reliability and accuracy of the predictions for clinical implementation of PG rays for range/dose verification. Important aspects to consider include improving the accuracy of physics models in Monte Carlo simulations, increasing the speed of calculations, validation of the applied Monte Carlo codes, comparing measurements and expected results for heterogeneous targets, and analysing uncertainties (quantifying the influence of CT calibrations, etc) [65]. These will be discussed further in Section 2.4.

1.5 Research Scope and Motivation of this Thesis

Although significant research efforts have been made and prototype detection systems developed, PG range verification remains absent in clinical routine. Dose monitoring using PG rays requires further research efforts, particularly on the methodology and technology. The technique requires real-time BP tracking as well as on-line quantitative element analysis of tissue in the BP region. The latter can be achieved via PG spectral measurement and analysis, such that the obtained tissue composition information along with the CT numbers from the treatment planning system (TPS) may be used to accurately determine the tissue dose. This thesis therefore spans three major areas of work:

(i) Geant4 Monte Carlo simulations investigating the emission and detection (for an ideal case) characteristics of PG rays from particle beam irradiations for potential hybrid systems. Hybrid PG detection systems, utilising multiple features of PG rays simultaneously, such as energy and TOF information, may significantly improve PG range monitoring and toward *in vivo* dosimetry. Recommendations on optimal PG detection methodologies and technologies resulted from this work.

(ii) Exploring suitable detector technology for energy- and time-resolved PG measurements. The wide energy range of PG emissions and instantaneous count rates calls for high resolution, fast and efficient gamma ray detector technology. Thus, experimental studies were performed to investigate a suitable choice for fast PG measurements from a range of commercially available scintillation detectors.

(iii) Studying the performance of simulations used for PG range verification and dose monitoring in a more realistic, clinical scenario. Clinical PG measurements have been compared to expected outcomes obtained from Monte Carlo simulations to quantify the accuracy of the results deriving from the in-silico calculations. This study is important because of the extensive use of Monte Carlo simulations to develop PG detection systems, and in practice, whereby the PG range/dose monitoring method may rely on comparing measured data with expected outcomes to determine deviations from the prescribed treatment plan.

The novelty of this project is such that it combines several areas of research to improve the techniques (detection methodology and technology) and resources (simulation codes which play a major role in both research and clinical practice) of using PG rays for BP tracking and toward *in vivo* dosimetry in particle therapy. Furthermore, the characteristic properties of PG emission and detection have been investigated for proton and carbon ion beam irradiation, as well as helium ions for which the PG distributions have not yet been widely studied. The work of this thesis will aid in developing optimal strategies of PG detection for real-time dose

monitoring in particle therapy and support the implementation of clinically feasible PG systems for improving cancer treatment QA.

The work involved in this project was conducted at three major sites: the Centre for Medical Radiation Physics (CMRP) at the University of Wollongong, Australia, the Australian Nuclear Science and Technology Organisation (ANSTO) in Lucas Heights, Australia, and the Massachusetts General Hospital (MGH) in Boston, USA. Geant4 simulations to characterise PG emission were performed at CMRP, thanks to the UOW IMTS High Performance Computing (HPC) Cluster and access to Australia's National Computing Infrastructure (NCI) Raijin and Gadi. Detector characterisations to determine a suitable scintillation detector for fast and efficient PG ray measurements were performed at the Nuclear Stewardship facility at ANSTO. TOPAS modelling and clinical PG ray measurements were performed in the Radiation Oncology Research Department and Francis H. Burr Proton Therapy Center at MGH.

Since this project spans across three different areas of work, Chapters 3-5 of this thesis each present a research topic, while Chapter 2 presents a literature review of particle therapy and the role of PG rays for *in vivo* beam range verification and dosimetry. Chapter 3 contains the simulation work performed at the CMRP to characterise the emission and detection properties of PG rays. Chapter 4 presents the experimental measurements performed at ANSTO to characterise several scintillation detectors and determine a suitable choice for PG ray measurements. Chapter 5 shows simulation and experimental work performed at MGH in relation to the MGH PG detection system prototype. Finally, Chapter 6 presents a summary of the research performed and a conclusion based on the findings of this work, as well as future perspectives.

2 Literature Review

2.1 The Physics of Particle Therapy

Charged particles, such as protons, alpha particles and heavier nuclei, undergo two fundamental interactions with the atoms of the tissue they traverse, *electromagnetic* and *nuclear* interactions. Electromagnetic interactions are Coulomb interactions with atomic electrons – which results in energy loss via ionisation of target atoms and determines the range of the particles – or with the atomic nucleus – which results in lateral scattering and determines the lateral beam spread. Nuclear interactions are particle-nucleus interactions that contribute significantly less to energy loss but results in the loss of beam fluence and the generation of various secondary particles such as protons, neutrons, gamma rays and light fragments [22]. Figure 3 shows illustrations of the particle interaction mechanisms.

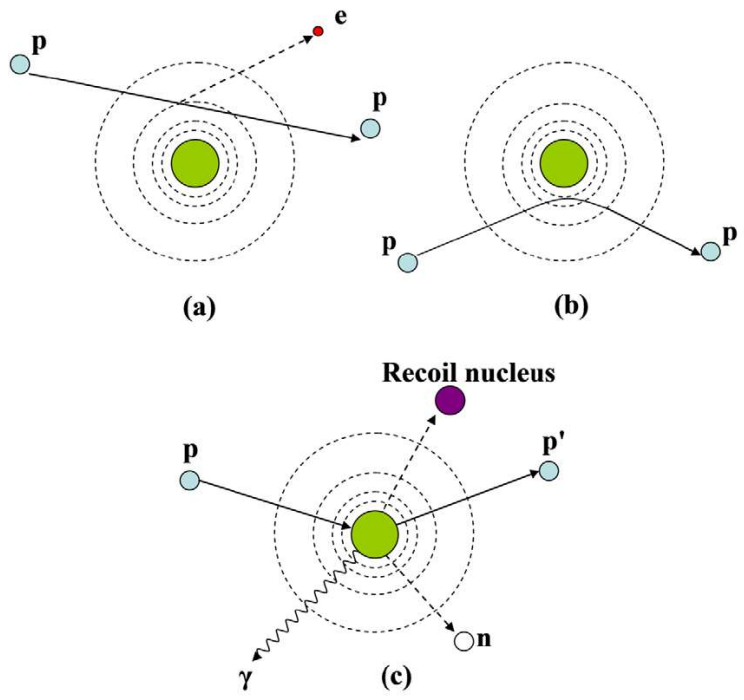

Figure 3: Illustration of particle interaction mechanisms: electromagnetic interactions (a) inelastic Coulomb interaction of the particle with atomic electrons (energy loss) and (b) elastic Coulomb scattering of the particle with atomic nucleus (lateral scattering/beam spread), and nuclear interactions (c) non-elastic interaction of the particle with the atomic nucleus (loss of beam fluence and fragmentation). (p: proton, e: electron, n: neutron, γ: gamma ray). From Ref. [22].

2.1.1 Electromagnetic Interactions

2.1.1.1 Energy Loss

For moderately relativistic charged particles (the general case in particle therapy) the predominant energy loss of the particles is via inelastic Coulomb interactions with atomic electrons i.e. ionisation and excitation of the atomic shell electrons. An electron ejected from the atom, called a delta (δ) ray, may have enough energy to cause ionisation itself along a separate track from the primary particle. The energy loss via Coulomb interactions with the atomic nucleus is minor [65].

The energy loss can be quantified by the stopping power S (or LET, described later in Section 2.1.3) with units of energy/distance given by the differential energy loss for the particle within the material divided by the corresponding differential path length [66]:

$$S = -\frac{dE}{dx} \tag{1}$$

The stopping power describes the mean energy loss as it is defined for a beam, not an individual particle [22]. For a large energy range in terms of mean energy loss and shell corrections in the Bethe-Bloch formula [67,68], including Barkas–Anderson–Bloch corrections [69-72]:

$$S = \frac{4\pi^2 N_A e^4}{mc^2}\frac{Z_P^2}{\beta^2}\rho\frac{Z_T}{A_T}\left[\ln\left(\frac{2mc^2\beta^2\gamma^2}{I}\right) - \beta^2 - \frac{C(\beta)}{Z_T} + Z_P L_1(\beta) + Z_P^2 L_2(\beta) + L_3(\beta)\right] \tag{2}$$

where e is the electronic charge, N_A is Avogadro's number, m is electron mass, Z_p is the charge number of the projectile, β is the relative velocity of the projectile, Z_T is the atomic number of the material, A_T is the molar mass of the material, ρ is density of the material, and I is the mean ionisation potential/excitation energy of the material. $\beta = v/c$, where v is the velocity of the projectile and c is the speed of light, and $\gamma = (1-\beta^2)^{-1/2}$. C is the shell correction term, L_1 is Barkas correction, L_2 is the Bloch term and L_3 is Mott and density corrections. Due to the $1/\beta^2$ dependence, the energy loss increases as the particle energy decreases. The Bethe-Bloch formula is generally considered accurate at high energies, while other models are used to describe energy loss at lower particle energies such as the Lindhard theory [73] (where β becomes less than the orbital electron velocity) and the Anderson-Ziegler model [74] (where the Bethe-Bloch and Lindhard models can be joined by a polynomial). Detailed discussion of the Bethe-Bloch formula can be found elsewhere [7,69-72].

As the particles continue to lose kinetic energy, they eventually come to a stop, and so the range is often referred to as the continuous-slowing-down-approximation (CSDA). The CSDA range as evaluated from the stopping power is:

$$R_{CSDA} = \int_0^L dx = \int_E^0 \frac{dE}{dE/dx} \tag{3}$$

where E is the initial energy and L is the maximum range. The continuous ionisation energy losses of charged particles are normally modelled in Monte Carlo codes analytically (down to ~2 MeV), based on a continuous-slow-down-approach that builds on the Bethe-Bloch equation, including relevant correction factors for Z_p [65]. Thus the range (like the stopping power) is essentially an average quantity defined for a beam, not for individual particles [22]. Figure 4 shows the mass stopping power and corresponding range as a function of proton energy in water. The Bethe-Bloch formula shows that the energy loss is proportional to the inverse square of the particle velocity ($1/v^2$ classically and $1/\beta^2$ relativistically) and the square of the ion charge, with no dependence on the projectile mass. Since the energy loss is predominantly due to Coulomb interactions between projectile and atomic electrons, the linear stopping power is also proportional to the material mass density ($N_A \rho Z_T / A_T$) [22]. For the same energy per nucleon the proton range is about three times the range of ^{12}C, while protons and ^{4}He ions have the same range at the same velocity [69].

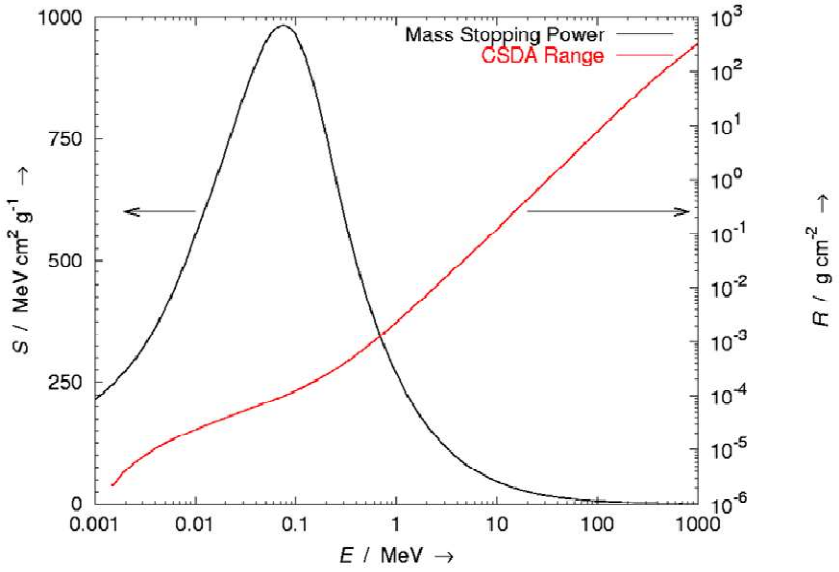

Figure 4: Plots showing the mass stopping power S as a function of proton energy E in liquid water, and the corresponding range R calculated using the S values with the CSDA. From Ref. [22].

The shape of the Bragg curve (position and height of the BP) is governed by several factors such as energy loss and stopping power, the removal of primary particles and the

emission of secondary particles from nuclear reactions, and the accumulation of lateral deflections from MCS (see Figure 5). As the particle velocity decreases with penetration depth, the interaction cross section increases and the energy loss increases, thereby causing the characteristic BP [22]. Additionally, as the particles slow down they get partly neutralised by the material through electron pickup, which reduces the particles' effective charge $(Z_p)_{\text{eff}}$ or Z_{eff} (which must replace Z_p in equation 2) and therefore the Bragg curve exhibits the sharp fall-off as the particles lose energy and stop [65,66]. The statistical fluctuation in energy loss of the particles cause the broadening in the BP, generally referred to as energy straggling or longitudinal straggling. The energy loss straggling is described by the asymmetric Vavilov distribution [75] that is approximated by a Gaussian function in the limit of many collisions [76,77]:

$$f(\Delta E) = \frac{1}{\sqrt{2\pi\sigma}} e^{(\Delta E - \overline{\Delta E})^2/2\sigma^2} \tag{4}$$

where $\sigma = 4\pi Z_{\text{eff}} Z_t e^4 N \Delta x (1 - \frac{\beta^2}{2}/1 - \beta^2)$. The energy loss variance σ_E^2 can be used to determine the range straggling variance:

$$\sigma_R^2 = \int_0^{E_i} \frac{d\sigma_E}{dx} \left(\frac{dE}{dx}\right)^{-3} dE \tag{5}$$

From this equation, the range straggling variance as a function of depth x in the material can be written as [78]:

$$\frac{d\sigma_R}{dx} = 4\pi N e^4 \frac{z^{*2}(x)}{\frac{dE}{dx}^2(x)} \tag{6}$$

where N is the material electron density and z^* is the effective charge of the projectile.

The relative range straggling of a particle with energy E and mass M is almost constant:

$$\frac{\sigma_R}{R} = \frac{1}{\sqrt{M}} f\left(\frac{E}{Mc^2}\right) \tag{7}$$

where f is a slowly varying function that depends on the material [79]. Due to the $1/\sqrt{M}$ dependence, the relative straggling is smaller for heavier ions than for protons e.g. a factor of 3.5 for ^{12}C ions [7,69].

Energy loss straggling varies with distance along the particle track; initially the distribution is narrow but becomes wider and more skewed with depth, and before the particle range the distribution narrows again due to the significant decrease in mean particle energy (see

Figure 5) [66]. Although the energy loss from MCS is negligible, it also contributes to lateral broadening of the pencil beam and a reduction of beam fluence [22,65].

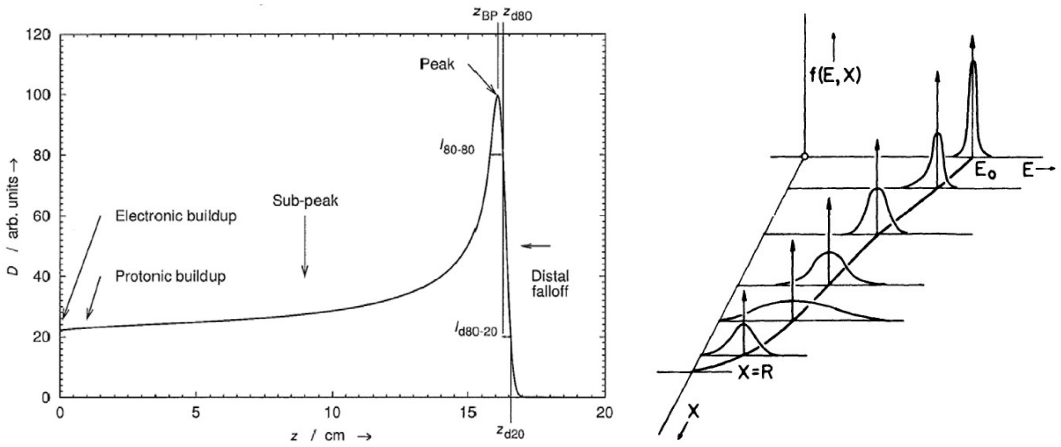

Figure 5: Left: Shape of a mono-energetic pristine BP (absorbed dose D vs depth z) for an initial 154 MeV broad proton beam. The protonic buildup region (buildup of secondary protons) is mainly attributed to proton-induced non-elastic nuclear interactions. The sub-peak region is where the stopping power's dependence on the inverse-square of the proton velocity is most significant, nuclear reactions cause removal of protons and liberation of secondary particles, and accumulation of lateral deflections (very small fields) from MCS. (z_{BP}, z_{d80}, z_{d20}: depth of maximum dose at the BP, distal-80% and distal-20% depths, respectively. $l_{80\text{-}80}$, $l_{d80\text{-}20}$: 80%-to-80% pristine peak width, distance between distal-80% and distal-20% depths, respectively). From Ref. [22]. **Right**: Energy E distributions of an initially mono-energetic beam of charged particles along penetration depth X. From Ref. [66].

2.1.1.2 Lateral Beam Spread

The beam spread is predominantly caused by elastic Coulomb interactions with atomic nuclei, but secondary particles produced by nuclear fragmentation reactions also contribute to the spread. *Single scattering* gives a small deviation angle on average, while *plural scattering* refers to a greater number of Coulomb scattering events but less than a few tens of interactions which occurs in thin targets [69]. In thicker targets, MCS dominates the lateral scattering and hence the beam spread. A theoretical calculation of the scattering angle was performed by Molière (1948) [80], and other more practical derivations have been performed [81-84]. For small angles, the angular spread can be approximated by a Gaussian distribution with a standard deviation given by [82,83]:

$$\sigma_\theta[\text{rad}] = \frac{14.1\ \text{MeV}}{\beta pc} Z_p \sqrt{\frac{d}{L_{rad}}}\left[1 + \frac{1}{9} log_{10}\left(\frac{d}{L_{rad}}\right)\right] \tag{8}$$

where d is the thickness and L_{rad} is the radiation length of the absorber material. This equation shows that the angular spread increases for thicker targets and materials of higher atomic

number. The scattering for a particular particle decreases at higher energy due to the $1/\beta pc$ term [69]. For particles with the same range, the heavier ions undergo smaller scattering e.g. the angular spread for ^{12}C ions is three times less than that for protons for a 15.6 cm range in water (150 MeV protons and 285 MeV/u ^{12}C ions) [7].

The angular beam spread in practice arises mainly from two sources: scattering caused by materials in front of the patient, and scattering within the patient. At low energies, the former represents the dominant contribution due to the distance (0.5-1.0 m) the beam travels before entering the patient, while the latter is the dominant contribution at higher energies due to the larger penetration depths [7]. Although MCS in the scattering foils in the treatment head allows the beam to spread laterally to useful dimensions in proton therapy, MCS in the treatment head and patient blurs lateral penumbral sharpness. These factors, as well as implanted metal objects such as fiducial markers, need to be considered in clinical practice regarding the effects of MCS [22].

2.1.2 Nuclear Interactions

Charged particles may interact elastically or non-elastically with the atomic nucleus. In elastic collisions, the kinetic energy is conserved and the nucleus remains intact; they are due to strong rather than electromagnetic interactions, and although do not occur frequently they still cause broadening of the beam. On the other hand, in non-elastic collisions the total kinetic energy is not conserved, whereby the nucleus is transformed and secondary particles may be knocked out by the projectile [22,65]. As discussed in Section 1.3, it is these secondary particles that may be used for beam range verification/dosimetry in particle therapy treatment delivery.

To enter the nucleus, particles need to have sufficient energy to overcome the Coulomb barrier of the nucleus, which depends on its atomic number. The Coulomb barrier can be described by $B = Zze^2/R$, where Z and z are the atomic numbers of the projectile and target, e is the electric charge, and R is the distance (cm) at which the Coulomb repulsion can be overcome [85]. In the atomic nuclei of biologically relevant elements, such as oxygen and carbon, the total inelastic cross section for proton-induced nuclear reactions has a threshold of the order of 8 MeV [22].

Gamma rays emitted via de-excitation of the nucleus have energies that are essentially equal to the difference in energy between the initial and final nuclear states. PG emission usually occurs without beta decay, depending on the reaction channel, but if so then the gamma rays will appear with a half-life characteristic of the parent beta decay but with energy reflecting the energy level structure of the daughter nucleus [66]. Prominant PG ray emissions include: 2.23 and 2.74 MeV (single escape peaks), 5.11 MeV (double escape peak), and 5.62 and 6.13

MeV (single escape peaks) from ^{16}O; 4.19 MeV (double escape peak), and 4.70 and 5.21 MeV (single escape peaks) from ^{15}O; and 3.42 MeV (double escape peak), and 3.93 and 4.44 MeV (single escape peaks) from ^{12}C [86].

The spatial distribution of the absorbed dose is therefore altered by the presence of nuclear interactions, since some of the kinetic energy that would be deposited as local ionisation and excitation is instead carried away by neutrons and gamma rays [86]. The correlation between incident particle dose deposition and PG ray emission is therefore not one-to-one, since (at typical particle therapy energies) charged particles deposit dose primarly by imparting energy to atomic electrons through electromagnetic interactions whereas PG rays (and positron emitter production in the PET method) arise from nuclear reactions.

Nuclear interactions cause a significant loss of beam fluence and a build-up of lower-Z fragments. This becomes more pronounced with increasing penetration depth, for which the exponentially diminishing flux of primary particles causes the peak-to-entrance dose ratio to gradually decrease [7]. Nuclear fragmentation is an important aspect in particle therapy, particularly heavy ion therapy. In a typical carbon therapy treatment, only 50% of the primary ions reach the BP while the remaining undergo fragmentation [69]. The fragments contribute to the broadening of the BP due to straggling, and move (typically forward directed) with approximately the same velocity as the incident particles, which generally have longer ranges and thus cause the dose tail beyond the BP (also more pronounced at larger depths) [7]. Figure 6 shows an example of the depth dose profiles of primary 330 MeV/u ^{12}C ions and the associated secondary fragments (left), and build-up curves of secondary fragments produced by 400 MeV/u ^{12}C ions (right), in water. In practice, where opposite beams are used, the dose tail is within the high dose region in the patient, but in single beam angles projectile fragmentation becomes non-negligible to the normal tissue dose. This is a concern for normal tissue effects in heavy ion therapy, whereas in proton therapy the concern is target fragmentation [69].

In most Monte Carlo codes, the probability of the incident particles not having undergone a nuclear interaction after travelling a distance x, or in other words the number of particles remaining at depth x (which depends on the inelastic nuclear cross section), in a material is given by:

$$P(x) = \frac{N(x)}{N(0)} = e^{-\frac{x}{\lambda_{\text{int}}}} \tag{9}$$

where $N(0)$ is the number of incident particles, $N(x)$ is the number of incident particles after a distance x, and the mean free path or interaction length is given by $\lambda_{\text{int}} = A_t/N_A\sigma\rho$, where σ is the total cross section [65].

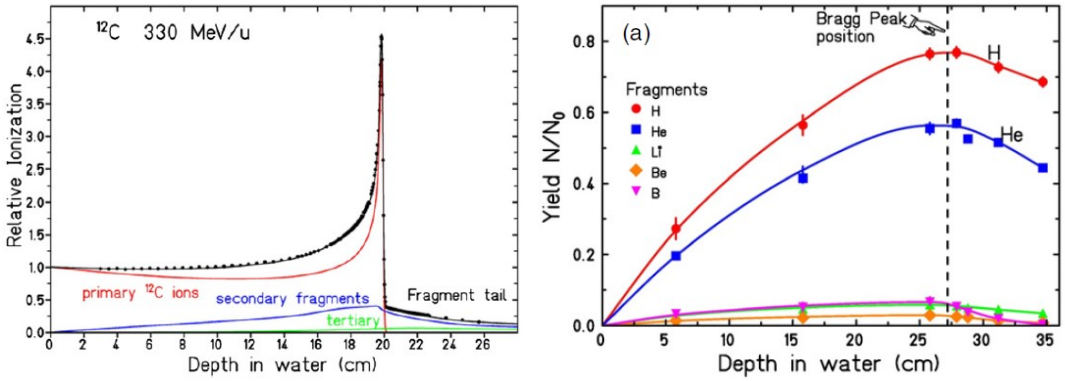

Figure 6: Left: Depth dose profiles of primary 330 MeV/u ^{12}C ions and the associated secondary/tertiary fragments in water. **Right:** Build-up curves of secondary fragments produced by 400 MeV/u ^{12}C ions in water. From Ref. [87].

The modelling of nuclear reaction processes involving protons and heavier ions are slightly different; Figure 7 illustrates the reaction process of protons and that of heavier ions with target nuclei. Proton-nucleus interactions initiate a series of nucleon-nucleus collisions which leads to the emission of secondary particles and to equilibration of the remnant nucleus. This process can be described in three stages: intra-nuclear cascade (INC), pre-equilibrium and de-excitation. The (generalised) INC describes the incident particle interacting with quasi-free nucleons in the target nucleus through a series of two-body interactions. In pre-equilibrium, the energy of the particles has reached a lower limit (few tens of MeV) but the nucleus is not yet in thermal equilibrium. Finally, de-excitation depends on the mass of the target nucleus and the remaining energy, for which the remaining energy can be dissipated via nuclear evaporation, fission, Fermi-breakup or gamma emission [65].

For heavier ions, nucleus-nucleus interactions are variants of the *abrasion-ablation* model [88]. During abrasion, the projectile and target nuclei overlap and an excited quasi-projectile (with most of the initial velocity) and a quasi-target fragment (at rest) are formed, as well as several excited light fragments. During ablation, the projectile, target and fragments that remain de-excite by evaporating light nuclei or fragments. Here, both projectile and target nuclei can fragment, in comparison to protons where only the target nuclei can fragment [65].

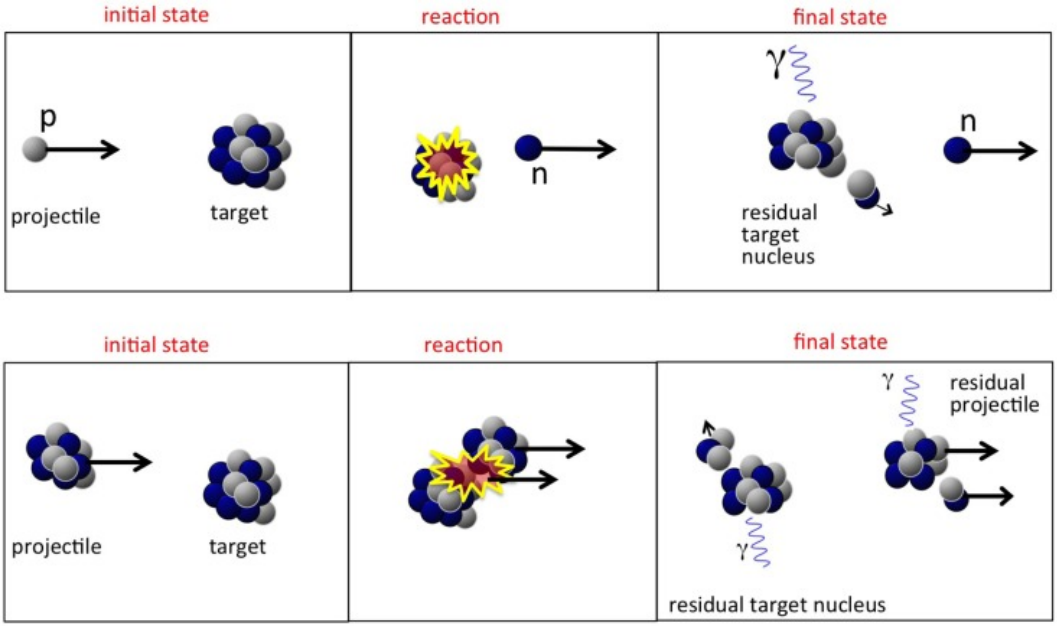

Figure 7: Top: Illustration showing a nucleon-nucleus reaction for protons, whereby a neutron is created and a gamma emitted from the residual target nucleus. **Bottom**: Illustration showing a nucleus-nucleus reaction for heavy ions, whereby light fragments are created and gamma rays can be emitted from both residual projectile and target nuclei. From Ref. [65].

2.1.3 Comparison of Different Ion Species

Aside from protons and carbon ions which are used clinically in particle therapy today, other ions are gaining interest such as helium, lithium, oxygen and neon [89-93]. In this thesis, proton, helium and carbon ions are studied, so the discussion in this section will focus on these three particle species. The main differences between protons and heavier ions, such as helium and carbon, are that heavier ions exhibit reduced multiple scattering inside the patient, result in a dose tail beyond the BP due to secondary fragments that are produced from nuclear reactions along the beam path, and have an increased LET, RBE and OER [7,94]. The RBE for heavier ions is low in the plateau region and increases to a significant enhancement in the BP. The average RBE for protons is around 1.1 [95], while for carbon ions the RBE distribution in the target volume varies between 2 and 5 [96,97] and for helium ions between around 1.2 and 2.9 [98,99]. The RBE is largely a reflection of LET, which is related to DNA damage; the greater the RBE the higher the LET, and in turn, more cellular damage that is less likely to repair, in addition to improved effectiveness in killing hypoxic cells that are normally radioresistant [89,100]. Hence, this is related to the OER which, as stated in Tommasino et al. (2015) [89], is "defined as the ratio of doses under hypoxia to normoxic conditions needed to obtain the same biological effect". Lighter ions, such as protons and helium, produce high LET at the distal edge of the BP only, whereas carbon ions produce high LET in the entire BP resulting in high LET to

healthy tissue proximal to the BP [89]. Furthermore, the projectile particles caused by nuclear fragmentation reactions have the same velocity as the primary particles but with reduced mass and charge. This results in a complex radiation field which contribute a low LET dose to the tumour, and since low LET particles travel further in tissue they may also contribute to a dose to normal tissue beyond the BP [7,100]. Due to the Z^2 dependence of LET, fewer carbon ions are necessary to deposit the same amount of physical dose as protons. Considering the higher RBE in the SOBP region, typically 10^2 times more protons than carbon ions are required to irradiate a given tumour volume at the same therapeutic dose [57].

Studies have explored and compared the physical and biological properties of various ions [101-105]. It has been found that the charge collection efficiency for heavier ions is lower due to less lateral and longitudinal straggling and superior ionisation density. The beam width of secondary particles was found to be larger for helium ions than for carbon ions, which corresponds to the lighter fragments originating from the fragmentation of helium ions and since fragments from heavier ions are more forward directed [104]. Yet, the lateral straggling of helium ions due to MCS was shown to be about half that of protons [106]. From depth and lateral dose distributions, the SOBP characteristics for the different ions seem to be consistent. Helium ions offer a lower fragmentation tail and an advantageous entrance dose compared to heavier ions, with similar lateral and distal fall-off properties [104]. A recent study [91] presented a simulation model for therapeutic ^{4}He beams, experimentally validated by means of physical and biological dosimetries, and showed that detailed treatment planning studies with such beams is possible. Yet heavier ions remain of clinical interest for certain types of tumours, such as hypoxic tumours, due to the difference in achievable LET [104].

As with dosimetric comparisons between the ion species, the secondary radiation field also differs, and hence in the PG emission. Due to the greater number of fragmentations, heavier ions produce more PG rays than protons per projectile. The PG yields for carbon ions are higher than those for protons, generally by a factor of 5-6 [57]. The secondary particles are also a source of PG ray production, both in the build-up region and beyond the BP, justifying the need for discrimination techniques (e.g. TOF) for carbon ions. The PG fall-off is therefore more well-defined for protons compared to carbon ions, with less background. Hence, it is unlikely that millimetric precision can be achieved for on-line carbon ion verification with the gamma cameras currently under development; efficiencies of the order of 10^{-2} would be required [57]. The prompt photons produced by various ions in a PMMA target were recently studied [94], where measurements confirmed that ^{4}He beams of therapeutic energy produce non-negligible prompt photon yields, with resolutions below 2-3 mm obtained in different scenarios, supporting the feasibility of ^{4}He and ^{12}C beams for PG range verification techniques.

Unlike protons and carbon ions, clinical data available to support simulations for helium ions is limited. Although experimental studies have been performed [91,94,106-108], further measurements of dose profiles and fragmentation cross sections would help to benchmark and improve the beam models adopted in Monte Carlo codes. Further experimental efforts would also be beneficial to implement helium (and other) ions in treatment planning software, such as obtaining RBE data over a wide range of energies and cell lines. This would be important in the future, where radiation-quality optimised treatments based on particle species selection may be personalised to the patient and the specific disease [89].

2.2 Gamma Ray Detection and Measurement

2.2.1 General Properties of Radiation Detectors

This section presents general properties of radiation detectors that are relevant to Chapter 4 of this thesis, where the study on the characterisation of scintillation detectors for potential hybrid PG detection systems for fast and efficiency beam range monitoring is given.

2.2.1.1 Energy Resolution and Detection Efficiency

The *energy resolution* of a detector describes its ability to resolve fine detail in the incident radiation energy, or to distinguish between two energies close together. It is commonly written as:

$$R = \frac{FWHM}{H_0} \tag{10}$$

where $FWHM$ is the full-width-at-half-maximum of the detector response function (peak in the differential pulse height spectrum) and H_0 is the centroid of that peak. R is therefore a dimensionless fraction that is commonly expressed as a percentage; the smaller this value, the better the energy resolution of a detector. That is, the peak width reflects the amount of fluctuations recorded from pulse to pulse regardless that each event deposited the same energy in the detector. Semiconductor detectors used for alpha spectroscopy can have an energy resolution <1%, while scintillation detectors used for gamma ray spectroscopy range from 3% to 10% [66].

The *detection efficiency* describes the ability of a detector to record events considering the number of radiation quanta (particles or photons) incident on the detector. The detection efficiency is divided into two classes: absolute and intrinsic. *Absolute detection efficiency* is dependent on both the detector itself and geometric properties, such as distance from the radiation source to the detector, and is defined as:

$$\varepsilon_{abs} = \frac{number\ of\ pulses\ recorded}{number\ of\ radiation\ quanta\ emitted\ by\ source} \quad (11)$$

Intrinsic detection efficiency mostly depends on the detector material, radiation energy, and the detector thickness in the direction of radiation incidence, and is defined as:

$$\varepsilon_{int} = \frac{number\ of\ pulses\ recorded}{number\ of\ radiation\ quanta\ incident\ on\ detector} \quad (12)$$

For isotropic sources, the absolute and intrinsic efficiencies are related by $\varepsilon_{int} = \varepsilon_{abs} \cdot (4\pi/\Omega)$, where Ω is the solid angle of the detector subtended from the source position [66]. Further discussion on detection efficiency will be discussed in Chapter 4.

2.2.1.2 Dead Time

The term *dead time* (or *resolving time*) refers to the minimum time separation between two events such that they can be recorded as two individual pulses. The time limitation may arise from the detector processes or associated electronics. For example, for scintillation detectors, the dead time is the combination of three time intervals: time taken to produce the scintillation (i.e. the decay time of the scintillator), time taken for electron multiplication in the photocathode (order of 20-40 ns), and time taken to amplify and record the signal. The resulting dead time of a scintillatior is of the order to 1-5 μs, in comparison to gas-filled detectors which is much larger, in the order of tens to hundreds of microseconds [109].

2.2.2 Conventional Gamma Detector Technology

Here, the focus is on scintillation detectors, outlining the physics of their operation and performance in terms of timing, since they are investigated as potential PG measurement devices in Chapter 4 of this thesis. Associated photo-detectors for scintillation light readout are also discussed, specifically *photomultiplier tubes* (PMTs) and *silicon photomultipliers* (SiPMs). An overview of pulse processing, shaping and timing is also given, which are also relevant for the study presented in Chapter 4.

2.2.2.1 Scintillation Detectors

Scintillation detectors are used for a wide range of applications, for the detection and spectroscopy of ionising radiation. The choice of scintillation material is subject to the specific application, such that there is a compromise between the properties of the particular scintillator. Ideally, a scintillator should be of high efficiency, the light yield should be proportional to the deposited energy over a wide range, the decay time of induced luminescence should be short to generate fast signal pulses, the index of refraction should be near that of glass (~1.5) to allow

efficient coupling to a PMT (discussed further in the next section) or other light sensor, among other factors [66].

Scintillation in inorganic materials depends on the energy states which are governed by the crystal lattice of the material. With energy absorption, electrons can rise from the *valence band* (where electrons are essentially bound at lattice sites) to the *conduction band* (where electrons move freely through the crystal) leaving a hole in the valence band (electron-hole pair), and when the electron returns to the valence band the de-excitation results in the emission of a visible photon. To increase the probability of visible photon emission, small amounts of impurities (*activators*) are added to the scintillator which creates energy states within the *forbidden band* (between the lower and upper bands where electrons cannot exist in pure crystals). The energy structure of the de-excitation sites (*luminescence centres* or *recombination centres*) in the crystal lattice governs the emission spectrum of the scintillator [66,109].

From the creation of electron-hole pairs, the positive hole quickly drifts to an activator site and ionises it while the electron moves freely through the crystal until it encounters such an ionised activator. The electron can arrive at the activator site and create its own set of excited energy states. If transition to the ground state is possible in an excited configuration activator site, the de-excitation will occur rapidly and with high chance of a photon emission. Such excited states commonly have lifetimes of the order of 30-500 ns [66]. The decay time of the excited states therefore determines the emitted scintillation light timing characteristics. A possible scenario that can occur is electron capture at the activator site, termed *quenching*, whereby no photon is produced. Moreover, electron-hole pairs can alternatively move together in a loose configuration referred to as an *exciton*. They move freely through the crystal until they reach an activator atom site, where excited activator configurations can again be formed and scintillation light produced from the de-excitation to the ground state [66,109].

For the detection of photons, scintillators have superior timing resolution and good energy resolution, whereas for charged particles, they have good timing resolution but semiconductor detectors have better energy resolution. Gas-filled detectors have very low efficiency of gamma rays and x-rays compared with scintillation detectors, since the incident radiation travels through the low-density gas with few interactions. Also, for scintillators, alpha- and beta-gamma radiation measurement (simultaneous and separate) can be achieved by pulse analysis, the size and weight can be much lower, the temperature range is not limited by condensation, they do not require gas supply or gas refilling, and the uniformity of the response across the sensitive area is comparable to gas-filled counters. Scintillators are an excellent choice for particular applications with the advantage of excellent efficiency, high precision, high

counting rates achievable, relatively simple experimental set-up and accurate energy/intensity measurement i.e. spectroscopy (particularly for gamma rays) [110,111].

2.2.2.2 Photo-detectors for Scintillation Light Readout

A PMT is an instrument that converts the weak light output of a scintillator into a usable electrical signal. The main components of a PMT include: a *photocathode*, *focusing electrodes*, *dynodes* and *anode*. These components are enclosed within a vacuum tube in order for low-energy electrons to be accelerated efficiently by internal electric fields, such that the photocathode is at negative potential and the anode at positive potential. Figure 8 shows the elements and basic principles of a PMT. The photocathode is a photosensitive layer that converts the incident scintillation light to a few hundred low-energy electrons (photoelectrons). Dynodes are electrodes that re-emit electrons once energy is deposited in its surface by incident electrons. Amplification results in 10^7-10^{10} electrons from a typical scintillation pulse and are then sufficient to serve as the electrical signal for the original scintillation event; this charge is collected at the photosensitive anode for the output signal. PMTs generally perform amplification linearly, such that the output pulse at the anode remains proportional to the number of initial photoelectrons across a wide range of amplitudes [30,66,109].

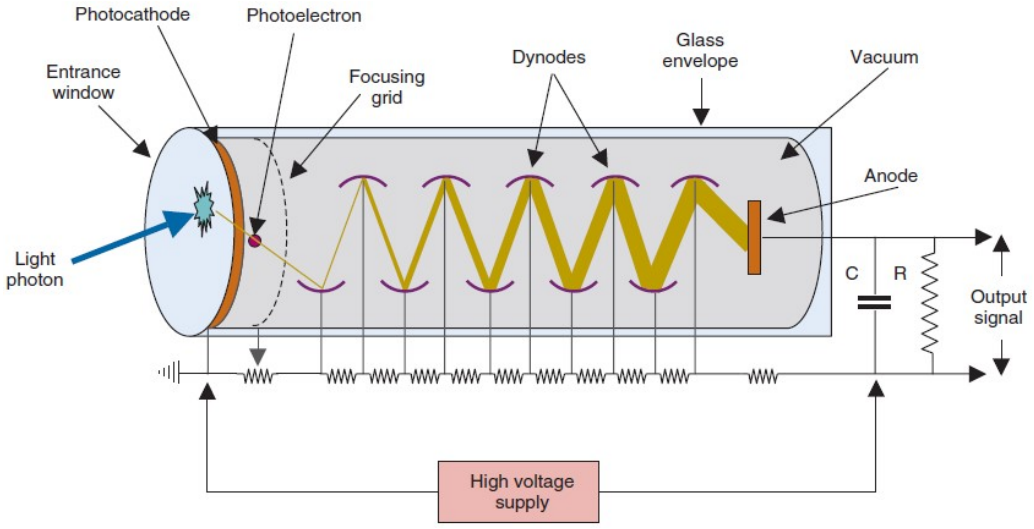

Figure 8: The components and basic principles of a PMT. From Ref. [30].

A SiPM is a semiconductor device that consists of an array of small *avalanche photodiode* (APD) cells (tens of microns) produced using complementary metal-oxide semiconductor (CMOS) processes on a silicon chip and operated in Geiger mode. Avalanche photodiodes feature an internal gain through which high electric fields increase the number of collected charge carriers. Geiger mode refers to the principle that charges produced in the initial

interaction are multiplied without limit, but quenching by an active or passive external circuit ceases the self-sustaining avalanche. The avalanche photodiode cells are so small that the probability for a scintillation photon to hit a cell during a scintillation pulse is low. The number of cells producing an avalanche is thus proportional to the number of incident scintillation photons. When operated in Geiger mode, the output of each cell are close in amplitude, and adding these in parallel generates an analogue pulse where the amplitude is proportional to the number of photons detected [66].

The time characteristics of a PMT is determined solely by the electron trajectories, since the time for electron emission in the photocathode and dynodes is very short (0.1 ns or less). The average time taken for an electron burst to occur at the anode from the corresponding photon arrival at the photocathode is termed the *electron transit time*; ranging from 20-80 ns for various designs of PMTs [66]. However, in most timing applications the transit time is not of great importance since it generally introduces only a fixed delay in the derived signal. The time width of the pulse of electrons arriving at the anode is more important. This *transit time spread* is primarily due to the distance between the photocathode and first dynode; photocathodes are therefore usually curved to minimise the affect across its diameter. The variation in emitted photoelectron velocities is another source of spread in the transit time, but can be minimised by employing a large voltage difference between the photocathode and first dynode. Operating the PMT at maximum voltage permissible is generally done for superior timing performance, as a high inter-dynode voltage can also decrease the effect of time spread in the electron multiplier region. However, improving the time response of the PMT can be a compromise to the photoelectron collection efficiency and therefore the electron gain; the time resolution is basically inversely proportional to the square root of the number of photoelectrons per pulse [66,112,113].

Photodiodes (or SiPMs) are also effective devices for coincidence and other timing applications, such that the time response is comparable to that of PMTs since the distances in which the charges move are relatively small. The rise time of SiPMs is determined by the avalanche formation rise time and the variation in the transit times of signals arriving from different points on the sensor's active area; careful design of the tracking to minimise the transit time spread can improve the rise time. On the other hand, the decay time of a pulse (or recovery time of the sensor) is determined by the microcell (operating unit of a single photon avalanche diode and quench resistor) recharge time constant, given by $\tau_{RC} = C_d(R_q + R_s \cdot N)$, where C_d is the microcell effective capacitance, R_q is the microcell quench resistor, R_s is any resistance in series with the sensor, and N is the total number of microcells in the sensor. Although the microcell can respond during the recovery time, the gain will be reduced proportional to the

reduced overvoltage. The percentage of sensor surface area that is sensitive to light is termed the *fill factor*. For a lower fill factor (smaller microcells) the recovery times are shorter and the dynamic range is larger, but compromises to a lower photon detection efficiency and gain, and results in lower capacitances [114]. For single-celled avalanche photodiode SiPMs, timing resolutions on the order of tens of picoseconds are achievable, while for array cells are on the order of hundreds of picoseconds [66].

Advances in semiconductor photodiodes have led to them potentially replacing PMTs for particular applications. Photodiodes generally offer higher quantum efficiency and so potentially superior energy resolution, lower power consumption, compact size, improved ruggedness and insusceptibility to magnetic fields. However, SiPMs have a nonlinear response to intense light pulses such that the probability of hitting a cell is no longer low, but a correction based on an initial calibration can restore linearity. Thermal noise and dark noise are additional challenges, as is the dependence of SiPM gain, noise and photon detection efficiency on temperature and voltage [66].

2.2.2.3 Pulse Processing, Shaping and Timing

The output signal from a PMT or SiPM becomes the input to the pulse processing system, where the series of current pulses occur randomly and typically vary in amplitude and duration. The system output is generally a count rate (rate of pulses that meet specific criteria) or an energy spectrum (pulse energy depositions in the detector). The main components of a typical pulse processing chain include: a *preamplifier*, *shaping amplifier*, discriminator or trigger, and counter or *multichannel analyser* (MCA). The preamplifier integrates the current pulse to generate a voltage step that is proportional to the corresponding charge in the detector. The shaping amplifier then converts this signal into a suitable form, where the output voltage pulse height is proportional to the deposited charge. The output should return to baseline as quickly as possible to prevent pulses from overlapping, or *pulse pile-up*, which in turn distorts the measurement. High- and low-frequency noise filtering is also performed by the shaping amplifier to improve the signal-to-noise ratio. The shaping amplifier is therefore characterised by a shaping time constant that relates to its output pulse duration; a short shaping time minimises pulse pile-up but is a trade-off to greater noise. Shaped pulses then go through a selection process; an *integral discriminator* selects all pulses with height above a particular threshold, whereas a *differential discriminator* (or *single channel analyser*) selects those with height between upper and lower thresholds. The output result is an accumulation of the selected events over a certain period of time, which can be presented with a counter or MCA. A counter simply counts the number of selected events over the certain time period, whereas an MCA

measures and assigns the pulse height of selected events to a particular range or channel to produce a pulse height spectrum [66,109].

Signal pulses can either be *linear*, whereby the pulse amplitude and at times the shape holds information, or *logic*, whereby the pulse only carries information through its presence or particular arrival time. A *linear tail pulse* has its leading edge time determined by the detector charge collection time, while its decay (return to zero) is determined by the time constant of the collection circuit; the latter must be larger than the former to ensure complete charge collection. The *rise time* of the leading edge of linear tail pulses is an important property in particular applications, which is commonly defined as the time interval between 10% and 90% of the pulse's final amplitude. On the other hand, the *decay time* is commonly used to refer to the time interval between 90% and 10% along the pulse tail. With regards to scintillators, the decay time characterises the prompt scintillation yield from a material [66,113].

Since the amplitude of pulses correlates to the charge Q deposited in the detector, pulse pile-up can be a major issue. Shaping the pulses in such a way that significantly reduces the pulse tail, but maintaining the proportionality of its amplitude to Q, is an ideal solution. Shaping may be in the form of a CR (capacitor-resistor) differentiator/high-pass filter, RC (resistor-capacitor) integrator/low-pass filter, CR-RC shaping, Gaussian shaping, active filter shaping, triangular or trapezoidal shaping. Shaped linear pulses commonly have a time width of several microseconds only, compared to 50 or 100 μs decay times of tail pulses [66]. Pulses can pile-up on the tails of preceding pulses which have not completely decayed to zero, such that a superposition of pulses arises, or there may be an undershoot of the preceding pulse, either of which result in the amplitude no longer being an adequate measure of Q; referred to as *tail pile-up*. The use of pole-zero cancellation or active baseline restoration techniques can solve these issues [66]. Another form of pulse pile-up is where two pulses occur so close in time that they are treated as one pulse; referred to as *peak pile-up*. This has a major effect on the amplitude of the recorded pulse, for which the combined pulse will have amplitude equal to the sum of the two individual pulses. Commercial linear amplifiers are generally capable of discarding pulses that are expected to be affected by pile-up. *Pulse shape discrimination* can also be employed, since piled-up pulses have a different shape to those not affected by pile-up. *Digital pulse processing* is a technique which allows rejection of pile-up as well as the possibility to recover information lost by pile-up [66].

As with pulse height measurement, obtaining timing information is another common goal in many applications, the accuracy of which depends on the properties of the detector being employed as well as the type of electronics used for signal processing. The characteristics of timing heavily depend on the dynamic range (amplitude) of the signal pulses; better timing

performance is achieved for systems that have signal pulses confined to a narrow range of amplitudes [66]. Time pick-off units, or triggers, are essential in timing measurements; they are devices that generate a logic pulse whose leading edge signifies the time at which an input linear pulse occurs. Sources of uncertainty may be due to *time jitter*, when the input pulse amplitude is constant (e.g. electronic noise, statistical fluctuations), or *amplitude walk*, when the input pulse amplitude varies. *Leading edge triggering* is the easiest, most direct and common method, whereby the pulse is triggered when it crosses a fixed discrimination level. Setting the discrimination level very low minimises the effects of amplitude walk, but setting the level in a steep slope region on the pulse leading edge minimises time jitter; optimal time resolution is achieved for levels set at around 10-20% of the average pulse amplitude [66]. Figure 9 shows time jitter and amplitude walk in the leading edge triggering method.

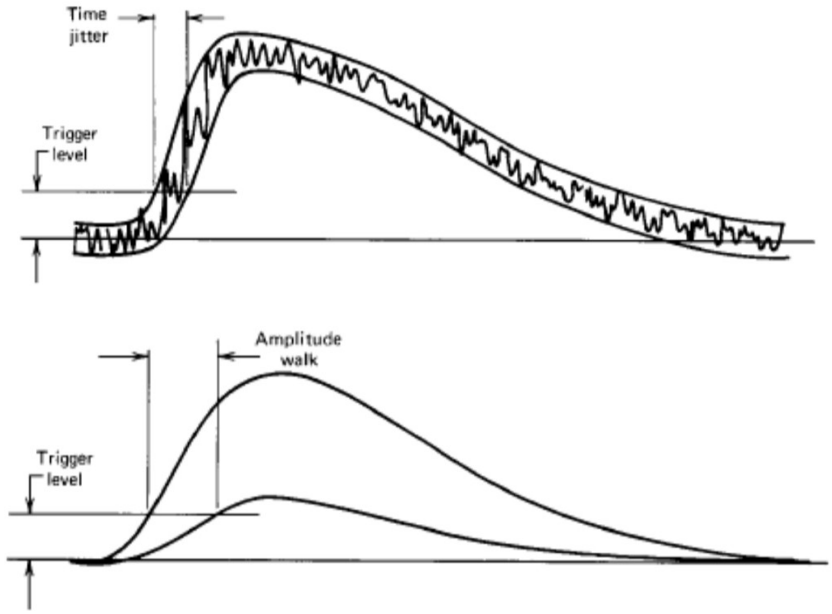

Figure 9: Top: Time jitter in leading edge triggering resulting from random noise. Signal pulses with the same amplitude and shape, but with random noise, are enclosed in an envelope. **Bottom**: Amplitude walk in leading edge triggering. Two pulses that have the same time of occurrence and shape, but different amplitude, cross the trigger level at different times. From Ref. [66].

2.2.3 Challenges of Detector Technology for Prompt Gamma Measurement

As mentioned in the previous chapter, PG emissions from charged particle therapy present complicated spectral distributions of high-energy, broad range of discrete energy lines with strong interference background from neutrons and other stray radiation induced continua. These impose significant challenges on detector technology for PG measurements. Hybrid PG detection methods are desired to combine the spectral and temporal information of PG rays.

This requires advanced detector technology with high stopping power, high energy and timing resolutions for both energy- and time-resolved spectral measurements.

Another challenge is on the detector system load capability for high instantaneous count rates (~10^7 events per second) from pencil beam spot scanning. This requires fast detector response with ultra-fast electronics and data acquisition systems, as well as innovative data processing techniques such as pile-up rejection, scatter rejection, spectral line extraction, etc.

A recent breakthrough of clinical prototype for proton range verification has been demonstrated from the Massachusetts General Hospital (MGH) group [59]. This prototype utilised a high-performance detector array based on $LaBr_3$(Ce) for energy- and time-resolved spectral measurements of PG rays. The gamma ray backgrounds from neutron-induced and proton-induced continua can be well resolved and rejected. Then, the discrete PG lines can be well resolved and obtained in both energy and time dimensions.

2.2.4 Overview of Advanced Detectors for Prompt Gamma Detection

To overcome the challenges stated in the previous section, advanced detectors based on fast, dense and high light yield scintillators are desirable to provide high-throughput measurements with high energy and timing resolutions. For a typical PBS treatment, estimating 10^8 incident protons per second at a beam current of 2 nA, PG timing detection systems should have a time resolution equal or better than ~200 ps FWHM (i.e. not exceed the minimum bunch spread of 200 ps FWHM at 230 MeV), energy resolution <5% FWHM at 662 keV (to support sharp energy cuts and clearly identify PG emission lines), detector and data acquisition counting rates >10^6 counts per second to achieve statistics of 10^4 for the PG rays of interest (to determine range variations of 5 mm with >80% probability) [60].

Cerium-activated lanthanide halide and cerium bromide scintillators have very promising properties to meet the requirements for PG detection. Energy resolutions of <3% at 662 keV and timing properties down to 100 ps can be achieved with $LaBr_3$(Ce) detectors in optimal conditions, with crystal size being one variable studied and various PMTs [115-119]. $CeBr_3$ has very short rise (<1 ns) and decay (17-24 ns) times, good energy resolution <4% at 662 keV, excellent time resolution of 120-150 ps FWHM for ^{60}Co energies, high count rates and reasonable photo-absorption probability [60,120-122] (see Table 1). $CeBr_3$ was also found to have an energy resolution of 2.2% at the higher PG energy of 4.4 MeV, with a time resolution of 190 ps FWHM [123]. However, $CeBr_3$ is limited by its characteristic scintillation self-absorption and re-emission processes which cause a lower light yield compared to $LaBr_3$(Ce). Yet due to the reduced intrinsic activity of $CeBr_3$, its detection sensitivity is, on average, around 5 times greater than that of $LaBr_3$(Ce) [124].

Other scintillators are also commercially available, such as $SrI_2(Eu)$, GYGAG(Ce), CLYC, CLLB, CLLC and CLLBC. A study characterising $SrI_2(Eu)$, $CeBr_3$ and GYGAG(Ce) found energy resolutions at 662 keV of 4.0% for $SrI_2(Eu)$, 4.4% for $CeBr_3$ and 5.2% for GYGAG(Ce) [125] (see Table 1). The study showed $SrI_2(Eu)$ having an excellent energy resolution but a very long decay time, whereas $CeBr_3$ had the fastest response with a good energy resolution, and GYGAG(Ce) had high efficiency with good energy resolution and the possibility to be produced in all shapes/dimensions.

The elpasolite crystal family, including CLYC ($Cs_2LiYCl_6(Ce)$), CLLC ($Cs_2LiLaCl_6(Ce)$), CLLB ($Cs_2LiLaBr_6(Ce)$), CLYB ($Cs_2LiYBr_6(Ce)$) and CLLBC ($Cs_2LiLaBr_{6-x}Cl_x(Ce)$), are very promising scintillation detectors for identifying and discriminating gamma and neutron radiations. They have been widely studied by several groups [126-131]. CLYC has an energy resolution better than NaI(Tl) but worse than $LaBr_3(Ce)$, yet features at least 100 times less internal radiation than $LaBr_3(Ce)$. CLYC also has very high efficiency in identifying thermal neutrons, particularly if enriched with ^6Li as it uses the reaction $^6Li + n = {}^3H + \alpha$ which has a cross section of 940 barns for thermal neutrons [132]. The pulse shape produced by gamma rays is characterised by a quicker rise and decay time compared to the neutron pulse, while also containing the core-to-valence luminescence (CVL) component of the scintillation light which is not present in the pulse produced by thermal neutrons. Pulse shape discrimination techniques can therefore be used to distinguish gamma rays and neutrons. In a recent study, two CLYC scintillators were characterised, one enriched at 95% of ^6Li and another at 99% of ^7Li [125]. Energy resolutions at 662 keV were found to be 4.8% for the crystal enriched with ^6Li and 4.5% for that with ^7Li. The decay time for the fast component of the gamma ray signal for CLYC was found to be 72 ns, while for CLLBC was 89 ns and CLYB was 53 ns [127]. The gamma-neutron discrimination can be utilised for further improvement of PG measurements; such study has not yet been reported and is worth for further exploration.

And so, the requirements for a good PG range monitoring system can be achieved with available detector systems, but achieving the requirements simultaneously for potential hybrid systems is a challenge. Table 1 presents a summary of scintillation detector performance achieved in various studies.

When choosing a scintillator for a particular detection system, the applicability should be explicitly verified and optimal conditions can be achieved depending on the crystal volume, doping percentage, the PMT used and associated electronics [124,132,133]. A technique known as *co-doping* has the potential to increase the scintillation crystal proportionality and detector mechanical properties, whereby the reliability and energy resolution of the detector are significantly improved. The non-linearity between low-energy electrons and scintillator photons

is predominantly induced by non-radiative electron recombination, which is related to hole mobility in inorganic crystals. Better linearity is achieved with larger hole mobility, and therefore better energy resolution. Inserting a secondary dopant, such as Sr++ in $LaBr_3$(Ce) or Ca++ in $CeBr_3$ can improve detector performance, for example, achieving an energy resolution of 2% for $LaBr_3$(Ce) and 3% for $CeBr_3$, at 661 keV [133]. Commercial PMTs are generally matched for a particular scintillator size and coupling mechanism/material. To reach superior time resolutions, PMTs should be specifically designed and trigger set-ups improved, such that the time resolution has a dependence on the scintillation decay time and the number of photoelectrons [123]. Operating the PMT at higher bias voltage and optimising the constant fraction discriminator (CFD) settings (external delay and walk adjustment) with respect to the timing resolution have also been explored for improving timing properties [122].

Table 1: Summary of energy resolutions and timing properties of several scintillators published in the literature, with reference given.

Scintillation detector	Energy resolution at 662 keV (%)	Rise time (ns)	Decay time (ns)	Timing resolution FWHM (ps)
$LaBr_3$(Ce)	2.4 [117]	0.7 [134]	15 [134]	107 [116]
	3.1 [124]	10 [118]	16 [124]	
	3.2 [134]		~20 [116]	
	<4 [118]		25 [118]	
$LaCl_3$(Ce)	3.2 [135]		20 [135]	181 [135]
	3.5 [117]		~25 [116]	
	3.8 [136]			
$CeBr_3$	~3.6 [121]	0.1 [121]	17 [121]	189 (at 4.4 MeV) [123]
	4.3 [124]	<1 [120]	17 [124]	
	4.4 [125]	~18 [125]	17-24 [120]	
	4.6 [123]		~70 [125]	
SrI_2(Eu)	3.0 [137]		1200 [137]	824 (at 4.4 MeV) [123]
	3.3 [123]		~7000 [125]	
	4.0 [125]			
NaI(Tl)	6.1 [117]		~210 [116]	856 (at 4.4 MeV) [123]
	9.0 [123]			
CLYC	4.8 (95% 6Li) [125]	5 [129]	65 [129]	
	4.5 (99% 7Li) [125]		72 [127]	
CLLBC	4.1 [138]		~55 [138]	
			89 [127]	

2.3 Current Research Status of Prompt Gamma for *in vivo* Beam Range Verification and Dosimetry

The use of PG rays for monitoring the beam range in particle therapy was first proposed by Stichelbaut and Jongen in 2003 [139], and a proof of principle was performed by Min et al. (2006) [27] with a collimated detector for proton beam irradiation of a water phantom. The close correlation between the PG emission and the BP position was reported within 1-2 mm accuracy. Since then, many authors have reiterated the feasibility of utilising PG emission for range verification, with simulations and experimental work being performed to understand PG emission during particle beam irradiations and its use for monitoring the BP during treatment, as well as to optimise PG detection methodology and overcome the challenges of PG detection technology.

The viability of employing PG rays for *in vivo* BP tracking for mono-energetic particle beams of therapeutic energies has been demonstrated [26,91,140-142], particularly for proton beams with heavier ions, such as helium and carbon, becoming of greater interest. The notion has also been demonstrated for passively scattered SOBP fields. The good correlation between the production position and intensity of PG rays with the dose delivered has been shown in homogeneous and heterogeneous media. However, as the PG production fall-off position does not exactly equal the dose profile fall-off, since they result from different physical mechanisms, a consistent PG-BP fall-off difference may be a key factor to enable direct correlation of the distributions [23,140].

The characteristics of PG emission during particle irradiations have been studied for a range of target compositions. The gamma energy spectrum has been shown to be characteristic to the elemental composition of the irradiated material, with emission lines from specific nuclear de-excitations determined: ^{16}O, single escape peaks 6.13 and 5.62 MeV, double escape peak 5.11 MeV, and single escape peaks 2.74 and 2.23 MeV; ^{15}O, single escape peaks 5.21 and 4.70 MeV, and double escape peak 4.19 MeV; and ^{12}C, single escape peaks 4.44 and 3.93 MeV, and double escape peak 3.42 MeV [26]. The PG emission line of 6.13 MeV was found to be directly proportional to the oxygen concentration in a volume of irradiated tissues, whereas the 4.44 MeV PG peak is dependent on both carbon and oxygen concentration [26]. The relative intensity of gamma emission peaks was found to be a function of both the elemental concentration and the physical density of the tissue [143]. Due to the characteristic spectra of PG rays, which depends on the medium composition, the PG signal can potentially be used to determine the elemental composition of the irradiated tissue [26,28,140]. A greater yield of low-energy gamma rays are produced during irradiation, though it is the higher energy gamma rays that have been found to better discriminate the distal dose fall-off, since these high-energy

gamma rays experience less scattering when traversing and leaving the target and so their production has improved localisation with respect to the dose fall-off [27,141].

The capability of verifying the beam range *in vivo* using PG rays depends greatly on the design optimisation of not only intrinsically efficient detectors, but also detector position relative to the target to maximise detection efficiency. The angular dependence of PG detection has therefore also been investigated [144]. It was found that regardless of proton beam energy, the total PG and ^{16}O gamma detection rates were higher at locations proximal to the proton treatment nozzle, with no significant dependence on the azimuthal angular rotation of the detector around the beam axis. Another study found that for a narrow angular collimation window, the PG profile displays a steep fall-off that is well-correlated with the BP, whereas a wider window allows for gamma spatial profiles to be detected while still exhibiting a good fall-off correlation with the BP position [145].

The interference background induced by neutrons presents one main challenge for accurate BP tracking using PG detection, particularly for heavier ions, such as carbon, due to nuclear fragmentation reactions. Exploiting the timing properties of PG rays has been shown to be a promising method for overcoming this challenge. A TOF technique to reject the neutron background of PGI by means of a shifting 1 ns TOF acceptance window, which accounts for proton propagation through the patient, has been studied [145] (see Figure 10). The Monte Carlo codes predicted than at a proton energy of 200 MeV, more than 99.6% of neutrons are rejected between initial entrance and the proton range. Testa et al. (2010) [142] implemented this TOF technique experimentally for 95 and 305 MeV/u ^{12}C beams irradiating PMMA and water phantoms. A clear correlation was obtained between the carbon ion range and the PG profile. The study demonstrated that a collimated set-up can be used to detect single photons by means of TOF measurements at therapeutic ion energies. As well, the detected photon count rates provide sufficient statistics to allow real-time control of the longitudinal BP position under clinical conditions [142]. The TOF technique, which differentiates the PG signal from the interference background, does not only improve the PG signal-to-noise ratio, but could also eliminate the need for heavy shielding around the detectors in the clinic.

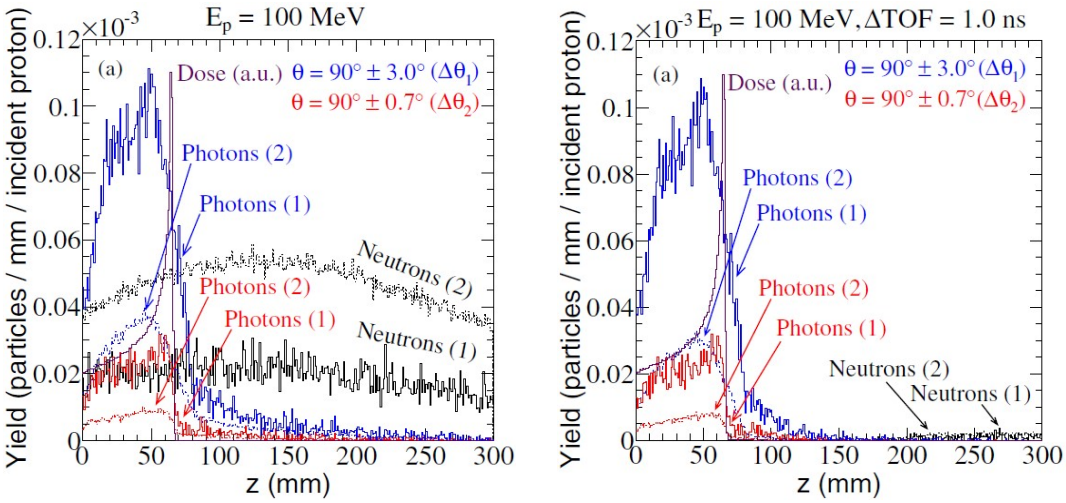

Figure 10: Yield of PG rays (blue and red) and neutrons (black) registered in the detector, and depth dose profile for a mono-energetic 100 MeV proton pencil beam, as a function of the longitudinal distance *z* in a PMMA phantom (purple), without (left) and with (right) a 1 ns shifting TOF acceptance window. PG profiles are shown for a narrow angular collimation window $\Delta\theta_2$ (red) and a wide window $\Delta\theta_1$ (blue). Simulated data with Geant4 is presented as (1) and MCNPX as (2). Bin width along *z* is 1 mm. Depth dose was calculated with Geant4 and is given in arbitrary units (a.u.). From Ref. [145].

The behaviour of PG rays during proton beam irradiation is quite well-understood. Several studies for carbon ions have been performed mainly with TOF techniques [146-148]. However, further research is still required to fully understand the use of PG rays for *in vivo* range and dose verification, mainly for other heavy ions which are becoming of greater interest. Recent dosimetry characteristics studies of helium ions have shown their potential to offer a more conformal treatment in clinical applications, which would result in increased tumour control [89,91,104], but the PG emission characteristics from helium ion irradiation have not yet been widely studied [94]. This knowledge is also required for the development of clinically suitable and reliable PG detection systems. For accurate and efficient range/dose verification using PG emission, the detection system is required to measure the high-energy PG rays and determine with millimetre precision their production position, in addition to excellent timing resolution (particularly if the temporal characteristics of PG rays are to be employed also).

Detector designs and developments have advanced through the years, but the challenges of PG detection technology are still present, which inhibit this technique from becoming a clinically wide-spread application for particle therapy QA. Several avenues of employing PG rays for range verification have been explored, including imaging and non-imaging modalities. Techniques to overcome some of the PG detection challenges have also been studied, with a particular interest in utilising the timing properties of PG rays for discriminating the PG signal from the interference background induced by neutrons, as well as for BP tracking itself.

2.3.1 Prompt Gamma Imaging (PGI)

Various imaging detector designs have been explored for locating the position of PG origination, including passive (mechanical) collimation systems [27,149-152] such as slit cameras placed perpendicular to the beam direction which offer a 1D projection of the ion track, and active (electronic) collimation systems [153-156] which rely on Compton kinematics to trace the gamma source and offer 2D or 3D images.

2.3.1.1 Passive Collimation Imaging System

In the proof of principle study, Min et al. (2006) [27] constructed a multi-layered collimator system to measure PG rays while moderating and capturing fast neutrons, and preventing interference gamma rays from reaching the scintillation detector. The correlation between the PG production distribution and the BP was found to be within 1-2 mm difference in position at 100 MeV proton beam energy.

In another study, a pinhole camera was designed to image PG rays while shielding neutrons and stray gamma rays, with the aperture shape and position selected in order to view the endpoint of the proton range [149]. A 0.2 mm shift in the peak of the total gamma distribution was observed for an energy variation of 1 MeV. This study showed that pinhole cameras may be a simple and viable tool for dose deposition verification in a patient, when the therapeutic beam range is less than a few centimetres.

Slit cameras have also been developed and tested for real-time beam range monitoring [150] (see Figure 11). The 1D projection of the beam path shows the gamma profile sharply decrease at the BP, such that gamma rays predominantly produced by primary protons along the beam path are emitted isotropically and not heavily influenced by scattering before exiting the target, and so the fluence of these gamma rays indicate the beam range. Gamma rays between 4 and 5 MeV were found to offer the most useful information for identifying the beam range. The prototype slit camera with knife-edge aperture using the HiCam system in Ref. [150] achieved a 1-2 mm standard deviation on estimating the beam range. A recent Geant4 study by Kim et al. (2019) [157] for a multi-slit PG camera showed that merging the PG distributions of several individual spots improved the statistical precision of the measurement. Beam range verification accuracy within ~1.4 mm error was achieved, demonstrating the viability of the technique to improve PG statistics. Knife-edge shaped slits provide a larger field-of-view than parallel-edge slits, and a higher photon collection efficiency can be obtained compared with a pinhole camera. A knife-edge slit in combination with a position-sensitive gamma camera placed perpendicular to the beam direction has been studied [151], and results showed that under common therapy

conditions for proton spot scanning, sufficient data may be collected during one spot-step (~10 ms) to locate the distal dose edge with a 1σ accuracy of better than 1 mm.

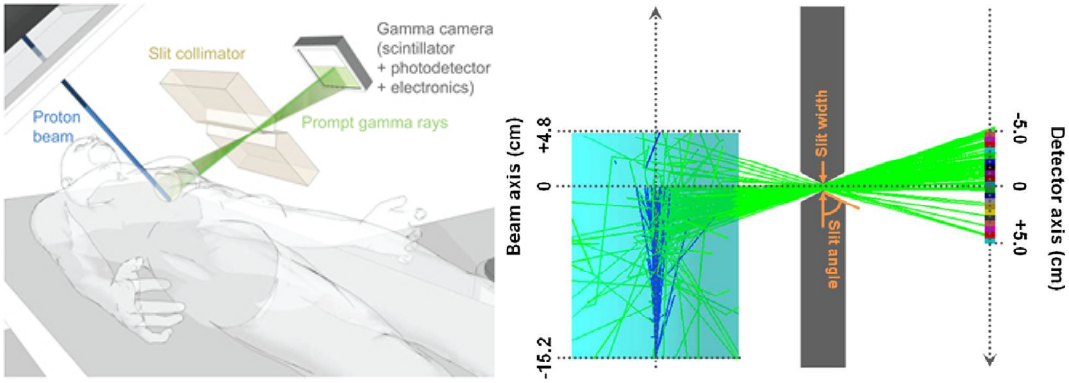

Figure 11: Left: Concept of the PGI method with a slit camera, whereby the slit collimation gives a 1D projection of PG emissions along the beam path on a scintillation detector. From Ref. [158]. **Right**: Simulated incident 160 MeV protons (blue) and secondary photons (green) which are emitted and reach the detector after passing through the collimator. From Ref. [150].

Recently, Richter et al. (2016) [152] performed clinical proton therapy measurements with a prototype knife-edge shaped slit camera developed by IBA. The prototype consisted of an array of 40 individual scintillation detectors arranged in two rows and optimised for detecting gamma rays of 3-6 MeV. The PG depth distribution was measured during passive scattered proton therapy (PSPT) treatment of a head and neck tumour for seven consecutive fractions. Inter-fractional global range variations in the range of ±2 mm were obtained for all evaluated fractions. Xie et al. (2017) [159] also employed a knife-edge slit camera, performing clinical range verification for a brain cancer patient where the measured profiles of individual pencil beam spots were compared to predicted profiles from the treatment plan. With a spot aggregation kernel of 7 mm sigma, 52 spots could be retrieved with accuracy better than 1 mm. The group demonstrated the feasibility of PGI for *in vivo* proton beam range verification in actively delivered PBS on spot-by-spot tracking. However, the count statistics is still one of the main issues in such systems to achieve higher statistical precision. Petzoldt et al. (2018) [160] derived a geometrical correction model for a knife-edge slit camera from Monte Carlo simulations in water. The correction considered four parameters: the beam range, the distance between collimator and beam axis, the distance between camera and collimator, and the offset in the beam direction between the BP position and the camera field-of-view centre. The geometric correction was shown to improve the agreement between simulated and measured PG profiles which improved range retrieval and the accuracy for absolute range verification.

Mechanically collimated PG cameras may be a more straightforward approach, and the slit width can be adjusted to optimise system efficiency and resolution, but the neutron

background and stray gamma rays have presented a challenge in early configurations, requiring thick layers of collimation. Electronically collimated systems, on the other hand, measure the position and energy of scattered photons and electrons to reconstruct the location and direction of incident gamma rays by means of Compton kinematics.

2.3.1.2 Active Collimation Imaging System

Compton cameras use multi-stage detectors in which the energy deposited and position of each gamma ray interaction is measured while scattering in the various stages of the camera, and the gamma ray is traced back to its position of origin. That is, from the interaction positions and deposited energies the direction of the incident gamma can be restricted to a cone with Compton kinematics. The vertex of the gamma origin is then obtained via the superposition of the multiple cones. Compton cameras offer an increased efficiency of potentially up to two orders of magnitude compared to collimated gamma cameras, since performance-limiting absorbing collimators are replaced by an electronically operating collimator [153-156]. Double-scattering Compton cameras enable direct analytical reconstruction and offer an improved spatial resolution [154]. Richard et al. (2011) [154] performed a Monte Carlo simulation study on design guidelines for a double-scattering Compton camera for PGI during ion beam therapy. In order to maximise the camera efficiency and minimise the spatial resolution, the source-to-camera distance should be considerably small, the detectors should be relatively thick, and the area of the second scatter detector should be larger than the first with the absorber detector larger than the second scatter detector. Recently, Draeger et al. (2019) [161] demonstrated the feasibility of a single Compton camera prototype to perform 3D PGI for proton range verification; detecting beam range shifts as small as 2 mm for a 2 Gy spot. A three-stage Compton camera has also been studied in terms of design specifications and to determine its feasibility to measure and image PG rays emitted during proton beam irradiation [155] (see Figure 12). Geant4 was used to model three high-purity germanium detector stages arranged in parallel-plane geometry, with an isotropic gamma source (0-15 MeV) used to determine the lateral width and thickness of the detector stages that yielded the optimal detection efficiency, and then a proton beam (50-250 MeV) irradiating a tissue phantom used to determine the overall efficiency of the camera. Overall efficiencies varied from ~10^{-6} to 10^{-3} PG rays detected per incident proton, and the suitability of a three-stage Compton camera for PGI during proton therapy was demonstrated. In order to minimise the radiation damage resulting from neutrons, as well as the cost, and the need for cryogenic coolants in the case of high-purity germanium, room-temperature alternatives such as cadmium zinc telluride (CZT) and cerium bromide ($CeBr_3$) would be more suitable. CZT is a semiconductor detector which offers good energy resolution for high-energy gamma rays, yet it lacks in sensitivity for high-energy gamma and is poor for timing measurements. Alternatively, $CeBr_3$ is a scintillator which offers good energy

resolution, excellent sensitivity and timing for high-energy gamma measurements. The feasibility and effectiveness of using the stochastic origin ensemble (SOE) algorithm for reconstructing proton pencil beam images from a three-stage Compton camera and for modelling the distal fall-off of secondary gamma emission has also been demonstrated [24]. Yao et al. (2019) [162] proposed modifications of origin ensembles with resolution recovery (OE-RR) algorithm based on Markov chains [163] to accelerate the algorithm and improve image quality. The modifications were in calculating the acceptance probability to implement ensemble transitions, using random sampling method in sequence to obtain the initial event density distribution in the volume of interest based on corrected values, and a correction for the finite energy resolution. The results demonstrated good resolution recovery and accurate estimation of the PG emission peak and distal fall-off with significantly faster reconstruction.

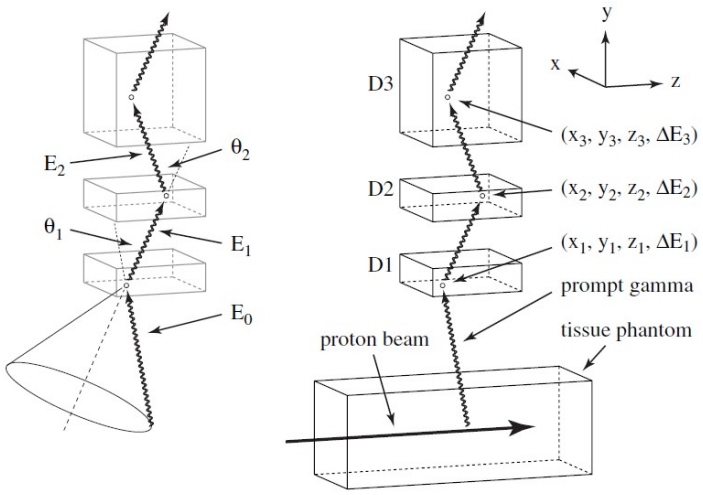

Figure 12: Concept of a three-stage Compton camera (two scatter detectors and one absorber detector). The gamma rays with energies (E_0, E_1, E_2) scatter in the detectors (D1, D2, D3) with Compton scatter angles (θ_1, θ_2). The projected cone (into the target/patient) is used to reconstruct the images. The interaction position and energy deposition in each detector is shown. From Ref. [155].

An alternative method, such as the electron tracking Compton camera (ETCC) has been developed for reconstructing 3D tracks of scattered electrons in the Compton process for sub-MeV and MeV gamma rays [164]. The direction of the incident gamma ray is determined for each individual photon by measuring the direction and energy of the recoil gamma ray as well as the scattered electron. Background rejection is realised with Compton kinematics of a residual measured angle between the recoil electron and scattered gamma ray. The ETCC comprises of a gaseous time projection chamber (TPC) for 3D tracking of the electrons, and pixel scintillator arrays (PSAs) for detecting recoil gamma rays. Tests have been performed with 140 MeV proton beam irradiation of a water target [165]. The TPC ($10 \times 10 \times 15$ cm^3) was filled with Argon and C_2H_6 (9:1) at 1 atm pressure, based on micro pixel chamber (μ-PIC). The

PSAs were GSO(Ce) ($6 \times 6 \times 26$ mm^3) coupled to a multi-anode PMT (H8500). The overall efficiency of the system was determined to be ~3×10^{-6}. 2D PG images showed correlation to the BP position, but further study and improvements are required.

Gamma electron vertex imaging (GEVI) was explored in a simulation study by Kim et al. (2012) [166]. The technique relies on the conversion of high-energy gamma rays, by Compton scattering, to electrons which are subsequently traced by hodoscopes to determine the location of the gamma source of vertices of the nuclear interactions. A prototype system was developed for proton beam range measurements [167]. It comprised a beryllium (Be) plate, two double-sided silicon strip detectors (DSSDs), a plastic scintillation detector, as well as dedicated signal processing and DAQ systems. The 1.08 mm thick Be plate (electron converter) was chosen to ensure a high probability of Compton scattering and limit MCS on the converted electrons. The DSSDs were used to determine the trajectories of the converted electrons, each with an active area of 50×50 mm^2 and 16 strips on each side, with thickness of 150 and 300 μm for the first and second layer, respectively. The plastic scintillator ($100 \times 100 \times 20$ mm^3) measured the energy of the converted electrons. Triple coincidence logic and multiple energy windows were used to select only PG events. The detectors of the GEVI prototype were evaluated for electronic noise, energy and timing resolution, with the imaging capability tested with a ^{90}Sr beta source, a ^{60}Co gamma source, and a 45 MeV proton beam incident on a PMMA phantom. The study showed promising results for imaging PG vertices from proton irradiation. More recently, Kim et al. (2018) [168] performed experimental measurements of GEVI for proton therapy and determined a beam range verification accuracy within 2.7 mm. Although the group demonstrated the feasibility of GEVI for real-time beam range monitoring, further work for practical clinical applications are necessary, such as experiments for various number of protons, phantom materials, and beam incidence position and size. Though, the technique is promising since GEVI requires no mechanical collimation, provides higher imaging sensitivity than other PGI systems, and offers the potential to obtain images of almost no noise, i.e. using triple-coincidence logic and triple energy windows, only trajectories of the electrons produced from the PG rays can be selected, thereby effectively excluding proton and neutron signals from the detection system [168].

In conclusion, extensive work has been carried out in the area of PGI for BP tracking during particle therapy treatment delivery. However, the count statistics remains a major issue in PGI systems to achieve higher statistical precision of *in vivo* beam range verification. The slit cameras only offer 1D range information in the longitudinal beam direction, lacking information in the lateral spread. Compton cameras may offer 2D or 3D imaging but such systems suffer from challenges in detectors and image reconstruction to achieve clinically acceptable images [169]. Other monitoring techniques using PG rays are also being explored, which take

advantage of specific characteristics of PG emission. For example, novel techniques exploiting the temporal properties of PG rays have the potential to offer a simpler means of beam range verification, and eliminate the need for expensive, bulky equipment in the clinic. The following non-imaging approaches for *in vivo* beam range verification have an advantage of low footprint detector set-up in clinical practice.

2.3.2 Prompt Gamma Spectroscopy (PGS)

This method of beam range verification directly relates measurements of discrete PG lines to nuclear reaction cross sections. Verburg et al. (2014) [170] studied this concept with the aim to develop a method entirely based on quantitative physics models and is robust in the presence of tissue with an unknown elemental composition. Differential cross sections were measured for 15 PG lines from proton-nuclear interactions with ^{12}C and ^{16}O at proton energies up to 150 MeV. Fitting measured cross sections with detector models, an optimisation method was developed to simultaneously determine the proton range and the composition of the irradiated tissue. A small-scale prototype detector was also used to test experimentally this method with various phantoms. Cerium-doped lanthanum (III) bromide ($LaBr_3(Ce)$) crystal was used as the primary detector, read out by PMTs, with a tungsten collimator (127 mm thickness, 9.5 mm slit opening). The prototype achieved statistical precision of ~1 mm standard deviation for absolute range verification and 0.4 mm for relative verification, based on 5 pencil beams delivering 5×10^8 protons. However, improving the detection efficiency by an order of magnitude was anticipated to be feasible for a full-scale system and can achieve the clinically required dose for millimetre accuracy [170]. More recently, preliminary experimental measurements of the full-scale prototype were published in Hueso-González et al. (2018) [59]. The energy- and time-resolved spectral measurements of PG rays were employed with slit collimation and integrated with a Monte Carlo simulation-based treatment planning system. In realistic clinical conditions, the clinical prototype can verify the absolute range of the proton pencil beams with high spatial precision (1.1 mm). In this approach, the temporal information of PG rays was used to reject the background gamma rays from proton-induced and neutron-induced continua, but the temporal information could further be employed with hybrid PG detection systems for extracting beam range information.

2.3.3 Prompt Gamma Timing (PGT)

PGT is a novel method of range assessment proposed by Golnik et al. (2014) [171], which is based on an elementary physical effect whereby ions traversing tissue have a time interval of transit from entering the patient to stopping in the target volume. It has been determined that protons with a 5-20 cm range have a 1-2 ns transit time. Since the transit time increases with the particle range, there are measureable effects in the PGT spectra that can be

used for beam range tracking. The PGT spectrum was defined in this study as the transit time of the ion through the material as well as the flight time of the PG ray to the detector. In this study, kinematical relations were used to describe the relationship between PG emission and resultant time profiles. The technique was explored for homogeneous and inhomogeneous targets. Proton irradiation experimental measurements were also performed to verify the concept, at the AGOR cyclotron KVI-CART University of Groningen. The proton beam energy was fixed at 150 MeV for all the experiments, with various PMMA and graphite targets irradiated, and PGT spectra measured with a GAGG(Ce) scintillator coupled to a Photonis PMT. Model calculations precisely reproduced the experimental results. The analysis was focused to an energy window ROI set to 4.3-4.5 MeV. The proton transit time was shown to directly correlate to, and be measurable, with statistical moments such as the mean μ and standard deviation σ of the PGT spectra, and hence also correlate to the proton range (see Figure 13). A change in the target position corresponded to a change in the PGT spectrum mean. Increasing the thickness of protons traversing the target from 5 to 15 cm led to a broadening in the PGT spectra, which was also observed when increasing the beam energy from 50 to 230 MeV corresponding to a change in the range from 2 to 17 cm. Range variations of 2 mm were expected to be clearly detectable with this monitoring approach [171]. More recently, Werner et al. (2017) [172] demonstrated the feasibility of the PGT method to enable range verification with 2-3 mm accuracy in clinical conditions. Six PG detection units were employed, each consisting of a 2" × 1" diameter or 2" × 2" diameter $CeBr_3$ scintillation detectors, with no collimation hardware; the use of multiple detectors improves the measured statistics. The main limiting factors of this method were identified as the long-term phase shifts and strongly damped phase oscillations between the RF and proton bunches after changing the beam energy between PBS layers. Yet, introducing a bunch phase monitor may improve the accuracy of the method. Further work by the group is being conducted to construct a 'PGT snout' that integrates up to 8 $CeBr_3$/U100 detection units in the beam delivery system of the proton therapy facility [172]. Unlike PET and other collimated PGI systems, PGT is based on straightforward measurements with an uncollimated detector, and could perhaps be used for active treatment control [171].

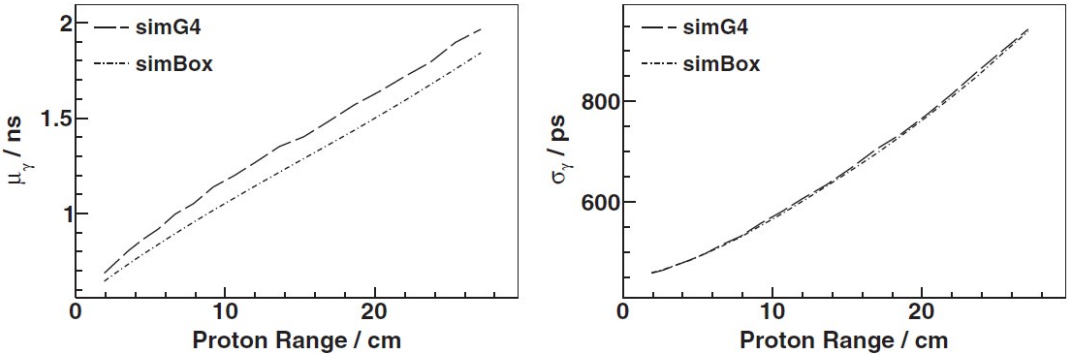

Figure 13: Range-dependent mean μ_γ (left) and standard deviation σ_γ (right) values of modelled PGT spectra. Proton energies are in the range of 50 to 230 MeV, corresponding to proton ranges of 2 to 27 cm in a PMMA target. The assumed system time resolution is 450 ps. From Ref. [171].

2.3.4 Prompt Gamma Peak Integration (PGPI)

PGPI is a technique that has also been introduced as a simple and cost-effective means of detecting deviations from the prescribed treatment during particle therapy, using the integrals of uncollimated PG timing distributions. As with the PGT method, the correlation of the mean value and width of TOF distributions with the energy and range of incident particles is utilised. However, this PGPI technique uses, in addition, the integral to verify the beam range and energy deposited, thus approaching *in vivo* dosimetry. Krimmer et al. (2017) [173] performed measurements with 65 MeV protons, where the proton range inside a homogeneous PMMA target was varied using a modulator wheel. Scintillation detectors $LaBr_3$(Ce) (25.4 × 25.4 × 72.2 mm^3) and BaF_2 (hexagonal shaped, with an edge length of 50 mm and length of 140 mm) were positioned at 90° or 45°, with respect to the beamline, to reduce background events (since neutrons are predominantly forward emitted). PG rays registered with the $LaBr_3$(Ce) scintillator were read out via a dedicated DAQ card. The high frequency signal of the accelerator served as time reference for determining the TOF. The measured variation of the PG TOF peak integrals as a function of the modulator position was found to be consistent with simulations. With 10^8 incident protons and detectors covering a solid angle of 25 msr (corresponding to a diameter of 3-4 inch at a distance of 50 cm from the beam axis), deviations of a few per cent in the PG count rate can be detected. For the configuration in the study, this change in count rate corresponded to a 3 mm change in the proton range in a PMMA target. A displacement of the target toward or away from the detector alters the PG count rate due to the difference in the absorption, whose effect is of the same order of magnitude as a possible deviation to be detected. Moreover, simulations showed that the signals from multiple detectors may be combined as ratios to obtain information about the target placement or as (geometric) mean which is independent on the

actual target position. This technique may be a simple monitoring device used independently from other monitoring devices of the beamline [173].

Each approach developed to utilise PG rays for beam range monitoring for particle therapy treatment delivery has its own advantages and limitations. The techniques however exploit one specific feature of the PG rays (such as spatial in PGI, energy in PGS and time in PGT), where complementary features are used for event filtering (such as using timing information in PGI and PGS for reducing background interference caused by neutrons) rather than extracting range information [19]. Hybrid detection methods may instead be essential in overcoming the challenges of a broad- and high-energy PG ray distribution, significant interference background, high instantaneous count rates, and compatibility constraints with patient irradiation. This therefore calls for systematic studies of PG ray emission and detection characteristics in multi-dimensions of space, energy and time.

2.4 The Role of Monte Carlo Simulations in *in vivo* Dosimetry Using Prompt Gamma

Monte Carlo simulations play a crucial role in *in vivo* range and dosimetry verifications with PG rays because such verifications are based on comparisons between measured data and predicated ones. The role of simulations and PG has been reviewed by Krimmer et al. (2018) [57] and that of Monte Carlo simulations in the context of range uncertainties discussed by Paganetti (2012) [9]. In this section, some of these aspects are mentioned but focus is placed upon the topics of relevance to this thesis.

Simulation tools are not only employed for the research of PG rays as reviewed in the previous section, they are also used clinically as a means of comparing the obtained measurements with expected outcomes. The predicted results are obtained from simulations that are based on specific DICOM data (patient planning CT volume and treatment plan) and beam models (radiation quality). Thus, it is important that the physics models and data in the simulation are accurate and reliable, since the production of PG rays depends on the particle energy and target nucleus [57].

The predicted outcomes may be obtained via Monte Carlo or analytical methods. Using Monte Carlo to simulate PG emissions for treatment plans can be very time consuming [174-176]. Ways to improve efficiency include, for example, a GPU-oriented implementation of the Monte Carlo engine, such as goCMC which can accurately calculate dose within a few tens of seconds (without electron and neutron transport) and CUDA gPMC which can improve the efficiency by three orders of magnitude [177,178]. Approximate methods, such as condensed

history transport and basic Variance Reduction Techniques (VRT), can also improve efficiency, which are already implemented in most Monte Carlo packages [179]. Analytical models using ray-tracing is more efficient, whereby PG emission profiles are generally precomputed with Monte Carlo simulations (e.g. PENELOPE [180]) and scored in tables while getting proton differential cross section data from ICRU report No. 63 [181] [57].

In the work of this thesis, the Monte Carlo simulation tools Geant4 (GEometry ANd Tracking) [182,183] and TOPAS (TOol for PArticle Simulation) [184] were employed to investigate PG rays for range verification and toward *in vivo* dosimetry in particle therapy. Geant4 is a Monte Carlo code written in C++ and uses the Object-Oriented Technology for simulating the passage of particles through matter [185]. It is used from High Energy Physics to medical physics, nuclear and accelerator physics, as well as space science. Geant4 provides a complete set of tools for radiation physics related problems, including extensive physics capability coupled with powerful geometry functionality. It also has other components, such as tracking, detector response modelling, visualisation, event biasing techniques, analysis, etc [186]. TOPAS is dedicated to proton therapy simulations. It wraps and extends the Geant4 simulation toolkit with a unique parameter control system that allows the user to assemble and control a rich library of simulations objects, such as geometry components, particle sources, scorers, etc, with no need to write C++ code. However, simulation objects in C++ code may still be implemented in TOPAS via an extension mechanism. The full flexibility of Geant4 can be exploited while user-written objects benefit from underlying functionality of TOPAS base classes and the parameter system [187].

Geant4 has been extremely popular for the development and clinical implementation of particle therapy techniques. Validation studies of the Geant4 models for protons [174,188-193], carbon ions [174,194-199] and helium ions [200] have been performed. TOPAS has also been used in several studies, particularly for proton therapy applications [201-204]. A validation of TOPAS was performed for proton therapy treatments with passive scattering at MGH based on routinely performed QA measurements [205], and the feasibility and accuracy of TOPAS for carbon ion therapy has been investigated [206].

In terms of calculating the stopping power and particle range in Monte Carlo, the main uncertainties are from the material density and the ionisation energy I_e in water. As mentioned in Section 1.2, stopping powers obtained from CT scans have uncertainties, such as calibration of the CT scanner and conversion from HU. Stopping power models in Monte Carlo are typically benchmarked with standard QA in-house dosimetry measurements performed with ionisation chambers, calorimeters, and Faraday cups. The validation of these models at therapeutic energies is important [65]. In terms of the PG emission and yield, uncertainties in

modelling nuclear interactions are mainly from cross sections, where total cross sections and double differential (energy and angle) cross sections are most relevant. Uncertainties also arise when tissue composition is inferred from CT scans. Dosimetry can assist in the validation of nuclear models, which can be done in-house with Faraday cup measurements, but it is often impossible to perform direct experimental validation [57,65].

Several studies have evaluated nuclear models for secondary particle production and depth-dose profiles, and quantitatively characterised PG emission yields with Monte Carlo codes [174,207-212]. Differences of the PG emission between Monte Carlo codes and existing evaluated data exist depending on the target and gamma line under consideration. Le Foulher et al. (2010) [207] compared simulation with experiments and found that simulations overestimate PG detection yields by a factor of 12. Verburg et al. (2012) [143] simulated proton-induced nuclear reactions using Geant4 and MCNP6 with TALYS and EMPIRE, and optimised input parameters and model selection. The results were compared to evaluated ENDF/B-VII cross sections, where model estimates of the total gamma production near the end-of-range differed by a factor of about 2. Recent efforts to assess and improve the accuracy of PG productions in Geant4 physics for particle therapy have been reported. Dedes et al. (2014) [208] found improvements of the Geant4 hadronic models when decreasing the width of the Gaussian wave function in the QMD model. Jeyasugiththan et al. (2015) [209] found that the precompound model with modified initial exciton state of 2 produced more accurate discrete gamma lines in comparing with available gamma production cross section data. Vanstelle et al. (2017) [212] found INCL++ to more accurately reproduce PG emission compared to BIC and QMD, in comparing with experimental data. Further work is required for the improvement of hadronic models and differential cross sections as well as PG yield measurements from particles at clinical energy range [22]. Although experiments have been performed for protons [170,211,213] and carbon ions [94,148,214] to evaluate PG emission yields, more precise nuclear physics models and accurate data for predicting the PG distribution are necessary in clinical routine [57].

2.5 Further Research Required in the Prompt Gamma Method

After years of research, the first clinical application of PGI-based range verification was performed with the knife-edge slit camera design by Richter et al. (2016) [152], with successful measurements of PG profiles during proton therapy, obtaining inter-fractional global range variations in the range of ±2 mm for all evaluated fractions. With the same camera design, Xie et al. (2017) [159] also performed clinical measurements and obtained range shift precision better than 2 mm. However, despite the developments for using PG rays to promote *in vivo*

particle beam range verification and beam dose delivery in real-time, the technology remains clinically unavailable.

Dedicated detector systems are required to overcome the challenges of the broad PG energy spectrum, large background, high instantaneous count rates, and compatibility constraints with patient irradiation [24,28,140]. Hybrid detector systems, which utilise more than one feature of PG rays for extracting range information or dosimetry have potential, but a system that meets the requirements of such PG measurement require further research efforts; excellent energy and time resolution, high-throughput spectroscopy, and comprehensive data analysis and reconstruction [19]. As well, although studies have shown a good correlation between the PG production position and dose delivered, there is no exact one-to-one relationship representing this correlation since they result from different physical processes. Hence, numerous factors influence the accuracy of beam range and dose verification using PG rays, including also changes in the primary particle energy and phantom properties [215]. A recent study from Krimmer et al. (2017) [173] showed that the count variations of the PG TOF peak integral have a strong correlation with the beam range deviation. Further investigation into the effect of heterogeneous targets, beam type and energy, as well as the necessary technology for fast timing detection, may lead to a simple cost-effective technique for particle range verification during particle therapy treatment. Furthermore, the challenges of Monte Carlo codes should also be addressed to improve the accuracy and efficiency of the codes for use with the PG method.

Our project aims to further develop the understanding of PG ray characteristics with determining optimal methodologies for PG detection, detector technology requirements and toward potential hybrid systems, and the performance of Monte Carlo codes.

3 Characterisation of Prompt Gamma Rays for Beam Range Verification

The detection of PG rays is challenging due to the broad and relatively high-energy range (compared to PET) with strong interference background from neutrons and other stray radiations. Innovative detection methods, by utilising either or complementary features of PG ray characteristics, are pursued to extract the PG signal from the background; this can therefore lead to hybrid PG detection systems. Hence, the Monte Carlo simulation Toolkit Geant4 [182,183] was adopted in this study for the characterisation of PG rays in terms of energy, space and time to determine optimal detection methodologies and technologies for particle beam range monitoring. Initially, a homogeneous spherical-shaped water phantom was used to characterise the emission and detection with an ideal detecting sphere surface encompassing the phantom. In this study, three different ion species were investigated: proton, helium (^{4}He) and carbon (^{12}C). Each particle beam was simulated at four different energies to also observe the influence of varying beam range on PG emission and detection profiles for range monitoring purposes. To study the PG characteristics from various target materials and the effect of phantom geometry, homogeneous cylindrical-shaped water, polymethyl methacrylate (PMMA) and adipose tissue phantoms were also irradiated with the same three ion species. To then investigate the PG characteristics from heterogeneous phantoms, a realistic head phantom, the Computerized Imaging Reference Systems (CIRS) paediatric head phantom, Giacometti et al. (2017) [216], was modelled in the Geant4 simulation as treatment target and irradiated with 100 MeV protons. The model was also adapted such that the head phantom was made water-based, with only the air-pockets remaining. This allows direct comparison between a water-based and realistic head phantom, to investigate the effect of modelling a realistic target treatment, with different tissues, on the proton beam range as well as the characteristic properties of PG rays.

Part of the work in this chapter has been published in *Characterization of prompt gamma ray emission for in vivo range verification in particle therapy: A simulation study*, Physica Medica, 62, 2019 (Ref. [217]). Certain figures have been reproduced from the publication.

3.1 Monte Carlo Geant4 Simulation Set-up

3.1.1 Homogeneous Spherical and Cylindrical Phantoms

Geant4 (version 10.02.p02) was used to investigate the characteristic emission of PG rays from particle beam irradiations of a homogeneous spherical-shaped water phantom (density of 1 g/cm^3). The simulation set-up is shown in Figure 14. Mono-energetic pencil beams of proton, ^{4}He and ^{12}C ions were studied, irradiating the phantoms with the beam axis crossing the centre of the phantom. The primary particles originate at the phantom surface, such that they do not interact with air before reaching the target; the beam is therefore not degraded before irradiating the phantom. The phantom size was chosen as 40 cm diameter to represent the size of a human abdomen, and for simplicity, a spherical shape was initially used. Depth dose curves were obtained by calculating the energy deposited in the phantom along the direction of incidence of the beam (z-axis). The bin size of the depth dose profile was 1 mm. At the position of the BP the energy deposited along the x-axis was also calculated, for a longitudinal width of 10 mm. Proton and ^{4}He beams of 62, 150, 200 and 250 MeV/u, and ^{12}C beams of 120, 285, 385 and 490 MeV/u were simulated. These energies correspond to ranges (80% distal dose fall-off) of approximately 30, 160, 260 and 380 mm in water, as determined from the simulation results of this thesis. These values are consistent with NIST [218] for proton/helium ions and SRIM [219] for carbon ions taking into consideration that they calculate the ranges with the CSDA and projected range algorithm (PRAL), respectively. These energies were chosen since they are typical of therapy treatment for the respective particle types with the exception of the energies 250 MeV/u of ^{4}He and 490 MeV/u of ^{12}C, which were also included for comparison.

To study the characteristic PG emission from different material compositions and the PG detection from phantom geometric effects, the study was repeated for cylindrical-shaped water, PMMA and adipose tissue materials of 40 cm diameter and 40 cm height. Adopting the same set-up, the cylindrical phantoms replace the spherical phantoms in Figure 14. The cylinder phantom materials were based on the Geant4 NIST materials database [220]: water (H_2O, density of 1.0 g/cm^3), plexiglass ($C_5H_8O_2$, density of 1.19 g/cm^3) (also referred to as PMMA) and adipose tissue (ICRP) (primarily H (11.4%), C (59.8%) and O (27.8%) with 0.7% N, density of 0.95 g/cm^3). The particle beam energies for each phantom were:

Water – *proton* 61, 149, 197, 248 MeV, *^{4}He* 60, 148, 196, 247 MeV/u, *^{12}C* 112, 282, 380, 486 MeV/u;

PMMA – *proton* 66, 163, 216, 272 MeV, *^{4}He* 65, 162, 215, 271 MeV/u, *^{12}C* 122, 309, 418, 536 MeV/u; and

Tissue – *proton* 60, 147, 195, 245 MeV, ^{4}He 59, 146, 194, 244 MeV/u, ^{12}C 109, 280, 379, 484 MeV/u.

These energies correspond to ranges of approximately 30, 160, 260 and 380 mm, such that the deviation between the respective beam range in the phantoms were within 3 mm.

In all cases, the number of incident particles was 10^8 for protons, 10^7 for ^{4}He ions and 10^6 for ^{12}C ions to obtain a statistical uncertainty of 5% in the yield of PG rays. The statistical uncertainty was calculated with $1/\sqrt{N}$, where N is the number of counts. The uncertainties are purely statistical; those that affect physics concepts are not taken into account here.

Characterising the photon and neutron radiation fields escaping the phantom provides beneficial information which assists in choosing potential PG detectors. To score the photons and neutrons that are emitted from the phantom, an air-filled idealised detecting sphere surface (referred to as *detection sphere*) encompassing the phantom was used, with a diameter of 100 cm. When the photon/neutron traverses the surface of the sphere, they are counted.

A fixed point-of-reference, corresponding to the centre of the Geant4 simulation coordinate system (see Figure 14), was chosen at the surface of the phantom for simplicity. An alternative option would have been to select the BP position as point-of-reference, however, this position varies within the phantom depending on the particle beam energy, therefore it was not identified as a suitable reference point for all the simulation set-ups considered; the chosen point-of-reference is similar to the clinical practice of having a fixed point-of-reference on the patient surface.

The angular emission characteristics of PG rays was studied in terms of the polar angle θ between the incident beam direction and the line connecting the point-of-reference to the point P traversed by the photon on the detection sphere (see Figure 14). φ is the azimuthal angle between the x-axis and the line connecting the point-of-reference to the point P traversed by the photon on the detection sphere. The angular emission study allows identifying eventual preferential PG emission directions, which would allow identifying preferential locations of the PG detector/s to maximise the detected PG yield and minimise the neutron yield.

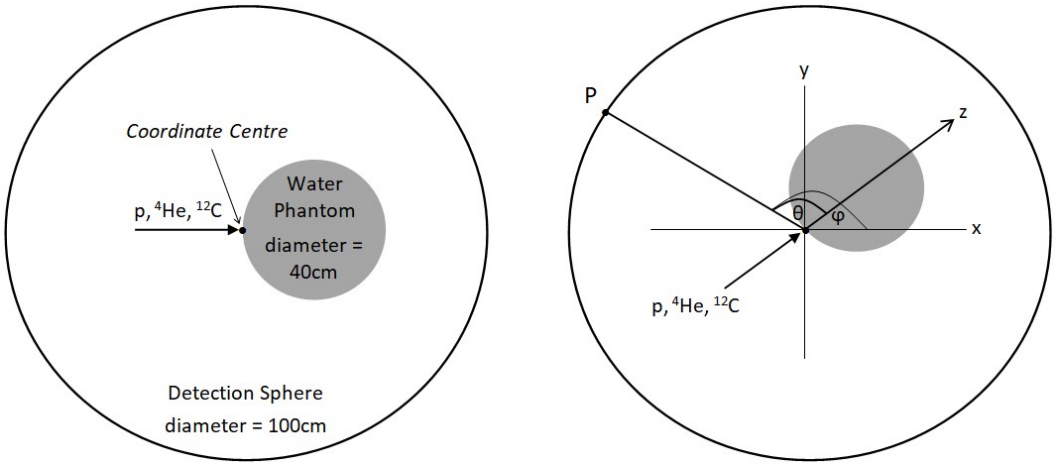

Figure 14: Left: Geometrical simulation set-up of the spherical water phantom in an air-filled detection sphere. **Right**: The angle θ is formed from the longitudinal beam direction (z-axis) with the line connecting the centre of the coordinate system and the point *P*. *P* is the PG detection position on the detection sphere traversed by the photons, and φ is the azimuthal angle. For the case of the cylindrical phantom, it replaces the spherical phantom in the simulation set-up, with the main axis along the direction of the incident beam.

A modularised Geant4 Physics List was used which included both electromagnetic (*G4EmStandardPhysics_option3*) and hadronic physics processes (*QGSP_BIC_HP*). The *G4RadioactiveDecayPhysics* and *G4HadronElasticPhysicsHP* modules were active. The *QGSP_BIC_HP* was chosen as it was found adequate for proton and carbon therapy studies in Ref. [190,199,221]. Total cross sections are described by the Glauber-Gribov theory [222] and the final state of inelastic scattering is generated by the Binary Cascade model [223]. The High Precision (HP) Neutron Data Libraries [224] were used to more accurately model the neutron interactions from thermal energies up to 20 MeV.

The simulation output consisted of the yield of photons and neutrons generated within the phantom, and those that reach the detection spherical surface. The yield was normalised to the number of incident particles on the phantom. The PG emission time was calculated as the time interval between the origin of the primary particle in the simulation (particle incident on the surface of the phantom) and the time of origin of the PG ray in the phantom. The PG detection time, defined as TOF, was calculated as the time interval between the origin of the primary particle in the simulation and the time when the PG ray reaches the detection sphere. The gamma TOF distribution mean and integral were retrieved from the simulation.

The primary PG rays are referred to those produced from the primary particle interactions, and the secondary PG rays are referred to those produced from the interactions of the secondary radiation field. The primary and secondary PG rays were differentiated to more closely study their correlation to the particle beam range.

In the post-simulation data analysis, several parameters of PG emission and detection were investigated: R, the particle beam range defined as the position of 80% BP distal fall-off along the beam path in the phantom; R_{PG}, the PG range defined as the position of 80% PG emission yield fall-off in the phantom; Δ*fall-off*, the difference $R - R_{\mathrm{PG}}$ used to quantify the longitudinal correlation between the PG emission fall-off and the beam range; Δ*FWHM*, the difference between the lateral PG emission distribution FWHM and lateral dose distribution FWHM for a 10 mm longitudinal thickness at the BP position; T_{PG}, the 80% fall-off of the PG emission time distribution; and T_{W}, the time difference between 80% rise and fall-off of the TOF spectra peak.

The energy spectrum of all photons generated in the water phantom, via any physical interaction process, allowed the observation of the prominent PG emission lines and the selection of two energy regions of interest: an energy threshold of $\geq$1 MeV, which eliminates the low-energy background photon counts [225] (e.g. positron annihilation photons at 0.511 MeV), and a 3.0-7.0 MeV energy window, which includes the prominent PG emission lines and has been employed in previous studies [176,226]. The energy threshold and window were used to analyse the PG emission yield, the spatial correlation between PG rays and the BP position, and the temporal and detection properties. In addition, in Section 3.4, when calculating the PG emission yield to deposited energy ratio for the different ion species, the energy deposited and scored at the BP maximum was taken.

3.1.2 Realistic DICOM-formulated Head Phantom

The high resolution voxelised head phantom utilised in this work was created from the CT scan of the ATOM® Model 715 HN, CIRS Inc., Norfolk, VA, paediatric head phantom. In this study, Geant4 (version 10.04.p02) was used to simulate a mono-energetic 100 MeV proton beam irradiating the realistic head phantom. At this energy, the proton CSDA range is 7.7 cm in water and 8.1 cm in adipose tissue (ICRP) according to NIST [218]. The proton beam energy was chosen so that the position of the BP corresponds to the centre of the phantom. The beam had a radius of 2.5 mm and a sigma_r (traverse standard deviation of beam position profile) of 11 mm. The protons are incident on the left-side of the head phantom, with an air gap between the initialisation of the beam to the phantom surface of approximately 30 cm, which is a common distance in particle therapy. Figure 15 shows an image of the realistic head phantom as implemented in the Geant4 simulation. 10^9 incident protons were simulated to obtain a statistical uncertainty of 3% in the yield of PG rays. Depth dose curves were obtained by calculating the energy deposited in the phantom along the direction of incidence of the beam (x-axis). The bin size of the depth dose profile was 1 mm. This study also included the idealised detecting spherical surface as used in the previous section; in this case the centre of the

detection sphere corresponds to the centre of the phantom. This was done so to have the centre of the detection sphere and phantom correspond also to the position of the BP; as mentioned, the proton beam energy of 100 MeV was chosen to have the beam range at the centre of the phantom. The Geant4 physics, scoring/simulation output, and post-simulation data analysis are as described in the previous section. Additionally, the realistic heterogeneous head phantom as readily available in Geant4 was modified to obtain a water-based head phantom. That is, air pockets in the phantom remained unmodified while all other voxels were changed to water (density of 1 g/cm^3) such that only two materials, air and water, made up the head phantom.

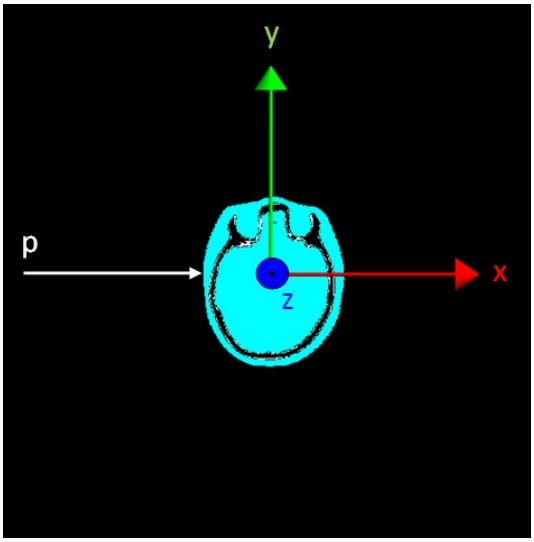

Figure 15: Geant4 visualisation of a slice of the realistic head phantom, as implemented in the Geant4 extended example DICOM [216]. The proton beam is not to scale.

3.2 Energy Spectra of Prompt Gamma Emission

In this section, the results for the PG emission spectra of proton, ^{4}He and ^{12}C ions irradiating water, PMMA and adipose tissue phantoms are presented. PG rays have a broad energy spectrum with strong interference background from secondary neutrons and stray gamma rays, which makes their detection a challenge. And so, an optimal energy threshold or window to be applied potentially in practice for improving the PG signal-to-noise ratio was investigated. Additionally, the PG spectrum is characteristic to the elemental composition of the target material, and so this aspect was also investigated for both homogeneous and heterogeneous (a realistic paediatric head) phantoms.

3.2.1 Homogeneous Phantoms

In this study, the energy spectra of photons generated within the spherical water phantom was first examined. Figure 16 shows the spectra resulting from any physical

interaction (including gamma photons induced by neutrons) for the three beam particle types. A consistent shape over a wide energy range is seen in the spectra for each particle type, with several characteristic emission lines produced by inelastic particle-nuclei interactions with major constituent elements of the phantom material.

Positron annihilation from the decay of ^{15}O and ^{11}C nuclei, among other isotopes, contributes to the 0.511 MeV peak. Secondary thermal neutron capture by hydrogen nuclei results in the 2.22 MeV peak. A 2.31 MeV peak arises from $^{14}N^*$ by proton and alpha spallation reactions with ^{16}O [227], which may be difficult for a detector to resolve from the 2.22 MeV emission line. The prominent PG emission lines are observed with energy 4.44, 5.21 and 6.13 MeV, which are the most proposed for beam range verification. The 4.44 MeV PG emission line originates from the de-excitation of $^{12}C^*$ nuclei, derived from nuclear interactions of particles with oxygen nuclei. The 5.21 and 6.13 MeV PG emission lines arise from $^{15}O^*$ and $^{16}O^*$ de-excitations, respectively. The distinctive 6.92 and 7.12 MeV lines are higher nuclear level emissions from $^{16}O^*$. The intensity of 4.44, 5.21 and 6.13 MeV lines are comparable to the 2.31 MeV line, but the 2.31 MeV line could be challenging to detect since it could be merged with the neutron capture line and detection will depend on the energy resolution of the detector. The 0.718 MeV PG line can also potentially be used for beam range verification but it may too be challenging to resolve in some detectors, such as LYSO detectors where detector intrinsic radioactivity may interfere with the PG signal.

The energy spectra of gamma ray emission within PMMA and adipose tissue phantoms also show a spectrum characteristic to the elemental composition of the materials. Figure 17 shows the spectra from homogeneous cylindrical water, PMMA and tissue phantoms for the three beam particle species with a range of ~16 cm in the materials. A higher concentration of carbon or oxygen in the target material is representative in the corresponding gamma emission spectra. The gamma energy spectra from PMMA and tissue show a larger intensity of the 4.44 MeV line due to the higher concentration of carbon in the materials. On the other hand, the water phantom gives a larger intensity peak at the 5.21 and 6.13 MeV lines due to its larger concentration of oxygen when compared to the other materials under study. In addition, two peaks are seen to arise in the spectra from PMMA and tissue targets, at 3.21 and 4.94 MeV, from ^{12}C and ^{13}C respectively, which are not present in the spectra obtained with the water phantom. The characteristic gamma emission spectra, which are dependent on the elemental composition of the irradiated target can thus be exploited for identifying the target material, as studied in Ref. [26,28,140].

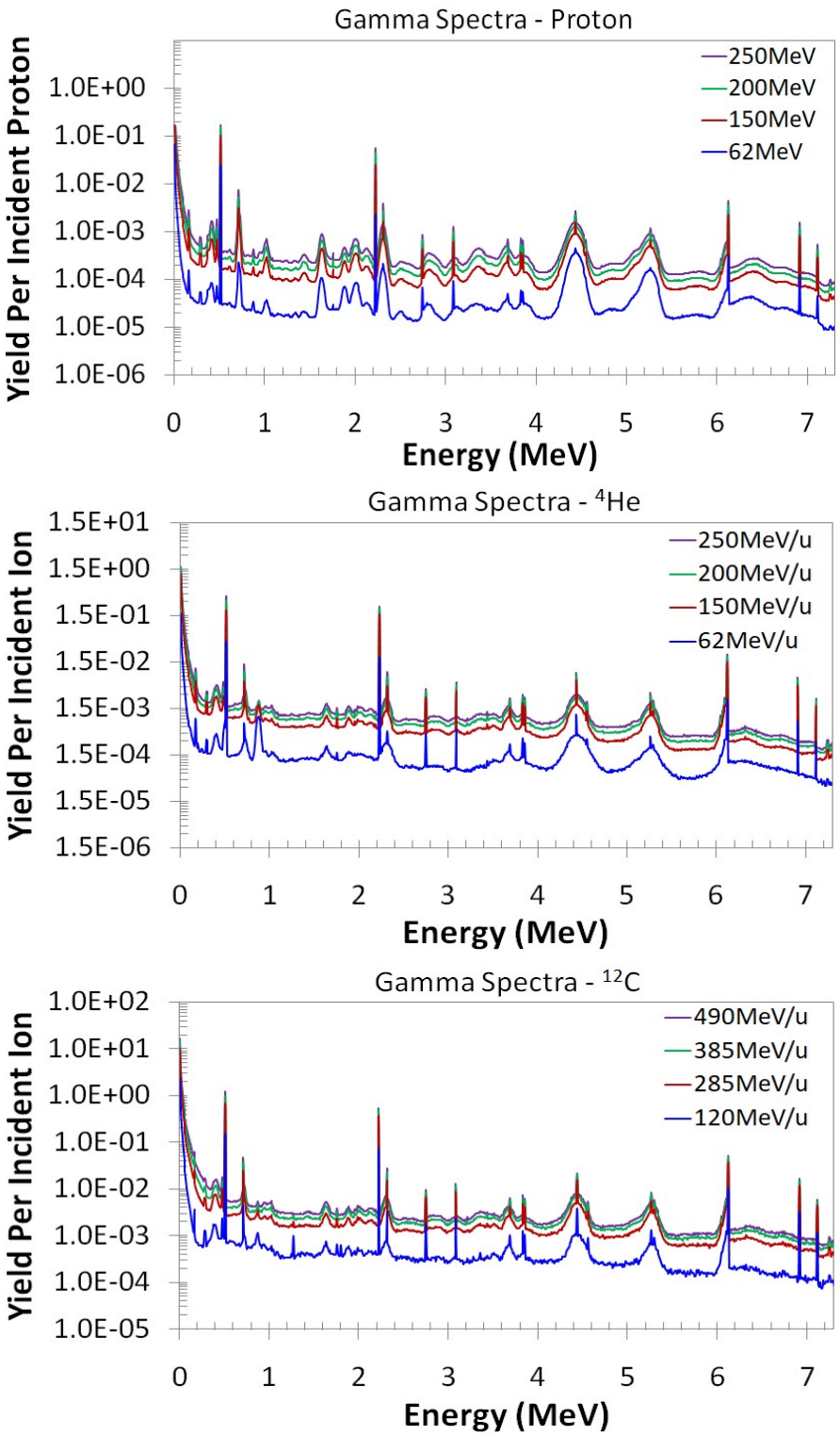

Figure 16: Energy spectra of photons generated in the homogeneous spherical water phantom deriving from pencil beams of protons, ^{4}He and ^{12}C ions. The emission lines are characteristic to the major constituent elements of the phantom material. The distinctive PG emission lines of energy 4.44, 5.21 and 6.13 MeV result from ^{12}C, ^{15}O and ^{16}O nuclear de-excitations, respectively.

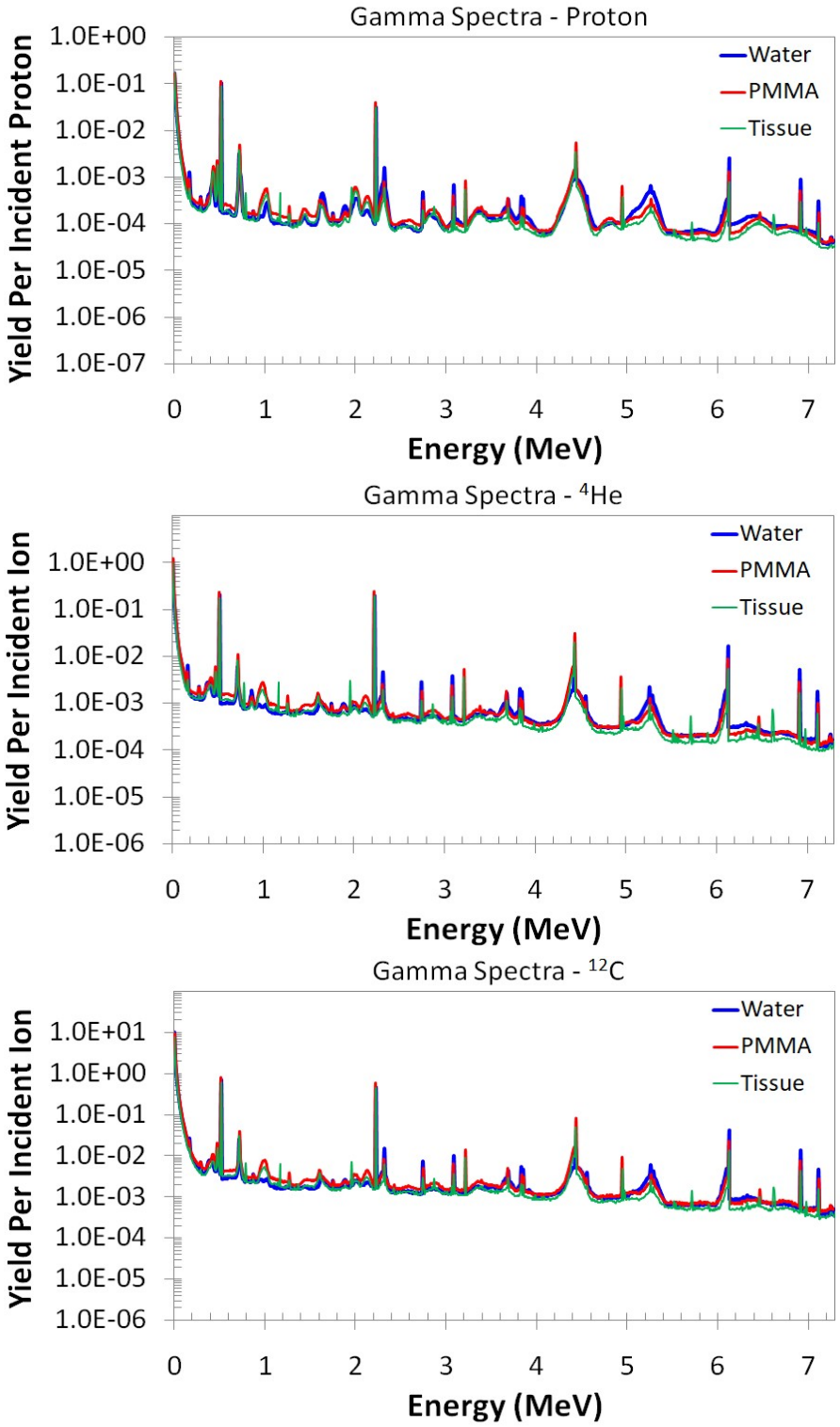

Figure 17: Energy spectra of photons generated in the homogeneous cylindrical water, PMMA and adipose tissue phantoms deriving from pencil beams of protons, ^{4}He and ^{12}C ions with a range of ~16 cm in the materials. The emission lines are characteristic to the major constituent elements of the phantom material. The distinctive PG emission lines of energy 4.44, 5.21 and 6.13 MeV result from ^{12}C, ^{15}O and ^{16}O nuclear de-excitations, respectively.

3.2.2 Realistic Head Phantom

Figure 18 shows the energy spectra of photons originating within the water-based and realistic heterogeneous head phantoms, which show PG emission peaks characteristic to the elemental compositions of the phantom. The 2.31 MeV peak from ^{14}N is clearly evident in the spectra arising primarily from the air pockets in the phantom: the material of air in the model comprises 70% nitrogen. However, as mentioned in the previous section, this peak may be difficult for a detector to resolve from the 2.22 MeV peak. The prominent PG emission lines of 4.44, 5.21 and 6.13 MeV from ^{12}C, ^{15}O and ^{16}O nuclei, respectively, remain dominant in the spectrum. In the water-based head phantom the intensity of emission peaks from oxygen (e.g. 5.21 and 6.13 MeV) appear larger, while in the realistic phantom those from carbon (e.g. 3.21 and 4.44 MeV) are larger, as expected, since for example materials such as adipose tissue comprise 60% carbon and trabecular bone comprise 40% carbon.

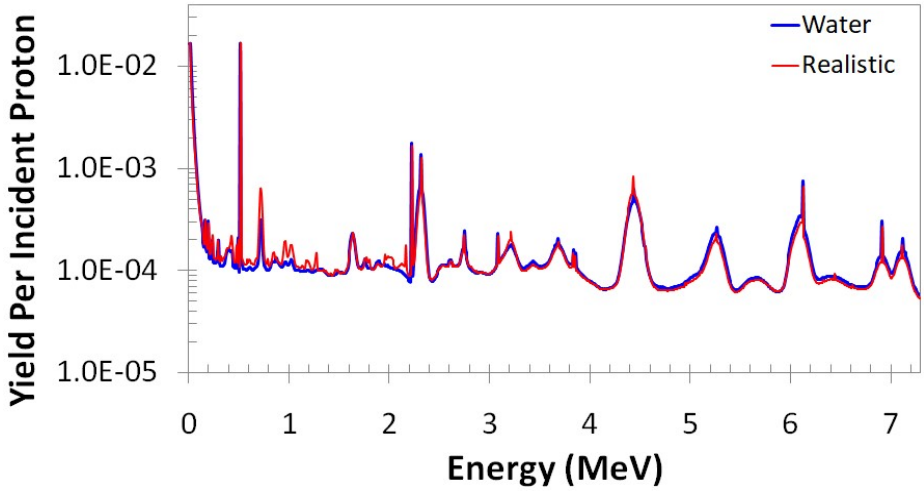

Figure 18: Energy spectra of photons generated in the water-based and realistic head phantoms irradiated with a 100 MeV proton beam. The emission lines are characteristic to the major constituent elements of the phantom material. The distinctive PG emission lines of energy 4.44, 5.21 and 6.13 MeV result from ^{12}C, ^{15}O and ^{16}O nuclear de-excitations, respectively.

The relative intensity of emission lines for the prominent PG energies 4.44, 5.21 and 6.13 MeV from ^{12}C, ^{15}O and ^{16}O, respectively, show a dependency on the material composition of the target. In water, the 6.13 MeV emission line from ^{16}O is largest, followed by the 4.44 and 5.21 MeV lines. In PMMA and adipose tissue, as with the realistic head phantom, the 4.44 MeV emission line is seen to increase, due to the greater concentration of carbon in the materials. In considering evaluated nuclear cross section libraries ENDF/B-VIII.0 [228] and TENDL-2017 [229], for which the IAEA website [230] was referred to, the simulation is seen to reproduce these prominent PG emission lines relatively reasonably. For example, cross section data from ENDF/B-VIII.0 show for ^{16}O(p,χ)^{16}O a maximum of ~0.40 barns at an incident proton energy

of ~10 MeV, while for $^{12}C(p,\chi)^{12}C$ a maximum of ~0.25 barns at ~8 MeV, and for $^{16}O(p,\chi)^{15}O$ a maximum of ~0.1 barns at ~30 MeV. However, for incident helium ions cross section data from TENDL-2017 suggest that the emission yield for $^{12}C(^{4}He,\chi)^{12}C$ reactions is greater than $^{16}O(^{4}He,\chi)^{16}O$, followed by $^{16}O(^{4}He,\chi)^{15}O$, with a maximum cross section of ~0.3 barns for $^{12}C(^{4}He,\chi)^{12}C$ and ~0.14 barns for $^{16}O(^{4}He,\chi)^{16}O$ for an incident ion energy of ~35 MeV, and a maximum cross section of ~0.1 barns for $^{16}O(^{4}He,\chi)^{15}O$ at ~40 MeV. The simulated gamma energy spectra from PMMA and tissue phantoms seem to agree with the cross section data available in the literature [230], although the greater concentration of carbon in the materials is also an influencing factor. Yet in the water phantom the 4.44 MeV emission line from ^{4}He irradiation appears to be underestimated.

3.3 Spatial Correlation between Prompt Gamma Emission and Particle Beam Range

In this section, the results of the PG emission spatial correlation with the particle beam range are presented. The spatial correlation between PG production and dose deposition is not one-to-one, since the two result from different physical processes. Here, the correlation was studied quantitatively in homogeneous and heterogeneous phantoms to observe the correlation resulting in the different types of targets. PG rays were also differentiated into primary and secondary to more closely study their respective correlation to the beam range.

3.3.1 Homogeneous Phantoms

Figure 19 shows the longitudinal and lateral distribution of gamma rays with an applied 1 MeV threshold originating in the phantom. The Bragg curve (depicted for a range of ~16 cm) is plotted with the total, primary and secondary gamma ray longitudinal emission distribution to show their correlation with the dose deposition. The primary PG profile is seen to exhibit the closest correlating relationship to the beam range regarding the sharpness and fall-off in the BP region, which can offer reliable BP monitoring in particle therapy. The secondary PG profile, which is more dominant in the heaver ions compared to protons, shows a broader distribution with a long tail beyond the BP downstream, which could cause significant interference for BP monitoring. A discontinuity can be seen in the PG emission of ^{4}He and ^{12}C beams, which may be due to the transition to the precompound model at low energy nuclear reactions. The transition between high- and low-energy nuclear reaction models occurs at around 140 mm for ^{4}He and at around 160 mm for ^{12}C. The lateral profiles of PG emissions are consistent with the lateral dose spreads; the PG emissions are broader with increasing beam energy, and the carbon ion beam shows narrower lateral spread than the proton beam, as expected.

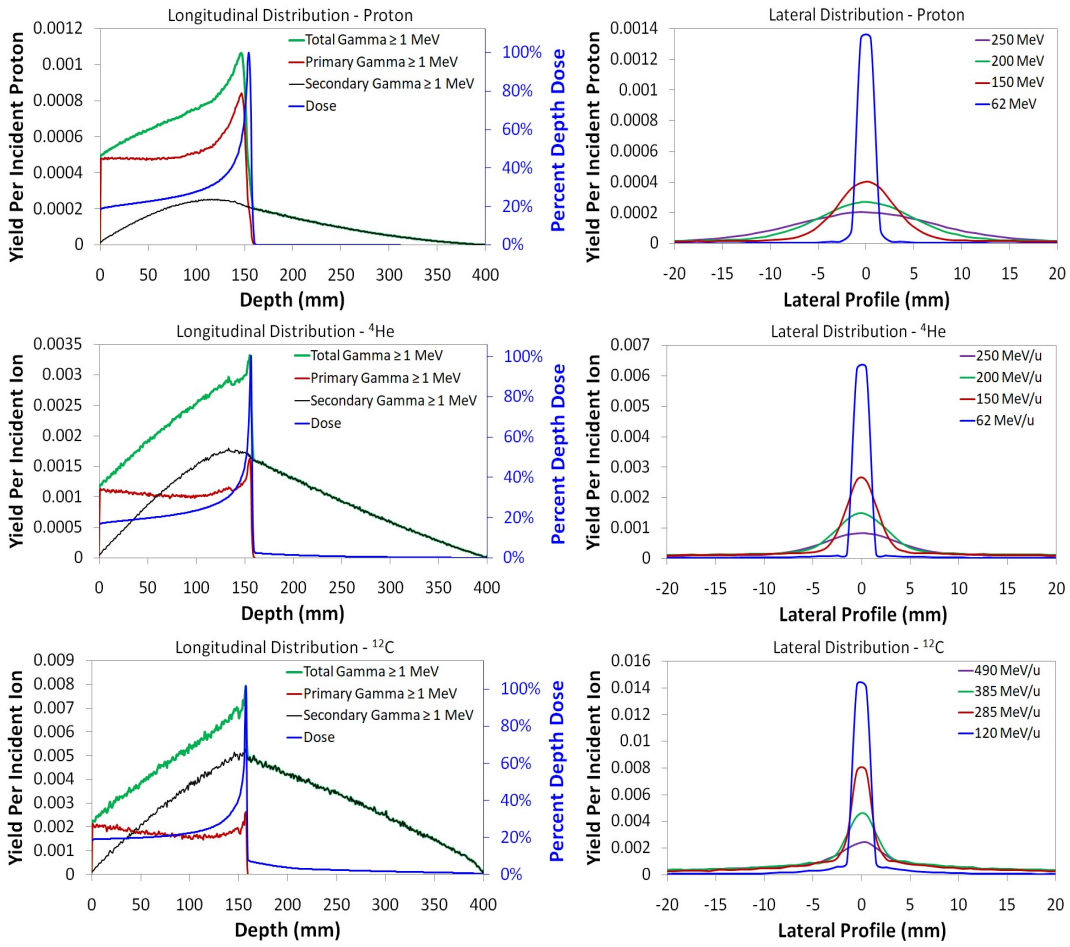

Figure 19: Left: Longitudinal yield distribution of total, primary and secondary gamma rays ≥1 MeV originating in the water phantom for protons (150 MeV), ^{4}He (150 MeV/u) and ^{12}C (285 MeV/u) ions. The percent depth dose is normalised to the dose maximum at the Bragg peak. **Right**: Lateral yield distribution of total gamma rays ≥1 MeV for a longitudinal width of 10 mm at the BP positions for each of the beam energies.

Table 2 presents data for the particle beam range and corresponding PG range for the applied energy threshold and window, for each incident particle type and energy studied. The quantified longitudinal difference, Δ*fall-off*, shows that the PG rays within 3.0-7.0 MeV offer better correlation to the particle range, particularly in the case of incident protons. For a ~16 cm beam range, the Δ*fall-off* values are (-5.1 ± 0.5) mm, (+0.2 ± 0.5) mm and (+0.3 ± 0.5) mm, for proton, ^{4}He and ^{12}C ions, respectively. Negative Δ*fall-off* values indicate that the PG range is upstream of the particle range, while positive values indicate downstream of the particle range. It was found that the selected energy window offers a lower gamma statistical yield (see Table 5), whereas the energy threshold which still incorporates the prominent PG rays while eliminating low-energy background counts offers the benefit of a higher yield with good particle-PG range correlation, i.e. Δ*fall-off* values of within ~1.2 mm for ^{4}He and ^{12}C ions. Helium and carbon ions are seen to offer an improved accuracy (Δ*fall-off*) in estimating the

beam range compared to protons. The quantified lateral difference, Δ*FWHM*, shows millimetre conformity of the PG production with the dose deposition laterally.

Table 2: Particle beam range and corresponding PG range for the applied energy threshold and window studied, for each particle beam type and energy. The Δ*fall-off* and Δ*FWHM*, defined in Section 3.1.1, are reported for quantitative evaluation.

Particle type	Beam energy (MeV/u)	Gamma energy selection (MeV)	R (±0.5 mm)	R_{PG} (±0.1 mm)	Δ*fall-off* * (±0.5 mm)	Lateral dose FWHM (±0.2 mm)	Lateral PG FWHM (±0.2 mm)	Δ*FWHM* (±0.3 mm)
Proton	62	≥1	31.9	27.0	-4.9	1.2	1.0	0.2
		3.0-7.0		27.2	-4.7		1.0	0.2
	150	≥1	155.5	150.2	-5.3	7.1	6.7	0.4
		3.0-7.0		150.4	-5.1		6.7	0.4
	200	≥1	256.3	250.8	-5.5	11.9	11.8	0.1
		3.0-7.0		251.4	-4.9		11.4	0.5
	250	≥1	374.7	368.2	-6.2	17.5	16.4	1.1
		3.0-7.0		369.6	-5.1		16.6	0.9
^{4}He	62	≥1	32.2	31.8	-0.4	0.7	0.6	0.1
		3.0-7.0		32.0	-0.2		0.6	0.1
	150	≥1	156.6	156.6	0.	3.5	3.6	0.1
		3.0-7.0		156.8	+0.2		3.5	0.
	200	≥1	258.2	258.3	+0.1	5.9	6.3	0.4
		3.0-7.0		258.4	+0.2		6.1	0.2
	250	≥1	377.4	377.4	0.	8.5	9.0	0.5
		3.0-7.0		377.4	0.		9.4	0.9
^{12}C	120	≥1	35.2	35.5	+0.3	0.3	0.4	0.1
		3.0-7.0		35.4	+0.2		0.4	0.1
	285	≥1	157.3	157.8	+0.5	1.9	2.0	0.1
		3.0-7.0		157.6	+0.3		1.8	0.1
	385	≥1	257.5	258.7	+1.2	3.1	3.4	0.3
		3.0-7.0		258.3	+0.8		3.3	0.2
	490	≥1	377.7	378.7	+1.0	4.5	5.2	0.7
		3.0-7.0		378.6	+0.9		4.8	0.3

* Negative values indicate that the PG range is upstream of the particle range, while positive values indicate downstream of the particle range.

Table 3 presents the data for the particle beam range and corresponding PG range for each incident particle type with a range of ~16 cm in water, PMMA and adipose tissue. The quantified longitudinal difference, Δ*fall-off*, is found to not vary largely between the three homogeneous phantoms, i.e. within ~1.4 mm for protons and within only ~0.3 mm for ^{4}He/^{12}C

ions. Rather, a more considerable difference is observed between the ion species, with Δ*fall-off* values of around 5-6 mm for protons and around 0-1 mm for ^{4}He/^{12}C ions. This suggests that for the case of homogeneous targets, regardless of composition, there is a somewhat consistent PG-BP fall-off correlation for a particular beam type.

Table 3: Particle beam range and corresponding PG range in water, PMMA and adipose tissue for the applied energy threshold and window studied, for each particle beam type with ~16 cm range. The Δ*fall-off*, defined in Section 3.1.1, is reported for quantitative evaluation.

Particle type	Phantom material	Gamma energy selection (MeV)	R (±0.5 mm)	R_{PG} (±0.1 mm)	Δ*fall-off* * (±0.5 mm)
Proton	Water	≥1	156.2	150.9	-5.3
		3.0-7.0		151.0	-5.2
	PMMA	≥1	156.8	151.3	-5.5
		3.0-7.0		152.2	-4.6
	Tissue	≥1	156.0	149.6	-6.4
		3.0-7.0		150.0	-6.0
^{4}He	Water	≥1	155.4	155.2	-0.2
		3.0-7.0		155.2	-0.2
	PMMA	≥1	156.4	156.6	+0.2
		3.0-7.0		156.6	+0.2
	Tissue	≥1	155.3	155.4	+0.1
		3.0-7.0		155.6	+0.3
^{12}C	Water	≥1	155.3	155.7	+0.4
		3.0-7.0		155.6	+0.3
	PMMA	≥1	156.3	156.7	+0.4
		3.0-7.0		156.4	+0.1
	Tissue	≥1	155.3	155.9	+0.6
		3.0-7.0		155.3	0.

* Negative values indicate that the PG range is upstream of the particle range, while positive values indicate downstream of the particle range.

3.3.2 Realistic Head Phantom

The longitudinal emission distribution of gamma rays within the head phantoms rises and falls in relation to the beam entering the various materials of the phantom, such that the emission is sensitive to the elemental composition and the medium density. In higher density materials (e.g. bone) the gamma emission increases and in lower density materials (e.g. air) the gamma emission decreases. The published work, Zarifi et al. (2017) [231] (see Appendix 1), shows effects of target inhomogeneity, whereby the PG emission from a proton beam irradiating a multi-layered phantom was investigated.

Figure 20 shows the longitudinal distribution of total, primary and secondary gamma rays with a threshold of 1 MeV originating in the water-based and realistic head phantoms. The Bragg curve is also plotted to show the correlation of the gamma emission with the dose deposition. A (3.6 ± 0.7) mm shift in the proton beam range is seen between the water-based and realistic head phantoms, whereby the PG emission closely correlates to this shift. That is, for both phantoms the PG-BP fall-off difference remains at around 2-3 mm (see Table 4). This suggests that the PG emission fall-off closely correlates to the BP fall-off for heterogeneous targets as well as homogeneous ones.

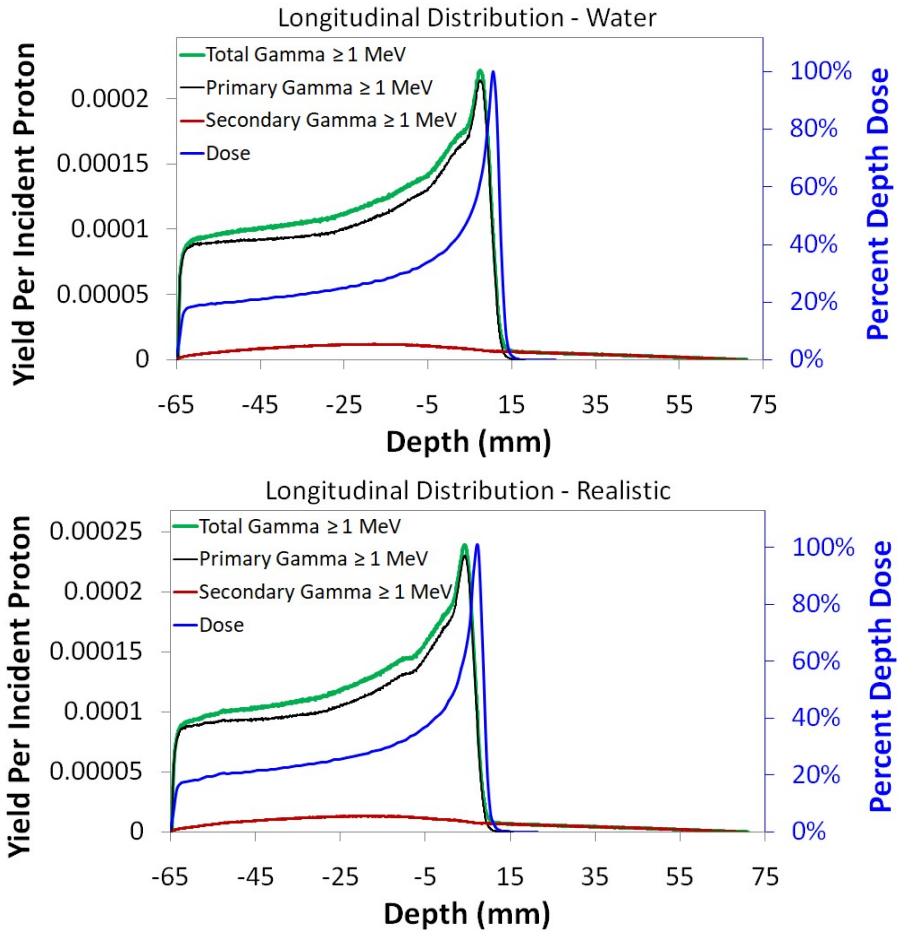

Figure 20: Longitudinal yield distribution of total, primary and secondary gamma rays ≥1 MeV originating in the water-based and realistic head phantom for 100 MeV protons. The percent depth dose is normalised to the dose maximum at the Bragg peak. A (3.6 ± 0.7) mm shift in the proton beam range is seen between the two phantoms, and the PG emission closely correlates (~2 mm) to this shift.

Table 4: Particle beam range and corresponding PG range in the water-based and realistic head phantom for the applied energy threshold and window studied, for a proton beam of 100 MeV. The Δ*fall-off*, defined in Section 3.1.1, is reported for quantitative evaluation.

Head phantom	Gamma energy selection (MeV)	R (±0.5 mm)	R_{PG} (±0.1 mm)	Δ*fall-off* * (±0.5 mm)
Water-based	≥1	76.1	73.7	-2.4
	3.0-7.0		73.5	-2.6
Realistic	≥1	72.5	70.2	-2.3
	3.0-7.0		70.3	-2.2

* Negative values indicate that the PG range is upstream of the particle range.

It is therefore seen from these results that the primary PG emissions from the beam's nuclear interactions offer the closest correlation to the deposited dose with sharp fall-off in the region of the BP, which is most suitable for BP monitoring in particle therapy. The PG-BP correlations are better for the heavier ions (millimetre accuracy) than for proton beams (within ~7 mm). In studying the quantified longitudinal difference between three different homogeneous target materials, a larger difference is observed between the ion species rather than the Δ*fall-off* values for a particular material. This suggests that for homogeneous targets the PG emission fall-off consistently correlates to the BP fall-off for a particular beam type. The PG emission fall-off was also seen to closely correlate (within ~3 mm) to the BP fall-off for heterogeneous targets (water-based and realistic head phantoms) as well as the homogeneous ones. In the lateral spread, the PG emission and dose deposition were also observed to be correlated with millimetre accuracy. These properties indicate that the PG signal is a reliable means for *in vivo* beam range verification and dose monitoring in particle therapy. However, the primary and secondary PG rays are not quite differentiable in experimental measurements, such that the measurable PG signal is largely masked by the concurrent emission of secondary PG rays which arise from the nuclear reactions of secondary particles/fragments created along the primary ion path. This becomes a greater challenge for heavy ions whereby the secondary PG emissions (broad distribution and tail beyond the BP region) are more prominent.

3.4 Prompt Gamma Emission and Detectable Yield

In this section, the results on the emission yield of PG rays orginiating within the phantom and the detectable yield of those reaching the idealised detection sphere are presented. The possible available statistics, which may be one challenge for range verification in particle therapy due to the specific beam delivery structure and intensity constraints, were investigated. The PG emission yield and corresponding dose deposition was also investigated to determine a possible correlation which may be valuable to *in vivo* dosimetry.

3.4.1 Homogeneous Phantoms

Table 5 presents the yield values of gamma photons originating in the spherical water phantom and those reaching the detection sphere, and with applied energy threshold/window, normalised to the number of incident particles on the phantom. For each beam type, the PG emission yield increases with particle depth, as expected. The ^{12}C beam produces the highest yield of gamma emission, with a relatively larger yield of low-energy photon counts. For example, comparing the beam types with the same range of ~16 cm, the total gamma yield per incident particle is 0.87 for 150 MeV protons, 2.60 for 150 MeV/u ^{4}He ions and 17.35 for 285 MeV/u ^{12}C ions, while the yield for PG rays within 3.0-7.0 MeV is 0.07, 0.22 and 0.62, respectively. This gives a ratio of total gamma to PG of 12.4, 11.8 and 28.0 for proton, ^{4}He and ^{12}C, respectively. In other words, for 150 MeV protons the energy deposited at the BP maximum is ~3 MeV/ion, with a PG yield of ~7×10^{-4} /ion, which corresponds to ~2×10^{-4} PG rays emitted per MeV deposited energy at the BP. For 150 MeV/u ^{4}He ions the energy deposited at the BP maximum is ~13 MeV/ion, with a PG yield of ~1×10^{-3} /ion, and ~8×10^{-5} PG/MeV at the BP. For 285 MeV/u ^{12}C ions the energy deposited at the BP maximum is ~69 MeV/ion, with a PG yield of ~4×10^{-3} /ion, and ~6×10^{-5} PG/MeV at the BP.

The detectable yield is less than the emission yield as expected, since the gamma rays interact within the water phantom and can eventually be absorbed. The detectable PG yield within 3.0-7.0 MeV on the detection sphere is found to be around 65%. The results again show that the ^{12}C beam produces a larger yield of detectable PG rays per incident ion compared to the proton and ^{4}He beams. The PG yield within 3.0-7.0 MeV per incident particle for the beams with ~16 cm range is 0.05 for protons (150 MeV), 0.14 for ^{4}He (150 MeV/u) ions and 0.40 for ^{12}C (285 MeV/u) ions.

Table 6 presents the yield values of gamma photons originating in the cylindrical water, PMMA and adipose tissue phantoms and those reaching the detection sphere, normalised to the number of incident particles on the phantom, for a beam range of ~16 cm. For each particle type, the gamma yield is greatest in the PMMA target and least in the tissue target. For example, for water, PMMA and tissue phantoms the total gamma yield per incident particle is 0.90, 0.92 and 0.74, respectively for protons, 2.70, 2.87 and 2.27, respectively for ^{4}He ions, and 17.73, 17.94 and 14.39, respectively for ^{12}C ions. In other words, for protons in water, ~1×10^{-4} PG rays within 3.0-7.0 MeV are emitted per MeV deposited at the BP maximum, i.e. ~3 MeV/ion with PG yield of ~3×10^{-4} /ion. Table 7 presents this quantitiative data for each particle type and target material. The detectable PG yield within 3.0-7.0 MeV on the detection sphere is found to be around 60% for a beam range of ~16 cm within the cylindrical phantoms.

Table 5: Yield of gamma photons originating within the spherical water phantom and those reaching the detection sphere once emitted from the phantom. The simulation statistical uncertainty is within 5%.

Particle type	Particle beam energy (MeV/u)	Gamma energy selection (MeV)	Gamma yield per incident particle	
			In phantom	Detection sphere
Proton	62	No window	0.19	0.06
		≥1	0.03	0.02
		3.0-7.0	0.02	0.01
	150	No window	0.87	0.25
		≥1	0.13	0.09
		3.0-7.0	0.07	0.05
	200	No window	1.40	0.39
		≥1	0.20	0.14
		3.0-7.0	0.10	0.07
	250	No window	1.95	0.53
		≥1	0.27	0.19
		3.0-7.0	0.13	0.09
^{4}He	62	No window	0.41	0.17
		≥1	0.10	0.08
		3.0-7.0	0.05	0.04
	150	No window	2.60	0.86
		≥1	0.54	0.36
		3.0-7.0	0.22	0.14
	200	No window	4.00	1.25
		≥1	0.77	0.51
		3.0-7.0	0.32	0.20
	250	No window	5.20	1.55
		≥1	0.90	0.61
		3.0-7.0	0.38	0.25
^{12}C	120	No window	3.91	0.73
		≥1	0.32	0.23
		3.0-7.0	0.15	0.10
	285	No window	17.35	2.94
		≥1	1.42	0.95
		3.0-7.0	0.62	0.40
	385	No window	25.02	4.25
		≥1	2.00	1.35
		3.0-7.0	0.86	0.56
	490	No window	30.40	5.42
		≥1	2.44	1.66
		3.0-7.0	1.01	0.67

Table 6: Yield values of gamma photons originating within the cylindrical water, PMMA and adipose tissue phantoms for the beam energy corresponding to a range of ~16 cm, and the gamma yield reaching the detection sphere once emitted from the phantom. The simulation statistical uncertainty is within 1%.

Particle type	Phantom material	Gamma energy selection (MeV)	Gamma yield per incident particle	
			In phantom	Detection sphere
Proton	Water	No window	0.90	0.25
		≥1	0.14	0.09
		3.0-7.0	0.07	0.04
	PMMA	No window	0.92	0.28
		≥1	0.15	0.09
		3.0-7.0	0.07	0.04
	Tissue	No window	0.74	0.23
		≥1	0.12	0.08
		3.0-7.0	0.05	0.03
^{4}He	Water	No window	2.70	0.89
		≥1	0.59	0.37
		3.0-7.0	0.23	0.14
	PMMA	No window	2.87	1.03
		≥1	0.69	0.41
		3.0-7.0	0.25	0.14
	Tissue	No window	2.27	0.84
		≥1	0.53	0.34
		3.0-7.0	0.18	0.11
^{12}C	Water	No window	17.73	2.91
		≥1	1.56	0.98
		3.0-7.0	0.65	0.40
	PMMA	No window	17.94	3.45
		≥1	1.93	1.12
		3.0-7.0	0.74	0.42
	Tissue	No window	14.39	2.78
		≥1	1.41	0.90
		3.0-7.0	0.51	0.32

Table 7: Yield values of PG rays within 3.0-7.0 MeV emitted per MeV deposited at the BP maximum within the cylindrical water, PMMA and adipose tissue phantoms for the beam energy corresponding to a range of ~16 cm. The simulation statistical uncertainty is within 1%.

Particle type	Phantom material	PG/ion	MeV/ion	PG/MeV
Proton	Water	$\sim 3\times10^{-4}$	~3	$\sim 1\times10^{-4}$
	PMMA	$\sim 4\times10^{-4}$	~3	$\sim 1\times10^{-4}$
	Tissue	$\sim 3\times10^{-4}$	~3	$\sim 1\times10^{-4}$
^{4}He	Water	$\sim 1\times10^{-3}$	~13	$\sim 8\times10^{-5}$
	PMMA	$\sim 2\times10^{-3}$	~12	$\sim 2\times10^{-4}$
	Tissue	$\sim 1\times10^{-3}$	~12	$\sim 8\times10^{-5}$
^{12}C	Water	$\sim 3\times10^{-3}$	~70	$\sim 4\times10^{-5}$
	PMMA	$\sim 4\times10^{-3}$	~65	$\sim 6\times10^{-5}$
	Tissue	$\sim 3\times10^{-3}$	~71	$\sim 4\times10^{-5}$

3.4.2 Realistic Head Phantom

Table 8 presents the yield values of gamma photons originating in the head phantoms and those reaching the detection sphere, normalised to the number of incident particles on the phantom. The gamma emission yields are found to be considerably different for the two targets; a factor of around 2-3 higher for the realistic head phantom than the water-based head phantom. The realistic to water-based head phantom ratio of total, $\geq$1 MeV and 3.0-7.0 MeV gamma yield is 2.2, 3.3 and 2.5, respectively. This is a result of the higher density materials within the realistic head phantom, in particular the bone structures. In other words, for 100 MeV protons in the water-based head phantom the energy deposited at the BP maximum is ~4.1 MeV/ion, with a PG yield within 3.0-7.0 MeV of $\sim 6\times10^{-4}$ /ion, which corresponds to $\sim 1\times10^{-4}$ PG rays emitted per MeV deposited energy at the BP. In the realistic head phantom the energy deposited at the BP maximum is ~4.3 MeV/ion, with a PG yield of $\sim 5\times10^{-4}$ /ion, and $\sim 5\times10^{-5}$ PG/MeV at the BP. In terms of dose at the BP position (1 mm thickness), $\sim 6\times10^{5}$ PG rays emitted in the water-based head phantom and $\sim 5\times10^{5}$ PG rays emitted in the realistic head phantom correspond to approximately 0.02 Gy and 0.03 Gy delivered, respectively.

The detectable PG yield within 3.0-7.0 MeV on the detection sphere is found to be 50% for the water-based head phantom and 80% for the realistic head phantom. Again, the higher yield of PG rays for the realistic head phantom compared to the water-based phantom may be due to factors such as elemental composition and material density. A higher concentration of elements such as carbon and oxygen increase the PG emission intensity at, for example, 4.44 and 6.13 MeV, respectively. At higher density media (compared to water), the PG production

yield also increases, and in lower density media, the gamma ray attenuation is less, resulting in an increased detectable yield.

Table 8: Yield values of gamma photons originating within the water-based and realistic head phantoms for 100 MeV proton beams, as well as the gamma yield reaching the detection sphere once emitted from the phantom. The simulation statistical uncertainty is within 3%.

Head phantom	Gamma energy selection (MeV)	Gamma yield per incident particle	
		In phantom	Detection sphere
Water-based	No window	0.19	0.06
	≥1	0.03	0.02
	3.0-7.0	0.02	0.01
Realistic	No window	0.41	0.17
	≥1	0.10	0.08
	3.0-7.0	0.05	0.04

An important concept in particle therapy is whether there are enough PG statistics for spot tracking in PBS. Considering a typical PBS proton beam with a rate of 10^8 protons per second and a spot duration of about 20 ms, each spot will have 2×10^6 incident protons. Taking the case of the realistic head phantom and if the simulated beam incidence is considered as a single spot, for 2×10^6 incident protons at 100 MeV, the total detectable PG yield at energy ≥1 MeV on the idealised detecting sphere would be ~1.6×10^5 with a production yield of ~2.0×10^5 within the phantom. Considering a 5×5 cm^2 detector size on the simulated sphere, the detectable PG counts are ~3×10^2, yielding a statistical error of about 6%. This implies that spot-by-spot monitoring using PG rays for this particular beam energy/geometry/detector size is a challenge in terms of obtaining sufficient statistics for clinical practice. However, improving the statistics can be achieved by accumulating data from several beam spots when they correspond to the same expected range, but this is at the expense of spatial resolution [57].

3.5 Angular Distribution for Detectable Prompt Gamma Rays

In this section, the results on the angular distribution of PG rays reaching the idealised detection sphere are presented. This would allow identifying eventual preferential PG emission propagation, and in turn, identifying preferential positions for the PG detector/s to maximise the detected PG yield and minimise the neutron yield. Moreover, two different shaped phantoms, spherical and cylindrical, were studied to investigate the phantom geometric effects on PG detection.

3.5.1 Homogeneous Phantoms

Figure 21 shows the angular distributions of total gamma rays reaching the idealised detection sphere once emitted from the spherical water phantom, normalised per incident ion per steradian, for each beam ion species and energy studied. At the low energies of 62 MeV/u (proton and ^{4}He beams) and 120 MeV/u (^{12}C beam), the detectable gamma rays are slightly preferred backward in θ = 100-180^{o} (angle θ is defined in Section 3.1.1, see Figure 14). Yet at higher beam energies the detectable gamma rays become more forward in θ = 20-40^{o}. Hence, with increasing depth of the BP position, the favourable PG detection is likely to be increasingly forward, and such forwardness appears to increase for the heavier ion species. The published work, Zarifi et al. (2017) [231] (see Appendix 1), shows further analysis from proton beam irradiations with respect to the BP position.

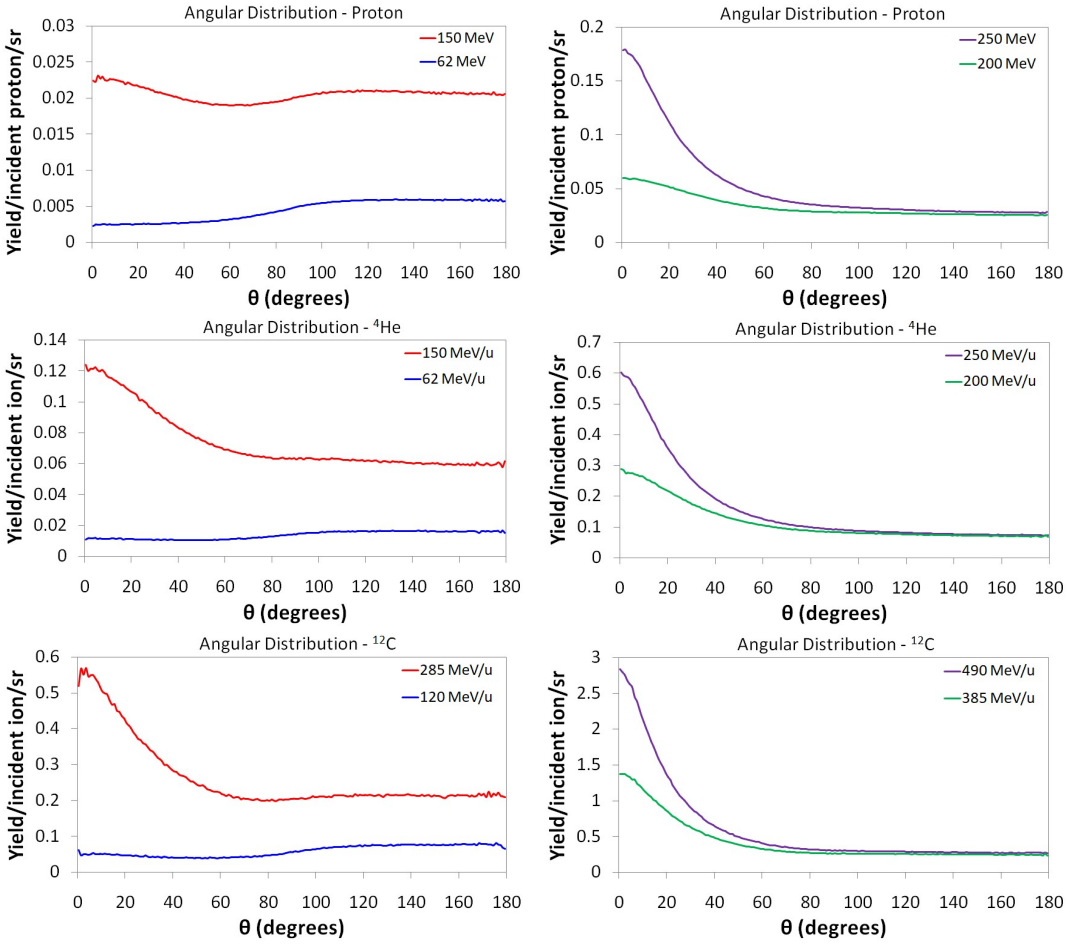

Figure 21: Angular distribution of total gamma rays reaching the idealised detecting sphere once emitted from the spherical water phantom normalised per incident ion per steradian for the lower two beam energies (left) and the higher two beam energies (right) for protons, ^{4}He and ^{12}C ions.

Figure 22 shows the angular distributions of total gamma rays reaching the idealised detection sphere once emitted from cylindrical phantoms for each beam ion species and the

lowest/highest energy, normalised per incident ion per steradian. At the lowest energy (a beam range of ~3 cm) the detectable gamma rays from the different phantom materials are slightly preferred in θ = 100-180°, whereas at the highest beam energy (a beam range of ~38 cm) the detectable gamma rays become more forward in θ = 20-40°. Hence, the angular detection distribution properties for the cylindrical phantoms (see Figure 22) are similar to those for the spherical phantoms (see Figure 21), such that with increasing depth of the BP position within the phantom the favourable PG detection is likely to be increasingly forward. However, the geometric effects of the phantom on the angular distribution are evident on the idealised detection sphere. The noticeable troughs in the plots are indicative of the greater path length the gamma rays travel within the phantom, and hence increased probability of attenuation/absorption and therefore reduced gamma yield.

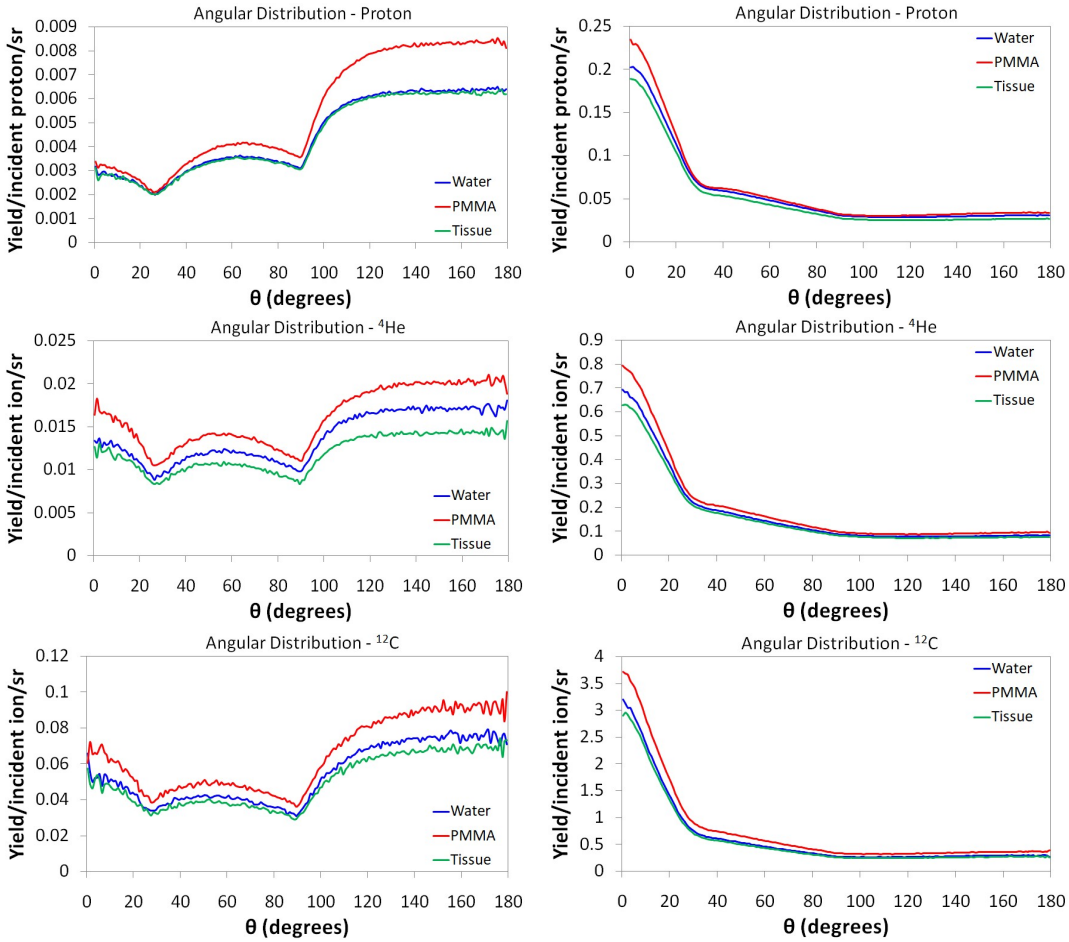

Figure 22: Angular distribution of total gamma rays reaching the idealised detecting sphere once emitted from the cylindrical water, PMMA and adipose tissue phantoms normalised per incident ion per steradian for the lowest beam energy (beam range of ~3 cm) (left) and the highest beam energies (beam range of ~38 cm) (right) for protons, ^{4}He and ^{12}C ions.

By using an idealised detecting sphere, the angular distribution of detectable PG rays was investigated as a global context, for each particle type and energy under study. The observed non-isotropic longitudinal distribution of the detectable gamma rays is likely due to the kinematics of the nuclear reactions. The default cascade model of Geant4 physics was employed in this simulation study, which does not take into account angular momentum coupling of the gamma quanta emitted in a cascade. Understanding the influence of activating angular momentum coupling on the angular distribution requires further study. Attenuation/absorption of gamma rays within the phantom was considered, and so the geometric effect (e.g. phantom shape and size) also play a role in the angular variances seen on the idealised detecting sphere. In replacing the sphere phantom with a cylinder phantom, it was seen (Figures 21 and 22) that the shape of the phantom does have a considerable effect on the angular distribution due to attenuation/absorption. Additionally, since the target is not in the centre of the detection sphere, this introduces a dependency from the origin of the PG rays with $1/r^2$. These factors may explain why the results of angular distribution in this study, which show a non-isotropic trend, are different to the experimental data in Ref. [94], for which no angular dependence was observed in the prompt photon yield at 90^o and 60^o measured with a LYSO detector (for deposited energy >2 MeV). Therefore, further investigation is necessary for the factors influencing the angular distribution of the detectable PG rays.

3.6 Temporal Properties of Prompt Gamma Emission and Detection: Relationship with Particle Beam Range

In this section, results on the timing properties of PG rays emitted within the phantom and those reaching the idealised detection sphere are presented. The relationship between the emission time and TOF distributions with the particle beam range were investigated, which may provide valuable information for *in vivo* range and dose monitoring using the temporal feature of PG rays, such as in the PGT [171] and PGPI [173] methods.

3.6.1 Homogeneous Phantoms

Figure 23 shows the emission time distribution of total gamma rays and those ≥1 MeV for each particle type and energy. The emission time profiles vary with particle energy, as expected, since the beam range/transit time also increases and so gamma rays are produced at greater depths in the phantom and hence at later time. The profiles with the applied threshold show a clear fall-off which is correlated to the dose profile fall-off. The PG emission time T_{PG} for gamma rays ≥1 MeV is (2.5 ± 0.1) ns, (2.7 ± 0.1) ns and (1.9 ± 0.1) ns for protons, ^{4}He and ^{12}C ions with a range of ~38 cm. The gamma ray emission time from carbon ions is seen to

be quicker than that of proton and helium ions; possibly due to the carbon ions moving at greater speed as they traverse the phantom. Similar time emission properties are seen for PMMA and adipose tissue, in Figures 24 and 25, respectively.

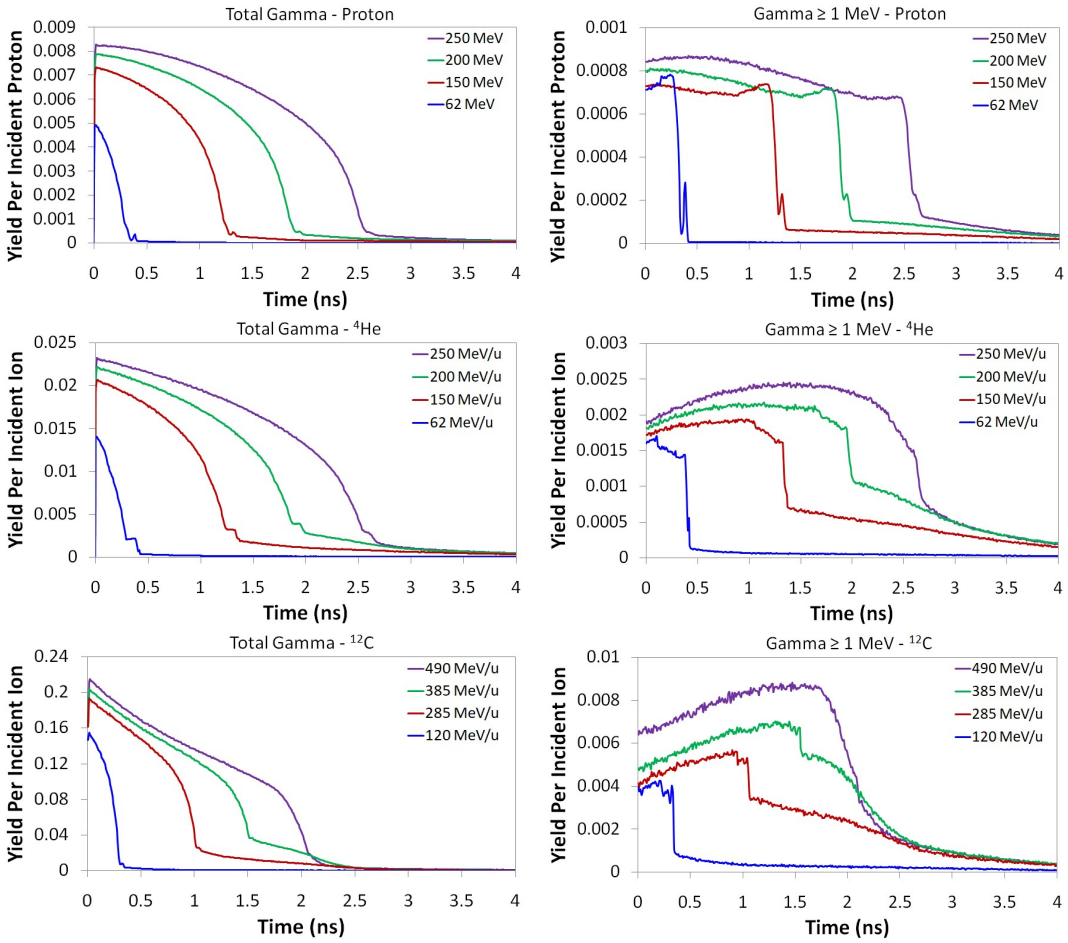

Figure 23: Emission time distribution of total gamma rays (left) and gamma rays ≥1 MeV (right) originating in the spherical water phantom for protons, ^{4}He and ^{12}C ions. The bin width is 0.01 ns.

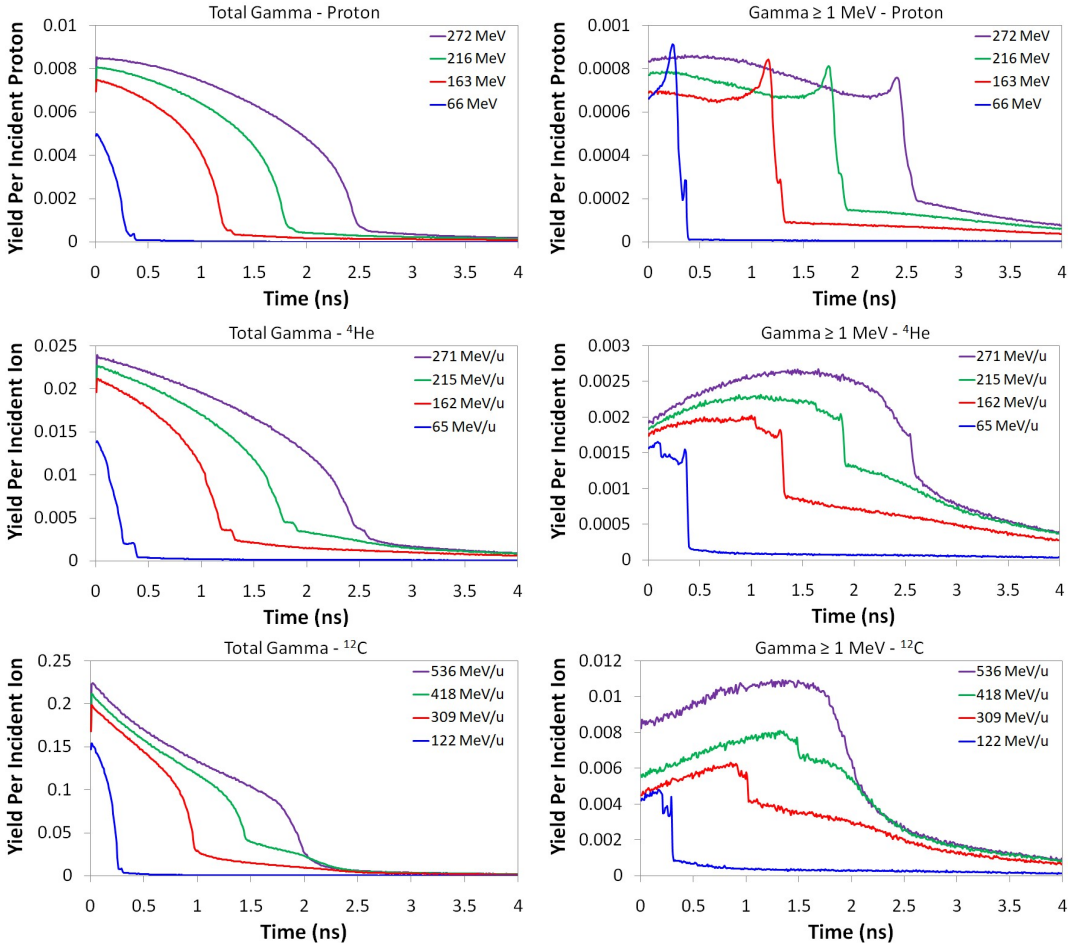

Figure 24: Emission time distribution of total gamma rays (left) and gamma rays ≥1 MeV (right) originating in the cylindrical PMMA phantom for protons, ^{4}He and ^{12}C ions. The bin width is 0.01 ns.

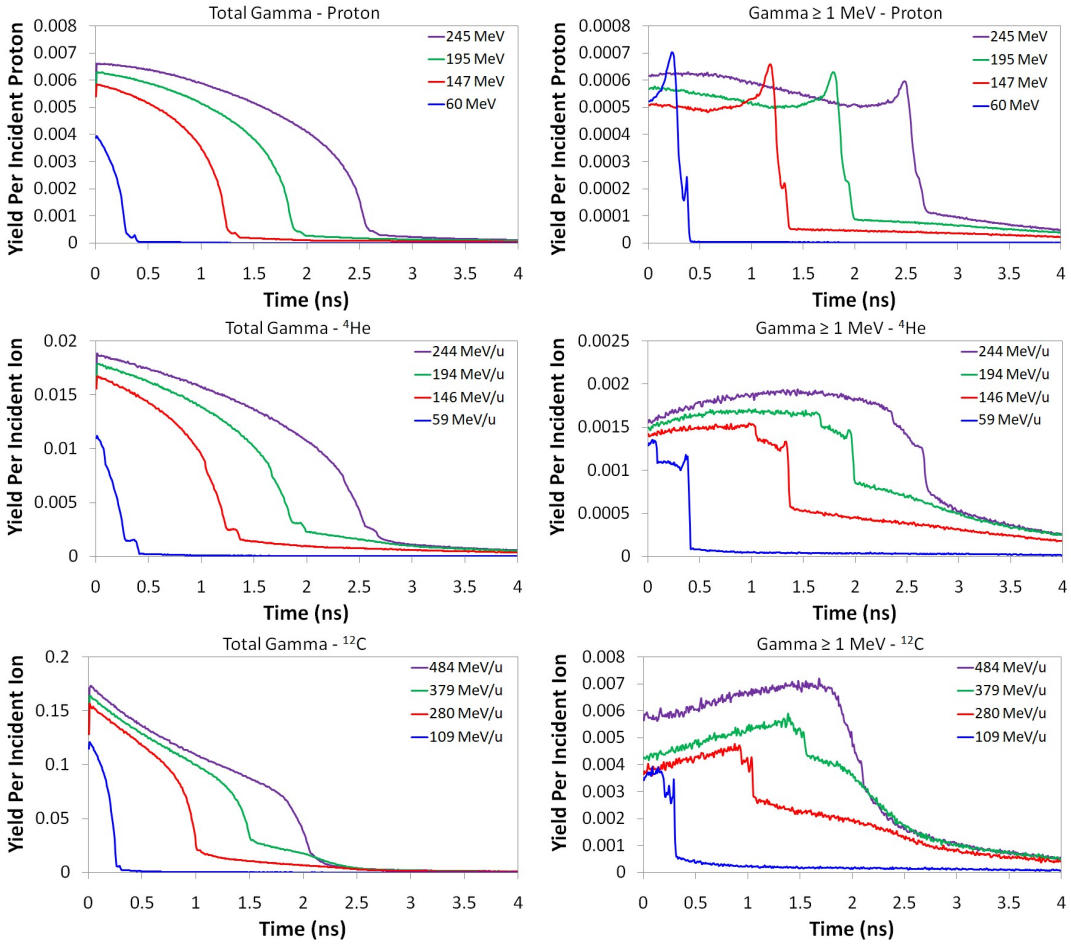

Figure 25: Emission time distribution of total gamma rays (left) and gamma rays ≥1 MeV (right) originating in the cylindrical adipose tissue phantom for protons, ^{4}He and ^{12}C ions. The bin width is 0.01 ns.

The TOF profiles of total gamma rays, neutrons and gamma rays ≥1 MeV reaching the idealised detecting sphere after emitted from the phantom are shown in Figure 26. As the incident particle energy increases their penetration depth (and travel time) becomes larger, hence the PG TOF peak mean exhibits a shift to longer TOF values while the peak width/integral increases. For proton beams, neutrons are not predominantly detected until around 3 ns, which may suggest another means of discriminating PG rays from the (neutron-induced) background and therefore improve the signal-to-background ratio of PG detection. In the case of heavier ions, this may be more difficult particularly at high beam energies for which there is a greater presence of neutron production and temporal overlap between PG and neutrons. Similar TOF properties are seen for PMMA and adipose tissue, in Figures 27 and 28, respectively.

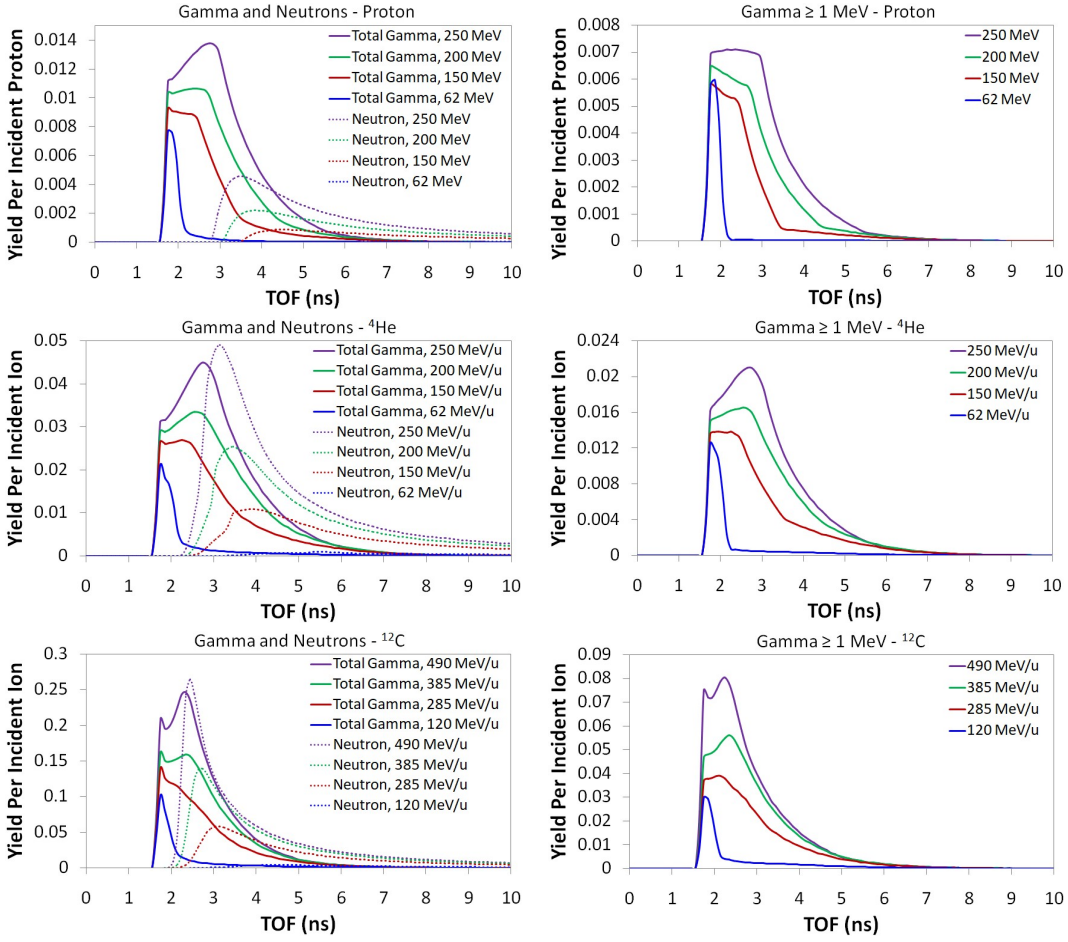

Figure 26: TOF spectra of total gamma and neutrons (left) and gamma rays ≥1 MeV (right) reaching the detection sphere once emitted from the spherical water phantom for protons, ^{4}He and ^{12}C ions. The bin width is 0.1 ns.

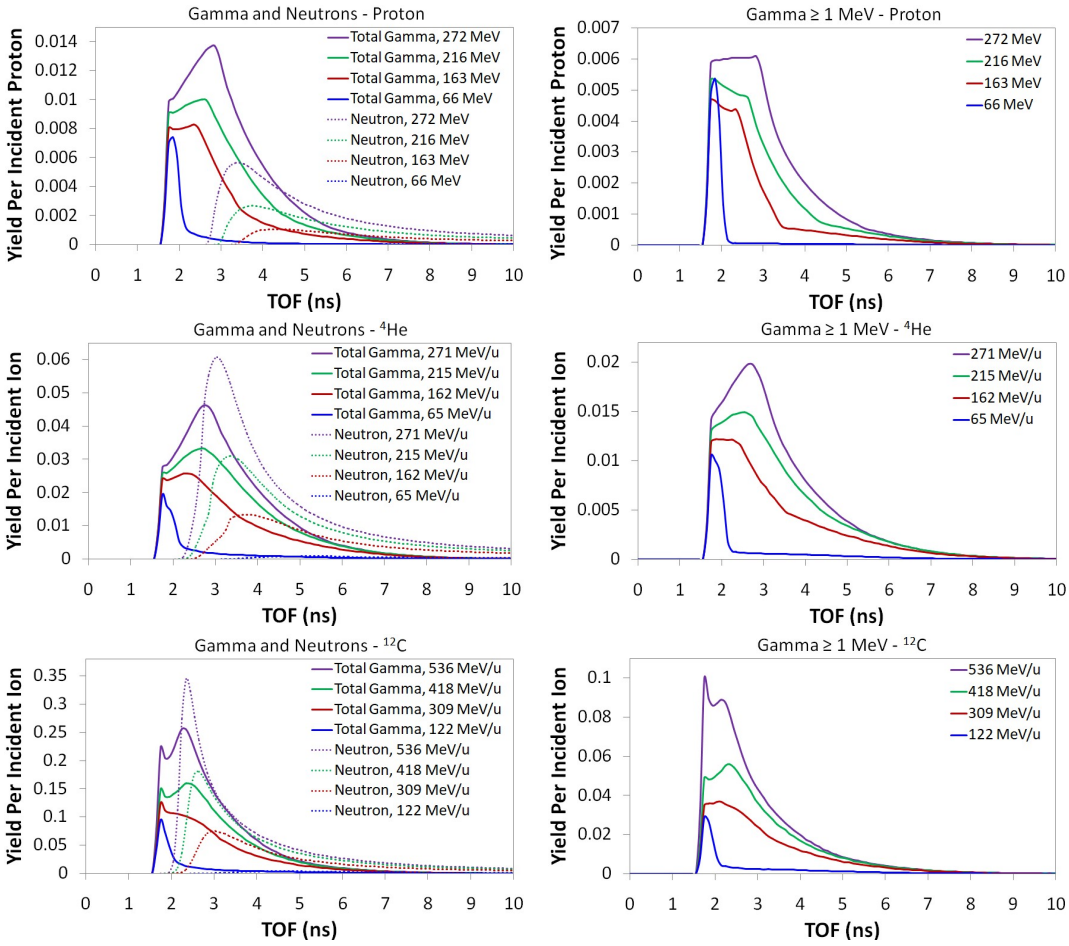

Figure 27: TOF spectra of total gamma and neutrons (left) and gamma rays ≥1 MeV (right) reaching the detection sphere once emitted from the cylindrical PMMA phantom for protons, ^{4}He and ^{12}C ions. The bin width is 0.1 ns.

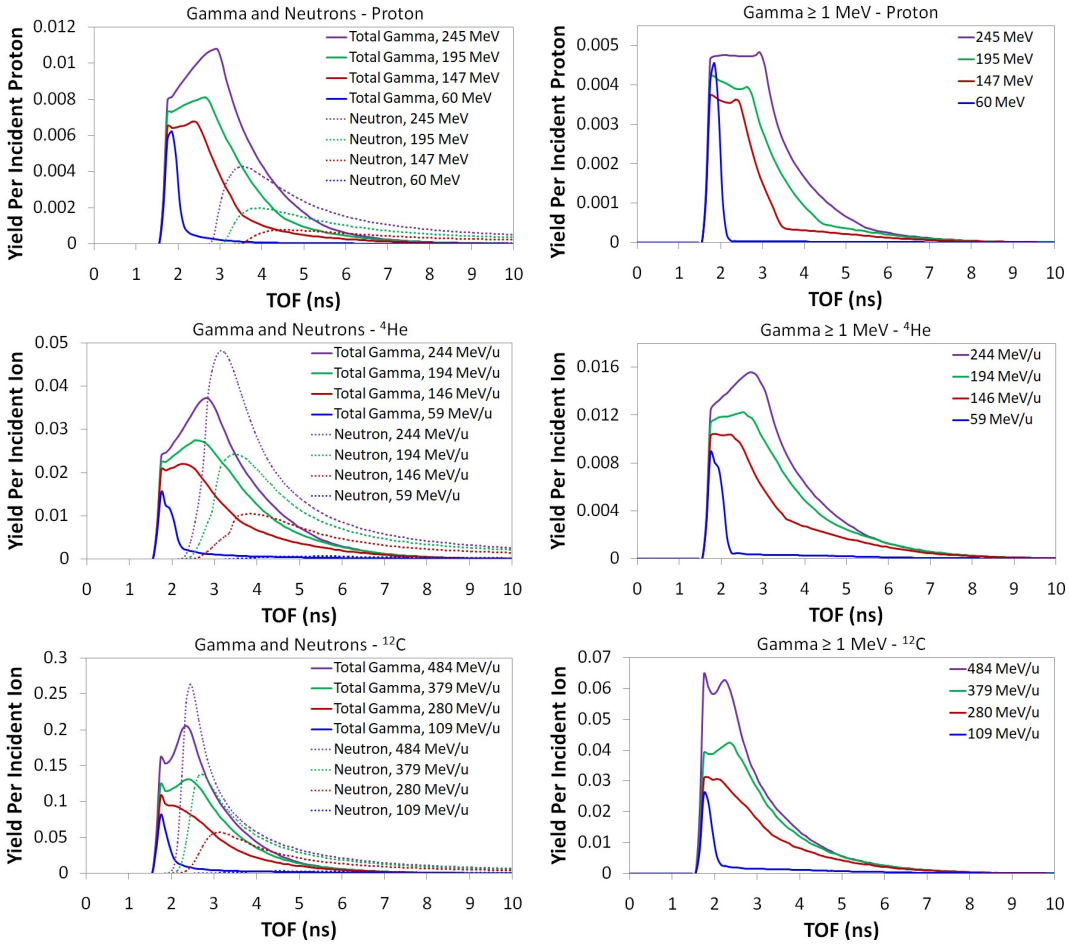

Figure 28: TOF spectra of total gamma and neutrons (left) and gamma rays ≥1 MeV (right) reaching the detection sphere once emitted from the cylindrical adipose tissue phantom for protons, ^{4}He and ^{12}C ions. The bin width is 0.1 ns.

Figures 29 and 30 show 2D representations of the TOF spectra of primary gamma rays and those ≥1 MeV along the polar angle θ for each beam type and energy, respectively. Both the angular and TOF distributions of PG rays reaching the detection sphere are seen to change with increasing particle energy. With respect to the phantom surface, PG detection is seen to be increasingly forward-peaked with higher beam energy (as also seen in Figure 21). In addition, the TOF width increases and its maximum shifts to longer time values, particularly for proton and ^{4}He ions, whereas ^{12}C ion irradiations show less widening/shift in the TOF distribution with greater local increase in PG yield. Applying an energy threshold of 1 MeV to the primary gamma rays reaching the detecting sphere is seen to almost entirely eliminate the TOF tail, such that only the highly localised TOF peak remains.

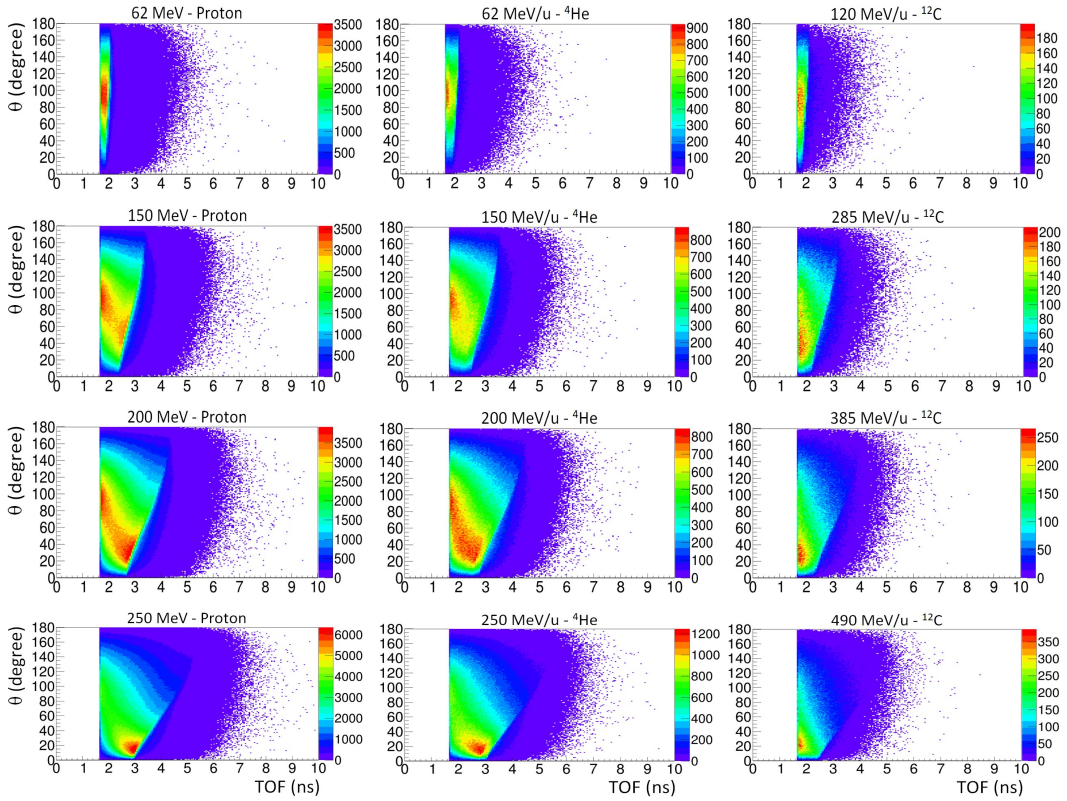

Figure 29: TOF spectra along the polar angle θ of primary gamma rays reaching the detection sphere once emitted from the phantom for protons, ^{4}He and ^{12}C ions.

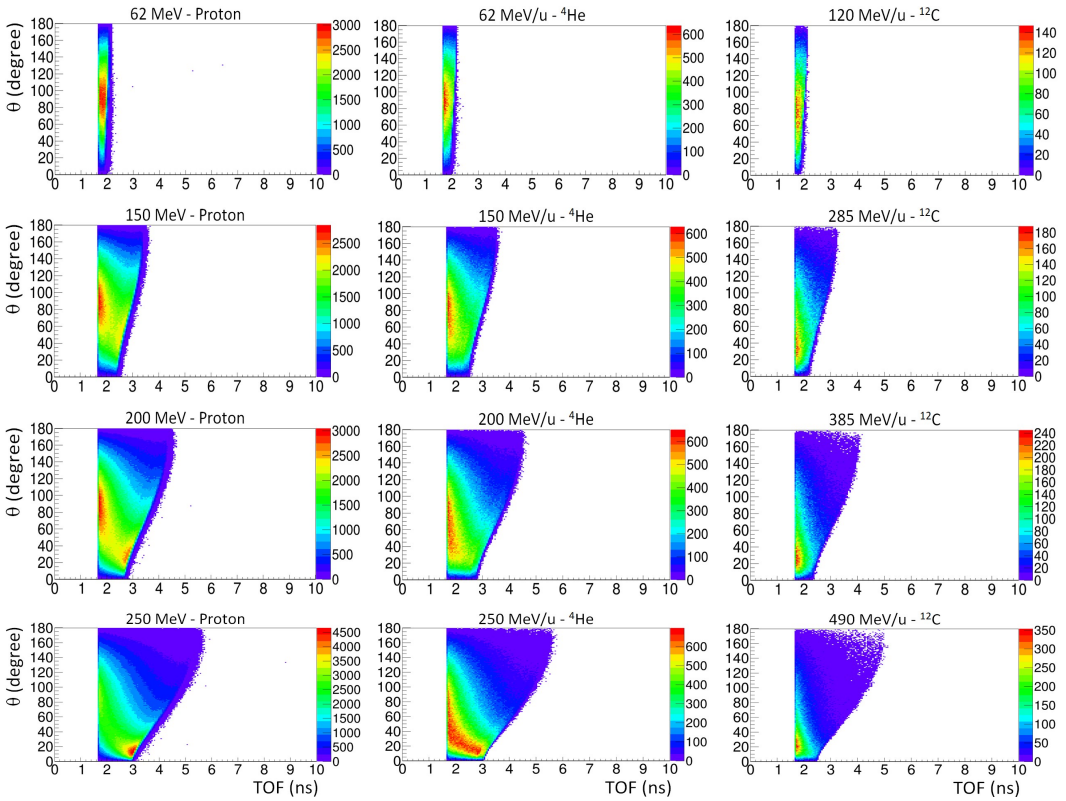

Figure 30: TOF spectra along the polar angle θ of primary gamma rays ≥1 MeV reaching the detection sphere once emitted from the phantom for protons, ^{4}He and ^{12}C ions.

Figure 31 shows the particle range plotted with the PG range and emission time, as well as PG TOF data (peak mean, width and integral), for each particle type and energy under study, irradiating a homogeneous spherical-shaped water phantom. The PG data are for those with 1 MeV energy threshold. The PG range offers good correlation with the particle range, as seen in Section 3.3. T_{PG} values show a linear increase with particle energy, since the PG emission time is correlated to the beam transit time and hence the beam range. For a global idealised detection set-up, the PG TOF peak mean and width are found to only slightly increase with particle energy, with a minor drop in the case of ^{12}C ions at higher energies. Conversely, the PG TOF peak integral values exhibit a greater linear increase with particle beam energy. This may suggest that a correlation between the PG range and corresponding emission yield with the beam's range and corresponding energy deposition could potentially serve as a means for *in vivo* dosimetry. In the case of the homogeneous PMMA and adipose tissue cylindrical-shaped phantoms, the quantitative correlation of PG emission with the beam range and PG detection properties are found to be consistent to those for the spherical water phantom, seen in Figures 32 and 33, respectively. This suggests that the quantitative PG emission and TOF detection data are a suitable means for range or dose monitoring for homogeneous phantoms of varying material and shape.

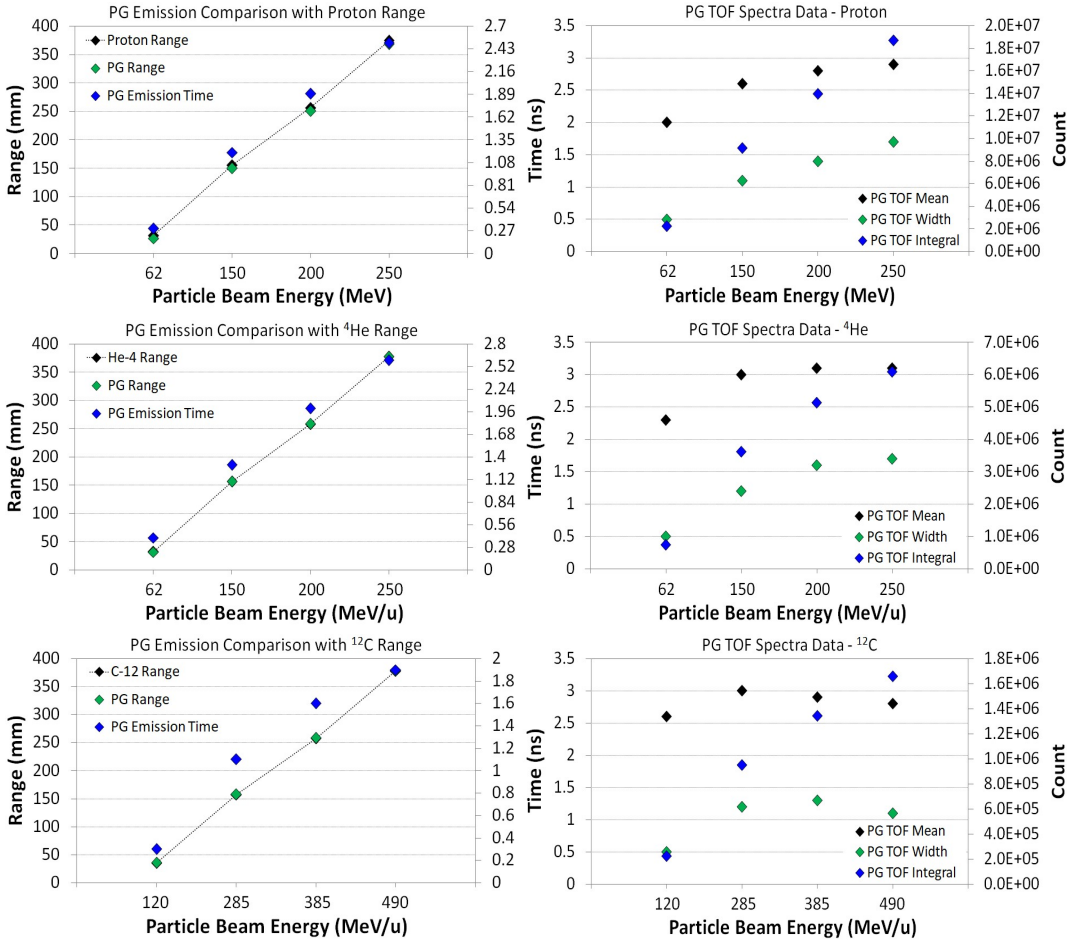

Figure 31: Quantitative comparison of the particle beam range with PG emission and detection data in the spherical water phantom for protons, ^{4}He and ^{12}C ions. **Left**: Particle beam range and corresponding PG range, with PG emission time. The dotted line joining the particle range values serves to guide the eye. **Right**: PG TOF peak mean, width and integral. All PG data are for gamma rays ≥1 MeV. The uncertainty in the beam range is 0.5 mm, PG range is 0.1 mm, emission time/TOF mean is 0.1 ns, and TOF width is 0.2 ns.

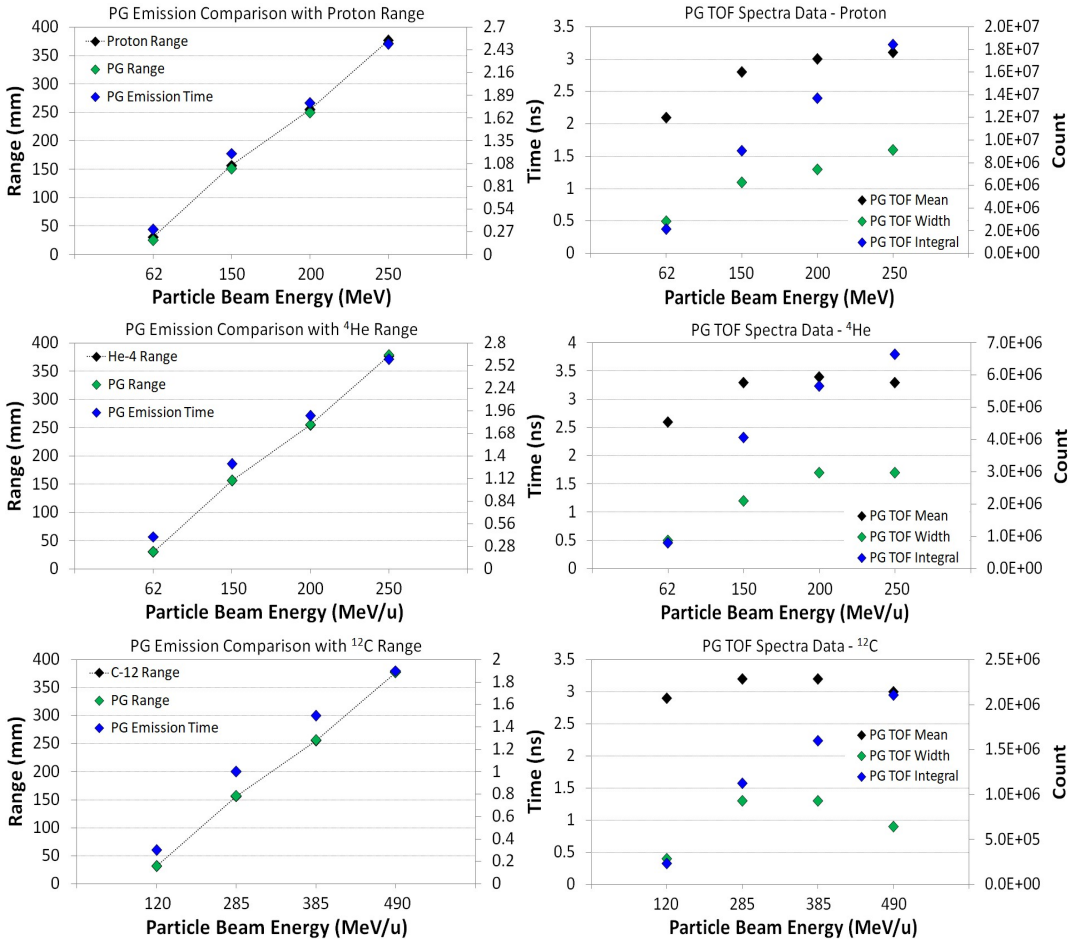

Figure 32: Quantitative comparison of the particle beam range with PG emission and detection data in the cylindrical PMMA phantom for protons, ^{4}He and ^{12}C ions. **Left**: Particle beam range and corresponding PG range, with PG emission time. The dotted line joining the particle range values serves to guide the eye. **Right**: PG TOF peak mean, width and integral. All PG data are for gamma rays ≥1 MeV. The uncertainty in the beam range is 0.5 mm, PG range is 0.1 mm, emission time/TOF mean is 0.1 ns, and TOF width is 0.2 ns.

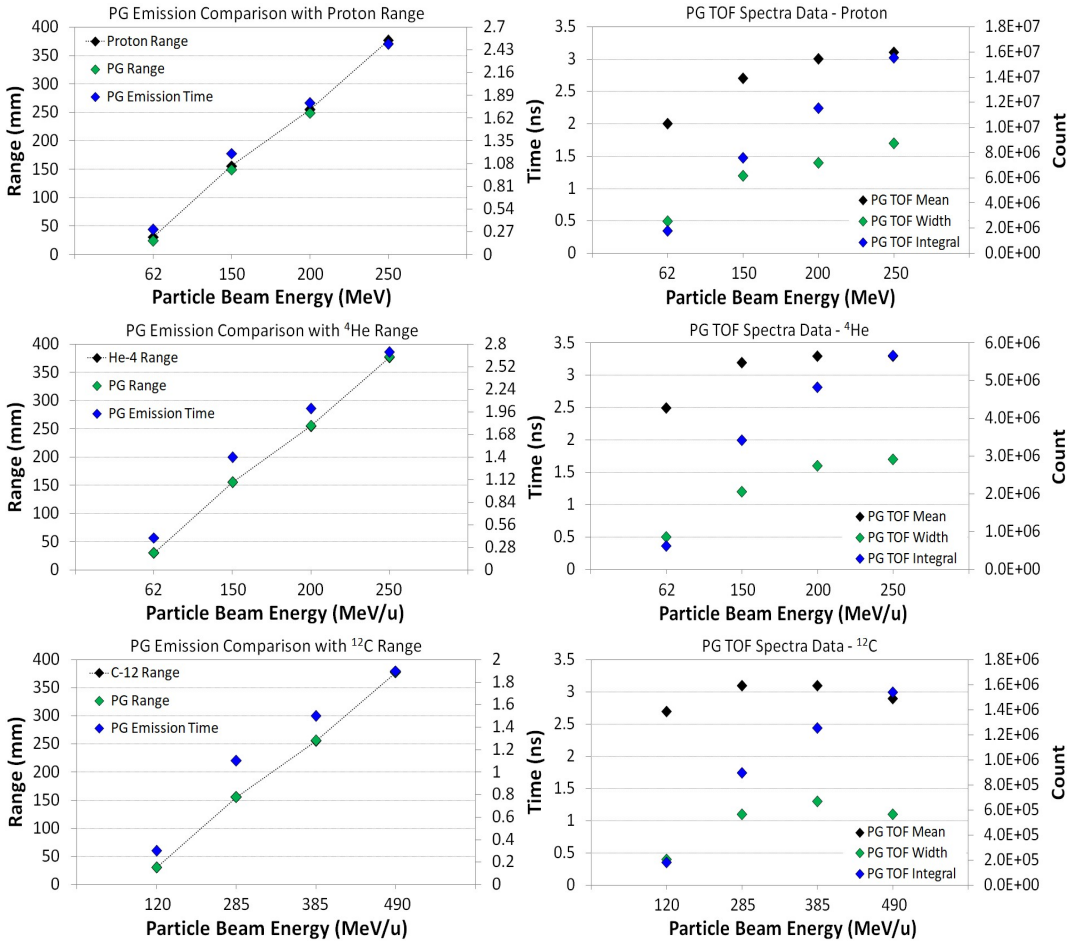

Figure 33: Quantitative comparison of the particle beam range with PG emission and detection data in the cylindrical adipose tissue phantom for protons, ^{4}He and ^{12}C ions. **Left**: Particle beam range and corresponding PG range, with PG emission time. The dotted line joining the particle range values serves to guide the eye. **Right**: PG TOF peak mean, width and integral. All PG data are for gamma rays ≥1 MeV. The uncertainty in the beam range is 0.5 mm, PG range is 0.1 mm, emission time/TOF mean is 0.1 ns, and TOF width is 0.2 ns.

3.6.2 Realistic Head Phantom

The PG production distribution was seen in Figure 20 to closely correlate to the shift in the proton beam range between the water-based and realistic head phantoms. Figure 34 shows the emission time distribution of total gamma rays and those ≥1 MeV within the phantoms. Although minor, the distributions show a profile fall-off difference between the two phantoms as a result of the beam range shift. The rise in the emission time profile at approximately 2.4 ns is due to the time taken for the protons to arrive at the phantom upon initialisation within the simulation. Figure 34 also shows the TOF spectra of total gamma rays and those ≥1 MeV, as well as neutrons, for the two head phantoms. The difference in proton beam range between the two phantoms is also shown in the TOF distribution of detected gamma rays, for which the integral and fall-off are different for the two cases. The TOF distribution of gamma rays emitted

from the water-based head phantom shows a fall-off in the profile at a slightly longer time than the gamma rays from the realistic phantom due to the greater depth of the proton beam range. The integral of the TOF spectrum of gamma rays from the realistic head phantom is slightly larger than that from the water-based phantom, which may be correlated to the higher energy gamma rays emitted from the realistic head phantom (see Figure 18) that are not attenuated within the phantom.

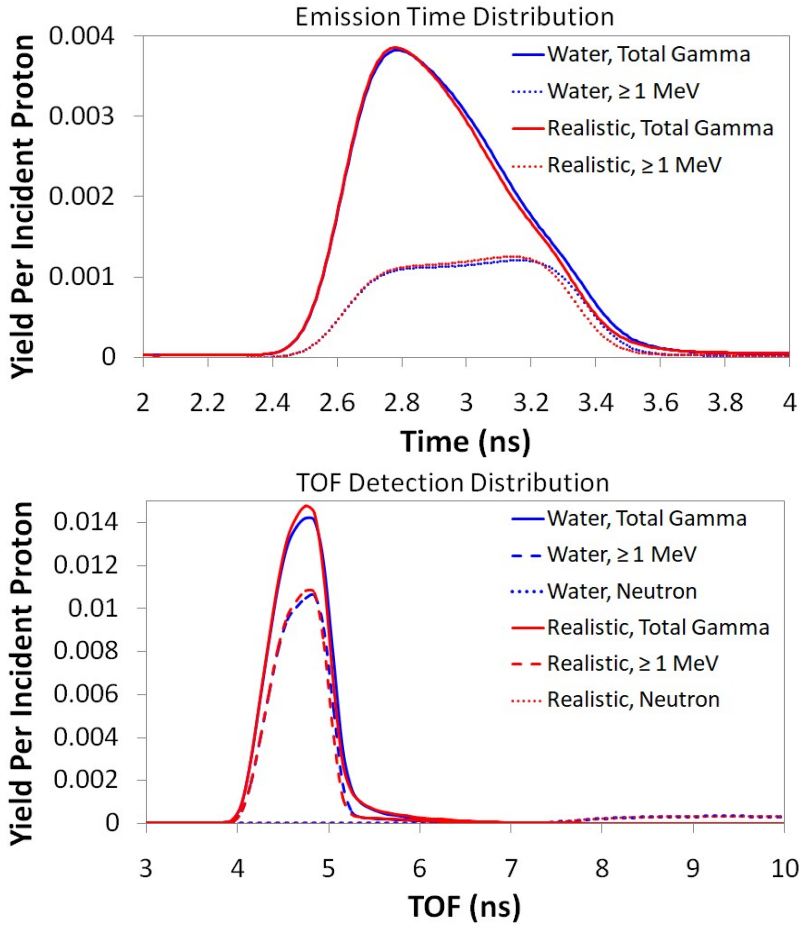

Figure 34: Top: Emission time distribution of total gamma rays and gamma rays ≥1 MeV originating in the water-based and realistic head phantoms. The bin width is 0.01 ns. **Bottom**: TOF spectra of total gamma, gamma rays ≥1 MeV and neutrons reaching the detection sphere once emitted from the head phantoms. The bin width is 0.1 ns. The proton beams irradiating the phantoms are of 100 MeV.

The temporal properties of emitted and detected PG rays were studied with the beam incidence marking the start time. As the PG emission time is associated with the beam transit time, the particle range can therefore be extracted from the measured PG TOF spectrum as well. The PGT [171] method retrieves the beam range by means of the TOF peak's mean and width while the PGPI [173] method makes use of the TOF spectrum count integral; the integral being a potential means for *in vivo* dosimetry. The PG TOF spectrum on the idealised detection sphere is most likely to reflect the intrinsic characteristics of the PG TOF spectroscopy from the

phantom. In practice, the realistic spectrum could be much more complicated and it largely depends on the nature of the delivered beam time structure as well as the detector's time resolution [232]. The very narrow time range of PG TOF (a few nanoseconds) implies that ultra-high time resolution of the detector (<1 ns) is needed in order to accurately extract the range/dose information from the measured PG TOF spectroscopy. Furthermore, the temporal separation between PG rays and neutrons can be exploited to discriminate the PG signal from the neutrons and neutron-induced backgrounds. This has been proposed by Testa et al. (2008) [146] for ^{12}C ions at low energies where the RF signal of the accelerator at the GANIL facility could be used as the start time reference. However, this technique is not suitable for synchrotron facilities, where instead a trigger signal from a fast transmission detector may be used. The TOF neutron rejection technique for protons was investigated using Monte Carlo simulations [145]. Hueso-González et al. (2018) [59] performed experimental measurements of the technique for protons accelerated by cyclotrons. However, the application of TOF for proton, ^{4}He and ^{12}C ions in synchrotron facilities at clinical energies and intensities has not yet been demonstrated experimentally. TOF may be inefficient for PG detection in proton therapy due to long bunch times from synchrotrons, while for carbon therapy the detection of individual ion impacts may be possible at mean intensities of 10^{7}-10^{8} ions/second by means of fast beam hodoscopes [57]. Combining the angular preference and TOF of PG measurements may further improve the PG signal-to-background ratio.

3.7 Discussion

In this study, the emission energy, position and time of PG rays in homogeneous water, PMMA and adipose tissue phantoms irradiated with three different particle types (proton, ^{4}He and ^{12}C ions) of varying energy were investigated using Geant4 simulations. Heterogeneous DICOM-formulated head phantoms (realistic and water-based) were also studied to explore the heterogeneity effects on PG range monitoring. The PG production and detectable yields, energy spectral, spatial and temporal correlation characteristics with the depth dose profile were quantified. A relatively low gamma ray energy threshold of 1 MeV was used to ensure higher statistics, while a PG energy window of 3.0-7.0 MeV (adopted in other studies [176,226]) was also included for comparison. This thesis study shows that the energy spectra of emitted gamma rays are characteristic to the elemental composition of the phantom materials. Higher concentrations of oxygen in the target result in greater intensity of the 5.21 and 6.13 MeV emission lines of the spectra, while higher concentrations of carbon result in greater intensity of the 4.44 MeV line. Hence, the characteristic gamma emission spectra from irradiated phantoms can be exploited to identify the target material.

The PG signal is seen to be a reliable means for *in vivo* range verification in particle therapy. The primary PG rays exhibit the closest correlation to the particle range but it is masked by the concurrent secondary PG rays; which may impose a greater challenge for BP tracking in heavy ion therapy (e.g. carbon ions) where secondary PG rays are dominant. The effects of target inhomogeneities are seen on the PG production distribution in relation to the beam crossing the various materials of the phantom, but the quantitative data shows that the PG-BP fall-off correlation is consistent for heterogeneous targets as well as homogeneous ones.

The angular distribution of detected PG rays was studied from spherical and cylindrical phantoms, which saw that geometric effects of the phantom play a role in the angular variances seen on the idealised detecting sphere due to attenuation/absorption of the gamma rays. The angular distribution was also seen to change with beam energy, which may suggest that a movable PG detector coordinated with respect to the beam range could serve to optimise the PG detection efficiency. The emission and detection (TOF) properties of PG rays showed a correlation with the particle beam range that is consistent between the homogeneous target geometries and materials under investigation in this study. The PG TOF peak integral showed a linear correlation to the increasing beam range for each of the particle species; this suggests that associating the PG range and corresponding emission yield with the beam's range and corresponding energy deposition may be a technique toward *in vivo* dosimetry. Combining an energy threshold/window to the PG TOF distribution, in addition to locating the PG detector/s at optimal angular positions, could serve to improve the PG signal-to-noise ratio, as seen in the 2D representations in Figure 30. The PG TOF spectroscopy encodes essential information on the particle range, and potentially dose, but the technique requires fast detection (excellent time resolution). Hybrid PG detection systems to exploit the energy, spatial and timing information is desirable for real-time range verification and dosimetry in particle therapy.

4 Scintillation Detector Characterisation for Prompt Gamma Measurement

Experimental work was performed at ANSTO to investigate a suitable scintillation detector for fast and efficient PG ray timing measurements. As described in the previous chapters, real-time range verification utilising the temporal information of the PG rays requires fast gamma ray detectors, data acquisition and analysis. This is also crucial for neutron rejection techniques and improving the PG signal-to-noise ratio. The detector's speed of response to a gamma ray detection event should complement its efficiency and energy resolution, such that the detector can handle the relatively high gamma yield and adequately resolve the PG emission energies. This is particularly important for gamma energy selections/windowing or spectroscopy techniques used for range/dose monitoring. Hybrid PG detection systems utilising more than one feature of PG rays have the potential to overcome the challenges of PG measurements and offer a simple technique for *in vivo* dosimetry. In this study, several scintillation detectors were characterised in terms of timing – signal rise and decay times – and spectroscopy – energy resolution and efficiency – to determine the most suitable choice for hybrid PG measurements.

4.1 Experimental Set-up of Scintillation Detector Characterisation

Table 9 lists the four radioactive sources used in this work, their predominant energies emitted and intensity of emission I_γ. The photopeak energies utilised for spectroscopic studies were 59.5 keV (^{241}Am), 356.0 keV (^{133}Ba), 661.7 keV (^{137}Cs), 1173.2 keV and 1332.5 keV (^{60}Co). The energies were selected to be easily resolvable by the detector material of interest whilst covering a wide energy range.

Table 10 lists the instruments used in the measurements and a short statement on their purpose. Figure 35 depicts the electronic circuit diagrams of the two experimental set-ups: the top set-up is best suited for timing measurements, while the bottom set-up is best suited for spectroscopy. Figure 35 (top) shows that when the charge sensitive preamplifier is used there is also a capacitor coupling from the detector, and an oscilloscope to display the output pulses. In this case, to record the rise and decay times the direct output of the detector, or the preamplifier pulses, were used. The preamplifier adds an additional rise time dependent on the amplifier used and the input capacitance. In this study, the Amptek A250 charge sensitive preamplifier was used, which has a rise time of 2.5 ns at 0 pF [233]. The capacitance added at the preamplifier

input, i.e. detector capacitance, slows the rise time at a rate of 0.17 ns/pF, while the output rise time is also limited by the speed of the detector [234]. The built-in charge sensitive preamplifier preserves the basic information carried by the magnitude of the charge Q, such that the circuit uses feedback to mostly eliminate the output amplitude dependence on the capacitance and restores proportionality to Q [66].

Table 9: Radiation sources used for detector characterisation measurements. The emission energies and intensity of emission were taken from Ref. [235].

Source	Photopeak energy (keV)	Intensity of emission, I_γ (%)
^{241}Am	26.3	2.40
	59.5	35.40
^{133}Ba	81.0	34.06
	276.4	7.16
	302.9	18.33
	356.0	62.05
	383.9	8.94
^{137}Cs	661.7	85.10
^{60}Co	1173.2	99.97
	1332.5	99.99

Table 10: Instruments used for detector characterisation measurements. The amplifier and power supply were mounted on a Nuclear Instrument Module (NIM).

Instrument	Purpose
Power supply	High voltage (HV) power supply (560 V)
Amptek A250 Preamplifier	Drive the input signal to the shaping amplifier (2.5 ns rise time)
Canberra 2025 Shaping Amplifier	Produce a gain in the signal amplitude and shapes the signal pulse into a Gaussian shaped pulse (1 μs shaping time)
LeCroy Oscilloscope Wavesurfer 44Xs	Display and analyse electronic signals (400 MHz bandwidth, 875 ps rise time)
Amptek Multichannel Analyzer (MCA) 8000A	Digitise the input signal from the shaping amplifier to obtain a pulse height spectrum
Personal computer (PC)	Access the ADMCA software for data analysis

Figure 35 (bottom) shows an RC feedback preamplifier preceding a shaping amplifier, followed by an MCA and PC. Part of the purpose of the preamplifier here is to stretch the signal fall into a quasi-square wave for integration by the shaping amplifier. For spectroscopy, a shaping amplifier is used to amplify and shape the pulse into a Gaussian for better signal-to-noise. The signal is then digitised with an MCA to obtain a pulse height spectrum which is displayed on a PC for further spectroscopic data analysis. That is, the use of a preamplifier with PMTs is better suited for spectroscopy applications where the preamplifier can be used to drive the input to the shaping amplifier, whereas for timing studies no shaping amplifier is necessary.

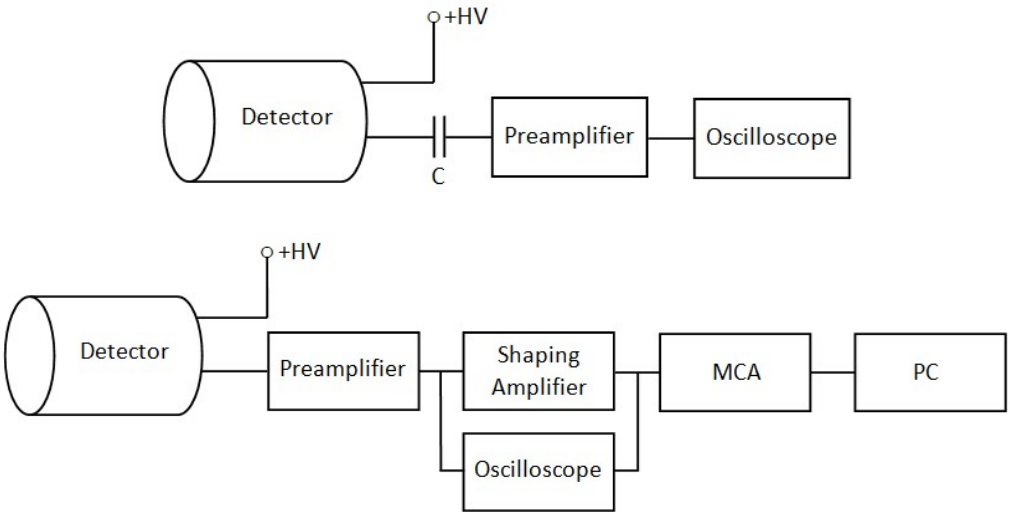

Figure 35: **Top**: Circuit diagram of experimental set-up for timing measurements, showing a capacitor coupling from the detector and a charge sensitive preamplifier. **Bottom**: Circuit diagram of set-up for spectroscopy, showing a preamplifier, shaping amplifier, MCA and PC. The oscilloscope is connected for display and analysis of signal pulses. The PMT or SiPM (not explicitly shown) is coupled to the detector.

Table 11 lists the scintillation detectors studied in this work as well as the crystal size and supplier. In the table, it is indicated whether the detector was coupled to either a PMT (gaseous-state) or SiPM (solid-state/semiconductor). $LaBr_3$(Ce) and $LaCl_3$(Ce) were studied with and without a built-in charge sensitive preamplifier. PMTs and SiPMs have similar response times, with time characteristics of a few nanoseconds rise times and ~10 ns decay times. For example, the Saint-Gobain detectors coupled PMTs or SiPMs have positive charge sensitive tail pulses with a ~50 µsec decay [236], and with for example a Photonis XP2060 PMT (coupled to a Ø1" × 1" $LaBr_3$(Ce) detector) having a rise time of 3 ns [237,238].

Table 11: Scintillation detectors characterised in terms of timing and spectroscopy. * indicates the detectors connected to a PMT and ** indicates the detectors connected to a SiPM. $LaBr_3(Ce)$ and $LaCl_3(Ce)$ were studied with and without a built-in preamplifier.

Scintillation detector material	Scintillator crystal size	Supplier
$LaBr_3(Ce)$ *	Ø1" × 1"	Saint Gobain
$LaCl_3(Ce)$ *	Ø1" × 1"	Saint Gobain
NaI(Tl) **	Ø2" × 2"	Saint Gobain
$CeBr_3$ **	Ø1.5" × 1.5"	Scionix Holland
$SrI_2(Eu)$ **	1 cm^3	Radiation Monitoring Devices (RMD)
CLYC **	1 cm^3	Radiation Monitoring Devices (RMD)
CLLBC376 **	Ø1.5" × 1.5"	Radiation Monitoring Devices (RMD)
CLLBC398 **	Ø1" × 1"	Radiation Monitoring Devices (RMD)
CLLBC406 **	Ø1.5" × 1.5"	Radiation Monitoring Devices (RMD)
CLLBC416 **	Ø1" × 1"	Radiation Monitoring Devices (RMD)

4.2 Response Time of the Scintillation Detectors

The timing properties of each scintillation detector was characterised in terms of the signal rise and decay time. The data were recorded using the oscilloscope by measuring the time at 10-90% (rise time) and 90-10% (decay time) of the signal amplitude. Figure 36 shows the signal waveforms of the various detectors under study, each normalised in the time axis to the 20 mV signal amplitude. The CLLBC376 and CLLBC398 waveforms displayed in the figure were averaged over four and five signal pulses, respectively, to remove pickup noise. Table 12 lists the rise and decay times of the detector signal waveform, as well as the corresponding amplitude for the recorded measurement. The data demonstrates that the $LaBr_3(Ce)$ and $LaCl_3(Ce)$ scintillation detectors connected to a PMT, with bypassing the built-in preamplifier, have the fastest timing properties among the detectors studied with sufficient current to still drive the shaping amplifier. These detectors show rise times of around 34 ns. As mentioned, part of the purpose of the RC feedback preamplifier is to stretch the signal fall into a quasi-square wave for integration by the shaping amplifier; this justifies the long signal tail (almost 100 μs decay time) for $LaBr_3(Ce)$ and $LaCl_3(Ce)$ with preamplifier. Thus, although the

preamplifier is best suited for spectroscopy applications and to improve the system energy resolution, its inclusion worsens the timing properties. Yet it is important that for hybrid PG detection systems, both energy and timing capabilities should be optimised, and improving one aspect should not come at the sacrifice of another. Comparing the scintillators coupled to SiPMs, those from the elpasolite crystal group were found to have relatively better timing properties; CLLBC398 and CLLBC416 were found to have ~200 ns rise times and ~2.5 μs decay times.

Since the measured rise times are much longer than the sampling rate of the oscilloscope, the main contribution to uncertainty is noise. That is, the oscilloscope used in this study had a rise time of 875 ps (which can be determined from the equation $t_r = 0.35/B$, where B is the bandwidth [239]) which is smaller than the measured rise times and so they are not bandwidth limited. Also, according to the Nyquist-Shannon sampling theorem [240-243], a sufficient sample rate f_s is achieved when $f_s > 2B$, where B is the bandwidth. The oscilloscope sample rate was 2.5 GS/s with a bandwidth of 400 MHz, so the theorem also holds. For the worst case scenario, there would be ~82 samples over the measured rise times of 34 ns, so the sampling rate is sufficient to reconstruct the high frequency components of the waveforms. For the vertical resolution, it was estimated that the SNR ≈ 12 in the spectrum for the worst case scenario, CLLBC398, and so the noise is not significant. In Table 12, the uncertainties are given as the standard deviation of three repeated measurements.

Comparing the CLLBC scintillation detectors, the influence of crystal size is also seen: CLLBC376 and CLLBC406 have size ∅1.5” × 1.5”, whereas CLLBC398 and CLLBC 416 have size ∅1” × 1”. The size of the scintillation crystal influences the light collection efficiency and uniformity of the scintillator. The largest possible fraction of light emitted isotropically should ideally be collected, but fluctuations occur due to the scintillation efficiency and non-perfect reflection conditions at the crystal surface. The non-uniform light collection can therefore introduce statistical broadening of the signal, particularly in large size crystals [66]. As seen in Figure 36, the CLLBC detectors of larger scintillation crystal size produce a broader signal waveform compared to those with smaller crystals.

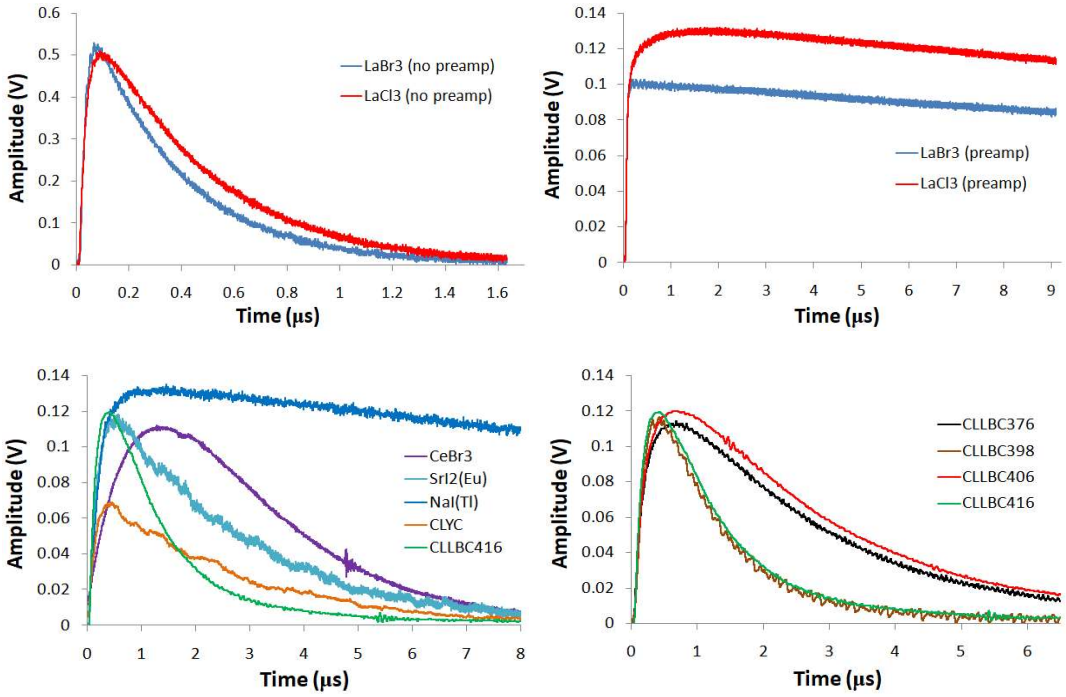

Figure 36: Signal waveforms for each scintillation detector studied. The waveforms in the bottom row figures are normalised in the time axis to the 20 mV signal amplitude for better visual comparison. The CLLBC376 and CLLBC398 waveforms were averaged across four and five signal pulses, respectively, to remove pickup noise. The bin size along the time axis in all figures is 0.4 ns.

Table 12: Timing properties of each scintillation detector, measured at 10-90% (rise time) and 90-10% (decay time) the signal amplitude. The uncertainty is given by the standard deviation of three repeated measurements.

Scintillation detector	Rise time (ns)	Decay time (µs)	Amplitude (mV)
$LaBr_3$(Ce) (preamp)	56.12 ± 1.53	96.33 ± 0.66	106.2 ± 8.7
(no preamp)	33.88 ± 0.12	0.79 ± 0.01	538.0 ± 10.2
$LaCl_3$(Ce) (preamp)	292.33 ± 2.90	95.18 ± 0.40	84.5 ± 12.7
(no preamp)	34.29 ± 5.66	0.89 ± 0.03	493.2 ± 22.4
$CeBr_3$	843.52 ± 24.27	6.25 ± 0.50	120.9 ± 4.6
SrI_2(Eu)	258.06 ± 0.85	5.85 ± 0.80	121.0 ± 17.2
NaI(Tl)	335.16 ± 22.38	78.83 ± 0.88	471.9 ± 3.5
CLYC	231.51 ± 20.69	5.80 ± 0.11	70.0 ± 1.5
CLLBC376	305.21 ± 7.33	6.11 ± 0.15	120.6 ± 2.8
CLLBC398	197.33 ± 6.24	2.55 ± 0.30	127.0 ± 9.7
CLLBC406	292.97 ± 7.83	5.78 ± 0.17	118.9 ± 5.1
CLLBC416	178.64 ± 10.51	2.45 ± 0.29	117.5 ± 13.5

Several studies have utilised $LaBr_3$(Ce) for PG range verification measurements due to its fast timing and superior detection capabilities [59,170,173,232]. Yet $CeBr_3$ has been determined as the best choice for PG timing range monitoring [60,123]. However, in this thesis study, $CeBr_3$ was found to be the slowest by over an order of magnitude with a rise time of around 840 ns. Overall, the recorded timing values are larger than values in the literature [66,244,245]. These discrepancies may be due to the PMT itself, which may present limitations on the signal response, but are representative of the standard matched scintillator and PMT detectors available commercially, compared to a specific high speed PMT with lower amplification. The $LaBr_3$(Ce) and $LaCl_3$(Ce) scintillation detectors were optically coupled to a PMT while the other detectors, including the $CeBr_3$, were coupled to a matched SiPM by the manufacturer. The response times of PMTs and SiPMs are comparable, with time characteristics of a few nanoseconds rise times and ~10 ns decay times. PMTs are generally stable and low noise, but bulky, affected by magnetic fields, and for a gain of 10^6 require a high bias voltage of 1-2 kV [114]. SiPMs maintain similar gains and speed to PMTs but have several advantages, such as requiring 20-30 times less power than PMTs (achieves high gain with a very low bias voltage of ~30 V), compact size, magnetic insensitivity, and higher photon detection efficiency of 50-60% compared to 35% for PMTs [114,246]. Shorter recovery times of SiPMs can be achieved with smaller microcells (lower fill factor), resulting in higher dynamic range and lower capacitances, but is a compromise to lower photon detection efficiency and gain [114].

4.3 Spectroscopy: Energy Resolution and Detection Efficiency

Spectroscopic data analysis was performed using the ADMCA software on a PC, where the MCA spectrum x-axis channels were calibrated to energy in units of keV. The energy resolution of each detector was calculated as a percentage using equation 10 (Chapter 2).

As mentioned in Chapter 2 of this thesis, there are two common types of detector efficiency: absolute detection efficiency and intrinsic detection efficiency. Counting efficiencies can also be categorised by the nature of events recorded, namely *peak detection efficiency* and *total detection efficiency*, the former being more commonly used. The peak detection efficiency is given by the number of events under the full energy peak in a differential pulse height spectrum divided by the number of radiation quanta emitted by the source. Total detection efficiency is given by the total number of events under the entire differential pulse height spectrum divided by the number of radiation quanta emitted by the source. In this study, the intrinsic peak detection efficiency was calculated with:

$$\varepsilon_{int} = \frac{N4\pi}{S\Omega} \tag{13}$$

where N is the number of events in the full energy peak, S is the number of radiation quanta emitted by the source, and $\Omega \cong A/d^2 = \pi a^2/d^2$ (for d >> a) where A is the detector area, a is the detector radius and d is source-detector distance [66]. That is, N is determined by the number of events in the full energy peak taken from the differential pulse height spectrum considering the photopeak intensity I_γ of which the number of events is true. The intensity values used in the calculations for each source are presented in Table 9. S is determined by the activity of the source considering the duration of the measurement. The activity of the source at the time of measurement can be determined with $A(t) = A(0)e^{-t/\tau}$ where $A(0)$ is the initial activity, t is the time since initial activity and τ is a decay constant whereby $\tau = T_{1/2}/ln2$ where $T_{1/2}$ is the radiation source half-life.

The detector thickness also governs the detection efficiency, since it relates to the gamma ray attenuation within the detectors. Depending on the crystal thickness, gamma rays can be partially or fully absorbed; a thicker crystal increases the probability of gamma ray attenuation and full absorption which therefore increases the detection efficiency. For example, for $LaBr_3$(Ce) at 1 inch thickness, around 60% of 662 keV gamma rays are absorbed [247]. For gamma rays of 4 MeV, the crystal thickness required to fully absorb the gamma ray would need to be >30 cm, with only around 40% being absorbed for a thickness of 1 inch. The impact of scintillator thickness should therefore be considered when comparing results in such characterisation studies, particularly for detector efficiency.

For the energy resolution measurements, the radiation sources were positioned close to the detectors (a few centimetres) while ensuring the dead time was still negligible, and the spectra acquired for 5 minutes to obtain sufficient statistics. For the efficiency measurements, the source-detector distance was 2 m; the distance between source and detector is an important parameter in the calculations, such that the further the source the more accurate the calculation.

Table 13 presents the energy resolution and efficiency of each detector at the photopeak energy of 662 keV. The energy resolution values recorded in this study agree within a factor of two with those given in the literature [66,244,245]. In this thesis study, CLYC and $LaBr_3$(Ce) were found to have the better energy resolution with values of 3.4% and 3.5%, respectively. However, between the two, $LaBr_3$(Ce) was seen to have the better efficiency; this could simply be due to its thicker crystal of 1 inch, compared to the 1 cm thickness of CLYC. Yet the CLLBC detectors of the same size as the $LaBr_3$(Ce) have comparable energy resolutions but poorer detection efficiency. Elpasolite detectors, such as CLYC and CLLBC, have the added advantage of gamma-neutron discrimination capabilities, whereby differences in the scintillation decay response/pulse shapes can be used to distinguish the two types of radiation [127,129,131].

Decay times, rather than rise times, are conventionally used for pulse shape discrimination as it is easier to measure.

Table 13: Energy resolution and detection efficiency at 662 keV, for each scintillator studied. Uncertainties were calculated with reference to error propagation (see for example, Knoll (2000) [66]).

Scintillation detector	Energy resolution (%)	Detection efficiency
$LaBr_3$(Ce)	3.5 ± 0.7	0.33 ± 0.02
$LaCl_3$(Ce)	4.4 ± 0.8	0.15 ± 0.01
$CeBr_3$	4.9 ± 0.9	0.30 ± 0.01
SrI_2(Eu)	3.6 ± 0.7	0.04 ± 0.01
NaI(Tl)	6.3 ± 1.0	0.24 ± 0.01
CLYC	3.4 ± 0.7	0.06 ± 0.01
CLLBC376	3.8 ± 0.8	0.17 ± 0.01
CLLBC398	4.1 ± 0.8	0.21 ± 0.01
CLLBC406	3.7 ± 0.8	0.21 ± 0.01
CLLBC416	4.1 ± 0.8	0.19 ± 0.01

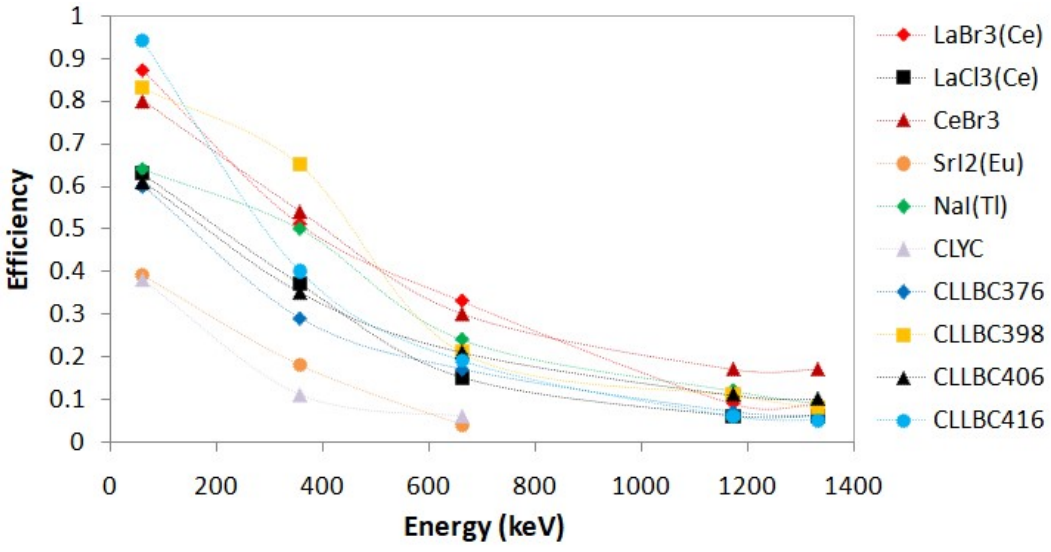

Figure 37: Intrinsic peak detection efficiency curves for each scintillator studied.

Figure 37 shows the intrinsic peak detection efficiency curves as a function of gamma ray energy for each detector studied. As expected, an exponential trend is seen across the energy range, such that at lower energies photoelectric absorption in the scintillator is dominant, where

the full energy of the photons are absorbed, while at higher energies Compton scattering and pair production are more probable. Although the $CeBr_3$ detector has a larger crystal, the detection efficiency is comparable (but slightly worse) than that of the $LaBr_3$(Ce) detector; yet both are superior in detection efficiency relative to the other scintillators studied.

4.4 Discussion

In this work, the energy- and time-resolved capabilities of several scintillation detectors were investigated to determine the most suitable for potential hybrid PG detection systems. Hybrid PG detection systems utilising more than one characteristic of PG rays have the potential to overcome present challenges and offer a simple technique for *in vivo* dosimetry. Yet achieving simultaneous resolved detection and data acquisition is challenging.

The results in this study showed that the $LaBr_3$(Ce) detector, without a built-in preamplifier and coupled to a PMT, offered the fastest timing capabilites, having shorter signal rise and decay times compared to the other detectors studied. Results also showed that $LaBr_3$(Ce) and CLYC offered better energy resolution, with $LaBr_3$(Ce) being the more efficient. Elpasolite crystals, such as CLYC and CLLBC, have the added ability of gamma-neutron discrimination via pulse shape differences between the two radiation types [127,129,131]. These scintillators therefore have the potential for hybrid systems utilising PG energy and time information in addition to simultaneous neutron discrimination. To the authors' knowledge, these elpasolite crystals have not yet been studied for the purpose of PG range monitoring in particle therapy.

In terms of efficiency, $LaBr_3$(Ce) and $CeBr_3$ were seen to be comparable but relatively superior than the other scintillation detectors across the energy range. Although $CeBr_3$ has been determined to be the best choice for PG timing measurements due to its fast response and superior energy resolution [60,123], $LaBr_3$(Ce) has been shown to be an adequate alternative, with the best compromise between timing and energy resolution, and utilised in several PG range verification studies [173,232], including the PGS measurements performed at MGH [59,170].

In practice, the choice of detector should ideally exhibit excellent energy and timing resolutions simultaneously, with superior efficiency for the high-energy PG rays. The data acquisition system accompanying the detector should also be fast enough to allow timing measurements that provide valuable data and real-time feedback. In addition, the overall detection system should have the capability to cope with the beam time structure and accurately synchronise with the accelerator RF; the bunch time spread is a key factor influencing the resolution of PG timing measurements. A proton bunch monitor that measures the bunch time

structure and potential phase drifts could be used to overcome these limitations. High-throughput and high-efficient PG detector systems are desired for simultaneous energy- and time-resolved PG measurements.

Future work investigating the scintillator performance for high-energy PG rays, through measurements and in clinical conditions, as well as possible hybrid detector systems, will be important as a means toward *in vivo* dosimetry for particle therapy QA.

5 Simulating Prompt Gamma Rays for Clinical Range Verification

Simulation tools are not only widely employed for the fundamental research concerning PG ray physics and detection concepts, but they are also used clinically, and a PG method may require comparing the obtained measurements with expected outcomes to determine deviations from the prescribed treatment plan. Thus, it is important that the physics models and data in the simulation are accurate and reliable for use in particle therapy beam range monitoring. In this study, simulations were performed to determine the performance of physics models available in Geant4/TOPAS for use in PG simulations. The simulation data were compared to measurements performed in the pencil beam scanning treatment gantry at the Francis H. Burr Proton Therapy Center, MGH, Boston USA. Preliminary measurements at MGH with the full-scale range verification prototype using PGS was published in Hueso-González et al. (2018) [59]; this paper should be referred to for details about the PGS detection system, measurements and data analysis. This chapter provides an overview of relevant information from Ref. [59] (Sections 5.1-5.2) followed by my research work (Sections 5.3-5.4).

TOPAS was used to model the MGH PGS detection system, incident proton beam and phantom. Simulation results were quantitatively compared with respect to the corresponding experimental data obtained for a pencil beam spot. Two Geant4 physics lists (which are also available in TOPAS), *QGSP_BIC_HP* and *QGSP_BIC_AllHP*, were investigated with Geant4 version 10.06.p01. Two phantom materials were explored, water and high-density polyethylene (HDPE), to determine the simulation reproducibility for oxygen and carbon, respectively. The same simulation was performed with Geant4 version 10.05.p01 for regression testing purposes. Hence, this study is performed to offer recommendations to the scientific community for simulating PG rays, which is a significant aspect in the current status of PG research, and potentially in practice, for *in vivo* range/dose monitoring.

5.1 Experimental Set-up of the Prompt Gamma Detection System

The MGH proton therapy treatment facility housed an IBA C230 cyclotron (Ion Beam Applications SA, Louvain-la-Neuve, Belgium) that accelerates protons to 230 MeV, which are then degraded by an energy selection system and transported to the treatment room through a ~35 metre beam line. The RF of the cyclotron is 106.3 MHz. The beam current for

all pencil beam layers is 2 nA incident on the phantom, which corresponds to approximately 100 protons per bunch every 9.4 ns. The reproducibility of the beam range in water is better than 0.5 mm [59].

The PGS detection system consisted of eight $LaBr_3(Ce)$ scintillation crystals (50.8 mm diameter, 76.2 mm length) coupled to a PMT and resting on a custom-built base. There were two rows of four detectors, each focusing on a different position along the beam direction, allowing for a larger field-of-view (FOV). The system was comprised of a tungsten collimator configuration: five tungsten slabs (each $25.4 \times 203.2 \times 127.0$ mm$^3 \pm 0.5$ mm) with a (12.7 ± 0.2) mm slit opening after the first and fourth slab (along the beam direction), and (6.4 ± 0.2) mm slit opening after the second slab (see Figure 38), as well as an acrylic front plate and aluminium aperture. The collimator spacing after the fourth slab was a trade-off between spatial resolution and detector efficiency, while the spacing after the first and second slab allow for a larger area of blocking background gamma rays (e.g. from the nozzle and range shifter) without additional tungsten slabs (i.e. increasing the weight of the detector body). The system (scintillators and electronics) can sustain high overall event rates of up to 10^7 events per second [59].

Figure 38 shows the experimental set-up configuration used for cross section optimisation measurements conducted by the MGH group. The PGS system remained in a fixed position perpendicular to the beam incidence during treatment delivery. The distance from isocentre (located centrally in the target volume) to the front face of the phantom (beam incidence) was (124.0 ± 0.5) mm. The measurements were performed with a single high-dose spot of 3×10^{10} protons delivered consecutively to 19 energy layers along the central beam axis. That is, no merging of lateral spots was performed; this therefore allows a better comparison with simulation results. Proton beam irradiation of water and HDPE phantoms were performed. The proton beam ranged between (100 ± 1) mm and (150 ± 1) mm water equivalent depth. The distance between isocentre and the collimator front plane was (150.0 ± 0.5) mm, including an air gap of (100.0 ± 0.5) mm (between collimator and phantom) which is clinically realistic. The reader is encouraged to see Ref. [59] for further details regarding the experimental set-up. For the purpose of this thesis study, to compare simulation and measurement, a single pencil beam spot in the most distal energy layer is used. Further details of the simulation modelling are given in Section 5.3.

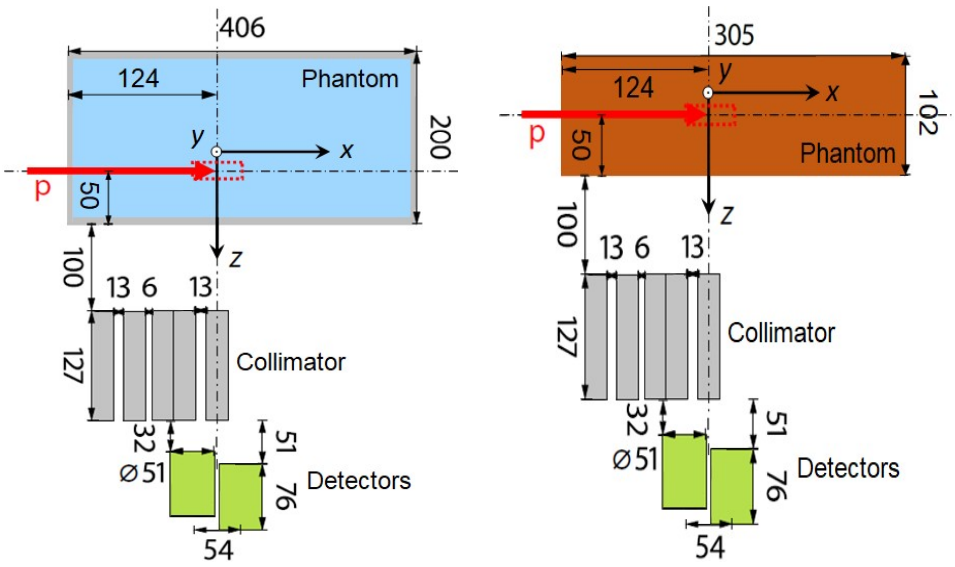

Figure 38: Schematic diagrams showing the experimental set-up configuration for the water phantom (left) and HDPE phantom (right). All units are in mm. The eight (two rows of four detectors) $LaBr_3(Ce)$ detectors are 50.8 mm in diameter and 76.2 mm in length. The collimator consists of five tungsten slabs (each 25.4 × 203.2 × 127.0 mm^3 ± 0.5 mm) with a (12.7 ± 0.2) mm slit opening after the first and fourth slab (along the beam direction), and (6.4 ± 0.2) mm slit opening after the second slab. For simplicity and clarity, the front plate and aluminium aperture (between collimator and phantom) are omitted. The red line indicates the proton pencil beam incidence on the phantom, and the centre of the target volume (red dotted-square) represents the position of isocentre in the treatment room. The distance from isocentre to the front face of the phantom was (124.0 ± 0.5) mm. The distance between isocentre and the collimator front plane was (150.0 ± 0.5) mm, with an air gap of (100.0 ± 0.5) mm. Figures adapted from Ref. [59] with permission.

5.2 Data Acquisition and Processing

The custom data acquisition system for the PGS detection system was synchronised with the beam delivery system and the cyclotron. The signals from the detector modules were independently read out with a 14-bit analog-to-digital converter that was phase-locked to the accelerator at a frequency twice that of the cyclotron RF for a sampling rate of ~2.13×10^8 samples per second. The data streams were processed in real-time by field-programmable gate arrays (FPGAs). An event was triggered when the digitised signal magnitude exceeded a predefined threshold. Integrating the area under the pulse signal over a time window of 200 ns was used to calculate the gamma ray energy. The gamma ray arrival time was determined by subtracting a delayed copy of the digital signal from the original and finding the zero crossing time of the resulting signal. The analysis of the arrival time was initially performed with a time resolution equal to the sample rate, followed by a polynomial interpolation to achieve sub-nanosecond resolution [59].

The acquired data were stored in a memory buffer that was continuously read out by the control software (custom C++ application) which performed several corrections to normalise the measurements to absolute units. Corrections included energy and time calibration, as well as pile-up and coincidence rejection. The corrected data were then combined in energy vs time histograms; two histograms were created for each proton pencil beam, i.e. one for each row of four detectors. The measured 2D histograms were split into three components iteratively [59]:

- proton-induced continuum, PG rays that undergo incoherent scattering in the detector or have scattered prior to reaching the detector;
- neutron-induced continuum, gamma rays that scatter before or inside the detector or from unresolved cascades; and
- resolved lines, whereby the continuum components (background) are subtracted from the measured to give the neutron-induced and proton-induced spectrum.

See Ref. [59] for an example of such 2D histograms. The proton-induced continuum is unresolved in energy but well-resolved in time, while the neutron-induced continuum is unresolved in both dimensions, and the resolved lines spectrum is resolved in both energy and time dimensions. The count rate in each detector was on the order of 10^6 events per second, such that an energy resolution of 1.3% FWHM at 6.1 MeV was achieved. Due to several sources of scatter such as the treatment head, phantom, couch, room walls and floor, half of the detected gamma rays make up the background. A small fraction of neutron-induced gamma rays are also produced in the collimator, but the majority of these will be re-absorbed internally [59].

In the PGS technique, the proton range for each pencil beam is determined by comparing the intensity of measured PG emission lines in the gamma ray energy spectrum to expected values obtained from a model. The model simulates the fundamental physical processes (including nuclear interactions, attenuation and detector system response) and predicts the PG emissions and detections. The PGS detection system geometry, CT to material conversion, proton stopping, PG emission, gamma ray attenuation and detection made up the model. Further details can be found in Ref. [59]. The reliability of such models/simulations is therefore important. Hence, for the purpose of this thesis study, the performance of Monte Carlo simulations was investigated, in particular, by comparing the intensity of simulated PG emission lines with measured data.

5.3 Modelling of the Prompt Gamma Detection System

TOPAS version 3.3.p1_expanded was used with Geant4 version 10.06.p01 to model the MGH PGS detection system, and proton beam irradiations of water and HDPE phantoms, as

performed in the experimental measurements. The TOPAS version used at MGH had been adapted to include the ParticleHP model (discussed later in this section).

Figure 39 shows an image of the simulation set-up with the water phantom. The same set-up applies to the HDPE phantom (see Figure 38). The simulation application includes the acrylic front plate and aluminium aperture of the collimator configuration. The water phantom ("G4_WATER", density of 1.0 g/cm^3) was 406 × 200 × 200 mm^3, including the acrylic ($C_5O_2H_8$, density of 1.19 g/cm^3) tank walls and base. The HDPE phantom (C_2H_4, density of 0.955 g/cm^3) was a 305 × 152 × 102 mm^3 solid block. The proton pencil beam in the simulation (and experiment) was incident on the phantom along the +x direction. In the simulation, the source of particles is located on the beam axis 20 cm upstream from the phantom front surface.

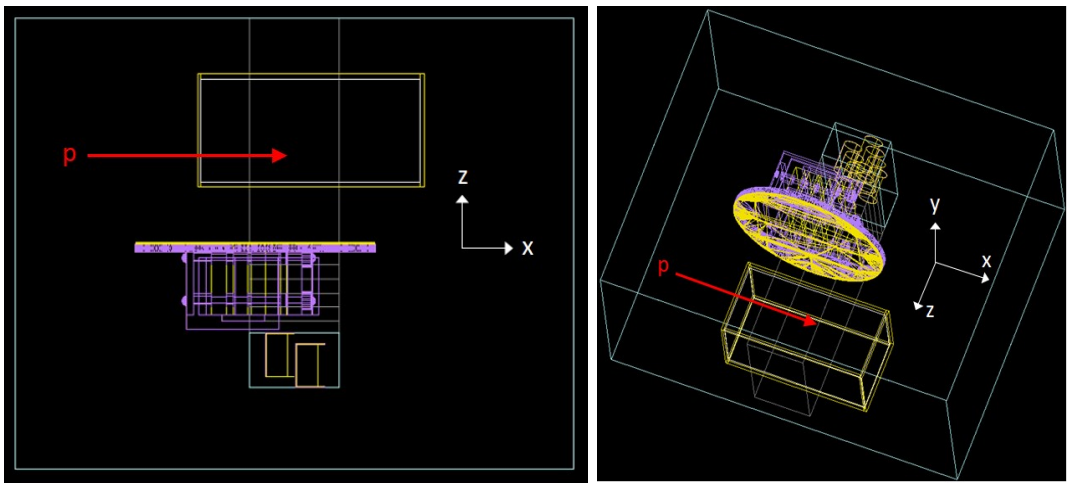

Figure 39: TOPAS model of the MGH PGS detection system with the water phantom, based on the experimental set-up. The proton beam is not to scale.

For the quantitative comparison between simulation and measurement, a single proton pencil beam spot was considered; the spot in the simulation was the equivalent as in the experiment in terms of beam parameters, incidental longitudinal and lateral position, as well as beam range (80% distal dose fall-off). The proton beam was incident along the central axis of the phantom in both model and experiment. The experimental proton beam range was (150 ± 1) mm in the water phantom and (149 ± 1) mm in the HDPE phantom. The simulation proton beam energies were tuned to obtain a simulated beam range within 1 mm agreement with the experiments; beam energy of 149.0 MeV for the water phantom and 147.5 MeV for the HDPE phantom. The number of simulated protons for the beam spot was 10^8 to obtain a 1% statistical uncertainty in the simulation results. The physical quantity, subject of comparison between simulation and experiment, was the absolute gamma ray counts per giga-protons (GP) (more details are given in the next section).

A TOPAS extension, written in C++, was included in the simulation framework to score the gamma rays interacting in each of the detectors. Total gamma rays, proton-induced and neutron-induced gamma rays were scored. The gamma ray energy deposition in the detector and TOF were recorded. The TOF was calculated as the interval of time between the generation of the proton beam to the gamma ray energy deposition in the detector. Optical photons, which arise from scintillation, although measured in the experiment, were not modelled in the simulation, and so the hypothesis is that all the optical photons were counted (reach the PMT window). Experimentally, not all gamma rays were counted due to, for example, selecting gamma rays between 1.4 and 7.2 MeV; this energy range of interest was thus also adopted to the simulation analysis. Within this energy range, corrections were applied for dead time, energy and time calibrations, pile-up and coincidence rejection, as discussed in Ref. [59]. A beam time spread (σ) of 0.38 ns [248] was also incorporated into the simulation to more accurately mimic the beam time structure of the proton therapy (accelerator) beam, such that the scoring of the gamma rays resembled a 9.4 ns proton bunch time. That is, the IBA 230 cyclotron at the MGH proton therapy centre has a RF of 106.3 MHz, and all pencil beam layers were delivered with the standard clinical system at the full beam current of 2 nA incident on the phantom, corresponding to a bunch of approximately 100 protons every 9.4 ns.

Simulation results using the Geant4 physics lists *QGSP_BIC_HP* and *QGSP_BIC_AllHP* were compared to investigate which physics approach was more accurate in reproducing the PGS output (i.e. gamma ray energy spectra). In particular, the two physics lists have the following features:

- *QGSP_BIC_HP* is used for hadrons up to 200 MeV with the high precision neutron (NeutronHP) data libraries used to model the neutron elastic and inelastic scattering, capture and fission, below 20 MeV [249,250]. Hadronic inelastic scattering of primary protons and neutrons on nucleons of the target nuclei is described by the Binary Intranuclear Cascade (BIC) model below ~10 GeV [197]. Following the BIC, the *Precompound* model describes the de-excitation of the remnant nucleus, followed by the Fermi breakup, neutron and light ion evaporation and photon evaporation models [249]. The *LightIonBinaryCascade* describes the intranuclear cascade of deuteron, triton, helium isotopes and heavier nuclei up to 6 GeV/n [221,249].
- *QGSP_BIC_AllHP* is identical to *QGSP_BIC_HP* but uses ParticleHP data libraries for protons, deuterons, tritons, helium-3 and alpha particles below 200 MeV [249]. That is, rather than using the Binary cascade model for these reactions, ParticleHP is used, which uses only evaluated nuclear data, mostly derived from the TALYS-based Evaluated Nuclear Data Library (TENDL) (i.e. TENDL-2014) with some isotopes from ENDF/B-VII.1 [251].

Therefore, in comparing *QGSP_BIC_HP* and *QGSP_BIC_AllHP*, it is predominantly a comparison between the Binary cascade and ParticleHP models.

The developers of Geant4 recommend the use of *QGSP_BIC_HP* for proton therapy studies, and indicate that *QGSP_BIC_AllHP* is promising [221,249]. *QGSP_BIC_HP* was found adequate for particle therapy studies in a recent benchmarking report by Arce et al. (2020) [221]. Hence, these physics lists were chosen to be studied in this work. While *QGSP_BIC_HP* has been studied for many years for proton and carbon ion therapy [173,176,202,205,225,252], *QGSP_BIC_AllHP* is a relatively new development and is worth to investigate its performance, particularly for PG rays and particle therapy.

When using *QGSP_BIC_HP*, the modularised Geant4 physics modules included the electromagnetic physics *G4EmStandardPhysics_option4*, *G4DecayPhysics*, *G4HadronElasticPhysicsHP* and *G4StoppingPhysics*, with *G4IonBinaryCascadePhysics* modelling the final state of inelastic scattering. When using *QGSP_BIC_AllHP*, the modularised modules *G4EmStandardPhysics_option4*, *G4DecayPhysics*, *G4HadronElasticPhysicsPHP*, *G4IonPhysicsPHP*, *G4IonElasticPhysics* and *G4StoppingPhysics* were active in the physics list.

5.4 Comparison Study of Simulation and Experimental Results

The simulation data were quantitatively compared to measurements in terms of absolute gamma ray counts per giga-protons (GP) for the two rows of detectors. The total gamma, proton- and neutron-induced gamma ray counts were studied, as well as the 4.44 and 6.13 MeV PG emission lines. The 2.22 MeV gamma ray line from neutron capture was also included to study the neutron production in the simulation. The neutron-induced interference background was also studied, in this case, by quantitatively comparing the simulated and measured count per GP per MeV at 4.44 and 6.13 MeV.

In the measurement, the total count was taken as the total events recorded. The neutron-induced gamma count was taken as the background of the total count TOF histogram (counts vs time), while the proton-induced gamma count was taken as the peak above this background baseline. In other words, the neutron-induced counts do not include prompt neutron counts with discrete energy lines. This results from the specific design of the Recursive Bisection Neutron Subtraction (ReBiNS) algorithm applied to the experimental results; see Ref. [59] for details.

In the simulation, the total gamma count was taken as the total gamma rays recorded. The total proton-induced count was retrieved from the TOF histogram of proton-induced gamma rays with no background subtraction. The total neutron-induced count was taken as the

background count of the neutron-induced gamma energy spectrum, i.e. not including prompt counts with discrete energy lines. The background from the simulations was retrieved using the ROOT TSpectrum class reference [253]. For the aforementioned total counts, the integrals were taken within the energy region 1.40-7.19 MeV, which is the same energy region of interest as in the measurement.

For the PG emission lines, the proton-induced 4.44 and 6.13 MeV lines were retrieved by subtracting the background of the proton-induced gamma energy spectrum and taking the integral of a Gaussian fit of the respective peak. The neutron-induced 2.22 MeV count was retrieved in the same manner.

5.4.1 Evaluating Geant4 Physics Lists: *QGSP_BIC_HP* and *QGSP_BIC_AllHP*

In this section, the simulation-measurement data comparison with the water phantom using Geant4 version 10.06.p01 is presented. Figure 40 shows simulated energy spectra for total gamma, proton- and neutron-induced gamma rays in detector row 1 obtained with the *QGSP_BIC_HP* physics list. That is, as in Ref. [59], 'detector row 0' is labelled here as detectors 0-3 and 'detector row 1' as detectors 4-7. The figure shows the proton- and neutron-induced components, which make up the total gamma spectrum. The prominent PG emission lines at 2.31 MeV (^{14}N*), 3.93 MeV (^{12}C*), 4.44 MeV (^{12}C*), 5.21 MeV (^{15}O*), 5.62 MeV (^{16}O*) and 6.13 MeV (^{16}O*) can be clearly seen. The 2.22 MeV line, arising from neutron capture by hydrogen, is also present.

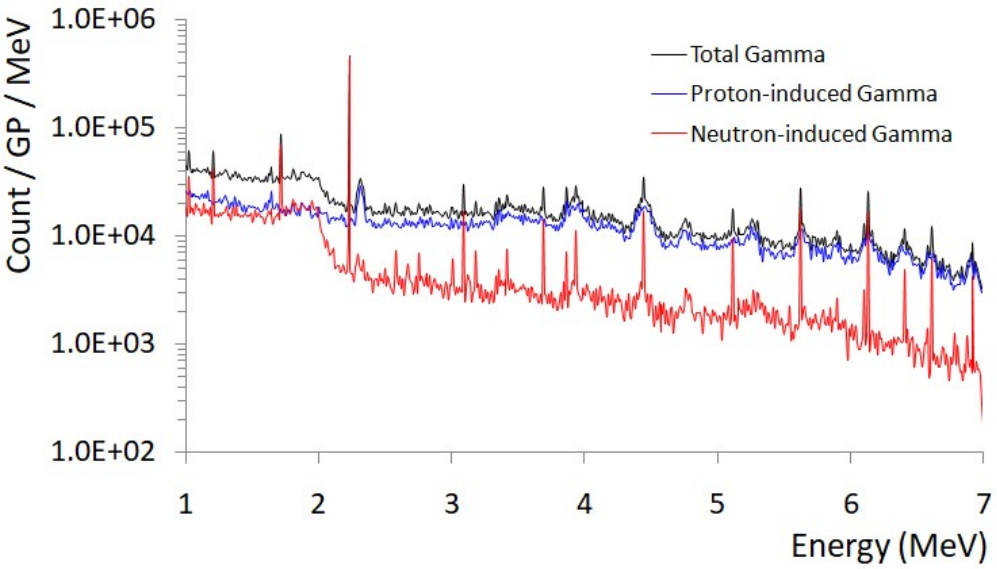

Figure 40: Simulated energy spectra of total gamma, proton- and neutron-induced gamma rays in detector row 1 from the water phantom using Geant4 10.06.p01 and the *QGSP_BIC_HP* physics list.

Figure 41 shows the energy spectra of proton-induced gamma rays in detector row 1 obtained from measurement and simulation using Geant4 physics lists *QGSP_BIC_HP* and *QGSP_BIC_AllHP*. The measured spectrum clearly showed the gamma emission lines, particularly the 3.93, 4.44, 5.21, 5.62 and 6.13 MeV lines. The relative intensities of measured gamma emission lines seemed to agree with evaluated nuclear cross section data [230], such that the intensity of lines from ^{16}O are larger than those from ^{12}C, followed by that from ^{15}O. A peak at 2.22 MeV from neutron capture remained present in the measured spectrum, since only the neutron continuum was subtracted from the measured data, such that the neutron discrete lines (energy resolved) were stored in the same histogram as the proton discrete lines. The use of the PG ray timing information was utilised in the PGS technique to reduce the interference of neutron-induced gamma rays, as discussed in Sections 5.2 and 5.4. Due to the dominating 2.22 MeV peak, the 2.31 MeV PG peak was barely visible in the measured spectrum, but could be seen in the simulated (using *QGSP_BIC_HP*) spectrum.

The simulated spectrum obtained with *QGSP_BIC_HP* (Binary cascade) showed good agreement with the 3.93 and 4.44 MeV peaks, but significant underestimation of the higher energy PG emission lines, and slight overestimation of the lower energy region in the spectrum. The *QGSP_BIC_AllHP* (ParticleHP) physics list showed an overall better base shape agreement with the measured spectrum across the energy range, but does not reproduce the PG emission lines. Further developments are still being made for ParticleHP, with some reactions not fully described due to limited evaluated data or incomplete implementation of the model [250], and *QGSP_BIC_AllHP* still needs extensive validation.

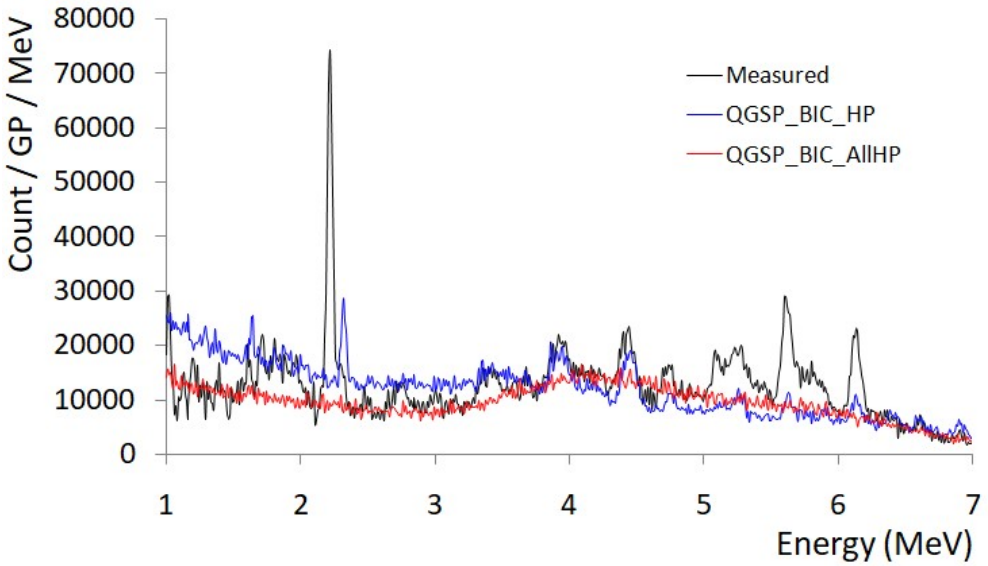

Figure 41: Energy spectra of proton-induced gamma rays in detector row 1 from the water phantom. The measured spectrum is shown with the simulated spectra using Geant4 (10.06.p01) physics lists *QGSP_BIC_HP* and *QGSP_BIC_AllHP*.

Figure 42 shows the measured and simulated neutron-induced gamma ray background curves from the water phantom for detector row 1, which indicate the contribution of neutron interference to the PG signal. The simulated background was seen to be significantly lower than the measured background. The simulated Count/GP/MeV around 4.44 MeV (1 MeV window) was a factor of ~5 lower than the measured count with *QGSP_BIC_HP* and factor of ~7 with *QGSP_BIC_AllHP*, while around 6.13 MeV (1 MeV window) the simulated count was a factor of ~5 and ~6 lower than the measured with *QGSP_BIC_HP* and *QGSP_BIC_AllHP*, respectively. The insert in the figure shows the measured data at 20%, to identify a possible correlation in the trend with the simulated plots; the largest differences were seen below ~3 MeV. These discrepancies should be further investigated, but may be due to sources of neutrons and neutron scatter that have not been taken into account in the simulation, as well as biases in the subtraction algorithms applied to the data (the measured data were obtained with an empirical background subtraction algorithm, such that changing the parameters may result in variations of the data).

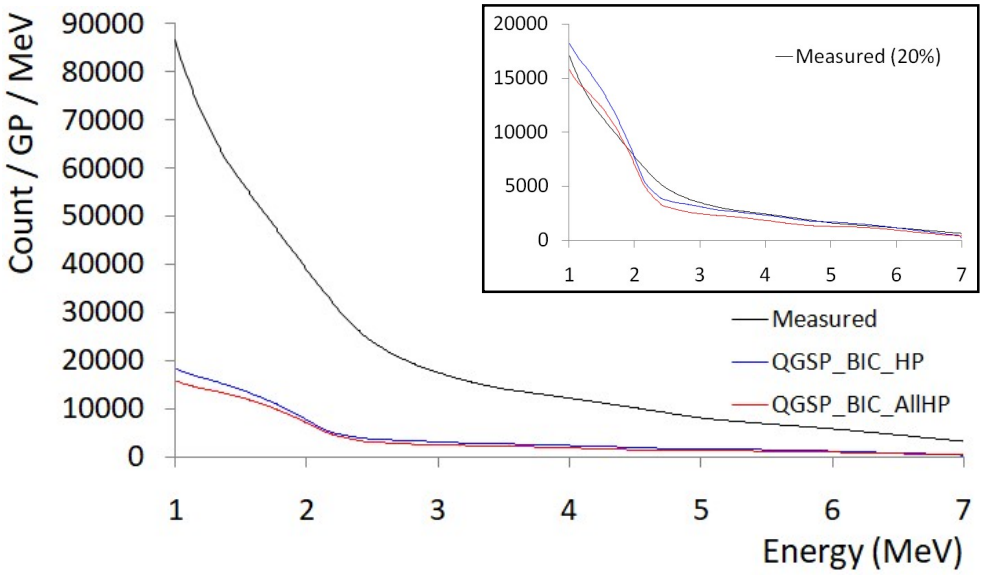

Figure 42: Measured and simulated neutron-induced gamma ray background curves for detector row 1 from the water phantom. The simulated plots were obtained using Geant4 (10.06.p01) physics lists *QGSP_BIC_HP* and *QGSP_BIC_AllHP*. The insert shows the measured plot at 20%, to identify a possible correlation in the trend with the simulated plots.

Table 14 presents the quantitative data of the total gamma, proton- and neutron-induced gamma counts, comparing simulated with measured values. The total proton-induced gamma count obtained from the simulation showed good agreement with the measured value; within a factor of two different. Since rounding of the yields were done only taking into account statistical errors, and there are additional systematic errors on the measurements (due to bias in the background subtraction algorithm, etc) and in the simulation (uncertainties in the yields,

differences among the physics lists, etc), the factor of two different is considered a reasonable result. In contrast to the total proton-induced count, the total neutron-induced gamma count exhibits a greater discrepancy between simulated and measured results, underestimating the measured value within a factor of 10 different. The total gamma count was reproduced by the simulation within a factor of four, with the divergence perhaps due to the discrepancy in the neutron-induced count. Moreover, summing the proton- and neutron-induced gamma counts in Table 14 (also Tables 16 and 18) do not exactly add up to the total gamma counts since, as mentioned, the total neutron-induced gamma ray count does not include prompt neutron counts with discrete energy lines.

Comparing the two Geant4 physics lists quantitatively, *QGSP_BIC_HP* was seen to deliver a better outcome. This may be due to *QGSP_BIC_HP* producing the gamma ray emission lines, whereas *QGSP_BIC_AllHP* does not, as seen in Figure 41. For example, for detector row 1, the simulated total proton-induced count is a factor of ~1.1 different to the measured count, while for *QGSP_BIC_AllHP* is a factor of ~1.4 different.

Table 14: Total gamma, proton- and neutron-induced gamma counts in the energy range of 1.40-7.19 MeV per giga-proton (GP) in the detector rows, obtained with Geant4 (10.06.p01) *QGSP_BIC_HP* and *QGSP_BIC_AllHP* physics lists, from proton beam irradiation of the water phantom. The total neutron-induced count was taken as the background (it does not include prompt counts with discrete energy lines). Rounding of the counts was done only taking into account statistical errors.

Data	Detector row	Total gamma count per GP	Proton-induced gamma count per GP	Neutron-induced gamma count per GP
QGSP_BIC_HP	0	41000	26100	10500
QGSP_BIC_AllHP	0	35300	21900	9700
Measured	0	**113600**	**32000**	**81500**
QGSP_BIC_HP	1	92100	63600	18000
QGSP_BIC_AllHP	1	78400	52200	15300
Measured	1	**162300**	**70600**	**91700**

Table 15 presents the quantitative data of the gamma ray energy spectra peak intensities, comparing simulated with measured values. Binary cascade reproduced the proton-induced 4.44 MeV PG emission line quite well (within a factor of ~1.5 for detector row 0, and ~1.1 for row 1), while significantly underestimating the 6.13 MeV PG peak (factor of ~15 for detector row 0, and ~4 for row 1). The proton-induced counts for *QGSP_BIC_AllHP* are omitted in Table 15, since this physics list does not reproduce the PG emission lines.

Both physics lists reproduce the neutron-induced 2.22 MeV line within a factor of two different to the measured data; NeutronHP data libraries are included in the modules to accurately model neutron interactions from thermal energies up to 20 MeV. As mentioned, experimentally, the measured data were obtained with an empirical background subtraction algorithm, such that changing the background subtraction parameters may result in slight variations in the measured data, and therefore may slightly bias the comparison.

Table 15: Absolute counts per giga-proton (GP) for the proton-induced 4.44 and 6.13 MeV PG peaks, and the neutron-induced 2.22 MeV peak, obtained with Geant4 (10.06.p01) *QGSP_BIC_HP* and *QGSP_BIC_AllHP* physics lists, from proton beam irradiation of the water phantom. The proton-induced counts from *QGSP_BIC_AllHP* are omitted since this physics list does not reproduce those PG emission lines. Rounding of the counts was done only taking into account statistical errors.

Data	Detector row	Proton-induced gamma count per GP		Neutron-induced gamma count per GP
		4.44	**6.13**	**2.22**
QGSP_BIC_HP	0	200	30	1690
QGSP_BIC_AllHP	0	-	-	1650
Measured	0	**300**	**460**	**1380**
QGSP_BIC_HP	1	990	320	4340
QGSP_BIC_AllHP	1	-	-	4170
Measured	1	**1100**	**1160**	**3120**

5.4.2 Evaluating the Reproducibility of Oxygen and Carbon: Water and HDPE

Here, the simulation-measurement data comparison for the HDPE phantom using Geant4 version 10.06.p01 is presented. Water is comprised of hydrogen and oxygen, while HDPE contains hydrogen and carbon, and so the ability for Monte Carlo to reproduce PG emission from oxygen and carbon elements can be investigated.

Figure 43 shows the energy spectra of proton-induced gamma rays in detector row 1 obtained from measurement and simulation. The measured spectra showed the gamma emission lines, particularly the 3.42, 3.93 and 4.44 MeV lines from $^{12}C^*$. The 5.21, 5.62 and 6.13 MeV peaks that arise from oxygen, and were evident in the energy spectrum from the water phantom (Figure 41), do not appear in this spectrum since HDPE is not comprised of oxygen. The simulated spectra obtained with both physics lists showed relatively good agreement to the measured spectrum outside the region of the PG peaks (i.e. ~3-5 MeV), while *QGSP_BIC_HP* significantly underestimates the PG emission lines. In contrast, the 3.42, 3.93 and 4.44 MeV

peaks were reproduced quite well in the water phantom, from which the carbon nuclei were produced from proton reactions with oxygen. This may suggest that simulated gamma emissions from oxygen are more reliable than those from carbon, but for energies below ~5 MeV, since those above ~5 MeV were also underestimated for the case of the water phantom.

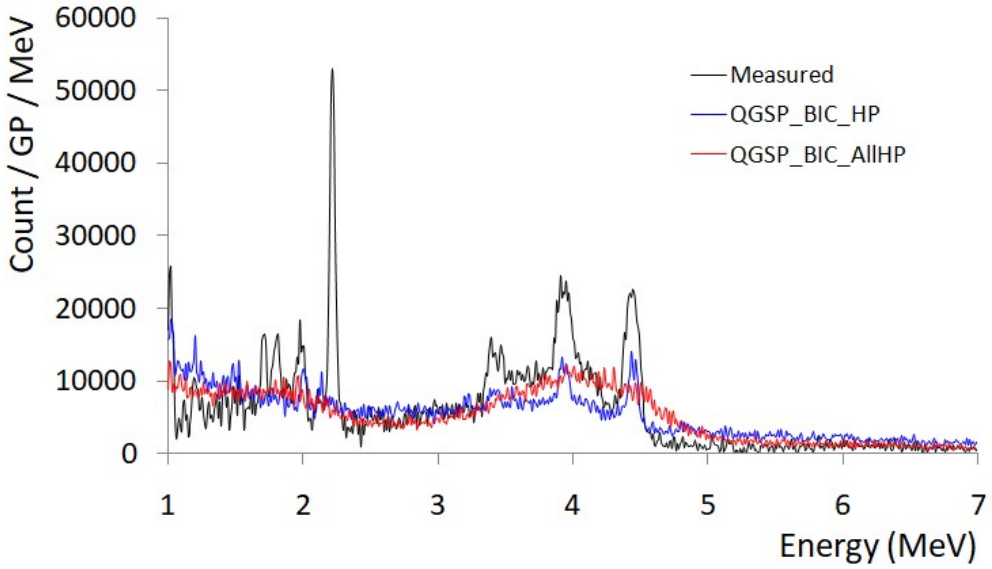

Figure 43: Energy spectra of proton-induced gamma rays in detector row 1 from the HDPE phantom. The measured spectrum is shown with the simulated spectra using Geant4 (10.06.p01) physics lists *QGSP_BIC_HP* and *QGSP_BIC_AllHP*.

Figure 44 shows the measured and simulated neutron-induced gamma ray background curves from the HDPE phantom for detector row 1. The insert in the figure shows the measured data at 20%. Both magnitude and trend of the simulated plots differ significantly to the measured. The simulated Count/GP/MeV around 4.44 MeV (1 MeV window) was a factor of ~8 lower than the measured count with both physics lists, while around 6.13 MeV (1 MeV window) the simulated count was a factor of ~9 and ~13 lower than the measured with *QGSP_BIC_HP* and *QGSP_BIC_AllHP*, respectively. The largest differences in the trend of the curves were seen below ~3 MeV and around 5 MeV.

Tables 16 and 17 present the quantitative data of the total counts, and the gamma ray energy spectra peak intensities, comparing simulated with measured values. Similar to the data from the water phantom, the simulated total gamma count was seen to be within a factor of four different to the measured count, the total proton-induced count was within a factor of two different, and the total neutron-induced count within a factor of 10 different. The proton-induced 4.44 MeV PG line obtained with *QGSP_BIC_HP* was within a factor of ~4.5 different to the measured count, which is a larger discrepancy than that for the water phantom (factor of ~1.5 different). As for the water phantom, the 2.22 MeV neutron-induced counts were seen to

be within a factor of two different. Again, the proton-induced counts for *QGSP_BIC_AllHP* are omitted in Table 17.

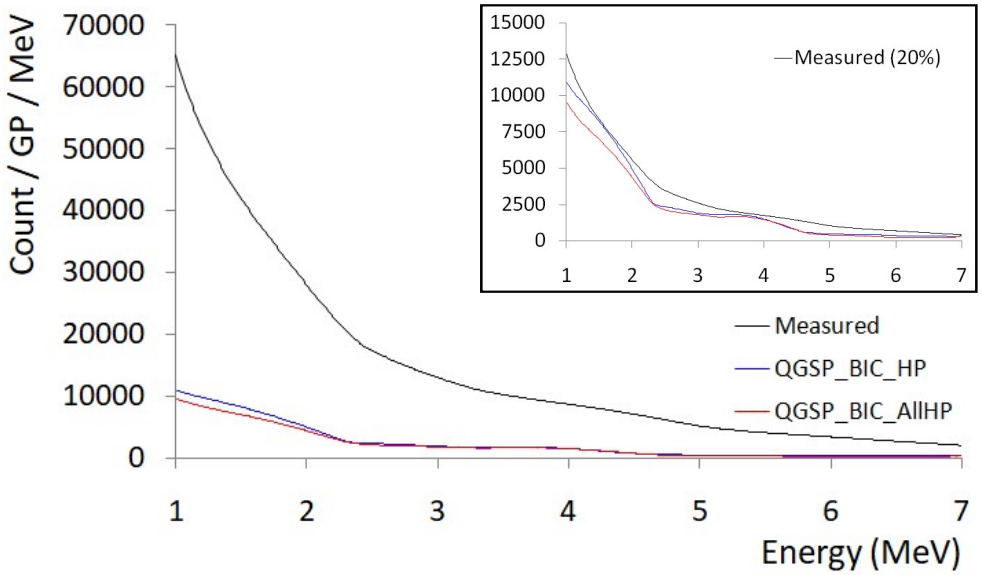

Figure 44: Measured and simulated neutron-induced gamma ray background curves for detector row 1 from the HDPE phantom. The simulated plots were obtained using Geant4 (10.06.p01) physics lists *QGSP_BIC_HP* and *QGSP_BIC_AllHP*. The insert shows the measured plot at 20%, to identify a possible correlation in the trend with the simulated plots.

Table 16: Total gamma, proton- and neutron-induced gamma counts in the energy range of 1.40-7.19 MeV per giga-proton (GP) in the detector rows, obtained with Geant4 (10.06.p01) *QGSP_BIC_HP* and *QGSP_BIC_AllHP* physics lists, from proton beam irradiation of the HDPE phantom. The total neutron-induced count was taken as the background (it does not include prompt counts with discrete energy lines). Rounding of the counts was done only taking into account statistical errors.

Data	Detector row	Total gamma count per GP	Proton-induced gamma count per GP	Neutron-induced gamma count per GP
QGSP_BIC_HP	0	24800	15100	6800
QGSP_BIC_AllHP	0	21500	12900	6600
Measured	0	**74700**	**13500**	**61200**
QGSP_BIC_HP	1	43600	28200	10100
QGSP_BIC_AllHP	1	41300	27500	9000
Measured	1	**97800**	**33200**	**64700**

Table 17: Absolute counts per giga-proton (GP) for the proton-induced 4.44 and 6.13 MeV PG peaks, and the neutron-induced 2.22 MeV peak, obtained with Geant4 (10.06.p01) *QGSP_BIC_HP* and *QGSP_BIC_AllHP* physics lists, from proton beam irradiation of the HDPE phantom. The proton-induced counts from *QGSP_BIC_AllHP* are omitted since this physics list does not reproduce those PG emission lines. Rounding of the counts was done only taking into account statistical errors.

Data	Detector row	Proton-induced gamma count per GP	Neutron-induced gamma count per GP
		4.44	**2.22**
QGSP_BIC_HP	0	140	820
QGSP_BIC_AllHP	0	-	590
Measured	0	**610**	**880**
QGSP_BIC_HP	1	670	1950
QGSP_BIC_AllHP	1	-	1650
Measured	1	**2130**	**2270**

5.4.3 Comparison of Geant4 Versions: 10.05.p01 and 10.06.p01

In a study to determine the variation of outcomes from two different versions of Geant4, simulations were performed with the *QGSP_BIC_HP* physics list and with the water phantom. Figure 45 shows the proton-induced gamma ray energy spectra from Geant4 10.05.p01 and 10.06.p01 with *QGSP_BIC_HP* physics list, along with the measured spectrum for comparison. In the lower energy region of the spectrum (below ~3.3 MeV), version 10.05.p01 was seen to better reproduce the measured data, where 10.06.p01 slightly overestimates. Both Geant4 versions reproduced the 3.93 and 4.44 MeV emission lines well, but significantly underestimate the higher energy PG lines (above ~4.5 MeV).

Tables 18 and 19 present the quantitative data of the total counts, and the gamma ray energy spectra peak intensities, comparing simulated with measured values. The Geant4 version 10.05.p01 reproduced the measured total gamma count within a factor of ~3.3, whereas 10.06.p01 reproduced the count within a factor of ~2.8. The total proton-induced count was reproduced better with 10.06.p01 than 10.05.p01, such that differences to the measured count were within a factor of ~1.2 and ~1.6, respectively. Both versions of Geant4 resulted in significant, within a factor of 10, underestimation of the total neutron-induced count. The proton-induced 4.44 MeV PG line was reproduced quite well by both versions, within a factor of ~1.3 with 10.05.p01 and ~1.5 with 10.06.p01, while the 6.13 MeV PG line was significantly underestimated. Again, the neutron-induced 2.22 MeV gamma line was within a factor of two different to the measured count.

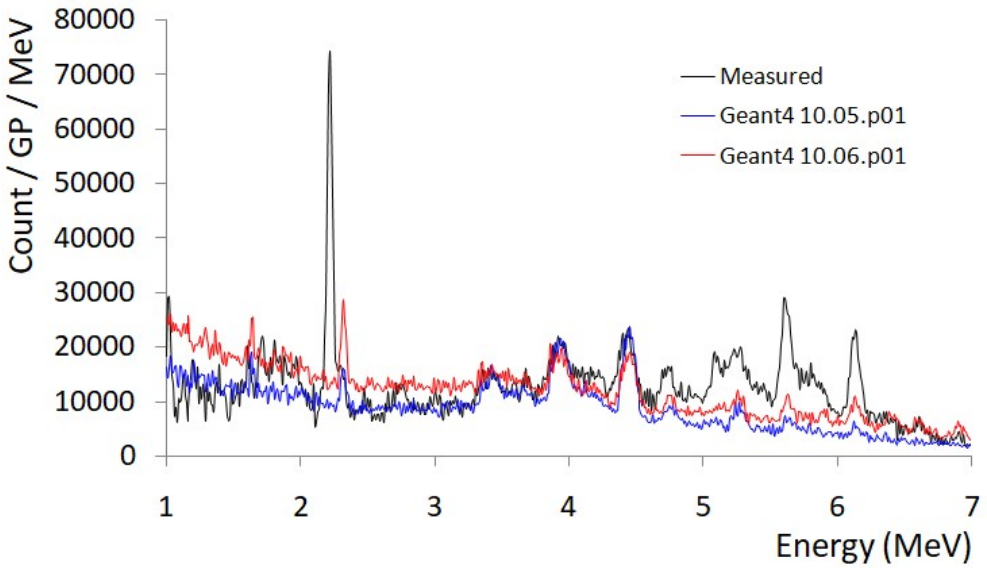

Figure 45: Energy spectra of proton-induced gamma rays in detector row 1 from the water phantom, using Geant4 versions 10.06.p01 and 10.05.p01 with the *QGSP_BIC_HP* physics list. The measured spectrum is also included for comparison.

Table 18: Total gamma, proton- and neutron-induced gamma counts in the energy range of 1.40-7.19 MeV per giga-proton (GP) in the detector rows, obtained with Geant4 (10.05.p01) *QGSP_BIC_HP* physics list, from proton beam irradiation of the water phantom. The total neutron-induced count was taken as the background (it does not include prompt counts with discrete energy lines). Rounding of the counts was done only taking into account statistical errors. Data from version 10.06.p01 (Table 14) are also added for comparison.

Data	Detector row	Total gamma count per GP	Proton-induced gamma count per GP	Neutron-induced gamma count per GP
10.05.p01	0	34000	20600	9500
10.06.p01	0	41000	26100	10500
Measured	0	**113600**	**32000**	**81500**
10.05.p01	1	73100	47200	16000
10.06.p01	1	92100	63600	18000
Measured	1	**162300**	**70600**	**91700**

Table 19: Absolute counts per giga-proton (GP) for the proton-induced 4.44 and 6.13 MeV PG peaks, and the neutron-induced 2.22 MeV peak, obtained with Geant4 (10.05.p01) *QGSP_BIC_HP* physics list, from proton beam irradiation of the water phantom. Rounding of the counts was done only taking into account statistical errors. Data from version 10.06.p01 (Table 15) are also added for comparison.

Data	Detector row	Proton-induced gamma count per GP		Neutron-induced gamma count per GP
		4.44	6.13	2.22
10.05.p01	0	270	10	1560
10.06.p01	0	200	30	1690
Measured	0	**300**	**460**	**1380**
10.05.p01	1	1390	120	4090
10.06.p01	1	990	320	4340
Measured	1	**1100**	**1160**	**3120**

5.5 Discussion

In this study, TOPAS was used to model the MGH PGS detection system, proton beam and phantom. Simulated and measured data were quantitatively compared in terms of the intensity of selected gamma emission peaks to determine the performance of Monte Carlo codes for PG ray simulations. ParticleHP showed an overall better base shape agreement with the measured proton-induced gamma ray spectrum across the energy range of interest (1-7 MeV), but it does not reproduce the PG emission lines. Binary cascade, although underestimated the PG emission lines above ~5 MeV, reproduced the 4.44 MeV PG line within a factor of ~1.1 (for detector row 1, from the water phantom). *QGSP_BIC_AllHP* is an experimental physics list which requires further work and validations, unlike *QGSP_BIC_HP* which has been developed and validated extensively. Some reactions are not fully described in ParticleHP due to limited evaluated data and implementation of the model is incomplete [250]. With further developments and improvements, ParticleHP could potentially be a suitable choice for simulating PG rays and associated detection systems. In the meantime, Binary cascade is a suitable choice, as it reproduces the gamma emission intensities around 4 MeV well, but for higher energy emissions the models need further improvement.

The simulated gamma ray energy spectra also showed characteristic differences between the water and HDPE phantoms. Data from the water phantom showed a better quantitative correlation, particularly in terms of the proton-induced PG emission line intensities. For example, the 4.44 MeV PG line obtained with *QGSP_BIC_HP* was within a factor of ~1.5

different to the measured count for the water phantom, and factor of ~4.5 different for the HDPE phantom. The 3.42, 3.93 and 4.44 MeV gamma ray peaks from $^{12}C^*$ were present in the spectra from both phantoms and reproduced better for the water phantom (see Figure 41) than the HDPE phantom (see Figure 43). This may suggest that gamma emissions from oxygen are more reliably reproduced than those from carbon. With further improvements to the models to achieve superior reproducibility of simulated to measured data, the composition of irradiated tissue could be predicted prior to measurement by means of PG spectroscopy.

Additionally, Geant4 versions 10.05.p01 and 10.06.p01 were compared for the case of the water phantom to observe the differences between various versions of the Monte Carlo toolkit. The main variation between the two versions was seen at energies below ~3.3 MeV and above ~4.5 MeV, while the simulated intensities of PG rays around 4 MeV were in good agreement with the measurement. That is, the 4.44 MeV PG line agreed with the measured data within a factor of ~1.3 with version 10.05.p01 and ~1.5 with 10.06.p01. These variations may be due to differences in the nuclear reaction data of the particular version, such that the parameters of models used to calculate the nuclear cross sections are generally tuned for different releases of Geant4.

High precision (HP) physics modules accurately model neutron interactions from thermal energies up to around 20 MeV. In this study, the simulation was seen to overestimate the 2.22 MeV neutron capture gamma ray peak from proton irradiation of the water phantom, within a factor of two different to the measured value, but significantly underestimate (within a factor of 10) the total neutron-induced gamma count. Generally, the number of neutrons captured in the target will be dependent on the energy distribution of created neutrons produced by the model, as well as the angular distribution and scattering accuracy of the models. The neutron-induced gamma count then depends on the accuracy of the PG distributions when the nucleus de-excites. Another factor to consider in modelling PG detection systems is the contribution of neutrons in an unwanted background gamma signal. In particle therapy, there are several sources of neutron production and scatter: components of the gantry, collimator, phantom, patient table, floor and walls, etc.

A simulation was performed testing the theory that the absence of the treatment room walls may play a role in the discrepancies seen for neutron-induced counts between simulated and measured data. The MGH treatment room walls [254] were modelled as concrete, taken as the NIST composition, density of 2.3 g/cm^3, as also used in Ref. [255]. The simulation retrieved the neutron-induced counts from the water phantom, with Geant4 version 10.06.p01 and *QGSP_BIC_HP* physics list. The data were compared to the case in which the treatment room walls were not modelled (Tables 14-15), and it was found that the data differed within 3% only.

This suggests that perhaps the treatment room walls have a minor impact on the background signal arising from neutrons, whereas a greater impact may be present from other sources of neutrons/scatter that are in closer proximity to the detection system, particularly the beam delivery nozzle, collimator and phantom. Hence, future PG simulations may benefit from taking into account these close-distance sources of neutrons and neutron scatter, to more accurately determine the influence on the PG signal.

It should also be noted that the results shown in this study only apply to the TOPAS and Geant4 versions studied. That is, depending on which version of Geant4 is used, the results can vary significantly, particularly for nuclear reaction data, as this is a domain of on-going improvement in Geant4. As well, rounding of the yields was done only taking into account statistical errors. Yet there are additional systematic errors on the experimental measurements (due to bias in the background subtraction algorithm, etc) and in the simulations (uncertainties in the yields, differences among the physics lists, etc).

The MGH PGS prototype detection system has demonstrated that hybrid PG detection from simultaneous energy- and time-resolved spectral measurements can provide superior beam range verification in realistic clinical conditions [59]. The remaining challenges are to explore clinical integration with treatment systems and practices.

In practice, Monte Carlo simulations could be used to generate PG distributions for real patient data obtained from CT scans of the patient, such that the PG data would be integrated into the TPS. The detection system would also be modelled, including the geometry and composition of the scintillators, collimators (if employed), etc, to predict the PG ray detection. Deviations from the prescribed treatment plan could then be determined by comparing the measured PG data with pre-calculated ones. Yet, this implies that the Monte Carlo codes providing the reference are indeed accurate. Although the PG energy lines are modelled well, the yields require further improvements. As seen in this study, simulated PG emission peak intensities as well as the background neutron contributions varied significantly from the measured data. Hence, the nuclear models and cross section data need improvement, with experimental data and extensive validations. Modelling the full treatment room could offer a better indication of the background contributions, but this may lead to long compute times. Accelerated Monte Carlo simulations are beneficial for the high patient throughput and real-time monitoring. Overcoming these limitations could see Monte Carlo codes advancing PG ray beam monitoring in clinical applications, by having a solid reference for comparing the measured data, and fast data analysis for real-time treatment delivery verification.

Conclusion

The research effort of this thesis was focused on PG detection methodology and technology from *in vivo* range verification towards non-invasive *in vivo* dosimetry for high-precision charged particle therapy. The ultimate goal is to pave an effective pathway in the development of clinically applicable and reliable PG detectors and procedures, which can further improve cancer treatment precision and release the full clinical efficacy of particle therapy. Three major aspects were investigated in this work: (i) systematic simulation studies of PG emission and detection characteristics in energy, space and time dimensions (Chapter 3). This has led to a proposal for hybrid PG detection to utilise multi-features of PG characteristics for enhanced beam range extraction. (ii) Characterisation of commercially available advanced scintillation crystals to explore suitable high-performance detectors for energy- and time-resolved PG ray measurements towards potential hybrid PG detection systems (Chapter 4). (iii) Evaluation of the performance of Geant4-based Monte Carlo simulation predictions with the experimental data from MGH's PGS system (Chapter 5). This was the first comprehensive evaluation study regarding the PG signal along with interference backgrounds in a realistic clinical condition. This work provides valuable information on Geant4 physics capability to investigate PG detection systems and predict outcomes for comparison to measured data to determine deviations from the prescribed treatment plan.

The PG emission characteristics from water, PMMA and adipose tissue targets, in either sphere or cylinder phantoms irradiated with three different particle types (proton, ^{4}He and ^{12}C) of varying beam energies, have been investigated using Geant4 simulations and presented in Chapter 3 of this thesis. The PG production yield, energy spectral characteristics and spatial correlation with the BP have been quantified [217,231]. The results of this work showed that the PG signal is a reliable means for *in vivo* BP tracking in particle therapy, particularly the primary PG rays generated from the incident particles. In this case, the closest correlation between the PG emission yield and particle beam range was found. The characteristic energy and spatial PG emission results for proton and carbon ion beams agreed with prior published results [57,140,150]. However, the concurrent secondary PG rays may impose a greater challenge for BP tracking in heavy-ion therapy, such as carbon ions, where secondary PG rays become dominant. The effects of target inhomogeneities were seen on the PG production distribution in relation to the beam crossing the various materials of the phantom, but the quantitative data shows that the PG-BP fall-off correlation is consistent for heterogeneous targets as well as homogeneous ones.

The detectable PG characteristics have been investigated by virtue of an air-filled idealised detecting sphere encompassing the phantoms. The spatial and temporal properties regarding PG propagation to the detecting sphere have been characterised with changing beam ranges. Several important points were found in this study:

(i) Energy- and time-resolved PG detections would be essential for high-precision BP tracking. The PG time properties can be utilised not only for interference background rejection but also for beam range extraction. The PG TOF encodes the essential information of the beam range but needs high time resolution measurements to retrieve it.

(ii) A non-isotropic longitudinal distribution of the detected PG rays was observed and showed a changing angular propagation distribution with beam energy. This may suggest that a movable PG detector coordinated with respect to the beam range could serve to optimise the detection efficiency of PG rays.

(iii) The geometric size and shape of phantoms also exhibit a considerable effect on the angular distribution. This indicates that the attenuation, absorption and scatter of PG rays inside the phantom are factors which should be taken into account in the development of quantitative *in vivo* range and dosimetry verifications.

(iv) Hybrid PG detection systems, to utilise the energy, timing and spatial characteristics of PG rays, is highly desirable for BP tracking in real-time.

This work has provided a solid basis for further PG system design.

The energy- and time-resolved spectroscopy capabilities of several scintillation detectors were also characterised in this work to determine a suitable choice for high-throughput and highly efficient hybrid PG ray systems. Presented in Chapter 4 of this thesis, $LaBr_3$(Ce), $LaCl_3$(Ce), NaI(Tl), $CeBr_3$, SrI_2(Eu), CLYC and CLLBC scintillators were studied in terms of rise/decay times, energy resolution and intrinsic peak detection efficiency. $LaBr_3$(Ce) and $LaCl_3$(Ce) scintillators were coupled to a PMT, whereas the others were coupled to a SiPM, while $LaBr_3$(Ce) and $LaCl_3$(Ce) were also studied with and without a built-in charge sensitive preamplifier. Comparable traits were seen when using a PMT or SiPM, and the inclusion or absence of a preamplifier. Although the preamplifier is generally best suited for spectroscopy applications and to improve the system energy resolution, this study showed that its inclusion worsens the timing properties. Yet it is crucial that, for hybrid PG detection systems, both energy and timing capabilities are optimised without a trade-off between the two features. The results in this work could therefore offer beneficial information for the development of hybrid PG detection systems.

The results showed that $LaBr_3$(Ce), without a built-in charge sensitive preamplifier, is an excellent choice for PG measurements due to its superior timing (34 ns rise time and 790 ns decay time) and energy resolution (3.5% at 662 keV). Other studies have also shown the potential of $LaBr_3$(Ce), which has been utilised in several PG beam range verification studies [173,232], including the PGS measurements performed at MGH [59,170]. Furthermore, elpasolite crystals such as CLYC and CLLBC have not yet been studied for the purpose of range monitoring in particle therapy using PG rays. They have the added ability of gamma-neutron discrimination, and therefore have the potential for hybrid systems utilising PG energy and time information in addition to simultaneous neutron discrimination. CLLBC detectors of various sizes were also studied, and it was seen that those of smaller crystal size produced a faster signal compared to those with larger crystal. Among those studied, CLYC was also seen to offer a good energy resolution of 3.4% at 662 keV.

A comparison study between simulated and measured gamma emission peak intensities was carried out to determine the performance of Monte Carlo codes for PG ray simulations in research and clinical applications. This study is presented in Chapter 5 of this thesis. TOPAS was used to model the MGH PGS detection system, proton beam and phantom. Two Geant4 physics lists, *QGSP_BIC_HP* and *QGSP_BIC_AllHP*, were investigated with Geant4 version 10.06.p01. Two phantom materials, water and HDPE, were also explored to determine the simulation reproducibility for oxygen and carbon elements, respectively. The simulations were repeated for Geant4 version 10.05.p01 for regression testing purposes. The total gamma, proton- and neutron-induced counts, as well as PG emission lines 4.44 and 6.13 MeV, were analysed and quantitatively compared for a specific proton pencil beam spot.

Several important points are highlighted from this study:

(i) The *QGSP_BIC_HP* physics list underestimates the higher energy (above ~5 MeV) PG emission lines, whereas *QGSP_BIC_AllHP* showed an overall better base shape agreement across the energy spectrum but does not reproduce the PG emission peaks. Therefore, this work showed that *QGSP_BIC_HP* is currently more suitable, as it reproduces the gamma emission intensities around 4 MeV quite well, e.g. the 4.44 MeV PG line agreed with the measured count within a factor of two for the case of the water phantom, but for higher energy emissions the models need further improvement.

(ii) Data from the water phantom showed a better quantitative correlation, particularly in terms of the proton-induced PG emission line intensities. This may suggest that simulated gamma emissions from oxygen are more reliably reproduced than those from carbon. Also, simulated gamma ray energy spectra

showed characteristic differences between water and HDPE; with further improvements to the models, the composition of irradiated tissue could be predicted and determined by means of PG spectroscopy.

(iii) The simulation overestimated the 2.22 MeV neutron capture peak in the gamma energy spectra from the water phantom within a factor of two compared with the measured data, but significantly underestimated (within a factor of 10) the total neutron-induced gamma count. This may be due to various factors, including sources of neutrons and unwanted background signal. Yet a difference of only 3% in the neutron-induced counts was seen when comparing simulated data with and without modelling the MGH treatment room walls. This suggests that future PG ray simulations may benefit from taking into account potential neutron sources in closer proximity to the measuring device, to more accurately predict the PG signal.

(iv) The comparison of the simulation results obtained with Geant4 versions 10.05.p01 and 10.06.p01 showed differences at energies below ~3.3 MeV and above ~4.5 MeV, while the simulated intensities of PG rays around 4 MeV were in good agreement with the measurement. That is, the 4.44 MeV PG line agreed with the measured data within a factor of ~1.3 with version 10.05.p01 and ~1.5 with 10.06.p01. Thus, simulation results can greatly depend on the Geant4 version utilised and it is therefore recommended to perform regression testing on some physical observables among different versions of Geant4, including the latest one.

The novelty of this project is such that it combines several areas of research to improve the PG detection methodology, detector technology and simulation resources for non-invasive real-time beam range monitoring in particle therapy. The characteristic properties of PG emission and detection have been investigated for not only proton and carbon beam irradiation, but also helium ions for which the PG distributions have not yet been widely studied. The results showed that there is the opportunity to optimise the strategy for PG detection and improve image formation with optimal energy, angular and TOF windows. Hence, combining space, energy and time methods could be utilised to improve the PG signal for range/dose monitoring. As well, several scintillators were characterised in terms of energy and timing properties for potential hybrid PG systems. To the authors' knowledge, elpasolite scintillation crystals have not yet been studied for the purpose of PG range monitoring in particle therapy, and therefore the results obtained here could also be beneficial to other groups. Moreover, a quantitative comparison study of Monte Carlo simulation data with experimental measurements conducted in a particle therapy facility was performed. Binary cascade was seen to reproduce

the measured data well, but the models need further improvement, particularly if PG spectroscopy is to be utilised for determining target material compositions, and in turn, exploited for *in vivo* dosimetry.

The PGS prototype detection system developed at MGH demonstrates the possibility of hybrid PG detection from simultaneous energy- and time-resolved spectral measurements with clinical proton beams, but challenges remain for its integration with clinical treatment systems and practices. As well, utilising both energy and time characteristics for the purpose of range verification, in addition to neutron background rejection, is worth further exploration. Superior detectors and data acquisition offering excellent energy and time resolutions simultaneously are desired, as well as the ability to cope with the beam time structure and accurately synchronise with the accelerator RF. Reliable Monte Carlo codes are also important, as they would provide the reference for which the measured data would be compared. The PG data and detection system would be incorporated into the TPS to obtain the predicted outcomes, with accelerated simulations beneficial for the high patient throughput and real-time monitoring. Yet the nuclear models and cross section data require further improvement, with experimental data and extensive validations.

Hence, this thesis work will aid in developing optimal PG detection strategies and support the implementation of clinically feasible PG systems for improving cancer treatment QA. Further studies investigating the scintillator performance for high-energy PG rays through measurements, and in clinical conditions, will be valuable for the development of high-resolution and high-performance novel detector systems with fast electronics and high-throughput processing. Future work will focus on the acquisition system and implementation of a hybrid PG detection system that utilises the energy- and time-resolved information, which is desirable and has strong potential for *in vivo* dosimetry during particle therapy.

Appendix 1 – Previous Publication

In Chapter 3, I referred to my previous publication, Zarifi et al. (2017) [231], which I include here for reference.

Physica Medica 33 (2017) 197–206

Contents lists available at ScienceDirect

Physica Medica

journal homepage: http://www.physicamedica.com

Original paper

Characterization of prompt gamma-ray emission with respect to the Bragg peak for proton beam range verification: A Monte Carlo study

Melek Zarifi [a], Susanna Guatelli [a], David Bolst [a], Brian Hutton [b], Anatoly Rosenfeld [a], Yujin Qi [a,*]

[a] Centre for Medical Radiation Physics, University of Wollongong, NSW, Australia
[b] Institute of Nuclear Medicine, University College London, London, UK

ARTICLE INFO

Article history:
Received 25 July 2016
Received in Revised form 6 October 2016
Accepted 11 December 2016
Available online 24 December 2016

Keywords:
Prompt gamma
Bragg peak
Proton therapy
Geant4

ABSTRACT

In this paper we report a Geant4 simulation study to investigate the characteristic prompt gamma (PG) emission in a water phantom for real-time monitoring of the Bragg peak (BP) during proton beam irradiation. The PG production, emission spatial correlation with the BP, and position preference for detection with respect to the BP have been quantified in different PG energy windows as a function of proton pencil-beam energy from 100 to 200 MeV. The PG response to small BP shifts was evaluated using a 2 cm-thick slab with different human body materials embedded in a water phantom. Our results show that the prominent characteristic PG emissions of 4.44, 5.21 and 6.13 MeV exhibit distinctive correlation with the dose deposition curve. The accuracy in BP position identification using these characteristic PG rays is highly consistent as the beam energy increases from 100 to 200 MeV. There exists a position preference for PG detection with respect to the BP position, which has a strong dependence on the proton beam energy and PG energies. It was also observed that a submillimeter shift of the BP position can be realized by using PG signals. These results indicate that the characteristic PG signal is sensitive and reliable for BP tracking. Although the maximization of the PG measurement associated with the BP is difficult, it can be optimized with energy and detection position preferences.

1. Introduction

The main advantage of proton therapy (PT), as compared to photon radiation therapy, is the finite beam range and localized energy deposition at the Bragg peak (BP) [1]. This provides a unique benefit for cancer radiotherapy, due to highly localized dose deposition to the tumor volume, while sparing critical organs-at-risk and minimizing dose to the normal tissue. However, the advantage of PT has not yet been fully exploited since there exists significant uncertainty [2] in predicting and determining the end-of-range of the beam in the patient during treatment planning and treatment delivery. The beam-range uncertainty could cause the BP to overshoot or undershoot the tumor and damage adjacent healthy tissue. Significant research efforts have been made in the development of clinically suitable and reliable *in vivo* beam-range verification techniques to ensure PT treatment quality [3].

Current research and development of *in vivo* beam-range verification techniques have mainly focused on the use of secondary prompt and delayed gamma rays that are produced by inelastic proton-nuclear interactions inside the patient [4]. Positron emission tomography (PET) has been adopted in clinical research of PT for post-treatment quality control [5]. It relies on the detection of 511 keV coincident photon pairs from the decay of positron emitting nuclei produced as a result of proton-nuclear interactions [6,7]. The delayed decay via positron emission of the short-lived radioisotopes on the order of 1–15 min has several major limitations, such as the inability to offer real-time monitoring, a relatively low yield, the positron range effect and biological washout effect, which affect the quantitative accuracy for beam-range verification. Prompt gamma (PG) rays are emitted almost instantaneously from the decay of the excited nuclear reaction products, which has the major advantage of enabling real-time tracking of the BP during beam delivery with no washout effect [8].

Spectroscopy studies [9] have revealed that proton-induced PG emission exhibits a broad energy spectrum in a wide range of 2–15 MeV and is dominated by a number of characteristic gamma-lines from specific elements of irradiated tissues. These PG rays provide rich information which is not only benefiting for *in vivo* beam-range tracking but also could be utilized to determine the concentration of specific elements such as oxygen within irradiated tumors and healthy tissue over the course of PT treatments [10].

* Corresponding author.
E-mail address: yujin@uow.edu.au (Y. Qi).

http://dx.doi.org/10.1016/j.ejmp.2016.12.011
1120-1797/

Significant research and development has been made to determine the feasibility of PG imaging for proton beam-range verification. A number of PG measurements of proton pencil beams have been reported, using a single detector [9,11,12], as well as a slit gamma camera [13–15] to detect PG signals integrated over a wide energy window between 3 and 6 MeV. Other detectors, such as multi-slit detectors [16] and Compton gamma cameras [17,18] have been proposed, and prototype systems are under development by several groups. Time-of-flight measurements have been identified as an effective way to reduce the interference background induced by neutrons [19].

Although initial studies [11,12] have found a good correlation between the BP position and the PG emission, their correlation relationship has complicated characteristics because they result from different physical processes. There is no exact one-to-one relationship existing between the PG emission and the dose deposition. The energy and intensity of the PG emission are sensitive to the elemental composition of tissues [9,10]. As pointed out in [20] there are many factors influencing the accuracy of beam range estimation using PG emission. Quantitative characterization of the correlation between these factors, particularly with respect to the BP, is of great importance to assess its limitation and aids in the design of a clinically reliable PG imaging system. A recent study from Verburg et al. [21] shows that identifying discrete PG lines could provide several benefits to improve the accuracy and efficiency of beam-range verification. Quantitative measurements of the characteristic PG rays can be used for precise proton range verification in the presence of tissue with an unknown composition [22].

In this work we focus on several characteristic PG emission lines generated from proton beam irradiation of a water phantom and quantitatively characterize their production and spatial emission correlation with the BP position as a function of proton beam energy. We further evaluate the feasibility of using PG emission lines to track the BP position shifts in a heterogeneous phantom containing slabs of difference body composition materials. This study will provide valuable information for the design and development of a clinically reliable PG imaging system to optimize the PG measurement for real-time BP tracking.

2. Methods

The Geant4 Monte Carlo Toolkit [23,24] (version 10.00) was used to investigate the correlation between the proton beam range and the production of PG rays from proton pencil beams incident on a homogeneous water phantom (density of 1 g/cm^3). The global simulation set-up is shown in Fig. 1. A mono-energetic proton pencil beam was used to irradiate the cylindrical water phantom with diameter 30 cm and height 50 cm along its central axis (along the z-axis). The energy deposition was calculated in the phantom along the direction of incidence of the protons so to obtain proton depth-dose curves. Proton beam energies of 100, 120, 140, 160, 180 and 200 MeV were simulated. This energy range was selected as it is typical of a PT treatment. The results can then be extrapolated for Spread-Out Bragg Peaks (SOBP) which originates from the superposition of monochromatic proton beams of different energies in scanning PT. An ideal detecting cylinder surface (called *detection cylinder*), with 100 cm diameter and 50 cm height, coaxially surrounding the phantom, was used to score the secondary gamma rays. The detection cylinder was modelled with its longitudinal axis in coincidence with that of the phantom.

The Geant4 physics list used in this simulation included both electromagnetic (Livermore Low Energy Package) and hadronic physics (QGSP_BIC_HP for protons, neutrons and pions, Binary Ion Cascade model for ions). The Radioactive decay module of Geant4 was active. The QGSP_BIC_HP was chosen as it includes the Binary cascade model which was found adequate for PT studies in [25].

The High Precision Neutron Data Libraries were used to model neutron interactions up to 20 MeV. The output of the simulation consisted of the emission yield Y of the secondary photons along the depth in the phantom. In particular, Y was calculated retrieving the energy and position of the photons when they originate in the phantom. Y was normalized to the number of incident protons on the phantom.

In the post-simulation data analysis, the proton beam range R was defined as the point with 50% BP distal fall-off along the beam path in the phantom. The range extracted from the PG emission (R_{PG}) was defined as the position with 50% PG yield fall-off in the phantom. The difference R-R_{PG}, denoted as Δ*fall-off*, was used to quantify the correlation between PG ray emission and the BP. The energy spectrum of all photons generated in the water phantom, via any physical interaction process was examined. From this spectrum, the prominent PG emission lines were selected with energy windows to study their yield and spatial correlation with respect to the BP.

The position of the gamma rays along the longitudinal axis when reaching the detection cylinder was retrieved from the

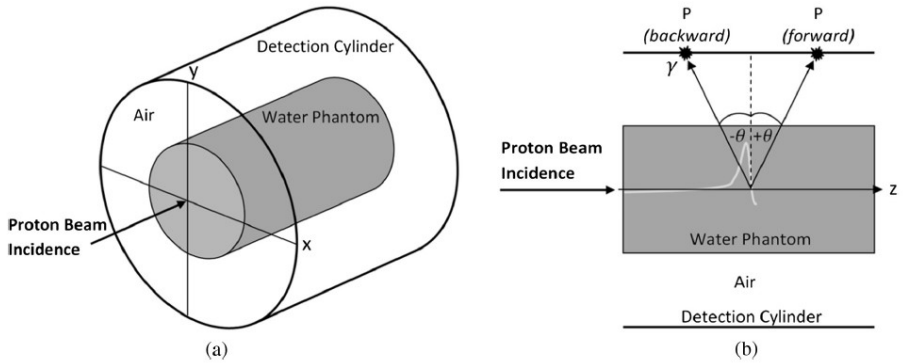

Figure 1. (a) The geometrical simulation setup of the cylindrical water phantom, in an air-filled detection cylinder coaxially surrounding the phantom. (b) Lateral view of the simulation setup. The angle θ is formed between P, the most probable point on the detector cylinder traversed by the photons, and the normal to the main axis of the phantom passing by the proton beam range R, defined as the point of 50% BP fall-off.

simulation as well. The distribution of the positions was then fitted and the most frequent position P was determined. P was then used to determine the polar angle θ formed between P and the normal to the main axis of the water phantom, passing through the proton beam range R (see Fig. 1(b)). θ allows one to calculate an eventual preferential position, defined with respect to the BP position, to locate the detector to maximize the number of detected PG rays. Positive and negative θ angles mean that the preferential detection position is forward (in the beam direction) and backward (opposite the beam direction) of the BP position, respectively. The results of the simulation are symmetric with respect to the azimuthal coordinate φ as expected.

To study the sensitivity of the PG signal with respect to BP shifts, 2 cm-thick cylindrical slabs of different human body composition materials were inserted in the water phantom upstream of the expected BP. A 200 MeV proton pencil beam was used in this study so as to ensure that the beam passed completely through all the slabs. The materials under study were tissue, muscle, bone and lung. These materials were defined in the simulation from the Geant4 NIST database: tissue ("Adipose Tissue ICRP", density of 0.92 g/cm^3), muscle ("Muscle Striated ICRU", density of 1.04 g/cm^3), bone ("Bone Compact ICRU", density of 1.85 g/cm^3), and lung ("Lung ICRP", density changed to 0.26 g/cm^3 to resemble a lung at end-inhalation). Two scenarios were considered: (1) one slab of each material in the water phantom; and (2) all four materials were stacked back-to-back in the water phantom to study the combined heterogeneity effect. Fig. 2 shows the simulation setup of the two scenarios considered for studying the PG emission deriving from heterogeneous phantoms. A total number of 10^7 incident proton events were simulated for each proton energy and simulation set-up under study to provide suitable statistics.

3. Results

3.1. Energy spectra and yield of prompt gamma emission in the water phantom

Fig. 3 shows the energy spectra of photons that originate in the water phantom from any physical interactions (including neutron-induced gamma photons), for three proton beam energies under study. The spectra show consistent shape and characteristics over a wide beam energy range. The energy spectra show several distinguishable emission lines that are produced by non-elastic proton-nuclei interactions with major constituent elements of the phantom material. A peak can be observed in the spectra at

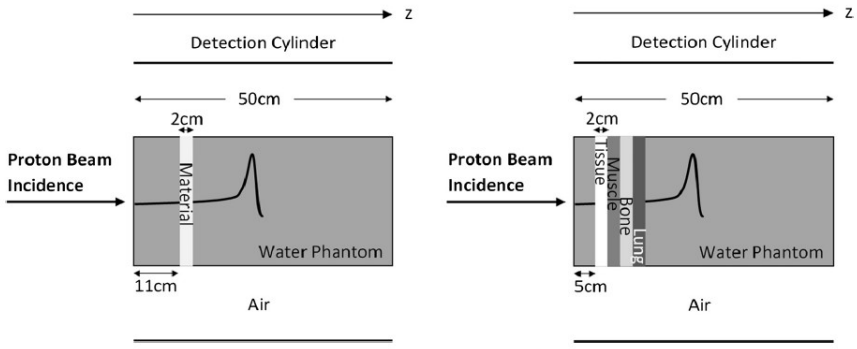

Figure 2. Geometrical simulation setup of the water phantom with 2 cm slabs of tissue, muscle, bone and lung. Two scenarios are considered: a single slab of each material is placed in the water phantom, in the same position for each material (left); and the slabs of materials are placed back-to-back in the water phantom (right).

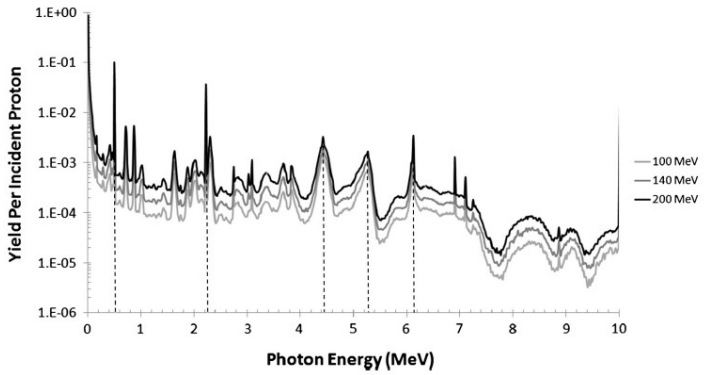

Figure 3. Energy spectra of photons generated in the cylindrical water phantom deriving from proton pencil beams of energy between 100 and 200 MeV. The gamma emission lines are characteristic of those emitted as a result of interactions on the major constituent elements of the phantom material. The PG emission lines of interest are of energy 4.44 MeV, 5.21 MeV and 6.13 MeV, generated by excited ^{12}C, ^{15}O and ^{16}O nuclei, respectively.

Table 1
Gamma photon yields obtained in different PG energy windows. The PG rays originate inside the water phantom. The statistical uncertainty affecting the results is within 1%.

Proton beam energy (MeV)	Photon energy window (MeV)	Photon yield per incident proton (%)
100	No window	39.64
	2.0–8.0	5.61
	4.2–4.6	1.14
	5.0–5.4	0.71
	5.9–6.3	0.40
	4.2–6.3	2.59
120	No window	56.75
	2.0–8.0	7.55
	4.2–4.6	1.40
	5.0–5.4	0.90
	5.9–6.3	0.53
	4.2–6.3	3.28
140	No window	75.39
	2.0–8.0	9.70
	4.2–4.6	1.67
	5.0–5.4	1.10
	5.9–6.3	0.66
	4.2–6.3	4.00
160	No window	95.20
	2.0–8.0	11.94
	4.2–4.6	1.95
	5.0–5.4	1.30
	5.9–6.3	0.80
	4.2–6.3	4.74
180	No window	115.99
	2.0–8.0	14.36
	4.2–4.6	2.24
	5.0–5.4	1.51
	5.9–6.3	0.95
	4.2–6.3	5.52
200	No window	137.40
	2.0–8.0	16.85
	4.2–4.6	2.53
	5.0–5.4	1.72
	5.9–6.3	1.09
	4.2–6.3	6.30

0.511 MeV, originated by the annihilation of positrons resulting from the decay of ^{15}O nuclei. The 2.22 MeV peak results from the capture of secondary thermal neutrons by hydrogen nuclei, and three prominent PG lines are observed with energy 4.44, 5.21 and 6.13 MeV. The 4.44 MeV PG emission line originates from the de-excitation of $^{12}C^{*}$ nuclei, originating from proton nuclear interactions with oxygen nuclei. The 5.21 and 6.13 MeV PG emission lines derive from $^{15}O^{*}$ and $^{16}O^{*}$ de-excitations, respectively. The characteristics of the individual PG lines are investigated by employing three equal-width energy windows of 4.2–4.6 MeV, 5.0–5.4 MeV, and 5.9–6.3 MeV. A larger energy window of 4.2–6.3 MeV is used to study the effect from all three PG emission lines taken as a whole. An additional wide energy window of 2.0–8.0 MeV, which has been investigated by other groups [17,18], is also used for comparison.

The yields in different photon energy windows for PG rays originating from the water phantom per incident proton are estimated and listed in Table 1. As expected, the PG yield increases with higher proton beam energy. For all the proton beam energies considered, the most abundant PG emission yield is found in the energy window between 4.2 and 6.3 MeV. The energy window 4.2–4.6 MeV has a higher yield than 5.0–5.4 MeV and 5.9–6.3 MeV.

3.2. Spatial correlation between prompt gamma emission and the proton beam range

The simulation results showed that the ranges of protons with energy between 100 and 200 MeV in water are from approximately 76–258 mm. Fig. 4 shows the longitudinal yield distribution of PG emission in an energy window of 2.0–8.0 MeV. The Bragg curve is plotted as well to show the correlation between PG and the BP. It can be observed that the total PG emission yield integrated over the 2.0–8.0 MeV energy window is relatively flat in the proton dose plateau and decreases rapidly near the proton end-of-range, regardless of the proton beam energy. The PG fall-off exhibits a close correspondence with the BP fall-off, which has been proposed for real-time BP tracking in PT. This observation agrees well with the experimental results from other research groups [11,12].

Fig. 5 shows the longitudinal distributions of characteristic PG rays in different energy windows produced in the water phantom with the corresponding Bragg peak, for proton beam energy of 200 MeV. All the three characteristic PG rays show a distinctive correlation with the Bragg curve but different precision for BP tracking. The 4.44 MeV PG rays in the 4.2–4.6 MeV window exhibit an emission distribution very similar to the Bragg curve shape and show sharp peak and fall-off near the end of the proton range. The 5.21 MeV PG rays in the 5.0–5.4 MeV window show a peak at a depth further from the BP. The 6.13 MeV PG rays in the energy window of 5.9–6.3 MeV exhibit the closest emission fall-off correlation with the BP but significantly lower PG yield than the other two PG lines. Yet the combined PG window of 4.2–6.3 MeV, which integrates the three PG emission lines, shows similar accuracy in

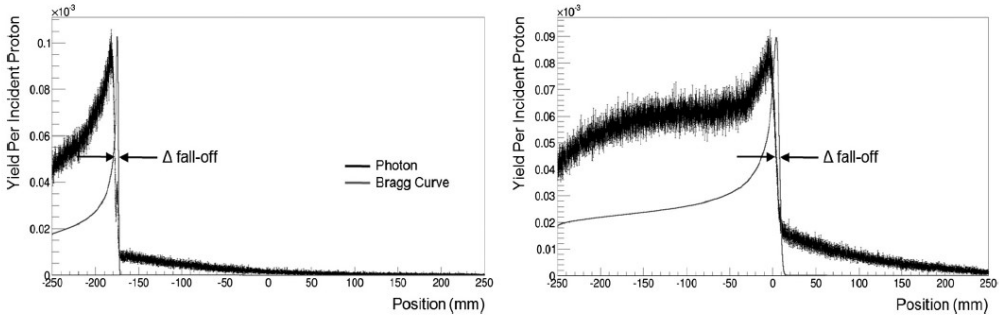

Figure 4. Longitudinal normalized yield distribution of PG rays in the energy window of 2.0–8.0 MeV with the Bragg curve in the water phantom, for 100 MeV (left) and 200 MeV (right) proton pencil-beam energies. The Bragg peak is normalized to the maximum of the gamma yield (the scale on the vertical-axis is arbitrary for the Bragg curve). The arrows indicate the *Δfall-off* as defined in Section 2.

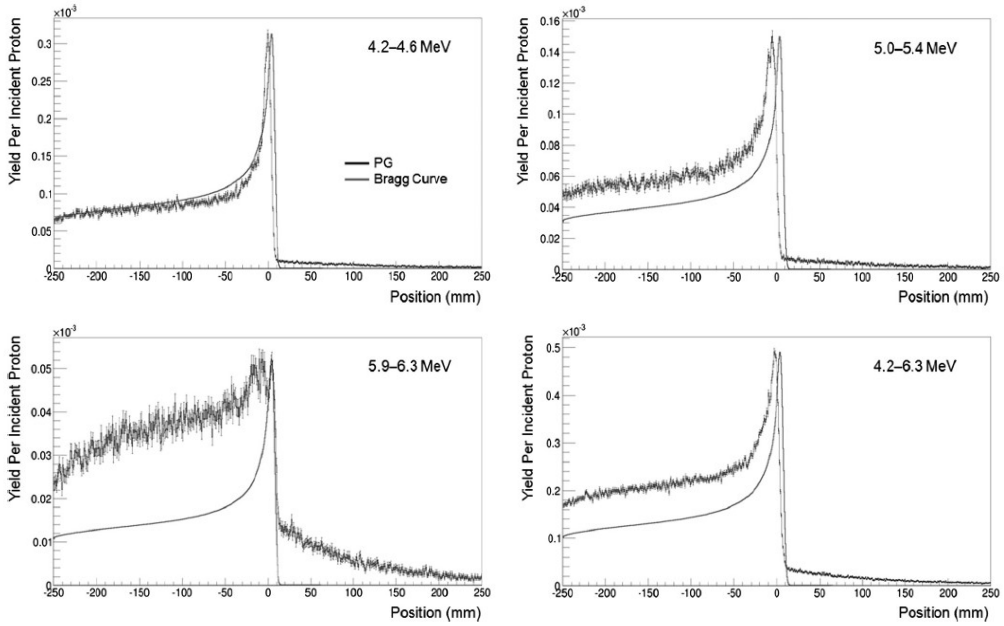

Figure 5. Longitudinal PG yield distribution correlation with the Bragg curve in the water phantom from different gamma energy windows with an incident 200 MeV proton pencil beam. The Bragg peak is normalized to the maximum of the gamma yield (the scale on the vertical-axis is arbitrary for the Bragg curve).

the PG peak (as compared to the BP) as the 4.2–4.6 MeV window since the 4.44 MeV PG has a dominant yield.

The quantified difference, *Δfall-off*, between 50% PG fall-off and proton beam range has been extracted from Fig. 5. Fig. 6 shows the *Δfall-off* to predict the proton beam range in the water phantom as a function of the energy of the incident proton beam. It can be observed that the three characteristic PG rays of 4.44, 5.21 and 6.13 MeV provide different range verification accuracy. The 6.13 MeV PG rays provide the highest accuracy of around 1 mm, however the yield of these PG rays is the lowest (see Table 1). The 5.21 MeV PG rays provide accuracy of around 8 mm while the 4.44 MeV PG rays provide accuracy of 4–5 mm. The combined 4.2–6.3 MeV PG energy window exhibits similar *Δfall-off* values as the 4.44 MeV PG rays. This happens because the 4.2–4.6 MeV energy window is the most dominant in the 4.2–6.3 MeV interval as observed in Section 3.1 (see Table 1), with the benefit of a higher

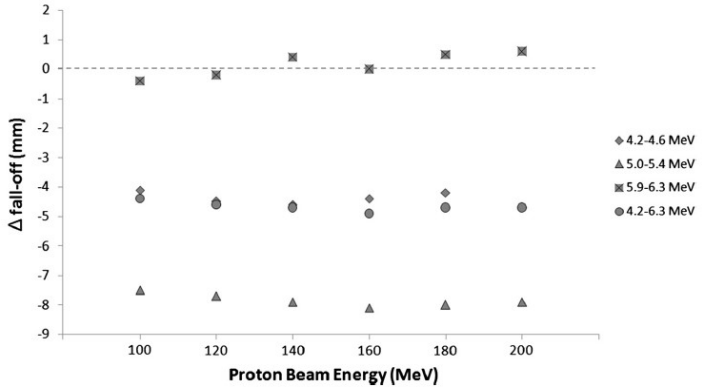

Figure 6. *Δfall-off*, defined in Section 2, quantifying the accuracy of determination of the proton beam range in the water phantom, as a function of the incident proton beam energy. The positive values represent 50% PG emission fall-off positions occurring after the proton beam range, while negative values before. The statistical uncertainty affecting *Δfall-off* values is within 0.1 mm.

Table 2
Detectable gamma photon yields in different energy windows. The PG rays exit the phantom and reach the surface of the detection cylinder. The simulation statistical uncertainty is within 1%.

Proton beam energy (MeV)	Photon energy window (MeV)	Photon yield per incident proton (%)
100	No window	4.35
	2.0–8.0	1.47
	4.2–4.6	0.28
	5.0–5.4	0.18
	5.9–6.3	0.10
	4.2–6.3	0.65
120	No window	6.29
	2.0–8.0	2.01
	4.2–4.6	0.35
	5.0–5.4	0.23
	5.9–6.3	0.14
	4.2–6.3	0.85
140	No window	8.55
	2.0–8.0	2.64
	4.2–4.6	0.44
	5.0–5.4	0.29
	5.9–6.3	0.18
	4.2–6.3	1.07
160	No window	10.98
	2.0–8.0	3.28
	4.2–4.6	0.52
	5.0–5.4	0.35
	5.9–6.3	0.23
	4.2–6.3	1.30
180	No window	13.71
	2.0–8.0	4.00
	4.2–4.6	0.60
	5.0–5.4	0.41
	5.9–6.3	0.27
	4.2–6.3	1.53
200	No window	16.52
	2.0–8.0	4.74
	4.2–4.6	0.69
	5.0–5.4	0.48
	5.9–6.3	0.32
	4.2–6.3	1.77

yield. The discrepancy between the BP fall-off and the PG fall-off exhibits a strong dependence on the PG energy window. However, different energy windows have large difference of the PG yields. These pose great challenges to the optimum PG detection requirement.

3.3. Determination of a preferential position for detection of prompt gamma rays with respect to the proton beam range

With the ideal detection cylinder surrounding the phantom, the number of detectable PG rays can be estimated. The yields of gamma rays that are produced inside the water phantom and reach the detection cylinder for each of the proton beam energies under study are reported in Table 2. As compared to the data in Table 1, it can be observed that the number of gamma photons per incident proton reaching the detection cylinder has significantly decreased, as expected, as they can interact in the water phantom and eventually be absorbed. For each of the beam energies, the 4.2–4.6 MeV energy window has a bigger yield than 5.0–5.4 MeV and 5.9–6.3 MeV. The yield of the entire 4.2–6.3 MeV energy window at the detection cylinder is approximately 25% of the yield of the same gamma rays that originate in the phantom.

Fig. 7 shows a typical longitudinal distribution of PG rays registered on the surface of the detection cylinder. A non-isotropic longitudinal distribution of PG rays is observed, as expected. There is no sharp fall-off at the position of the proton beam range. It shows that there exists a preferential position in the detection cylinder surface to maximize the geometrical efficiency of PG detection. The data were fitted by a 4th-order polynomial function to determine the maximum position of the PG yield distribution as a preferential detection position. With respect to the BP position, this preferential detection position has been quantified with a polar angle θ defined in Fig. 1 and in Section 2. For an incident 200 MeV proton beam, θ is $(-15 \pm 1)^\circ$, $(-12 \pm 1)^\circ$ and $(-11 \pm 1)^\circ$ for a PG energy window of 4.2–4.6 MeV, 5.0–5.4 MeV and 5.9–6.3 MeV, respectively. This means that the higher yield of detectable PG rays is found in a location backward of the BP fall-off position.

Fig. 8 shows the dependence of the preferential position for PG detection, expressed in terms of θ, on different PG energy windows as a function of the proton beam energy. The preferential position for PG detection shows a strong dependence on the beam energy. As the beam energy increases, the position maximizing the number of detectable PG rays becomes increasingly backward with respect to their BP position. The detection preferential position also shows a considerable variation with PG energy windows. The data show that selecting specific PG energy windows θ changes within 5 degrees only.

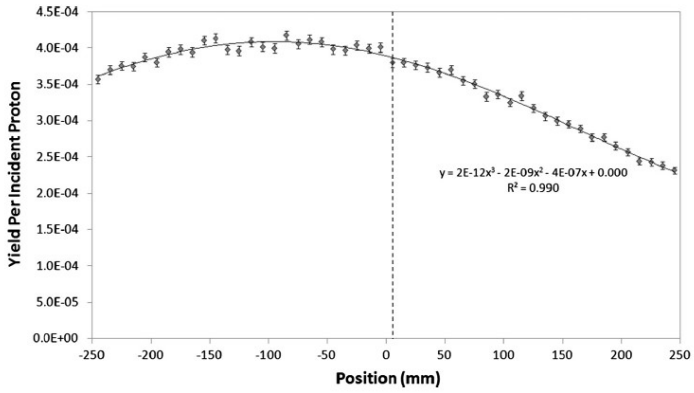

Figure 7. Longitudinal distribution of PG rays in 4.2–6.3 MeV reaching the surface of the detection cylinder once emitted from the water phantom, for an incident 200 MeV proton pencil beam. The data are fitted by a fourth-order polynomial function (solid line). The 50% BP fall-off position in the phantom is indicated with the dash-line.

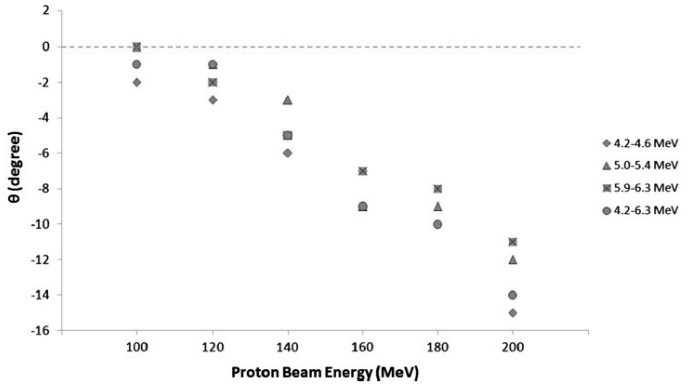

Figure 8. Preferential position for PG detection, quantified in terms of θ (see Fig. 1), with respect to the proton beam range. The uncertainty of θ values is estimated around 1°.

3.4. Detection of Bragg peak shift by means of prompt gamma emission: Feasibility study

Anatomical heterogeneities were introduced with a slab in the water phantom to evaluate the response of the PG signal to a BP shift. Figs. 9 and 10 show the yield of PG rays produced along the depth of the water phantom with single inserts of bone and lung, respectively. These two phantoms are shown because bone and lung exhibit the biggest variation of yields with respect to water. Tissue and muscle show more similar yields to water. The slab's effect on the PG yield is clearly evident at the slab's location (−140 mm to −120 mm) in Figs. 9 and 10, which shows a close correspondence to the dose deposition variation at the slab location. Fig. 11 shows the yield distribution of PG rays with all four material slabs stacked together (−200 mm to −120 mm).

It can be observed that the PG yield becomes maximum and then falls off close to the BP, as found in the case of the homogeneous water phantom. The yield of PG rays is found to be dependent on the material composition and density of the medium traversed by the proton beam. Bone comprises of ∼28% carbon, ∼41% oxygen and ∼6% hydrogen, whereas lung comprises of ∼10% carbon, ∼76% oxygen and ∼10% hydrogen. Tissue comprises

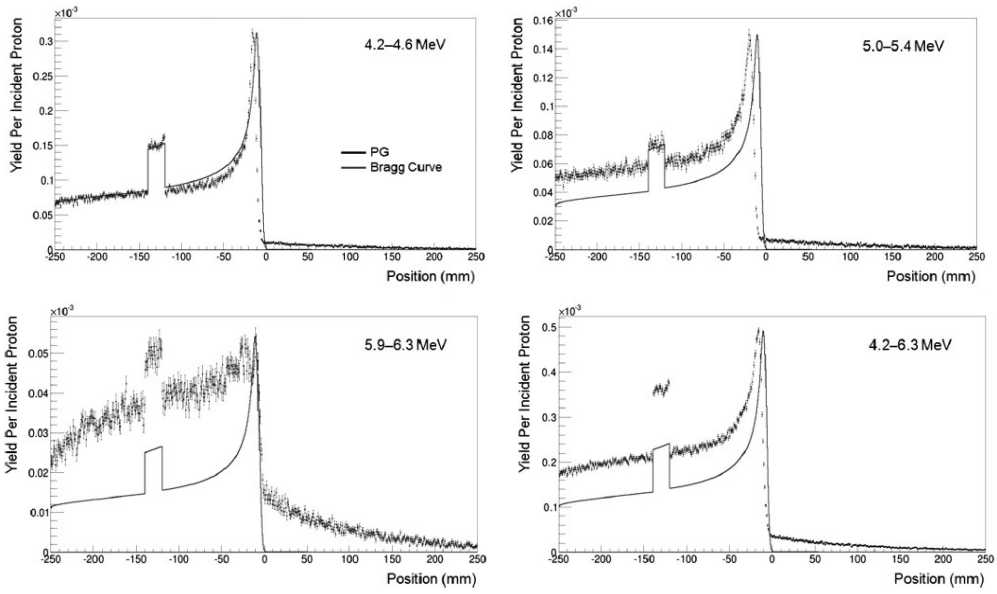

Figure 9. Longitudinal yield distribution of PG rays when they originate in the water phantom with the slab of bone material at the location of −140 mm to −120 mm. The Bragg peak is normalized to the maximum of the PG yield (the scale on the vertical-axis is arbitrary for the Bragg curve). The beam energy is 200 MeV and the PG energy window is indicated in each graph.

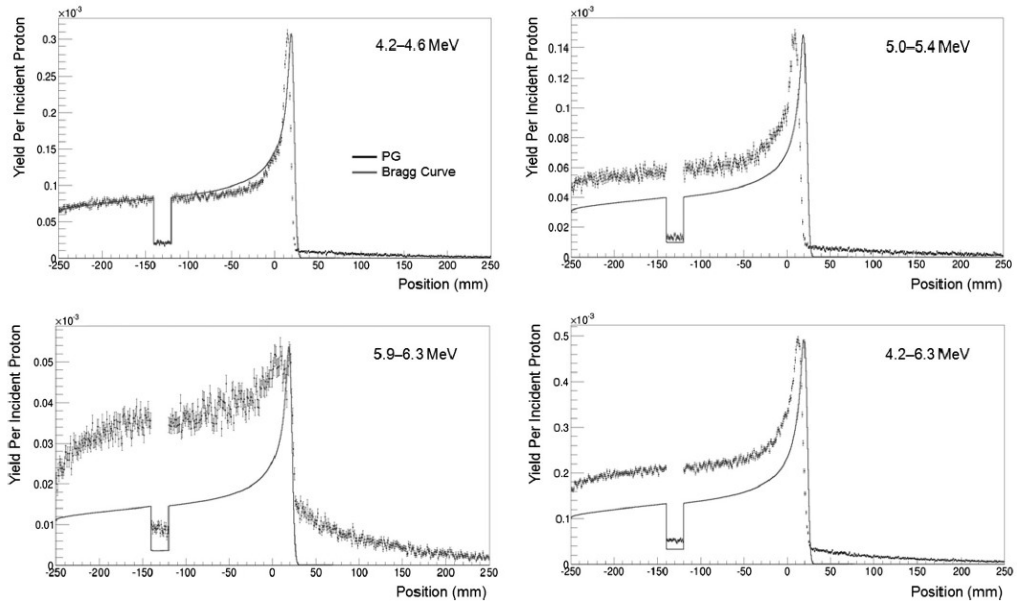

Figure 10. Longitudinal yield distribution of PG rays when they originate in the water phantom with the slab of lung material at the location of −140 mm to −120 mm. The Bragg peak is normalized to the maximum of the PG yield (the scale on the vertical-axis is arbitrary for the Bragg curve). The beam energy is 200 MeV and the PG energy window is indicated in each graph.

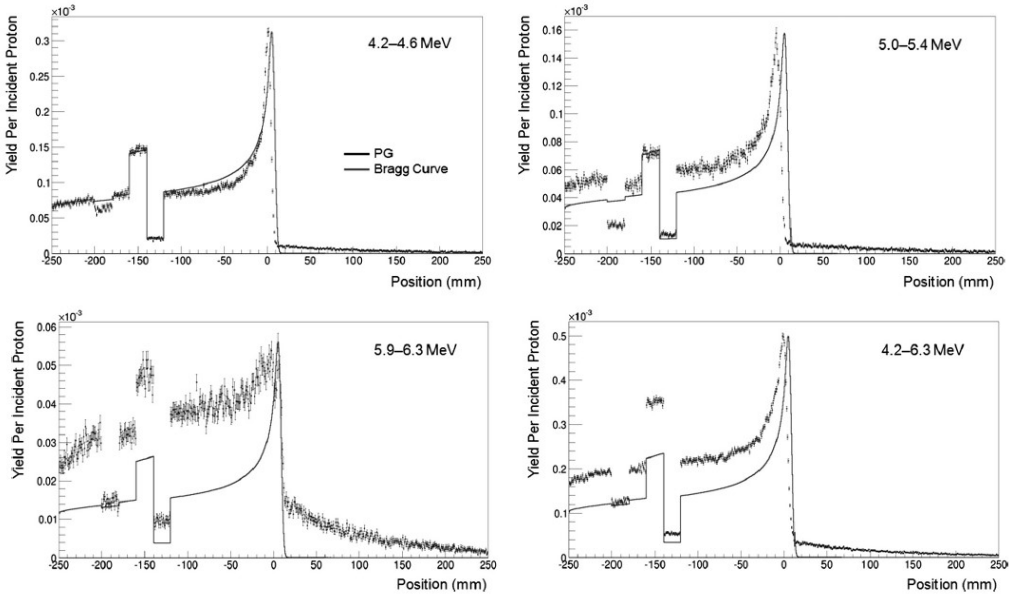

Figure 11. Longitudinal distribution of the yield of PG rays when they originate in the water phantom with all four stacked materials (tissue, muscle, bone and lung) at the location of −200 mm to −120 mm. The Bragg peak is normalized to the maximum of the PG yield (the scale on the vertical-axis is arbitrary for the Bragg curve). The beam energy is 200 MeV and the PG energy window is indicated in each graph.

Table 3
Comparison of BP shifts and the PG fall-off shifts between the slab-embedded water phantom and the homogeneous water phantom from the 200 MeV proton pencil-beam irradiation.

Phantom	Proton beam range (±0.1 mm)	Shift in proton beam range (±0.1 mm)	PG energy window (MeV)	50% PG emission fall-off (±0.1 mm)	Shift in 50% PG emission fall-off (±0.1 mm)
Water (homogeneous)	258.2	–	2.0–8.0	254.1	–
			4.2–4.6	253.5	–
			5.0–5.4	250.3	–
			5.9–6.3	258.8	–
			4.2–6.3	253.5	–
Tissue slab	258.9	0.7	2.0–8.0	254.9	0.8
			4.2–4.6	254.3	0.8
			5.0–5.4	250.6	0.3
			5.9–6.3	259.3	0.5
			4.2–6.3	254.3	0.8
Muscle slab	257.7	−0.5	2.0–8.0	253.4	−0.7
			4.2–4.6	253.1	−0.4
			5.0–5.4	249.8	−0.5
			5.9–6.3	258.0	−0.8
			4.2–6.3	253.3	−0.2
Bone slab	244.0	−14.2	2.0–8.0	240.0	−14.1
			4.2–4.6	239.2	−14.3
			5.0–5.4	236.2	−14.1
			5.9–6.3	244.6	−14.2
			4.2–6.3	239.4	−14.1
Lung slab	273.3	15.1	2.0–8.0	268.9	14.8
			4.2–4.6	268.8	15.3
			5.0–5.4	265.5	15.2
			5.9–6.3	273.7	14.9
			4.2–6.3	268.6	15.1
All material slabs	259.5	1.3	2.0–8.0	255.3	1.2
			4.2–4.6	254.7	1.2
			5.0–5.4	251.2	0.9
			5.9–6.3	259.9	1.1
			4.2–6.3	254.6	1.1

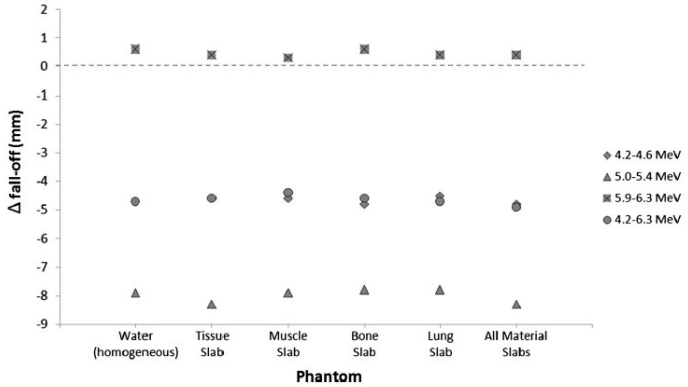

Figure 12. The *Δfall-off*, defined as the difference between the 50% PG fall-off and the proton beam range, is represented for each phantom under study. The statistical uncertainty affecting the *Δfall-off* is within 0.1 mm.

of ~64% carbon, ~23% oxygen and ~12% hydrogen, and muscle comprises of ~12% carbon, ~73% oxygen and ~10% hydrogen. As expected, the PG ray yield increases with density. The PG ray emission yield is lowest for lung and maximum for bone for the set of materials under study.

Table 3 reports the range of a 200 MeV proton beam in the water phantom with the insertion of different material slabs, as calculated by the Geant4 simulation. The suitability to use a PG emission signal to track BP position shifts is quantified by comparing the results of the slab-embedded water phantom with the homogeneous water phantom. It is observed that both bone and lung slabs cause a large shift in the BP position, greater than 10 mm. The PG signal is capable of tracking this shift with high accuracy. Tissue and muscle slabs cause a small shift in the BP position, less than 1 mm. The PG signal is also capable of detecting this submillimeter shift in the proton beam range.

Fig. 12 shows the *Δfall-off* between the PG emission and the proton beam range for each heterogeneous phantom considered.

The results obtained for the homogeneous water phantom are included as well for comparison. It can be observed that the Δ*fall-off* remains consistent for each slab-embedded heterogeneous phantom with a variation less than 1 mm in each of the PG energy windows. These data show that the PG emission signal shifts with the proton beam range to exhibit a consistent correlation to the BP regardless of the material placed in the beam path.

4. Discussion and conclusion

In this work, the emission of three characteristic PG signals (4.44, 5.21 and 6.13 MeV) produced by proton-oxygen nuclear interactions was investigated in a water phantom using Geant4 based simulations. The PG production and detectable yields, spatial correlation of PG longitudinal yield and preferential position for PG detection with respect to the BP as well as using the distal fall-off of the PG longitudinal yield to track BP shifts have been quantified in different PG energy windows as a function of the incident proton beam energy.

The results show that all three characteristic PG emissions exhibit distinctively close correlations with the proton depth-dose curve but offer different precision for beam-range estimations. Either individual or integrated PG emission of the three PG signals can be utilized for BP tracking. The selection of energy window for PG detection has a large effect on the accuracy of proton beam range estimation using PG emission. This is consistent with previous studies [13,20]. The 6.13 MeV PG rays can provide millimeter accuracy but significantly lower PG yield. These results are also in good agreement with the measurements by Verburg et al. [21]. An important finding in this study is that each of the three characteristic PG signals shows a consistent fall-off difference with respect to the actual beam range in the proton beam energy range of 100–200 MeV. This implies that such PG signals are also well suited for tracking the Spread-Out Bragg Peak.

By virtue of an ideal detection cylinder, the detectable PG yield has been estimated. In the simulation set-up considered, about 25% characteristic PG rays exit the phantom and reach the detection cylinder. The non-isotropic longitudinal distribution of PG emission results in a preferential position for PG detection in the detection cylinder, which could be utilized for maximizing the geometrical efficiency of PG measurement. However, this preferential position has a strong dependence on the beam energy. As the beam energy increases, the position maximizing the number of detectable PG rays gets increasingly backward with respect to their BP position. The detection preferential position also shows a considerable variation with PG energy windows. These make the maximization of the PG detection associated with the BP position difficult. However, the PG measurement can be optimized with energy and detection position preferences. Our results imply that the design of a PG detector with particular energy and geometrical acceptance preferences is desirable. Further work is necessary if the detection of PG associated with the BP is to be optimized with a specific PG detector system.

The PG longitudinal yield variation is sensitive to the elemental composition and the medium density in the heterogenetic phantoms, as also observed in previous work [9,10]. A submillimeter shift of the BP position due to tissue composition variations is clearly evident by the characteristic PG longitudinal yield. This indicates that PG emissions associated with proton interactions in tissue offer the potential for *in vivo* beam-range verification within 1 mm uncertainty, as observed in earlier research [11,14]. But the actual system resolution is mainly determined by the PG detector's property. Our results imply that the detector with PG spectroscopy measurement is favorable for high-precision BP tracking. Further study for the development of a high performance PG detector is under investigation, and the PT PG emission ability to track the position of the BP will be studied with a realistic human phantom in the near future.

Acknowledgement

This work was supported in part by the URC small grant of University of Wollongong (UOW). We also would like to thank the Information Technology Services of UOW for computing time and resources on the High Performance Computing Cluster.

References

[1] Wilson RR. Radiological use of fast protons. Radiology 1946;47:487–91.
[2] Lomax AJ. Intensity modulated proton therapy and its sensitivity to treatment uncertainties. 1: The potential effects of calculational uncertainties. Phys Med Biol 2008;53:1027–42.
[3] Richter C, Pausch G, Seco J, Bortfeld T, Enghardt W. Increasing precision in particle therapy: *in vivo* dosimetry and beyond. Phys Med 2014;30(Supp.1): e3–4.
[4] Knopf AC, Lomax A. In vivo proton range verification: a review. Phys Med Biol 2013;58:131–60.
[5] Parodi K, Paganetti H, Shih HA, Michaud S, Loeffler JS, Delaney TF, et al. Patient study of *in vivo* verification of beam delivery and range, using positron emission tomography and computed tomography imaging after proton therapy. Int J Rad Oncol Biol Phys 2007;68:920–34.
[6] Oelfke U, Lam GK, Atkins MS. Proton dose monitoring with PET: quantitative studies in Lucite. Phys Med Biol 1996;41:177–96.
[7] Parodi K, Enghardt W. Potential application of PET in quality assurance of proton therapy. Phys Med Biol 2000;45:N151–6.
[8] Moteabbed M, Espana S, Paganetti H. Monte Carlo patient study on the comparison of prompt gamma and PET imaging for range verification in proton therapy. Phys Med Biol 2011;56:1063–82.
[9] Polf JC, Peterson S, McCleskey M, Roeder BT, Spiridon A, Beddar S, et al. Measurement and calculation of characteristic prompt gamma ray spectra emitted during proton irradiation. Phys Med Biol 2009;54:N519–27.
[10] Polf JC, Panthi R, Mackin DS, McCleskey M, Saastamoinen A, Roeder BT, et al. Measurement of characteristic prompt gamma rays emitted from oxygen and carbon in tissue-equivalent samples during proton beam irradiation. Phys Med Biol 2013;58:5821–31.
[11] Min CH, Kim CH, Youn MY, Kim JW. Prompt gamma measurements for locating the dose falloff region in the proton therapy. Appl Phys Lett 2006;89:183517.
[12] Testa M, Bajard M, Chevallier M, Dauvergne D, Freud N, Henriquet P, et al. Real-time monitoring of the Bragg-peak position in ion therapy by means of single photon detection. Rad Environ Biophys 2010;49:337–43.
[13] Smeets J, Roellinghoff F, Prieels D, Stichelbaut F, Benilov A, Busca P, et al. Prompt gamma imaging with slit camera for real-time range control in proton therapy. Phys Med Biol 2012;57:3371–405.
[14] Bom V, Joulaeizadeh L, Beekman F. Real-time prompt gamma monitoring in spot-scanning proton therapy using imaging through a knife-edge-shaped slit. Phys Med Biol 2012;57:297–308.
[15] Perali I, Celani A, Bombelli L, Fiorini C, Camera F, Clemental E, et al. Prompt gamma imaging of proton pencil beams at clinical dose rate. Phys Med Biol 2014;59:5849–71.
[16] Min CH, Lee HR, Kim CH, Lee SB. Development of array-type prompt gamma measurement system for in vivo range verification in proton therapy. Med Phys 2012;39:2100–7.
[17] Peterson SW, Robertson D, Polf J. Optimizing a three-stage Compton camera for measuring prompt gamma rays emitted during proton radiotherapy. Phys Med Biol 2010;55:6841–56.
[18] Richard MH, Chevallier M, Dauvergne D, Freud N, Henriquet P, Le Foulher F, et al. Design guidelines for a double scattering Compton camera for prompt-γ imaging during ion beam therapy: a Monte Carlo simulation study. IEEE Trans Nucl Sci 2011;58:87–94.
[19] Biegun AK, Seravalli E, Lopes PC, Rinaldi I, Pinto M, Oxley DC, et al. Time-of-flight neutron rejection to improve prompt gamma imaging for proton range verification: a simulation study. Phys Med Biol 2012;57:6429–44.
[20] Janssen FMFC, Landry G, Cambraia Lopes P, Dedes G, Smeets J, Schaart DR, et al. Factors influencing the accuracy of beam range estimation in proton therapy using prompt gamma emission. Phys Med Biol 2014;59:4427–41.
[21] Verburg JM, Riley K, Bortfeld T, Seco J. Energy and time resolved detection of prompt gamma rays for proton range verification. Phys Med Biol 2013;58: L37–49.
[22] Verburg JM, Seco J. Proton range verification through prompt gamma-ray spectroscopy. Phys Med Biol 2014;59:7089–106.
[23] Agostinelli S, Allison J, Amako K, Apostolakis J, Araujo H, Arce P, et al. Geant4 – a simulation toolkit. Nucl Instrum Meth Phys Res A 2003;506:250–303.
[24] Allison J, Amako K, Apostolakis J, Araujo H, Arce P, Asai M, et al. Geant4 developments and applications. IEEE Trans Nucl Sci 2006;53:270–8.
[25] Zacharatou JC, Paganetti H. Physics settings for using the Geant4 toolkit in proton therapy. IEEE Trans Nucl Sci 2008;55:1018–25.

References

[1] Wilson RR 1946, Radiological use of fast protons, Radiology 47(5): p. 487-491.

[2] Levy RP, Fabrikant JI, Frankel KA, Phillips MH, Lyman JT, Lawrence JH, Tobias CA 1991, Heavy-charged-particle radiosurgery of the pituitary gland: clinical results of 840 patients, Stereotact. Funct. Neurosurg. 57(1-2): p. 22-35.

[3] Castro JR 1993, Heavy Ion Therapy: Bevalac Epoch, Lawrence Berkeley Laboratory University of California.

[4] Slater JM, Archambeau JO, Miller DW, Notarus MI, Preston W, Slater JD 1992, The proton treatment center at Loma Linda University Medical Center: rationale for and description of its development, Int. J. Radiat. Oncol. Biol. Phys. 22(2): p. 383-389.

[5] Particle Therapy Co-Operative Group (PTCOG), date accessed: 20/01/21 https://www.ptcog.ch/index.php/facilities-in-operation.

[6] Smith AR 2009, Vision 20/20: Proton Therapy, Am. Assoc. Phys. Med. 36(2): p. 556-568.

[7] Schardt D, Elsasser T, Schulz-Ertner D 2010, Heavy-ion tumor therapy: Physical and radiobiological benefits, Rev. Mod. Phys. 82(1): p. 383-425.

[8] Lomax AJ 2008, Intensity modulated proton therapy and its sensitivity to treatment uncertainties 1: The potential effects of calculational uncertainties, Phys. Med. Biol. 53(4): p. 1027-1042.

[9] Paganetti H 2012, Range uncertainties in proton therapy and the role of Monte Carlo simulations, Phys. Med. Biol. 57(11): p. R99-R117.

[10] Leeman JE, Romesser PB, Zhou Y, McBride S, Riaz N, Sherman E, Cohen MA, Cahlon O, Lee N 2017, Proton therapy for head and neck cancer: Expanding the therapeutic window, Lancet. Oncol. 18(5): p. e254-e265.

[11] Polf JC, Parodi K 2015, Imaging particle beams for cancer treatment, Physics Today 68(10): p. 28-33.

[12] Cormack AM 1963, Representation of a function by its line integrals, with some radiological applications, J. Appl. Phys. 34(9): p. 2722-2727.

[13] Hanson KM, Bradbury JN, Cannon TM, Hutson RL, Laubacher DB, Macek RJ, Paciotti MA, Taylor CA 1981, Computer tomography using proton energy loss, Phys. Med. Biol. 26(6): p. 965-983.

[14] Esposito M, Waltham C, Taylor JT, Manger S, Phoenix B, Price T, Poludniowski G, Green S, Evans PM, Allport PP, Manolopulos S, Nieto-Camero J, Symons J, Allinson NM 2018, PRaVDA: The first solid-state system for proton computed tomography, Phys. Med. 55: p. 149-154.

[15] Cassetta R, Piersimoni P, Riboldi M, Giacometti V, Bashkirov V, Baroni G, Ordonez C, Coutrakon G, Schulte R 2019, Accuracy of low-dose proton CT image registration for pretreatment alignment verification in reference to planning proton CT, J. Appl. Clin. Med. Phys. 20(4): p. 83-90.

[16] Bortfeld TR, Loeffler JS 2017, Three ways to make proton therapy affordable, Nature 549(7673): p. 451-453.

[17] Giordanengo S, Manganaro L, Vignati A 2017, Review of technologies and procedures of clinical dosimetry for scanned ion beam radiotherapy, Phys. Med. 43: p. 79-99.

[18] Trnková P, Knäusl B, Actis O, Bert C, Biegun AK, Boehlen TT, Furtado H, McClelland J, Mori S, Rinaldi I, Rucinski A, Knopf AC 2018, Clinical implementations of 4D pencil beam scanned particle therapy: Report on the 4D treatment planning workshop 2016 and 2017, Phys. Med. 54: p. 121-130.

[19] Pausch G, Berthold J, Enghardt W, Römer K, Straessner A, Wagner A, Werner T, Kögler T 2020, Detection systems for range monitoring in proton therapy: Needs and challenges, Nucl. Instrum. Methods Phys. Res. A 954: 161227.

[20] Knopf AC, Lomax A 2013, In vivo proton range verification: a review, Phys. Med. Biol. 58(15): p. 131-160.

[21] Carnicer A, Letellier V, Rucka G, Angellier G, Sauerwein W, Herault J 2012, Study of the secondary neutral radiation in proton therapy: Toward an indirect in vivo dosimetry, Med. Phys. 39(12): p. 7303-7316.

[22] Newhauser WD, Zhang R 2015, The physics of proton therapy, Phys. Med. Biol. 60(8): p. R155-R209.

[23] Moteabbed M, Espana S, Paganetti H 2011, Monte Carlo patient study on the comparison of prompt gamma and PET imaging for range verification in proton therapy, Phys. Med. Biol. 56(4): p. 1063-1082.

[24] Mackin D, Peterson S, Beddar S, Polf J 2012, Evaluation of a stochastic reconstruction algorithm for use in Compton camera imaging and beam range verification from secondary gamma emission during proton therapy, Phys. Med. Biol. 57(11): p. 3537-3553.

[25] Seco J, Verhaegen F, Hendee WR 2013, Monte Carlo Techniques in Radiation Therapy, Taylor & Francis Group, LLC.

[26] Polf JC, Panthi R, Mackin DS, McCleskey M, Saastamoinen A, Roeder BT, Beddar S 2013, Measurement of characteristic prompt gamma rays emitted from oxygen and carbon in tissue-equivalent samples during proton beam irradiation, Phys Med Biol. 58(17): p. 5821-5831.

[27] Min CH, Kim CH, Youn MY, Kim JW 2006, Prompt gamma measurements for locating the dose falloff region in the proton therapy, Appl. Phys. Lett. 89(18): 183517.

[28] Polf JC, Peterson S, McCleskey M, Roeder BT, Spiridon A, Beddar S, Trache L 2009, Measurement and calculation of characteristic prompt gamma ray spectra emitted during proton irradiation, Phys. Med. Biol. 54(22): p. N519-N527.

[29] Oelfke U, Lam GK, Atkins MS 1996, Proton dose monitoring with PET: quantitative studies in Lucite, Phys. Med. Biol. 41(1): p. 177-196.

[30] Cherry SR, Sorenson J, Phelps M 2012, Physics of Nuclear Medicine, Elsevier Inc.

[31] Zhu X, Fakhri GEI 2013, Proton therapy verification with PET imaging, Theranostics 3(10): p. 731-740.

[32] Parodi K, Ponisch F, Enghardt W 2005, Experimental study on the feasibility of in-beam PET for accurate monitoring of proton therapy, IEEE Trans. Nucl. Sci. 52(3): p. 778-786.

[33] Parodi K, Bortfeld T 2006, A filtering approach based on Gaussian-power law convolutions for local PET verification of proton radiotherapy, Phys. Med. Biol. 51(8): p. 1991-2009.

[34] Podgorsak EB 2005, Radiation Oncology Physics: A Handbook for Teachers and Students, International Atomic Energy Agency, Vienna.

[35] Gensheimer MF, Yock TI, Liebsch NJ, Sharp GC, Paganetti H, Madan N, Grant PE, Bortfeld T 2010, In vivo proton beam range verification using spine MRI changes, Int. J. Radiation Oncology Biol. Phys. 78(1): p. 268-275.

[36] Yuan Y, Andronesi OC, Bortfeld TR, Richter C, Wolf R, Guimaraes AR, Hong TS, Seco J 2013, Feasibility study of in vivo MRI based dosimetric verification of proton end-of-range for liver cancer patients, Radiother. Oncol. 106(3): p. 378-382.

[37] Amaldi U, Hajdas W, Iliescu S, Malakhov N, Samarati J, Sauli F, Watts D 2010, Advanced quality assurance for CNAO, Nucl. Instrum. Methods Phys. Res. A 617: p. 248-249.

[38] Henriquet P, Testa E, Chevallier M, Dauvergne D, Dedes G, Freud N, Krimmer J, Létang JM, Ray C, Richard MH, Sauli F 2012, Interaction vertex imaging (IVI) for carbon ion therapy monitoring: A feasibility study, Phys. Med. Biol. 57(14): p. 4655-4669.

[39] Finck C, Karakaya Y, Reithinger V, Rescigno R, Baudot J, Constanzo J, Juliani D, Krimmer J, Rinaldi I, Rousseau M, Testa E, Vanstalle M, Ray C 2017, Study for online range monitoring with the interaction vertex imaging method, Phys. Med. Biol. 62(24): p. 9220-9239.

[40] Hymers D, Mücher D 2019, Monte Carlo investigation of sub-millimeter range verification in carbon ion radiation therapy using interaction vertex imaging, Biomed. Phys. Eng. Express 5: 045025.

[41] Gwosch K, Hartmann B, Jakubek J, Granja C, Soukup P, Jäkel O, Martišíková M 2013, Non-invasive monitoring of therapeutic carbon ion beams in a homogeneous phantom by tracking of secondary ions, Phys. Med. Biol. 58(11): p. 3755-3773.

[42] Piersanti L, Bellini F, Bini F, Collamati F, De Lucia E, Durante M, Faccini R, Ferroni F, Fiore S, Iarocci E, La Tessa C, Marafini M, Mattei I, Patera V, Ortega PG, Sarti A, Schuy C, Sciubba A, Vanstalle M, Voena C 2014, Measurement of charged particle yields from PMMA irradiated by a 220 MeV/u ^{12}C beam, Phys. Med. Biol. 59(7): p. 1857-1872.

[43] Yamaguchi M, Nagao Y, Ando K, Yamamoto S, Toshito T, Kataoka J, Kawachi N 2016, Secondary-electron-bremsstrahlung imaging for proton therapy, Nucl. Instrum. Methods Phys. Res. A 833: p. 199-207.

[44] Ando K, Yamaguchi M, Yamamoto S, Toshito T, Kawachi N 2017, Development of a low-energy x-ray camera for the imaging of secondary electron bremsstrahlung x-ray emitted during proton irradiation for range estimation, Phys. Med. Biol. 62(12): p. 5006-5020.

[45] Yamaguchi M, Torikai K, Kawachi N, Shimada H, Satoh T, Nagao Y, Fujimaki S, Kokubun M, Watanabe S, Takahashi T, Arakawa K, Kamiya T, Nakano T 2012, Beam range estimation by measuring bremsstrahlung, Phys. Med. Biol. 57(10): p. 2843-2856.

[46] Yamaguchi M, Nagao Y, Ando K, Yamamoto S, Sakai M, Parajuli RK, Arakawa K, Kawachi N 2018, Imaging of monochromatic beams by measuring secondary electron bremsstrahlung for carbon-ion therapy using a pinhole x-ray camera, Phys. Med. Biol. 63(4): 045016.

[47] Assmann W, Kellnberger S, Reinhardt S, Lehrack S, Edlich A, Thirolf PG, Moser M, Dollinger G, Omar M, Ntziachristos V, Parodi K 2015, Ionoacoustic characterization of the proton Bragg peak with submillimeter accuracy, Med. Phys. 42(2): p. 567-574.

[48] Ahmad M, Xiang L, Yousefi S, Xing L 2015, Theoretical detection threshold of the proton-acoustic range verification technique, Med. Phys. 42(10): p. 5735-5744.

[49] Jones KC, Witztum A, Sehgal CM, Avery S 2014, Proton beam characterization by proton-induced acoustic emission: Simulation studies, Phys. Med. Biol. 59(21): p. 6549-6563.

[50] Grusell E, Medin J 2000, General characteristics of the use of silicon diode detectors for clinical dosimetry in proton beams, Phys. Med. Biol. 45(9): p. 2573-2582.

[51] Rosenfeld AB 2002, MOSFET dosimetry on modern radiation oncology modalities, Radiat. Prot. Dosimetry 101(1-4): p. 393-398.

[52] Lu HM, Mann G, Cascio E 2010, Investigation of an implantable dosimeter for single-point water equivalent path length verification in proton therapy, Med. Phys. 37(11): p. 5858-5866.

[53] Archambault L, Briere TM, Pönisch F, Beaulieu L, Kuban DA, Lee A, Beddar S 2010, Toward a real-time in vivo dosimetry system using plastic scintillation detectors, IJROBP 78(1): p. 280-287.

[54] Wootton L, Holmes C, Sahoo N, Beddar S 2015, Passively scattered proton beam entrance dosimetry with a plastic scintillation detector, Phys. Med. Biol. 60(3): p. 1185-1198.

[55] Zullo JR, Kudchadker RJ, Zhu XR, Sahoo N, Gillin MT 2010, LiF TLD-100 as a dosimeter in high energy proton beam therapy–Can it yield accurate results?, Med. Dosim. 35(1): p. 63-66.

[56] Sahoo N 2015, In vivo dosimetry for proton therapy, 2015 AAPM Summer School.

[57] Krimmer J, Dauvergne D, Létang JM, Testa É 2018, Prompt-gamma monitoring in hadrontherapy: A review, Nucl. Instrum. Methods Phys. Res. A 878: p. 58-73.

[58] Hueso-González F 2015, Nuclear methods for real-time range verification in proton therapy based on prompt gamma-ray imaging, Doctorate Thesis, Technische Universität Dresden / OncoRay.

[59] Hueso-González F, Rabe M, Ruggieri T, Bortfeld T, Verburg JM 2018, A full-scale clinical prototype for proton range verification using prompt gamma-ray spectroscopy, Phys. Med. Biol. 63(18): 185019.

[60] Pausch G, Petzoldt J, Berthel M, Enghardt W, Fiedler F, Golnik C, Hueso-González F, Lentering R, Römer K, Ruhnau K, Stein J, Wolf A, Kormoll T 2016, Scintillator-based high-throughput fast timing spectroscopy for real-time range verification in particle therapy, IEEE Trans. Nucl. Sci. 63(2): p. 664-672.

[61] Rinscheid A, Berthold J, Enghardt W, Golnik C, Fiedler F, Hueso-Gonzáles F, Kormoll T, Lentering R, Petzoldt J, Römer K, Ruhnau K, Stein J, Werner T, Wolf A, Reichert D, Pausch G 2016, Characterization of a fast timing and energy spectroscopy system for real-time range verification in particle therapy, IEEE NSS MIC paper N29-20.

[62] Rinscheid A 2016, Steps towards the clinical implementation of a digital spectrometer system for range verification in proton therapy, Master Thesis, Martin-Luther-Universität Halle / Technische Universität Dresden / OncoRay.

[63] Berthold J 2018, Single Plane Compton Imaging for Range Verification in Proton Therapy- A Proof-of-Principle Study, Master Thesis, Technische Universität Dresden / OncoRay.

[64] Buch F 2018, Measurement of the emission spectrum of prompt photons when irradiating homogeneous targets with protons, Master Thesis, Technische Universität Dresden / OncoRay.

[65] Kraan AC 2015, Range verification methods in particle therapy: Underlying physics and Monte Carlo modeling, Front. Oncol. 5(150): p. 1-27.

[66] Knoll GF 2000, Radiation Detection and Measurement, 3rd Ed., John Wiley & Sons, Inc.

[67] Bethe H 1930, Zur theorie des durchgangs scneller korpuskularstrahlen durch materie, Ann. Phys. 397(3): p. 325-400.

[68] Bloch F 1933, Zur bremsung rasch bewegter teilchen beim durchgang durch materie, Ann. Phys. 408(3): p. 285-320.

[69] Durante M, Paganetti H 2016, Nuclear physics in particle therapy: A review, Rep. Prog. Phys. 79(9): 096702.

[70] Ziegler JF 1999, The stopping of energetic light ions in elemental matter, J. Appl. Phys. 85(3): p. 1249-1272.

[71] Leo WR 1994, Techniques for Nuclear and Particle Physics Experiments, Second ed New York NY, Springer Verlag.

[72] Olive KA, Particle Data Group 2014, Review of Particle Physics, Chin. Phys. C38(9): 090001.

[73] Lindhard J, Nielsen V, Scharff M, Thomsen PV 1963, Integral equations governing radiation effects, Mat. Fys. Medd. Dan. Vid. Selsk. 33(10).

[74] Ziegler JF, Biersack JP, Littmark U, Anderson HH 1977, The Stopping and Ranges of Ions in Matter, New York Pergamon Press.

[75] Vavilov PV 1957, Ionizational losses of high energy heavy particles, Zh. Eksp. Teor. Fiz. 32: p. 920-923.

[76] Bohr N 1940, Scattering and stopping of fission fragments, Phys. Rev. 58: p. 654-655.

[77] Ahlen SP 1980, Theoretical and experimental aspects of the energy loss of relativistic heavily ionizing particles, Rev. Mod. Phys. 52: p. 121-173.

[78] Payne MG 1969, Energy straggling of heavy charged particles in thick absorbers, Phys. Rev. 185(2): p. 611-623.

[79] Rossi B 1952, High-Energy Particles, Prentice-Hall Physics Series, Prentice-Hall, Englewood Cliffs, NJ.

[80] Molière 1948, Theorie der streuung schneller geladener teilchen II, mehrfach-und vielfachstreuung, Z. Naturforsch. A 3A: p. 78-97.

[81] Lewis HW 1950, Multiple scattering in an infinite medium, Phys. Rev. 78(5): p. 526-529.

[82] Highland VL 1975, Some practical remarks on multiple scattering, Nucl. Instrum. Methods Phys. Res. 129: p. 497-499.

[83] Highland VL 1979, Erratum, Nucl. Instrum. Methods Phys. Res. 161: p. 171.

[84] Gottschalk B, Koehler AM, Schneider RJ, Sisterson JM, Wagner MS 1993, Multiple Coulomb scattering of 160 MeV protons, Nucl. Instrum. Methods Phys. Res. B 74(4): p. 467-490.

[85] International Atomic Energy Agency 2009, Cyclotron Produced Radionuclides: Physical Characteristics and Production Methods, Technical Reports Series No. 468, Vienna.

[86] Attix FH 2004, Introduction to Radiological Physics and Radiation Dosimetry, WILEY-VCH Verlag GmbH & KGaA, Weinheim.

[87] Haettner E, Iwase H, Krämer M, Kraft G, Schardt D 2013, Experimental study of nuclear fragmentation of 200 and 400 MeV/u ^{12}C ions in water for applications in particle therapy, Phys. Med. Biol. 58(23): p. 8265-8279.

[88] Serber R 1947, Nuclear reactions at high energies, Phys. Rev. 72: p. 1114-1115.

[89] Tommasino F, Scifoni E, Durante M 2015, New ions for therapy, Int. J. of Particle Ther. doi: 10.14338/IJPT-15-00027.1.

[90] Knäusl B, Fuchs H, Dieckmann K, Georg D 2016, Can particle beam therapy be improved using helium ions? – a planning study focusing on pediatric patients, Acta Oncol. 55(6): p. 751-759.

[91] Krämer M, Scifoni E, Schuy C, Rovituso M, Tinganelli W, Maler A, Kaderka R, Kraft-Weyrather W, Brons S, Tessonnier T, Parodi K, Durante M 2016, Helium ions for radiotherapy? Physical and biological verifications of a novel treatment modality, Med. Phys. 43(4): p. 1995-2004.

[92] Rovituso M, Tessa CL 2017, Nuclear interactions of new ions in cancer therapy: Impact on dosimetry, Transl. Cancer Res. 6(Suppl 5): p. S914-S933.

[93] Sokol O, Scifoni E, Tinganelli W, Kraft-Weyrather W, Wiedemann J, Maier A, Boscolo D, Friedrich T, Brons S, Durante M, Krämer M 2017, Oxygen beams for therapy: Advanced

biological treatment planning and experimental verification, Phys. Med. Biol. 62(19): p. 7798-7813.

[94] Mattei I, Bini F, Collamati F, De Lucia E, Frallicciardi PM, Iarocci E, Mancini-Terracciano C, Marafini M, Muraro S, Paramatti R, Patera V, Piersanti L, Pinci D, Rucinski A, Russomando A, Sarti A, Sciubba A, Solfaroli Camillocci E, Toppi M, Traini G, Voena C, Battistoni G 2017, Secondary radiation measurements for particle therapy applications: prompt photons produced by ^{4}He, ^{12}C and ^{16}O ion beams in a PMMA target, Phys. Med. Biol. 62(4): p. 1438-1455.

[95] Paganetti H, Niemierko A, Ancukiewicz M, Gerweck LE, Goitein M, Loeffler JS, Sutt HD 2002, Relative biological effectiveness (RBE) values for proton beam therapy, Int. J. Radiation Oncology Biol. Phys. 53(2): p. 407-421.

[96] Skarsgard LD 1998, Radiobiology with heavy charged particles: A historical review, Phys. Med. 14(Suppl 1): p. 1-19.

[97] Weyrather WK, Kraft G 2004, RBE of carbon ions: Experimental data and the strategy of RBE calculation for treatment planning, Radiother. Oncol. 73(Suppl 2): p. S161-S169.

[98] Saunders WM, Chen GTY, Austin-Seymour M, Castro JR, Collier JM, Gauger G, Gutin P, Phillips TL, Pitluck S, Walton RE, Zink SR 1985, Precision, high dose radiotherapy. II. Helium ion treatment of tumors adjacent to critical central nervous system structures, Int. J. Radiation Oncology Biol. Phys. 11: p. 1339-1347.

[99] Burigo L, Pshenichnov I, Mishustin I, Bleicher M 2013, Microdosimetry spectra and RBE of ^{1}H, ^{4}He, ^{7}Li and ^{12}C nuclei in water studied with Geant4 2014, Nucl. Instrum. Methods Phys. Res. B 320: p. 89-99.

[100] Allen C, Borak TB, Tsujii H, Nickoloff JA 2011, Heavy charged particle radiobiology: Using enhanced biological effectiveness and improved beam focusing to advance cancer therapy, Mutat. Res. 711(1-2): p. 150-157.

[101] Schwaab J, Brons S, Fieres J, Parodi K 2011, Experimental characterization of lateral profiles of scanned proton and carbon ion pencil beams for improved beam models in ion therapy treatment planning, Phys. Med. Biol. 56(24): p. 7813-7827.

[102] Kantemiris I, Karaiskos P, Papagiannis P, Angelopoulos A 2011, Dose and dose averaged LET comparison of ^{1}H, ^{4}He, ^{6}Li, ^{8}Be, ^{10}B, ^{12}C, ^{14}N, and ^{16}O ion beams forming a spread-out Bragg peak, Med. Phys. 38(12): p. 6585-6591.

[103] Desouky O, Zhou G 2016, Biophysical and radiobiological aspects of heavy charged particles, J. Taibah Univ. Sci. 10(2): p. 187-194.

[104] Tessonnier T, Mairani A, Brons S, Haberer T, Debus J, Parodi K 2017, Experimental dosimetric comparison of ^{1}H, ^{4}He, ^{12}C and ^{16}O scanned ion beams, Phys. Med. Biol. 62(10): p. 3958-3982.

[105] Tessonnier T, Mairani A, Chen W, Sala P, Cerutti F, Ferrari A, Haberer T, Debus J, Parodi K 2018, Proton and helium ion radiotherapy for meningioma tumors: A Monte Carlo-based treatment planning comparison, Radiation Oncology 13(2): p. 1-10.

[106] Kempe J, Gudowska I, Brahme A 2007, Depth absorbed and LET distributions of therapeutic ^{1}H, ^{4}He, ^{7}Li, and ^{12}C beams, Med. Phys. 34(1): p. 183-192.

[107] Tessonnier T, Mairani A, Brons S, Sala P, Cerutti F, Ferrari A, Heberer T, Debus J, Parodi K 2017, Helium ions at the Heidelberg ion beam therapy center: Comparisons between FLUKA Monte Carlo code predictions and dosimetric measurements, Phys. Med. Biol. 62(16): p. 6784-6803.

[108] Mein S, Dokic I, Klein C, Tessonnier T, Böhlen TT, Magro G, Bauer J, Ferrari A, Parodi K, Haberer T, Debus J, Abdollahi A, Mairani A 2019, Biophysical modeling and experimental validation of relative biological effectiveness (RBE) for ^{4}He ion beam therapy, Radiation Oncology 14(123): p. 1-16.

[109] Tsoulfanidis N, Landsberger S 2010, Measurement and Detection of Radiation, Boca Raton, CRC Press.

[110] Klett A, Haefner P, Reuter W 2006, Comparison of scintillation and gas filled detectors for contamination monitoring, IAEA Conference Record 39(29): 39075332.

[111] Saha GB 2006, Scintillation and Semiconductor Detectors, In: Physics and Radiobiology of Nuclear Medicine. Springer, New York, NY.

[112] Flyckt SO, Marmonier C 2002, Photomultiplier tubes basics and applications, Photonis p. 1-300.

[113] Hamamatsu Photonics K. K. 2007, Photomultiplier tubes basics and applications, Third Edition (Edition 3a) p. 1-308.

[114] SensL 2017, An Introduction to the Silicon Photomultiplier, Introduction to SiPM Technical Note, Rev. 6.0 p. 1-16.

[115] Iltis A, Mayhugh MR, Menge P, Rozsa CM, Selles O, Solovyev V 2006, Lanthanum halide scintillators: Properties and applications, Nucl. Instrum. Methods Phys. Res. A 563: p. 359-363.

[116] Moszyński M, Gierlik M, Kapusta M, Nassalski A, Szczęśniak T, Fontaine Ch, Lavoute P 2006, New Photonis XP20D0 photomultiplier for fast timing in nuclear medicine, Nucl. Instrum. Methods Phys. Res. A 567(1): p. 31-35.

[117] Choong WS, Derenzo SE, Moses WW 2005, Evaluation of production samples of the scintillators $LaBr_3$:Ce and $LaCl_3$:Ce. IAEA Conference Record 39(36): 39090869.

[118] Loher B, Savran D, Fiori E, Miklavec M, Pietralla N, Vancelj M 2012, High count rate γ-ray spectroscopy with $LaBr_3$:Ce scintillation detectors, Nucl. Instrum. Methods Phys. Res. A 686: p. 1-6.

[119] Weisshaar D, Wallace MS, Adrich P, Bazin D, Campbell CM, Cook JM, Ettenauer S, Gade A, Glasmacher T, McDaniel S, Obertelli A, Ratkiewicz A, Rogers AM, Siwek K, Tornga SR 2008, $LaBr_3$:Ce scintillators for in-beam gamma-ray spectroscopy with fast beams of rare isotopes, Nucl. Instrum. Methods Phys. Res. A 594: p. 56-60.

[120] Schmall JP, Surti S, Karp J 2015, Characterization of stackedcrystal PET detector designs for measurement of both TOF and DOI, Phys. Med. Biol. 60(9): p. 3549–3565.

[121] Shah KS, Glodo J, Higgins W, Loef EVDV, Moses WW, Derenzo SE, Weber MJ 2005, $CeBr_3$ scintillators for gamma-ray spectroscopy, IEEE Trans. Nucl. Sci. 52(6): p. 3157–3159.

[122] Fraile LM, Mach H, Vedia V, Olaizola B, Paziy V, Picado E, Udías JM 2013, Fast timing study of a $CeBr_3$ crystal: Time resolution below 120 ps at ^{60}Co energies, Nucl. Instrum. Methods Phys. Res. A 701: p. 235-242.

[123] Roemer K, Pausch G, Bemmerer D, Berthel M, Dreyer A, Golnik C, Hueso-González F, Kormoll T, Petzoldt J, Rohling H, Thirolf P, Wagner A, Wagner L, Weinberger D, Fiedler F 2015, Characterization of scintillator crystals for usage as prompt gamma monitors in particle therapy, JINST 10: P10033.

[124] Quarati FGA, Dorenbos P, Viezen JVD, Owens A, Selle M, Parthier L, Schotanus P 2013, Scintillation and detection characteristics of high-sensitivity $CeBr_3$ gamma-ray spectrometers, Nucl. Instrum. Methods Phys. Res. A 729: p. 596-604.

[125] Giaz A, Fossati V, Hull G, Camera F, Blasi N, Brambilla S, Ceruti S, Cherepy N, Million B, Pellegri L, Riboldi S 2015, Characterization of new scintillators: SrI_2:Eu, $CeBr_3$, GYGAG:Ce and CLYC:Ce, J. Phys. Conf. Ser. 620(1): 012003.

[126] Asztalos S, Hennig W 2010, CLYC versus stilbene: Optimization and comparison of two neutron-gamma discriminating scintillators, available: https://www.xia.com/Papers/CLYC_IEEE10cr.pdf.

[127] Coupland DDS, Budden BS, Stonehill LC 2015, Thermal variance investigation of scintillation mechanisms of $Cs_2LiLaBr_{6-x}Cl_x$:Ce (CLLBC) and Cs_2LiYBr_6:Ce (CLYB), IEEE NSS MIC p. 1-5.

[128] Glodo J, van Loef E, Hawrami R, Higgins WM, Churilov A, Shirwadkar U, Shah KS 2011, Selected properties of Cs_2LiYCl_6, $Cs_2LiLaCl_6$, and $Cs_2LiLaBr_6$ scintillators, IEEE Trans. Nucl. Sci. 58(1): p. 333-338.

[129] Glodo J, Hawrami R, Loef EV, Shirwadkar U, Shah KS 2012, Pulse shape discrimination with selected elpasolite crystals, IEEE Trans. Nucl. Sci. 59(5): p. 2328-2333.

[130] Kim HS, Smith MB, Koslowsky MR, Kwak SW, Ye SJ, Kim G 2017, Characterization of a CLYC detector and validation of the Monte Carlo simulation by measurement experiments, J. Radiat. Prot. Res. 42(1): p. 48-55.

[131] Liang F, Brands H, Hoy L, Preston J, Smith J 2018, Lithium-loaded scintillators coupled to a custom-designed silicon photomultiplier array for neutron and gamma-ray detection, IEEE Trans. Nucl. Sci. 65(8): p. 2162-2168.

[132] Camera F, Giaz A 2015, New scintillator materials for future and present facilities, AIP Conf. Proc. doi: 10.1063/1.4909582.

[133] Alekhin MS, de Haas JTM, Khodyuk IV, Krämer KW, Menge PR, Ouspenski V, Dorenbos P 2013, Improvements of γ-ray energy resolution of $LaBr_3:Ce^{3+}$ scintillation detectors by Sr^{2+} and Ca^{2+} co-doping, Appl. Phys. Lett. 102(16): 161915.

[134] Shah KS, Glodo J, Klugerman M, Moses WW, Derenzo SE, Weber MJ 2003, $LaBr_3$:Ce scintillators for gamma-ray spectroscopy, IEEE Trans. Nucl. Sci. 50(6): p. 2410-2413.

[135] Shah KS, Glodo J, Klugerman M, Cirignano L, Moses WW, Derenzo SE, Weber MJ 2003, $LaCl_3$:Ce scintillator for γ-ray detection, Nucl. Instrum. Methods Phys. Res. A 505: p. 76-81.

[136] Oberstedt A, Oberstedt S, Billnert R, Geerts W, Hambsch FJ, Karlsson J 2012, Identification of prompt fission γ-rays with lanthanum-chloride scintillation detectors, Nucl. Instrum. Methods Phys. Res. A 668: p. 14-20.

[137] van Loef EV, Wilson CM, Cherepy NJ, Hull G, Payne SA, Choong WS, Moses WW, Shah KS 2009, Crystal growth and scintillation properties of strontium iodide scintillators, IEEE Trans. Nucl. Sci. 56(3): p. 869-872.

[138] Guss PP, Stampahar TG, Mukhopadhyay S, Barzilov A, Guckes A 2014, Scintillation properties of a $Cs_2LiLa(Br_6)_{90\%}(Cl_6)_{10\%}:Ce^{3+}$ (CLLBC) crystal, SPIE Invited Paper doi: 10.1117/12.2060204.

[139] Stichelbaut F, Jongen Y 2003, Verification of the proton beams position in the patient by detection of prompt gamma-ray emission, PTCOG-39 San Francisco CA.

[140] Polf JC, Peterson S, Ciangaru G, Gillin M, Beddar S 2009, Prompt gamma-ray emission from biological tissues during proton irradiation: A preliminary study, Phys. Med. Biol. 54(3): p. 731-743.

[141] Kurosawa S, Kubo H, Ueno K, Kabuki S, Iwaki S, Takahashi M, Taniue K, Higashi N, Miuchi K, Tanimori T, Kim D, Kim J 2012, Prompt gamma detection for range verification in proton therapy, Curr. Appl. Phys. 12: p. 364-368.

[142] Testa M, Bajard M, Chevallier M, Dauvergne D, Freud N, Henriquet P, Karkar S, Le Foulher F, Létang JM, Plescak R, Ray C, Richard MH, Schardt D, Testa E 2010, Real-time monitoring of the Bragg-peak position in ion therapy by means of single photon detection, Radiat. Environ. Biophys. 49: p. 337-343.

[143] Verburg JM, Shih HA, Seco J 2012, Simulation of prompt gamma-ray emission proton radiotherapy, Phys. Med. Biol. 57(17): p. 5459-5472.

[144] Lee E, Polf JC, Mackin DS, Beddar S, Dolney D, Ainsley C, Kassaee A, Avery S 2014, Study of the angular dependence of a prompt gamma detector response during proton radiation therapy, Int. J. Particle Ther. 1(3): p. 731-744.

[145] Biegun AK, Seravalli E, Lopes PC, Rinaldi I, Pinto M, Oxley DC, Dendooven P, Verhaegen F, Parodi K, Crespo P, Schaart DR 2012, Time-of-flight neutron rejection to improve prompt gamma imaging for proton range verification: A simulation study, Phys. Med. Biol. 57(20): p. 6429-6444.

[146] Testa E, Bajard M, Chevallier M, Dauvergne D, Le Foulher F, Freud N, Létang JM, Poizat JC, Ray C, Testa M 2008, Monitoring the Bragg peak location of 73 MeV/u carbon ions by means of prompt γ-ray measurements, Appl. Phys. Lett. 93: 093506.

[147] Testa E, Bajard M, Chevallier M, Dauvergne D, Le Foulher F, Freud N, Létang JM, Poizat JC, Ray C, Testa M 2009, Dose profile monitoring with carbon ions by means of prompt-gamma measurements, Nucl. Instrum. Methods Phys. Res. B 267: p. 993-996.

[148] Pinto M, Bajard M, Brons S, Chevallier M, Dauvergne D, Dedes G, De Rydt M, Freud N, Krimmer J, La Tessa C, Létang JM, Parodi K, Pleskač R, Prieels D, Ray C, Rinaldi I, Roellinghoff F, Schardt D, Testa E, Testa M 2015, Absolute prompt-gamma yield measurements for ion beam therapy monitoring, Phys. Med. Biol. 60(2): p. 565-594.

[149] Kim D, Yim H, Kim JW 2009, Pinhole camera measurements of prompt gamma-ray for detection of beam range variation in proton therapy, J. Korean Phys. Soc. 55(4): p. 1673-1676.

[150] Smeets J, Roellinghoff F, Prieels D, Stichelbaut F, Benilov A, Busca P, Fiorini C, Peloso R, Basilavecchia M, Frizzi T, Dehaes JC, Dubus A 2012, Prompt gamma imaging with slit camera for real-time range control in proton therapy, Phys. Med. Biol. 57(11): p. 3371-3405.

[151] Bom V, Joulaeizadeh L, Beekman F 2012, Real-time prompt gamma monitoring in spot-scanning proton therapy using imaging through a knife-edge-shaped slit, Phys. Med. Biol. 57(2): p. 297-308.

[152] Richter C, Pausch G, Barczyk S, Priegnitz M, Keitz I, Thiele J, Smeets J, Stappen FV, Bombelli L, Fiorini C, Hotoiu L, Perali I, Prieels D, Enghardt W, Baumann M 2016, First clinical application of a prompt gamma based in vivo proton range verification system, Radiother. Oncol. 118: p. 232-237.

[153] Kormoll T, Fiedler F, Schöne S, Wüstemann J, Zuber K, Enghardt W 2011, A Compton imager for in-vivo dosimetry of proton beams – A design study, Nucl. Instrum. Methods Phys. Res. 626-627: p. 114-119.

[154] Richard MH, Chevallier M, Dauvergne D, Freud N, Henriquet P, Le Foulher F, Létang JM, Montarou G, Ray C, Roellinghoff F, Testa E, Testa M, Walenta AH 2011, Design guidelines for a double scattering Compton camera for prompt-γ imaging during ion beam therapy: A Monte Carlo simulation study, IEEE Trans. Nucl. Sci. 58(1): p. 87-94.

[155] Peterson SW, Robertson D, Polf J 2010, Optimizing a three-stage Compton camera for measuring prompt gamma rays emitted during proton radiotherapy, Phys. Med. Biol. 55(22): p. 6841-6856.

[156] Polf JC, Avery S, Mackin DS, Beddar S 2015, Imaging of prompt gamma rays emitted during delivery of clinical proton beams with a Compton camera: Feasibility studies for range verification, Phys. Med. Biol. 60(18): p. 7085-7099.

[157] Kim SH, Park J, Ku Y, Lee HS, Kim Y, Kim CH, Jeong H 2019, Improvement of statistics in proton beam range measurement by merging prompt gamma distributions: A preliminary study, J. Radiat. Prot. Res. 44(1): p. 1-7.

[158] Perali I, Celani A, Bombelli L, Fiorini C, Camera F, Clementel E, Henrotin S, Janssens G, Prieels D, Roellinghoff F, Smeets J, Stichelbaut F, Stappen FV 2014, Prompt gamma imaging of proton pencil beams at clinical dose rate, Phys. Med. Biol. 59(19): p. 5849-5871.

[159] Xie Y, Bentefour EH, Janssens G, Smeets J, Stappen FV, Hotoiu L, Yin L, Dolney D, Avery S, O'Grady F, Prieels D, McDonough J, Solberg TD, Lustig RA, Lin A, Teo BKK 2017, Prompt gamma imaging for in vivo range verification of pencil beam scanning proton therapy, Int. J. Radiation Oncol. Biol. Phys. 99(1): p. 210-218.

[160] Petzoldt J, Janssens G, Nenoff L, Richter C, Smeets J 2018, Correction of geometrical effects of a knife-edge slit camera for prompt gamma-based range verification in proton therapy, Instruments doi: 10.3390/instruments2040025.

[161] Draeger E, Mackin D, Peterson S, Chen H, Avery S, Beddar S, Polf JC 2019, Three-dimensional prompt gamma imaging for proton beam range verification, Phys. Med. Biol. 63(3): 035019.

[162] Yao Z, Xiao Y, Chen Z, Wang B, Hou Q 2019, Compton-based prompt gamma imaging using ordered origin ensemble algorithm with resolution recovery in proton therapy, Sci. Rep. 9(1): 1133.

[163] Andreyev A, Celler A, Ozsahin I, Sitek A 2016, Resolution recovery for Compton camera using origin ensemble algorithm, Med. Phys. 43(8): p. 4866-4876.

[164] Kabuki S, Hattori K, Kohara R, Kunieda E, Kubo A Kubo H, Miuchi K, Nakahara T, Nagayoshi T, Nishimura H, Okada Y, Orito R, Sekiya H, Shirahata T, Takada A, Tanimori T, Ueno K 2007, Development of Electron Tracking Compton Camera using micro pixel gas chamber for medical imaging, Nucl. Instrum. Methods Phys. Res. A 580: p. 1031-1035.

[165] Matsuoka Y, Tanimori T, Kubo H, Takada A, Parker JD, Mizumoto T, Mizumura Y, Iwaki S, Sawano T, Komura S, Kishimoto T, Oda M, Takemura T, Miyamoto S, Sonoda S, Tomono D, Miuchi K, Kabuki S, Kurosawa S 2015, Performance of a new electron-tracking Compton camera under intense radiations from a water target irradiated with a proton beam, JINST 10(1): C01053.

[166] Kim CH, Park JH, Seo H, Lee HR 2012, Gamma electron vertex imaging and application to beam range verification in proton therapy, Med. Phys. 39(2): p. 1001-1005.

[167] Lee HR, Kim SH, Park JH, Jung WG, Lim H, Kim CH 2017, Prototype system for proton beam range measurement based on gamma electron vertex imaging, Nucl. Instrum. Methods Phys. Res. A 857: p. 82-97.

[168] Kim CH, Lee HR, Kim SH, Part JH, Cho S, Jung WG 2018, Gamma electron vertex imaging for in-vivo beam-range measurement in proton therapy: Experimental results, Appl. Phys. Lett. 113(11): 114101.

[169] Rohling H, Priegnitz M, Schoene S, Schumann A, Enghardt W, Hueso-González F, Pausch G, Fiedler F 2017, Requirements for a Compton camera for in vivo range verification of proton therapy, Phys. Med. Biol. 62(7): p. 2795-2811.

[170] Verburg JM, Seco J 2014, Proton range verification through prompt gamma-ray spectroscopy, Phys. Med. Biol. 59(23): p. 7089-7106.

[171] Golnik C, Hueso-González F, Müller A, Dendooven P, Enghardt W, Fiedler F, Kormoll T, Roemer K, Petzoldt J, Wagner A, Pausch G 2014, Range assessment in particle therapy based on prompt γ-ray timing measurements, Phys. Med. Biol. 59(18): p. 5399-5422.

[172] Werner T, Berthold J, Enghardt W, Hueso-González F, Kogler T, Petzoldt J, Richter C, Rinscheid A, Römer K, Ruhnau K, Smeets J, Stein J, Straessner A, Wolf A, Pausch G 2017, Range verification in proton therapy gamma-ray timing (PGT): Steps toward clinical implementation, IEEE NSS MIC doi: 10.1109/NSSMIC.2017.8532807.

[173] Krimmer J, Angellier G, Balleyguier L, Dauvergne D, Freud N, Hérault J, Létang JM, Mathez J, Pinto M, Testa E, Zoccarato Y 2017, A cost-effective monitoring technique in particle therapy via uncollimated prompt gamma peak integration, Appl. Phys. Lett. 110(15): 154102.

[174] Robert C, Dedes G, Battistoni G, Böhlen TT, Buvat I, Cerutti F, Chin MPW, Ferrari A, Gueth P, Kurz C, Lestand L, Mairani A, Montarou G, Nicolini R, Ortega PG, Parodi K, Prezado Y, Sala PR, Sarrut D, Testa E 2013, Distributions of secondary particles in proton and carbon-ion therapy: A comparison between GATE/Geant4 and FLUKA Monte Carlo codes, Phys. Med. Biol. 58(9): p. 2879-2899.

[175] Dedes G, Parodi K 2015, Monte Carlo simulations of particle interactions with tissue in carbon ion therapy, Int. J. Particle Ther. doi: 10.14338/IJPT-15-00021.

[176] Schumann A, Petzoldt J, Dendooven P, Enghardt W, Golnik C, Hueso-González F, Kormoll T, Pausch G, Roemer K, Fiedler F 2015, Simulation and experimental verification of prompt gamma-ray emissions during proton irradiation, Phys. Med. Biol. 60(10): p. 4197-4207.

[177] Qin N, Pinto M, Tian Z, Dedes G, Pompos A, Jiang SB, Parodi K, Jia X 2017, Initial development of goCMC: A GPU-oriented fast cross-platform Monte Carlo engine for carbon ion therapy, Phys. Med. Biol. 62(9): p. 3682-3699.

[178] Giantsoudi D, Schuemann J, Jia X, Dowdell S, Jiang S, Paganetti H 2015, Validation of a GPU-based Monte Carlo code (gPMC) for proton radiation therapy: clinical cases study, Phys. Med. Biol. 60(6): p. 2257-2269.

[179] Seco J, Verhaegen F, Hendee WR 2013, Monte Carlo Techniques in Radiation Therapy, Taylor & Francis Group, LLC.

[180] Sterpin E, Janssens G, Smeets J, Stappen FV, Prieels D, Priegnitz M, Perali I, Vynckier S 2015, Analytical computation of prompt gamma ray emission and detection for proton range verification, Phys. Med. Biol. 60(12): p. 4915-4946.

[181] ICRU 2001, ICRU Report 63, Nuclear data for neutron and proton radiotherapy and for radiation protection, International Commission on Radiation Units and Measurements, Bethesda, MD USA.

[182] Agostinelli S, Allison J, Amako K, Apostolakis J, Araujo H, Arce P, Asai M, Axen D et al. 2003, Geant4–a simulation toolkit, Nucl. Instrum. Methods Phys. Res. A. 506(3): p. 250-303.

[183] Allison J, Amako K, Apostolakis J, Araujo H, Arce Dubois P, Asai M, Barrand G, Capra R et al. 2006, Geant4 developments and applications, IEEE Trans. Nucl. Sci. 53(1): p. 270-278.

[184] Perl J, Shin J, Schümann J, Faddegon B, Paganetti H 2012, TOPAS: An innovative proton Monte Carlo platform for research and clinical applications, Med. Phys. 39(11): p. 6818-6837.

[185] CERN, Geant4 A Simulation Toolkit, Geant4, data accessed: 13/05/15 http://geant4.cern.ch/.

[186] CERN, Geant4 A Simulation Toolkit, About Geant4, data accessed: 10/09/15 http://geant4.web.cern.ch/geant4/support/about.shtml.

[187] TOPAS Documentation. Release 3.1 2018. TOPAS MC Inc.

[188] Aso T, Kimura A, Tanaka S, Yoshida H, Kanematsu N, Sasaki T, Akagi T 2005, Verification of the dose distribution with Geant4 simulation for proton therapy, IEEE Trans. Nucl. Sci. 52(4): p. 896-901.

[189] Cirrone GAP, Cuttone G, Di Rosa F, Guatelli S, Mascialino B, Pia MG, Russo G 2006, Validation of Geant4 physics models for the simulation of the proton Bragg peak, IEEE NSS Conference Record doi: 10.1109/NSSMIC.2006.355969.

[190] Jarlskog CZ, Paganetti H 2008, Physics settings for using the Geant4 toolkit in proton therapy, IEEE Trans. Nucl. Sci. 55(3): p. 1018-1025.

[191] Grevillot L, Frisson T, Zahra N, Bertrand D, Stichelbaut F, Freud N, Sarrut D 2010, Optimization of GEANT4 settings for proton pencil beam scanning simulations using GATE, Nucl. Instrum. Methods Phys. Res. B 268(20): p. 3295-3305.

[192] Hall DC, Makarova A, Paganetti H, Gottschalk B 2015, Validation of nuclear models in Geant4 using the dose distribution of a 177 MeV proton pencil beam, Phys. Med. Biol. 61(1): p. N1-N10.

[193] Resch AF, Elia A, Fuchs H, Carlino A, Palmans H, Stock M, Georg D, Grevillot L 2019, Evaluation of electromagnetic and nuclear scattering models in GATE/Geant4 for proton therapy, Med. Phys. 46(5): p. 2444-2456.

[194] Lechner A, Ivanchenko VN, Knobloch J 2010, Validation of recent Geant4 physics models for application in carbon ion therapy, Nucl. Instrum. Methods Phys. Res. B 268: p. 2343-2354.

[195] Mishustin I, Pshenichnov I, Greiner W 2010, Modelling heavy-ion energy deposition in extended media, Eur. Phys. J. D. 60: p. 109-114.

[196] Pshenichnov I, Botvina A, Mishustin I, Greiner W 2010, Nuclear fragmentation reactions in extended media studied with the GEANT4 toolkit, Nucl. Instrum. Methods Phys. Res. B 268(15): p. 604-615.

[197] Böhlen TT, Cerutti F, Dosanjh M, Ferrari A, Gudowska I, Mairani A, Quesada JM 2010, Benchmarking nuclear models of FLUKA and GEANT4 for carbon ion therapy, Phys. Med. Biol. 55(19): p. 5833-5847.

[198] Toshito T, Bagulya A, Lechner A, Ivanchenko V, Maire M, Akagi T, Yamashita T 2011, Validation of new Geant4 electromagnetic physics models for ion therapy applications, Progr. Nucl. Sci. Technol. 2: p. 918-922.

[199] Bolst D, Cirrone GAP, Cuttone G, Folger G, Incerti S, Ivanchenko V, Koi T, Mancusi D, Pandola L, Romano F, Rosenfeld AB, Guatelli S 2017, Validation of Geant4 fragmentation for heavy ion therapy, Nucl. Instrum. Methods Phys. Res. A 869: p. 68-75.

[200] Pshenichnov I, Larionov A, Mishustin I, Greiner W 2007, PET monitoring of cancer therapy with 3He and 12C beams: A study with the GEANT4 toolkit, Phys. Med. Biol. 52(24): p. 7295-7312.

[201] Perl J, Shin J, Schümann J, Faddegon B, Paganetti H 2012, TOPAS: An innovative proton Monte Carlo platform for research and clinical applications, Med. Phys. 39(11): p. 6818-6837.

[202] Testa M, Min CH, Verburg JM, Schümann J, Lu HM, Paganetti H 2014, Range verification of passively scattered proton beams based on prompt gamma time patterns, Phys. Med. Biol. 59(15): p. 4181-4195.

[203] Verburg JM, Grassberger C, Dowdell S, Schuemann J, Seco J, Paganetti H 2016, Automated Monte Carlo simulation of proton therapy treatment plans, Technol. Cancer Res. Treat. 15(6): p. NP35-NP46.

[204] Prusator M, Ahmad S, Chen Y 2017, TOPAS simulation of the Mevion S250 compact proton therapy unit, J. Appl. Clin. Med. Phys. 18(3): p. 88-95.

[205] Testa M, Schümann J, Lu HM, Shin J, Faddegon B, Perl J, Paganetti H 2013, Experimental validation of the TOPAS Monte Carlo system for passive scattering proton therapy, Med. Phys. 40(12): 121719.

[206] Liu H, Zhang L, Chen Z, Liu X, Dai Z, Li Q, Xu XG 2017, A preliminary Monte Carlo study for the treatment head of a carbon-ion radiotherapy facility using TOPAS, EPJ Web Conf. 153: 04018.

[207] Le Foulher F, Bajard M, Chevallier M, Dauvergne D, Freud N, Henriquet P, Karkar S, Létang JM, Lestand L, Plescak R, Ray C, Schardt D, Testa E, Testa M 2010, Monte Carlo simulations of prompt-gamma emission during carbon ion irradiation, IEEE Trans. Nucl. Sci. 57(5): p. 2768-2772.

[208] Dedes G, Pinto M, Dauvergne D, Freud N, Krimmer J, Létang JM, Ray C, Testa E 2014, Assessment and improvements of Geant4 hadronic models in the context of prompt-gamma hadrontherapy monitoring, Phys. Med. Biol. 59(7): p. 1747-1772.

[209] Jeyasugiththan J, Peterson SW 2015, Evaluation of proton inelastic reaction models in Geant4 for prompt gamma production during proton radiotherapy, Phys. Med. Biol. 60(19): p. 7617-7635.

[210] Pinto M, Dauvergne D, Freud N, Krimmer J, Létang JM, Testa E 2016, Assessment of Geant4 prompt-gamma emission yields in the context of proton therapy monitoring, Front. Oncol. doi: 10.3389/fonc.2016.00010.

[211] Kelleter L, Wrońska A, Besuglow J, Konefał A, Laihem K, Leidner J, Magiera A, Parodi K, Rusiecka K, Stahl A, Tessonnier T 2017, Spectroscopic study of prompt-gamma emission for range verification in proton therapy, Phys. Med. 34: p. 7-17.

[212] Vanstalle M, Mattei I, Sarti A, Bellini F, Bini F, Collamati F, De Lucia E, Durante M, Faccini R, Ferroni F, Finck C, Fiore S, Marafini M, Patera V, Piersanti L, Rovituso M, Schuy C, Sciubba A, Traini G, Voena C, La Tessa C 2017, Benchmarking Geant4 hadronic models for prompt-γ monitoring in carbon ion therapy, Med. Phys. 44(8): p. 4276-4286.

[213] Verburg JM, Riley K, Bortfeld T, Seco J 2013, Energy- and time-resolved detection of prompt gamma-rays for proton range verification, Phys. Med. Biol. 58(20): L37-L49.

[214] Agodi C, Bellini F, Cirrone GAP, Collamati F, Cuttone G, De Lucia E, De Napoli M, Di Domenico A, Faccini R, Ferroni F, Fiore S, Gauzzi P, Iarocci E, Marafini M, Mattei I, Paoloni A, Patera V, Piersanti L, Romano F, Sarti A, Sciubba A, Voena C 2012, Precise measurement of prompt photon emission from 80 MeV/u carbon ion beam irradiation, JINST 7: P03001.

[215] Janssen FMFC, Landry G, Lopes PC, Dedes G, Smeets J, Schaart DR, Parodi K, Verhaegen F 2014, Factors influencing the accuracy of beam range estimation in proton therapy using prompt gamma emission, Phys. Med. Biol. 59(15): p. 4427-4441.

[216] Giacometti V, Guatelli S, Bazalova-Carter M, Rosenfeld AB, Schulte RW 2017, Development of a high resolution voxelised head phantom for medical physics applications, Phys. Med. 33: p. 182-188.

[217] Zarifi M, Guatelli S, Qi Y, Bolst D, Prokopovich D, Rosenfeld A 2019, Characterization of prompt gamma ray emission for in vivo range verification in particle therapy: A simulation study, Phys. Med. 62: p. 20-32.

[218] National Institute of Standards and Technology (NIST), Stopping-Power & Range Tables for Electrons, Protons, and Helium Ions, https://www.nist.gov/.

[219] Ziegler JF, Ziegler MD, Biersack JP 2010, The stopping and range of ions in matter (SRIM), Nucl. Instrum. Methods Phys. Res. B 268: p. 1818-1823, http://www.srim.org/.

[220] CERN, Geant4 Collaboration, GEANT4 Material Database.

[221] Arce P, Bolst D, Cutajar D, Guatelli S, Le A, Rosenfeld AB, Sakata D, Bordage M-C et al. 2020, Report on G4-Med, a Geant4 benchmarking system for medical physics applications developed by the Geant4 Medical Simulation Benchmarking Group, Med. Phys. doi: 10.1002/mp.14226.

[222] Grichine VM 2009, A simplified Glauber model for hadron-nucleus cross sections, Eur. Phys. J. C 62: p. 399-404.

[223] Folger G, Wellisch J, Ivanchenko VN 2004, The binary cascade: Nucleon nuclear reactions, Eur. Phys. J. A 21: p. 407-417.

[224] Mendoza E, Cano-Ott D, Evaluated neutron cross section libraries for the GEANT4 code (v2.0, 17/05/2018), International Atomic Energy Agency, https://www-nds.iaea.org/geant4/.

[225] Krimmer J, Chevallier M, Constanzo J, Dauvergne D, De Rydt M, Dedes G, Freud N, Henriquet P, Tessa CL, Létang JM, Pleskač R, Pinto M, Ray C, Reithinger V, Richard MH, Rinaldi I, Roellinghoff F, Schuy C, Testa E, Testa M 2015, Collimated prompt gamma TOF measurements with multi-slit multi-detector configurations, JINST 10: P01011.

[226] Lopes PC, Clementel E, Crespo P, Henrotin S, Huizenga J, Janssens G, Parodi K, Prieels D, Roellinghoff F, Smeets J, Stichelbaut F, Schaart DR 2015, Time-resolved imaging of prompt-gamma rays for proton range verification using a knife-edge slit camera based on digital photon counters, Phys. Med. Biol. 60(15): p. 6063-6085.

[227] Kozlovsky B, Murphy RJ, Ramaty R 2002, Nuclear deexcitation gamma-ray lines from accelerated particle interactions, Astrophys. J. Suppl. Ser. 141: p. 523-5241.

[228] Chadwick MB, Obložinský P, Herman M, Greene NM, McKnight RD, Smith DL, Young PG, MacFarlane RE et al. 2006, ENDF/B-VII.0: Next generation evaluated nuclear data library for nuclear science and technology, Nucl. Data Sheets 107: 2931.

[229] Koning AJ, Rochman D 2012, Modern nuclear data evaluation with the TALYS code system, Nucl. Data Sheets 113: p. 2841-2934.

[230] International Atomic Energy Agency, Nuclear Data Services, date accessed: 05/06/20 https://www-nds.iaea.org/.

[231] Zarifi M, Guatelli S, Bolst D, Hutton B, Rosenfeld A, Qi Y 2017, Characterization of prompt gamma-ray emission with respect to the Bragg peak for proton beam range verification: A Monte Carlo study, Phys. Med. 33: p. 197-206.

[232] Hueso-González F, Enghardt W, Fiedler F, Golnik C, Janssens G, Petzoldt J, Prieels D, Priegnitz M, Römer KE, Smeets J, Stappen FV, Wagner A, Pausch G 2015, First test of the prompt gamma ray timing method with heterogeneous targets at a clinical proton therapy facility, Phys. Med. Biol. 60(16): p. 6247-6272.

[233] Amptek 2017, Charge Sensitive Preamplifier A250, Specification Sheet.

[234] Cremat 2020, CR-110-R2.1 charge sensitive preamplifier: Application guide.

[235] WWW Table of Radioactive Isotopes, The Lund/LBNL Nuclear Data Search, date accessed: 30/05/18 http://nucleardata.nuclear.lu.se/toi/.

[236] Saint-Gobain Crystals 2020, User guide for SiPM based radiation sensors, Rev C MAN-690-001.

[237] Saint-Gobain Crystals 2019, Scintillation Products, Technical Note, Lanthanum Bromide Scintillators, Performance Summary.

[238] Photonis 2007, Photomultiplier Tube Catalogue, D-PMT-CAT2007.

[239] Orwiler B 1969, Vertical Amplifier Circuits, Circuit Concepts 1st ed., Beaverton, OR: Tektronix, p. 461.

[240] Shannon CE 1948, A mathematical theory of communication, Bell Sys. Tech. J. 27(3): p. 379-423.

[241] Shannon CE 1949, Communication in the presence of noise, Proc. IRE 37(1): p. 10-21.

[242] Nyquist H 1928, Certain topics in telegraph transmission theory, Trans. AIEE. 47(2): p. 617-644.

[243] Whittaker ET 1915, XVIII.–On the functions which are represented by the expansions of the interpolation theory, Proc. Royal Soc. Edinburgh, 35: p. 181-194.

[244] Derenzo S, Boswell M, Weber M, Brennan K, Lawrence Berkeley National Laboratory, Scintillation Properties, date accessed: 30/05/18 http://scintillator.lbl.gov/.

[245] Saint-Gobain Crystals, Scintillation Crystal Materials, date accessed: 30/05/18 https://www.crystals.saint-gobain.com/products/crystal-scintillation-materials.

[246] Saint-Gobain Crystals 2019, Revolutionary detection technology, 18113: p. 1-10.

[247] Saint-Gobain Crystals, Efficiency Calculations for Selected Scintillators, Efficiency Calculations Brochure.

[248] Petzoldt J, Roemer KE, Enghardt W, Fiedler F, Golnik C, Hueso-González F, Helmbrecht S, Kormoll T, Rohling H, Smeets J, Werner T, Pausch G 2016, Characterization of the microbunch time structure of proton pencil beams at a clinical treatment facility, Phys. Med. Biol. 61(6): p. 2432-2456.

[249] CERN 2020, Geant4 A Simulation Toolkit, Guide for Physics Lists Release 10.6, Rev4.1.

[250] CERN 2020, Geant4 A Simulation Toolkit, Physics Reference Manual Release 10.6, Rev4.1.

[251] Ribon A 2016, Geant4 Hadronic Physics: Highlights of version 10.2 and Work Plan for 2016, Geant4 Technical Forum.

[252] Chi Y, Chalise A, Shao Y, Jin M 2018, Comparison of prompt gamma yield from C-11 and C-12 ion beams using Monte Carlo simulations, IEEE NSS MIC doi: 10.1109/NSSMIC.2018.8824433.

[253] ROOT Reference Guide, TSpectrum Class Reference, date accessed: 15/07/19 https://root.cern.ch/doc/v608/classTSpectrum.html.

[254] Flanz J, Kooy H, DeLaney TF 2012, The Francis H. Burr Proton Therapy Center, Ion Beam Therapy 320: p. 597-609.

[255] Hoff G, Firmino SF, da Souza WP 2009, Influence of shielding composition on transmission curves determination for diagnostic radiology: A Monte Carlo study using the GEANT4 code, IEEE NSS Conference Record N13-93: p. 540-543.